ELECTROCHEMICAL, QUANTUM CHEMICAL CALCULATION AND MOLECULAR DYNAMIC SIMULATION STUDIES ON SOME QUINOXALINE DERIVATIVES AS CORROSION INHIBITORS FOR MILD STEEL IN ACIDIC MEDIUM

LUKMAN OLAWALE OLASUNKANMI

ELECTROCHEMICAL, QUANTUM CHEMICAL CALCULATION AND MOLECULAR DYNAMIC SIMULATION STUDIES ON SOME QUINOXALINE DERIVATIVES AS CORROSION INHIBITORS FOR MILD STEEL IN ACIDIC MEDIUM

LUKMAN OLAWALE OLASUNKANMI

B.Sc. (Hons), M.Sc., Obafemi Awolowo University, (OAU) Ile-Ife, Nigeria

A thesis submitted in fulfilment of the requirements for the award of Doctor of Philosophy (PhD) degree in the

Department of Chemistry

Faculty of Agriculture, Science and Technology,

North-West University (Mafikeng Campus)

Supervisor: Professor Eno E. Ebenso

November 2015

DECLARATION

I declare that this thesis and the work contained therein are carried out by me and appropriate references were cited where the intellectual properties of other researchers were referred.

.....

Lukman O. Olasunkanmi

November 2015

DEDICATION

To the ones I tout as the other three-quarters that complement me (my world): Omowumi, Olatomiwa and Olatomade in honour of their cooperation, perseverance and understanding.

TABLE OF CONTENTS

ACKNOWLEDGEMENT

All praises, thanks and adorations are due to Allah (Subhana Watahala), the author of authors, by whose decree everything comes through or otherwise: “the pen has been lifted and the ink has dried”. I simply thank God for everything!

My profound gratitude goes to my mentor and supervisor, Professor Eno E. Ebenso for granting me the opportunity of schooling under his tutelage, for believing in me, for his encouragement, support, and dedications to well-being and happiness of his students. Prof., you are just the best and you will forever be!

I sincerely acknowledge the combined funding supports from the Sasol Inzalo Foundation and National Research foundation (NRF) South Africa, for PhD fellowship, and also the financial support for academic staff training and development from the Tertiary Education Trust Fund (TETFund) Nigeria.

I acknowledge the contributions of the Centre of Research Excellence in Corrosion, Research Institute, King Fahd University of Petroleum and Minerals, Kingdom of Saudi Arabia, and Dr. Ime B. Obot for providing the software for, and assisting with the Molecular dynamics simulations studies.

I acknowledge the support and contributions of all members of Professor Ebenso’s research group (Material Science Innovation and Modelling Research Focus Area) including, Drs. Mwadham M. Kabanda, Abolanle S. Adekunle, Sasikumar Yesudass, Indra Bahdur, Baskar Ramaganthan, Mrs Fayemi, Messrs Alo, Murulana, Gnanapragasam, Ms Boikanyo and Mphuthi, to mention but a few. Colleagues, space will not permit me to mention all names and/or define “contributions-per-colleague” but sincerely, you have all contributed to this feat. My profound appreciations also go to Ms Maggy Medupe for always striving and ensuring that things go well with all us in the group. Thank you Ausi Maggy! I also thank Mr.

Francis Lugayizi for his assistance. I am grateful to all members of staff of the Department of Chemistry, NWU, Mafikeng Campus for their assistance in various forms.

I also use this opportunity to thank Mr. Adedamola Shobo, my flatmate and big brother at the Postgraduate Residence. Mafikeng would have been extremely boring without you. Special thanks to my "all-time" friends, Arch. Bode Olowolafe, Messrs Bode Sunmonu, Lukman Anisere, Olaonipekun Oyebanjo, and a whole lot of others whose names are too numerous to insert into this little space but have contributed to my academic pursuit thus far. I thank you all buddies! I also thank all my friends both in Nigeria and Mzansi, both Nigerians and South Africans that have made imparts in my life in one way or the other and thereby making this degree a reality.

My profound gratitude goes to all members of staff in the Department of Chemistry, Obafemi Awolowo University, Ile-Ife Nigeria for carrying my workloads with theirs while I was away pursuing this degree. I thank you all for your love and prayers.

I thank my father, Mr. Olasunkanmi Adigun and my mother Mrs Fatimah Olasunkanmi for their fervent prayers that have taken me thus far in life. I have come to know the power of prayer through you, dad and mum. I also acknowledge the supports I received from all my siblings. Thank you all. I thank my parents-in-law, Mr. and Mrs Ariyo for their constant prayer, and my sisters-in-law, Bushira and Monsurah Ariyo for their supports to my immediate family while I was away from home pursuing PhD degree in South Africa.

Special appreciations go to my wife, Riskat Omowumi Olasunkanmi (Nee Ariyo) for being my bone, flesh, and soul. Babe, I appreciate your cooperation, perseverance, love and prayers. Finally, I thank my son and daughter, Abdulsalam Olatomiwa and Sekinah Olatomade respectively for believing in my course and enduring the challenges of distance father-children relationship that we had to share while I was away from home. I love you kids.

ABSTRACT

This thesis reports the inhibition of mild steel (MS) corrosion in 1 M HCl solution by seventeen (17) selected quinoxaline derivatives that comprise the quinoxalinyl, pyrazolyl and phenyl rings in a single molecular entity. All the compounds investigated in this work contain the 6-(3-phenyl-4,5-dihydro-1H-pyrazol-5-yl)quinoxaline group and only differ in the substituent groups on the pyrazolyl and/or phenyl ring(s).

The adsorption characteristics and corrosion inhibition properties of these compounds were investigated for MS in 1 M HCl solution at 303 K using electrochemical, spectroscopic, quantum chemical calculation and molecular dynamic simulation methods.

All the studied compounds showed appreciable inhibition performances. The compounds inhibit MS corrosion by adsorbing on the active sites on the steel surface without changing the mechanism of the corrosion process. All the studied compounds are mixed-type inhibitors and their adsorption conforms to the Langmuir isotherm model. The trends of the inhibition efficiency are: Me-4-PQPB > Mt-3-PQPB > oxo-1,3-PQPB > Mt-4-PQPB (for GROUP I); PQDPP > PQBPB > PPQDPE (for GROUP II); MS-3-PQPP > MS-4-PQPP > MS-2-PQPP (for GROUP III); MS-3-PQPMS > MS-2-PQPMS > MS-4-PQPMS (for GROUP IV); and Mt-3-PQPP > Cl-4-PQPP, and also (based on average values of percentage inhibition efficiency) MS-2-PQPA > MS-4-PQPA (for GROUP V). The thermodynamic adsorption parameters for all the studied compounds suggest mixed physisorption and chemisorption mechanisms. Electrochemical impedance spectroscopy measurements revealed that the compounds adsorbed on MS surface to form protective film with pseudo-capacitive characteristics. It was deduced from the studies on the GROUP II compounds that the chain length/type of carbonyl substituent on the pyrazole ring affects the inhibition strength such that the most efficient compound in this group (PQDPP) is the one with the shortest carbonyl

chain and the observation is in agreement with the established trend of reactivity of carbonyl compounds. The combination of electronic and steric effects attributed to the methanesulphonamido group appeared to favour higher inhibition efficiency when the group is attached to position 3 compared to position 2 or 4 on the phenyl ring. This accounts for the highest inhibition efficiency observed for MS-3-PQPP (in GROUP III) and MS-3-PQPMS (in GROUP IV) compared to other compounds in their respective groups.

Quantum chemical parameters suggest that the studied compounds have the tendency of accepting charges from the metal in a retro-donation step during the donor-acceptor interactions between the inhibitor molecules and MS and that protonated species of the inhibitors might also be involved in the adsorption process. The HOMO, LUMO, and Fukui indices showed that the quinoxaline ring in all the studied compounds is generally electron-deficient, while the pyrazole ring is a π-electron rich centre in conformity with the general notion of the chemical reactivity of heterocyclic compounds. Molecular dynamic simulation studies revealed that the adsorption/binding energies of the inhibitor/Fe (110) systems for the GROUPs II, III, IV and V compounds are in good agreement with the order of inhibition efficiencies of the inhibitor molecules. The non-correlation of order of adsorption energies of the inhibitor/Fe (110) systems for the GROUP I compounds with the observed trend of protection efficiencies might be due to the fact that the theoretical simulation considers only non-covalent interactions, whilst both covalent and non-covalent interactions are most likely to feature in the experiment.

LIST OF ABBREVIATIONS

AM1	Austin model 1
AMBER	Assisted model building with energy refinement
CC	Coupled cluster theory
CE	Counter electrode
CFF	Consistent force field
CHARMM	Chemistry at Harvard macromolecular mechanics
CHEAT	Carbohydrate hydroxyls represented by external atoms
CI	configuration interaction
CNDO	Complete neglect of differential overlap
CPE	Constant phase element
DFT	Density functional theory
ECEPP	Empirical conformational energy program for peptides
EFF	Empirical force field
EHT	Extended Huckel theory
EIS	Electrochemical impedance spectroscopy
FMO	Frontier molecular orbital
GPES	General purpose electrochemical system
GROMOS	Gronigen molecular simulation
GTO/GTF	Gaussian-type orbital or function
GVB	Generalized valence bond
GVB	Generalized valence bond

HF	Hartree-Fock
HOMO	Highest occupied molecular orbital
HT	Huckel theory
INDO	Intermediate neglect of differential overlap
LCAO	Linear combination of atomic orbitals
LDA	Local density approximation
LPR	Linear polarization resistance
LSDA	Local spin density approximation
LUMO	Lowest unoccupied molecular orbital
MS	Mild Steel
MC	Monte Carlo
MCSCF	Multi-configurational self-consistent field
MD	Molecular dynamics
MINDO	Modified intermediate neglect of differential overlap
MM	Molecular mechanics
MMFF	Merck molecular force field
MNDO	Modified neglect of differential overlap
MO	Molecular orbital
MP	Moller-Plesset
NACE	National association of corrosion engineers
NDDO	Neglect of diatomic differential overlap
NDO	Neglect of differential overlap

OCP	Open circuit potential
OPLS	Optimized potentials for liquid simulation
PDP	Potentiodynamic polarization
PES	Potential energy surface
PM3	Parameterization method 3
PM6	Parameterization method 6
PPP	Pariser-Parr-Pople
PRDDO	Partial retention of diatomic differential overlap
QM	Quantum mechanics
RE	Reference electrode
RHF	Restricted Hartree-Fock
SAM1	Semi-ab initio method 1
SCF	Self-consistent field
SEM	Scanning electron microscope
SINDO	Symmetrically orthogonalized intermediate neglect of differential overlap
STO/STF	Slater-type orbital or function
SWE	Schrodinger wave equation
UFF	Universal force field
UHF	Unrestricted Hartree-Fock
VWN	Vosko, Wilks and Nusair
WE	Working electrode
ZAR	South African Rand

ZDO	Zero differential overlap
ZINDO	Zerner's intermediate neglect of differential overlap
Me-4-PQPB	1-[3-(4-methylphenyl)-5-(quinoxalin-6-yl)-4,5-dihydropyrazol-1-yl]butan-1-one
Mt-4-PQPB	1-(3-(4-methoxyphenyl)-5-(quinoxalin-6-yl)-4,5-dihydro-1H-pyrazol-1-yl)butan-1-one
Mt-3-PQPB	1-[3-(3-methoxyphenyl)-5-(quinoxalin-6-yl)-4,5-dihydropyrazol-1-yl]butan-1-one
Oxo-1,3-PQPB	1-[3-(2H-1,3-benzodioxol-5-yl)-5-(quinoxalin-6-yl)-4,5-dihydropyrazol-1-yl]butan-1-one
PQDPB	1-[3-phenyl-5-quinoxalin-6-yl-4,5-dihydropyrazol-1-yl]butan-1-one
PQDPP	1-(3-phenyl-5-(quinoxalin-6-yl)-4,5-dihydro-1H-pyrazol-1-yl)propan-1-one
PPQDPE	2-phenyl-1-[3-phenyl-5-(quinoxalin-6-yl)-4,5-dihydropyrazol-1-yl]ethanone
MS-4-PQPP	N-{4-[1-propanoyl-5-(quinoxalin-6-yl)-4,5-dihydropyrazol-3-yl]phenyl}methanesulfonamide
MS-2-PQPP	N-(2-(1-propanoyl-5-(quinoxalin-6-yl)-4,5-dihydro-1H-pyrazol-3-yl)phenyl)methanesulfonamide
MS-3-PQPP	N-(3-(1-propanoyl-5-(quinoxalin-6-yl)-4,5-dihydro-1H-pyrazol-3-yl)phenyl)methanesulfonamide
MS-4-PQPMS	N-(4-(1-(methanelsulfonyl)-5-(quinoxalin-6-yl)-4,5-dihydro-1H-pyrazol-3-yl)phenyl)methanesulfonamide
MS-3-PQPMS	N-{3-[1-(methylsulfonyl)-5-(quinoxalin-6-yl)-4,5-dihydro-1H-pyrazol-3-yl]phenyl}methanesulfonamide

MS-2-PQPMS	N-(2-(1-(methanesulfonyl)-5-(quinoxalin-6-yl)-4,5-dihydro-1H-pyrazol-3-yl)phenyl)methanesulfonamide
Mt-3-PQPP	1-[3-(3-methoxyphenyl)-5-(quinoxalin-6-yl)-4,5-dihydropyrazol-1-yl]propan-1-one
Cl-4-PQPP	1-(3-(4-chlorophenyl)-5-(quinoxalin-6-yl)-4,5-dihydro-1H-pyrazol-1-yl)propan-1-one
MS-4-PQPA	N-{4-[1-acetyl-5-(quinoxalin-6-yl)-4,5-dihydropyrazol-3-yl]phenyl}methanesulfonamide
MS-2-PQPA	N-{2-[1-acetyl-5-(quinoxalin-5-yl)-4,5-dihydropyrazol-3-yl]phenyl}methanesulfonamide

LIST OF FIGURES

LIST OF TABLES

CHAPTER 1

INTRODUCTION

1.1 Introduction and problem statement

Mild steel (MS) is an alloy of choice for various industrial and structural applications. This is due to its high strength to mass ratio and relatively low cost. Many industrial processes including acid pickling, acid cleaning, acid descaling and oil-well acidizing involve the use of mineral acids [1-4], which unarguably constitute strong corrosive environment for MS. For instance, oil-well acidizing is an essential production practice in the oil and gas industries during which a large amount of mineral acid is pumped into the oil-wells in order to improve productivity and injectivity of the oil-well [5]. Hydrochloric acid is used much often than other mineral acids in this regards as a result of its availability and economic advantage [2, 6-9]. Corrosion of MS constitutes serious economic loss and poses safety problems to the concerned industries. The average cost incurred on corrosion worldwide is estimated to be above $1.8-trillion, while the direct cost incurred on corrosion in South Africa is estimated to be around 130-billion ZAR [10]. A number of safety problems associated with steel corrosion may include breakdown of equipment and production lines, pipeline leakage and explosion etc., which may bring about fatal injuries in some extreme cases [11]. Therefore, industries continue to pay premium attention to the prevention of steel corrosion in order to reduce the effects of economic and safety problems associated with corrosion process.

Quinoxaline derivatives are among the non-toxic organic compounds with proven good corrosion inhibition properties [12, 13]. They are important class of nitrogen-containing heterocycles whose fragments are found in a large number of natural products and biologically active compounds possessing anti-inflammatory, antiviral, antiprotozoal, antibacterial, anticancer, antiulcer properties and kinase inhibitory activity [12-18]. A number of more efficient methods of synthesis of quinoxaline derivatives have been developed in the recent times due to the possibility of wide range of applications of the compounds [19-23].

The development of various relatively easy and efficient synthetic methods have led to continuous emergence of new quinoxaline compounds with extended/conjugated pi-electrons networks and multiple heteroatoms that portray them to be promising efficient corrosion inhibitors. Moreover, the adsorption behaviour and corrosion inhibition mechanisms of an inhibitor depend on quite a number of factors and may vary from one medium or protecting metal substrate to another. Therefore, investigation of the mode of adsorption, corrosion inhibition mechanisms and inhibition efficiencies of new potential inhibitors is an important area of chemical and material science research.

Survey of literature revealed that some works have been reported on applications of quinoxaline derivatives as inhibitors for Cu and steel corrosion in acidic media including HCl, HNO_3 and H_2SO_4 [12, 13, 24-31]. But despite the proven corrosion inhibition properties of this family of compounds, the number of literature reports on their inhibition potentials for MS in HCl is still few when compared to the large number of existing compounds belonging to this family. Even where such data on the corrosion inhibition properties of quinoxaline derivatives were reported for MS in HCl, comprehensive studies that combine electrochemical methods and theoretical techniques involving detailed quantum chemical calculations of neutral and protonated molecules, quantitative structure activity relationship (QSAR) and Monte Carlo simulations are very rare.

For this purpose, this doctoral research work investigates the adsorption behaviour and corrosion inhibition properties of some quinoxaline-based compounds on MS in HCl medium. The group of compounds investigated in this study are structurally related such that they all contain the 6-(3-phenyl-4,5-dihydro-1H-pyrazol-5-yl)quinoxaline as a common nucleus and differ only in the type and position of substituent groups, R and R` as shown in Figure 1.1. The seventeen compounds investigated in this work only differ in the type of the substituent groups, R as well as the type and position of the substituent groups, R`. These

compounds have not been considered as corrosion inhibitors in any previous works. The adsorption characteristics and corrosion inhibition properties of the compounds were studied using electrochemical methods, spectroscopic techniques, quantum chemical calculations, and Monte Carlo simulations approaches.

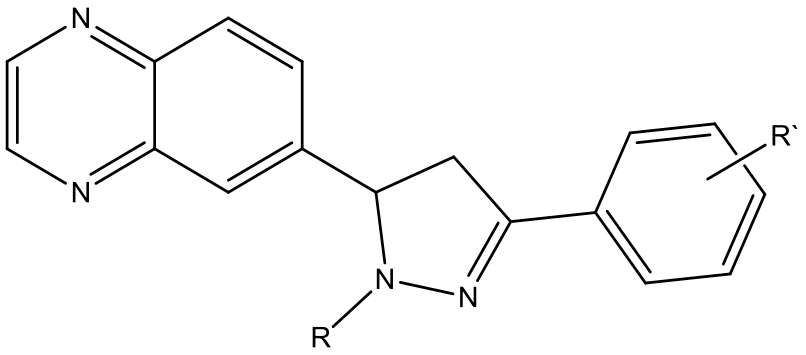

Figure 1.1. General molecular structure of the quinoxaline derivatives used in this study. The seventeen compounds reported in this work only differ in the type of the substituent group, R as well as the type and position of the substituent group, R`.

1.2 Aim and objectives of the study

The main aim of this study is to investigate the corrosion inhibition properties of a set of quinoxaline derivatives that contain common nucleus of the quinoxaline ring with 3-phenyl-4,5-dihydropyrazolyl substituent at position 6 of the ring. The specific objectives of the work include:

i. Investigation of corrosion inhibition efficiency of the studied compounds on MS corrosion in 1 M HCl solution using Tafel plots and electrochemical impedance spectroscopic (EIS) methods.

ii. Investigation of the corrosion inhibition mechanisms and modes of adsorption of the quinoxaline derivatives on MS in 1 M HCl solution.

iii. Investigation of interactions between MS and the studied quinoxaline derivatives in solution using spectroscopic techniques.

iv. Quantum chemical study on the propensity of the studied compounds to get protonated in acid medium.

v. Correlations of quantum chemically derived molecular and electronic parameters with the experimental results.

vi. Theoretical investigation of the mode of adsorption of the studied compounds on iron surface using the Monte Carlo simulations approach.

1.3 Scope of the study

The scope of the study reported in this thesis covers the adsorption and corrosion inhibition behaviour of seventeen quinoxaline derivatives on MS in 1 M HCl at room temperature using electrochemical, quantum chemical and Monte Carlo simulations methods.

CHAPTER 2

LITERATURE REVIEW

2.1 Basics of corrosion

The word “corrode” is a verb derived from the Latin word “*corrodere*”, which means “to gnaw into pieces”. The word “corrosion” is a noun derived from the word “corrode”. In literary language therefore, corrosion refers to the process by which a material is gnawed into pieces. In a more technical language and for the purpose of this thesis, corrosion is defined as the chemical or electrochemical reaction between a material and its environment that leads to the deterioration of the material and alteration of its intrinsic properties [32-35]. According to Stansbury and Buchanan [36], the term materials refer to substances used in the construction of machines, processing equipment, and other manufactured products. These include metals, polymers and ceramics. The environments may be a gas, liquid, hybrid solid-liquid, or even solid. Every environment is corrosive to some extent, and the corrosion rate depends among other factors on the degree of aggressiveness of the environment.

Although the definition of corrosion provided above is applicable to different forms of materials, corrosion is often reservedly used for metals and metal alloys. For this reason, corrosion has been described as retro-extractive metallurgy in which metals tend to return to their most stable natural states (ores) after their extracted (elemental) forms have been exposed to some natural or synthetic environments [33]. This description of corrosion was made by Fontana [33] and it considers corrosion of metals as a thermodynamically favourable process. The thermodynamic favourability of corrosion is attributed to the fact that metals are less stable in their elemental forms but more stable in their combined states as ores. Extraction of metals from their ores is a process that requires a large amount of energy and therefore cannot occur naturally. However, extracted metals in their elemental forms have the natural tendency to return their most stable states. Since it is not possible to reverse the law of thermodynamics, complete circumvention of corrosion process is simply, utterly impossible.

Notwithstanding the impossibility of avoidance of corrosion, various methods of reducing the rate at which corrosion reaction proceeds have been identified. These include material selection, coating, cathodic protection, special designs, and use of corrosion inhibitors [34, 37]. The suitability of a prevention method in checking the rate of metal corrosion depends on the nature of the metal, nature of the environment, and most importantly, the type of corrosion that is being combated. A detailed description of the corrosion behaviour of a material requires the knowledge of the identity and characteristics of the material. One of the reasons why studies on corrosion and corrosion prevention continue to be a dynamic area of research is the fact that the corrosion behaviour of a metal and its optimum prevention depend on quite a number of factors.

2.2 Types of corrosion

There is no simple classification for corrosion types or forms. Different authors have classified corrosion using different factors and criteria. Among the common classifications are those based on the corrosion mechanism and/or appearance of the corroded metal, However, corrosion forms can also be classified based on whether it is electrochemical or direct chemical reactions, and also based on the medium, which may be “wet” or “dry”. A “wet” corrosive medium is the one in which liquid or moisture is involved, while a “dry” corrosive environment usually contains high-temperature gases. Corrosion processes can be broadly classified as uniform/general and localized corrosion. There are various types of localized corrosion, which also can be divided into sub-categories as macroscopic and microscopic corrosion depending on the amount of metals dissolved in the process. Various forms of localized corrosion include galvanized corrosion, erosion corrosion, crevice, pitting, exfoliation and dealloying, which are in the macroscopic sub-category. Others include, intragranular, stress-corrosion, cracking, and corrosion fatigue, which are forms of

microscopic corrosion [33-35, 38-40]. This study focuses on uniform or general corrosion of MS in 1 M HCl medium.

2.3 Corrosion control methods

There are various methods of controlling corrosion just as there are different types of corrosion. Choosing a suitable corrosion control method depends on a number of factors such as the type of corrosion, nature of environment, nature of metal, maintenance or control cost etc. All the corrosion prevention/control methods have to do with either changing/modifying the material/metal or the active environment in a way that will reduce corrosion susceptibility [38]. However, no particular method has been adjudged to be most effective or suitable for all forms of corrosion. This makes all the methods to be relevant in one way or the other and still form important areas of research being explored by "corrosionists". Common corrosion control methods include:

- *Material selection:* this is a method of controlling corrosion by choosing a material that does not corrode (readily) in the prevailing environment. While choosing a corrosion resistance material is a good idea, such materials are usually very expensive thereby making the method sometimes impracticable. Striking a balance between material cost and optimum corrosion resistance material is generally not a straightforward task [35, 41-44].

- *Proper design:* this method has to do with adoption of special designs that eliminate accumulation of water on the metal surface, or metallic part of an equipment or structure. Proper design may offer a good and inexpensive method of corrosion prevention if all the necessary intricacies are put into consideration. However, the major challenge in using this method is that the choice of a design cannot be made rigid as it has to meet certain other crucial criteria apart from reducing corrosion propensity. More so, designers might lack adequate knowledge of corrosion properties of the metal and active environment unlike

corrosion engineers. A wrong design may be unnecessarily costly and yet not able to address corrosion problems (optimally) [35, 45, 46].

- *Cathodic and anodic protection:* this method involves modification of the electrochemical potential of the metal by shifting it to a more negative (cathodic) or a more positive (anodic) value. A more negative shift increases the immunity of the metal against corrosion thereby making it to be more reducing in the particular environment and it is called cathodic protection [35, 47-49]. On the other hand, a more positive shift enhances the passivity behaviour of the metal being protected such that it becomes more oxidizing in the corrosive environmental and it is referred to as anodic protection [35, 50-52].

- *Protective coatings:* metals and metal alloys are often coated with relatively inactive materials, which may be organic, metallic or non-metallic (inorganic) coatings. The coatings applied to a surface being protected may be multifunctional such that besides corrosion control, properties like aesthetic surface appearance, abrasion and impact resistance, electrical insulation etc. might also be added to the metal. The modes by which coatings and linings protect active metal surface include barrier protection in which the metal is completely isolated from the active environment, chemical inhibition in which some inhibitive pigments are added to paints reduce corrosion rate, or galvanic/sacrificial protection in which a more active metal is being used as coatings or linings [35, 53, 54].

- *Corrosion inhibitors:* this involves the use of chemical substances that can reduce corrosion rate in the active environment by adsorbing as a thin film on metal surface, inducing the formation of a thick corrosion product, forming a passive film, or changing the characteristics of the environment. Corrosion inhibitors may be considered as an integral part of protective coatings method as they may also form protective film or barrier on the substrate being

protected, or as a separate method of corrosion control due to other possible mechanisms or inhibition [35].

2.4 Mild (low carbon) steel: composition, uses, and corrosion problems

Carbon steels contain up to about 1.0% C and generally less than 2.0% of other alloy constituents by weight with the major constituent being iron (Fe) [35]. They are often subtly categorized into three classes depending on the percentage of C present in the steel. The low-carbon or MSs containing about 0.08 – 0.28% C, the medium-carbon steels with about 0.28 – 0.55% C, and the high-carbon groups containing about 0.5-1.0% C [55]. Other elements commonly employed as alloying materials for Fe include manganese, silicon, sulphur, phosphorus, chromium, molybdenum, nickel, vanadium and columbium [35, 55]. The amount of these constituents including carbon may vary depending on the required properties of the alloy. Carbon steels are used in large quantities in various areas including marine applications, nuclear and fossil fuel power plants, transportation, chemical processing, mining, construction, reaction vessels, tunnels, metal processing equipment etc. [35, 56]. They are characterized with relatively high mechanical strength and low cost compared to other metal alloys [57-61]. Each area of application of carbon steel is associated with some corrosion problems that threaten the life span of the steel. MS (MS) being relatively more corrosion resistant than the other groups of carbon steels has attracted much more attentions in various areas of applications. Though MS might be able to withstand the adversity in some corrosive atmospheres and waters, it cannot resist attack in very aggressive environments especially those containing solutions of strong acids such as HCl, H_2SO_4, or HNO_3, which are usually found in many industries.

2.5 Corrosion inhibitors

In order to reduce the rate of MS corrosion in common industrial corrosive environments, corrosion inhibitors are often added to the acid solutions used in the industries. According to the National Association of Corrosion Engineers (NACE), corrosion inhibitor is defined as a substance which retards corrosion when added to an aggressive/corrosive environment in small concentrations [62, 63]. The use of corrosion inhibitors has gained volume of attentions in the past few years because it is economical, convenient, and effective [64-71]. In addition, corrosion inhibitors can be added in situ during the production process, making it a flexible means of controlling corrosion. The existing data has revealed that organic compounds containing sulphur (S), nitrogen (N), oxygen (O) and/or phosphorus (P) heteroatoms, pi-electrons containing functional groups, and aromatic rings often exhibit good corrosion inhibition properties [67, 72-81]. Furthermore, it has been reported that the order of corrosion inhibition efficiency of organic compounds that differ only in the heteroatom is O < N < S < P, which is also related to their order of decreasing electronegativity: O (3.5) > N (3.0) > S (2.5) > P (2.1) [82-88]. This suggests that corrosion inhibition has to do with the tendency of organic molecules to adsorb on metallic surface through the electron donating sites (heteroatoms) in the inhibitor molecule. A less electronegative atom holds its electrons less tightly and makes its electrons readily available for favourable interactions with the metal during the adsorption process. In another development, N-containing organic compounds have been found to be more effective for inhibition in HCl medium, while S-containing compounds have been reported to give optimum inhibition performance in H_2SO_4 medium [89-91]. Compounds that contain two or more different heteroatoms have also been found to be show high corrosion inhibition potentials in acidic media [90, 91].

The choice of suitable corrosion inhibitors for a particular corrosion problem depends on a number of factors such as environmental friendliness, stability of the inhibitor molecule,

satisfactory inhibition efficiency, cost, etc. The specificity of inhibitive action of most of these compounds also sometimes necessitates the combination of two or more compounds as mixed inhibitors with synergistic characteristics to achieve optimum inhibition performance in the active environment. The quest for new class of non-toxic corrosion inhibitors with good inhibition efficiency is still an active area of research. More so, inhibitors may adsorb on metal surface by electrostatic interactions between neutral or protonated inhibitor molecules and charged metal surface [92]. Therefore, the study of the adsorption behaviour and corrosion inhibition mechanisms of new potential inhibitors is very important.

2.6 Metal in aqueous solutions and the theory of electrochemical corrosion

All metals with the exception of gold are considered to be in active state and undergo electrochemical reactions when exposed to an atmospheric or aqueous environment. The surface of active metals is covered by oxide films upon exposure to air. These oxide films generally have some passive characteristics and protect the metal surface from further direct contact with the environment [93, 94]. However, the oxide films tend to dissolve in aqueous solution especially in acidic medium thereby leaving a bare metal surface and the metal once again assumes the active state. The solubility of the oxide is much lower in near-neutral solutions than in acid solution and the extent of metal dissolution in the neutral medium tends to be smaller due to the relative intactness of the oxide film that covers the metal surface [93-95]. However, when there is a form of discontinuity in the metal, probably due to the presence of an inclusion or a grain boundary, the metal surface can be exposed at some localized points where the protective oxide film is thinner and the extent of dissolution at such points will be more than other areas. The presence of inhibiting anions in the near-neutral medium tends to slow down metal dissolution by stabilizing the oxide film and make

it a passivating oxide film, which can effectively prevent metal corrosion. During this period, the metal is said to be in the passive state [93, 96].

When the bare surface of a metal is exposed to an aqueous solution, the metal undergoes dissolution (corrosion); leading to the introduction of positively charged metal ions into the solution and the metal is left with electrons. This process can be summarized with the reaction equation:

$$M_{(s)} \rightarrow M^{n+}_{(aq)} + ne^- \quad (2.1)$$

where $M_{(s)}$ is the metallic atom at the metal surface in solid state, M^{n+} is the positively charged metal ion carrying *n* positive charges in aqueous solution, e- is the negatively charged electron, and *n* is the number of electrons. Equation 2.1 brings about an increase in the potential difference between the metal and the solution. This is due to the accumulation of residual negatively charged electrons on the metal surface. This potential difference, which is called the electrode potential or the potential of the metal becomes more negative [93, 94, 96]. This change in the potential tends to retard the dissolution of metal ions but to encourage the deposition of dissolved metal ions from the solution onto the metal, in other words, the reverse of the reaction represented by Equation 2.1 becomes favourable, and the reversible process can be expressed as:

$$M^{n+}_{(aq)} + ne^- \rightleftharpoons M_{(s)} \quad (2.2)$$

If the reversible dissolution and deposition reactions between metal and metal ions continue, the metal will reach a stable potential (reversible potential, E_r) at which the rate of dissolution equals to the rate of deposition. The value of E_r depends on the concentration of dissolved metal ions in solution and the standard reversible potential E^o for unit activity of dissolved metal ions, $a_M{}^{n+}$, and can be expressed as [35, 38, 93]:

$$E_{r,M^{n+}/M} = E^{o}_{M^{n+}/M} + \frac{RT}{nF}\ln a_{M^{n+}} \quad (2.3)$$

where R is the gas constant (8.314 $Jmol^{-1}K^{-1}$), T is the absolute temperature, F is the Faraday constant (96,500 $Cmol^{-1}$) and *n* the number of electrons transferred per ion. There is no further net dissolution of metal when the potential equals to the E_r. The net amount of metal that dissolves during the process depicted by Equation 2.2 is generally very small. In this regards, attainment of E_r could imply a halt of metal dissolution (corrosion reaction). However, this is generally not the case because in practice, the potential of a metal in solution does not reach the E_r but remains more positive due to the removal of the residual electrons from the metal by some co-reactions. In acidic medium, hydrogen ions from the solution tend to adsorb on metal surface and react with the residual electrons leading to the reduction of hydrogen ions and production of hydrogen gas according to the equation:

$$2H^{+}_{(aq)} + \quad 2e^{-} \quad \rightleftharpoons \quad H_{2(g)} \quad (2.4)$$

The hydrogen reduction reaction hinders the attainment of E_r and ensures continuous dissolution or corrosion of metal in solution. The hydrogen ion reduction reaction in Equation 2.4 is also reversible and has the tendency of attaining the reversible potential, $E_{r,H^{+}/H_2}$ given as [35, 37, 38, 93]:

$$E_{r,H^{+}/H_2} = E^{o}_{H^{+}/H_2} - \frac{RT}{F}\ln\frac{p_{H_2}^{1/2}}{a_{H^{+}}} \quad (2.5)$$

where p_{H_2} is the partial pressure of the hydrogen gas, a_M^{n+} is the unity activity of hydrogen ion in solution, $E^{o}_{H^{+}/H_2}$ is the standard hydrogen potential, while R, T and F retain their definitions as in Equation 2.3. In principle, attainment of $E_{r,H^{+}/H_2}$ can retard the reaction of hydrogen ions in Equation 2.4 and in turn slows down the metal dissolution reaction, but this is practically impossible as most of the real life situations involving metals in aqueous

solutions are opened systems in which hydrogen gas will constantly escape and the equilibrium will always tend to the right [93].

When the concentration of H^+ is very low especially in neutral solutions, the complementary reaction to metal dissolution is oxygen reduction. The oxygen molecules from the dissolved air are adsorbed on the metal surface and react with the residual electrons according to the equation:

$$O_{2(g)} + 2H_2O_{(l)} + 4e^- \rightleftharpoons 4OH^-_{(aq)} \quad (2.6)$$

Just like the H^+ reduction reaction, the reversible potential for the oxygen reduction reaction (Equation 2.6) is never attained. Hence, the corrosion of active metals in aqueous solutions generally proceeds by the combination of Equations 2.1 and 2.4 (in acidic medium) or Equations 2.1 and 2.6 (in near-neutral environments).

The modern theory of electrochemical corrosion was established based on the combination of the local cell model proposed by Evans [97] and the corrosion potential model proposed by Wagner and Traud [98] in the early twentieth century, and cited recently by Sato [99]. The electrochemical theory of corrosion describes metallic corrosion as a coupled electrochemical reaction consisting of two half-reactions; the anodic metal oxidation and the cathodic oxidant reduction. The corrosion process involves current flow by the movement of electrons or ions in solution. The four fundamental parts of an electrochemical cell, which are the anode, the cathode, the electrolyte and electrical connectivity are always present when corrosion occurs. During the corrosion reaction, the surface of the metal is generally polarized into the anode (where metal oxidation occurs) and the cathode (where reduction reaction occurs) due to potential difference between two areas on the metal surface. The metal being a bulk material ensures (electrical) connectivity between the anodic and cathodic parts in the corrosive environment, which serves as the electrolyte [37].

2.7 Measurement of electrochemical corrosion

The extent of electrochemical corrosion can be quantified by some kinetic parameters derived from electrochemical theories. Various electrochemical techniques have been successfully applied to study the kinetics and mechanisms of electrochemical corrosion of different metals or metal alloys in diverse aggressive media. These techniques include the potentiodynamic polarizations, Tafel plots, galvanostatic polarization, linear polarization resistance (LPR) method, cyclic voltammetry, electrochemical impedance spectroscopy (EIS), open circuit potential (OCP) measurements, etc. The two major electrochemical techniques used in the present study are Tafel plots and electrochemical impedance spectroscopy (EIS).

2.7.1 Potentiodynamic polarization and Tafel plots

This method is usually carried out in a three-electrode electrochemical cell system comprising the metal whose corrosion process is being investigated as the working electrode (WE), and two other electrodes, which are, the reference electrode (RE) and, the counter electrode (CE) all connected to a device called a potentiostat. A potentiostat allows the user to change the potential of the metal sample in a controlled manner and measure the current that flows as a function of applied potential. The equilibrium potential assumed by the metal in the absence of electrical connections or perturbations is called the open-circuit potential (OCP). Before any reasonable electrochemical corrosion measurement can be made, it is imperative that the metal attains a stable or equilibrium value of the OCP. The value of either the anodic or cathodic current at the OCP is called the corrosion current (i_{corr}), which is directly proportional to the corrosion rate of the metal. The i_{corr} cannot be measured directly but it can readily be estimated from the current-potential curves obtained when the equilibrium electrode (metal) potential is perturbed upon passage of current. The current-

potential curves especially those obtained under steady-state conditions are referred to as polarization curves [100, 101].

When the polarization curve is obtained under potentiodynamic condition, the curve is referred to as the potentiodynamic polarization curve. The larger the departure of the electrode potential from equilibrium value upon the passage of current, the larger the extent of polarization. The polarization is said to be ideal when the curve is characterized by a horizontal region of a current-potential curve. A typical ideal polarization curve is shown in Figure 2.1, where the vertical axis is the electrical potential and the horizontal axis is the logarithm of absolute current. The logarithmic value of the absolute current is more appropriate because of the wide range of current values that must be recorded during a corrosion experiment. The straight lines in Figure 2.1 represent the theoretical current of the anodic and cathodic reactions, while the curved lines refer to the total current, which is the sum of anodic and cathodic currents. The sharp point in the curve is actually the point where the current reverses polarity as the reaction changes from anodic to cathodic, or vice versa [101].

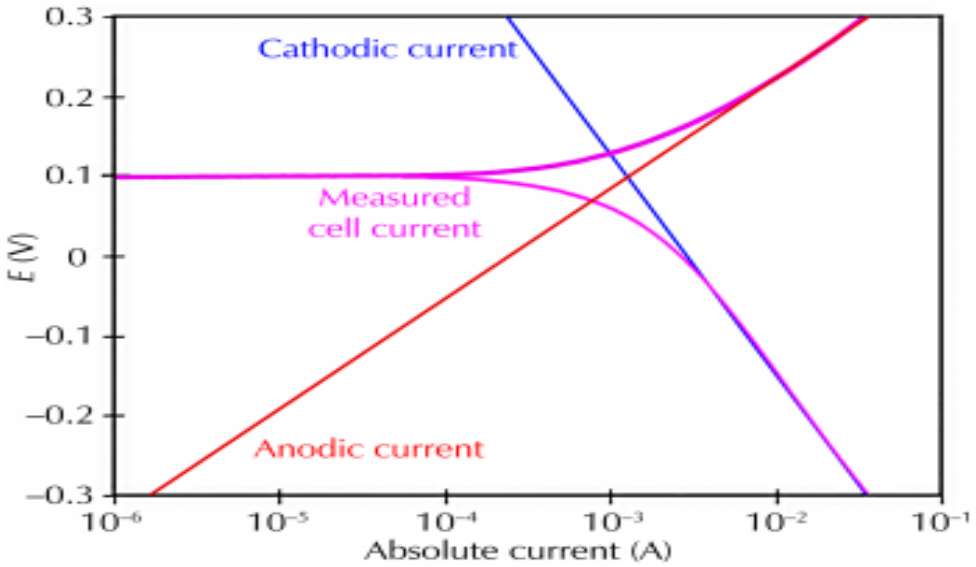

Figure 2.1. Polarization curve for a typical corrosion process showing the anodic, cathodic and measured currents [101].

Once the polarization curve is established, the i_{corr} can be estimated by fitting the measured data to a suitable theoretical model of the corrosion process. The Tafel analysis and/or Butler-Volmer models is/are often employed for this purpose. The corrosion process model assumes that the rates of both the anodic and cathodic reactions are controlled by the kinetics of the electron transfer reaction at the metal surface. An electrochemical reaction under kinetic control obeys the Tafel equation of the form [100, 101]:

$$i = i_o e^{\pm\frac{2.303(E-E_o)}{\beta}} \tag{2.7}$$

where the ± sign implies the equation is valid for both anodic and cathodic reactions, i is the current resulting from the reaction, i_o is the exchange current, E is the electrode/applied potential, E_o is the equilibrium potential (constant for a given reaction), and β is the reaction's Tafel constant (constant for a given reaction, i.e. anodic or cathodic, expressed in volts/decade). The term $E–E_o$ is referred to as the overpotential, often designated as η. The reaction Tafel constant, β, which may exist for either anodic or cathodic reaction or both can be expressed as [100, 101]:

$$\beta = \pm\frac{2.303RT}{\alpha nF} \tag{2.8}$$

where α is the transfer coefficient, n is the number of electrons involved in the reaction, R, T and F still retain their previous respective definitions.

The Tafel equation expressed in Equation 2.7 only describes the behavior of an isolated half-reaction. Whereas, a typical corrosion process involves two opposing half reactions, that is the anodic and cathodic half reactions. The Tafel equations for the anodic and cathodic reactions in a corrosion system can be combined to generate the Butler-Volmer equation [36, 100, 101]:

$$i = i_{corr}\left(e^{\frac{2.303(E-E_{corr})}{\beta_a}} - e^{-\frac{2.303(E-E_{corr})}{\beta_c}} \right) \quad (2.9)$$

where i is the measured current from the cell, i_{corr} is the corrosion current, E is the electrode/applied potential, E_{corr} is the corrosion potential, β_a is the anodic Tafel slope, and β_c is the cathodic Tafel slope.

The E_{corr} is the potential at which the rates both the anodic and cathodic corrosion processes are equal. That is, at the E_{corr}, the two exponential terms in Equation 2.9 are both equal to unity, which implies that the measured cell current, i is equal to zero. At any point near the E_{corr}, both the anodic and cathodic exponential terms contribute to the overall current. But as the potential is driven far away from the E_{corr} by the potentiostat, either the anodic or cathodic process predominates such that one of the two exponential terms can be ignored due to the extremely larger value of the other [36, 100, 101]. At this point, a plot of the logarithmic current (log i) versus E gives a straight line known as the Tafel plot. The corrosion process of an electrochemical system is said to be kinetically controlled when it exhibits Tafel regions on both sides of the E_{corr} [35, 36, 38, 100, 101]. In practice, many corrosion systems are kinetically controlled and thus obey the Butler-Volmer equation [100, 101]. Typical Tafel analysis is performed by extrapolating the linear regions of log i versus E plot to their point of intersection, that is, E_{corr}. The value of either the anodic or the cathodic current at the point of intersection is the i_{corr}. An ideal polarization curve for a representative corrosion process showing conventional Tafel analysis is shown in Figure 2.2. Unfortunately, many real-world corrosion processes are too complicated to exhibit sufficient linear Tafel regions that will ensure accurate deduction of i_{corr} by conventional extrapolation as shown in Figure 2.2. Common complications that feature in corrosion processes include [101, 102]:

- *Concentration polarization*: this occurs when the rate of a reaction is controlled by the rate at which reactants arrive at the surface of the WE. Often cathodic reactions show concentration polarization at higher currents when diffusion of oxygen or hydrogen ion is not fast enough to sustain the kinetically controlled rate.
- *Corrosion products or impurities*: this occurs when impurities, oxide films or other corrosion products (passivating or non-passivating) are deposited on the surface of the WE thereby altering the surface morphology. The original and the altered surfaces may have different values for the constant parameters in the Bulter-Volmer equation.
- *Preferential dissolution*: this happens when one component of an alloy undergoes preferential dissolution or corrosion reaction compared to other components.
- *Mixed control process*: simultaneous occurrence of more than one cathodic or anodic reaction, such as concurrent reduction of oxygen and hydrogen ions may also complicate the theoretical model of electrochemical corrosion measurement.
- *Potential (IR) drop*: errors in kinetic model may occur when the flow of cell current encounters impediment due to the cell solution resistance. This is also known as the ohmic (*IR*) drop across the electrolyte (cell solution), which brings about the difference between the controlled voltage and the measured voltage. This complication may be corrected or reduced significantly by ensuring proper cell geometry or using the IR-compensation tool in the potentiostat.

These complications may result in experimental log i versus E curves that do not exhibit well-defined linear regions. Evaluation of accurate icorr value could not be achieved from such curves using the simple Tafel analysis. Flitt and Schweinsberg [103] had demonstrated how such non-Tafel curves could be deconstructed or deconvoluted to obtain icorr and other relevant kinetic and thermodynamic parameters at improved level of accuracy. The work of Flitt and Schweinsberg describes the mathematical basis of SYMADEC, which

offers more sophisticated numerical fit for the more practical non-linear polarization curves. Similar well-developed iteration algorithms have been incorporated into most modern corrosion test software to perform a more sophisticated numerical fit to the Butler-Volmer equation. The measured data are fitted to Equation 2.9 by adjusting the values of E_{corr}, i_{corr}, β_a, and β_c. The curve-fitting method is advantageous because it does not require a well-behaved linear region of the curve.

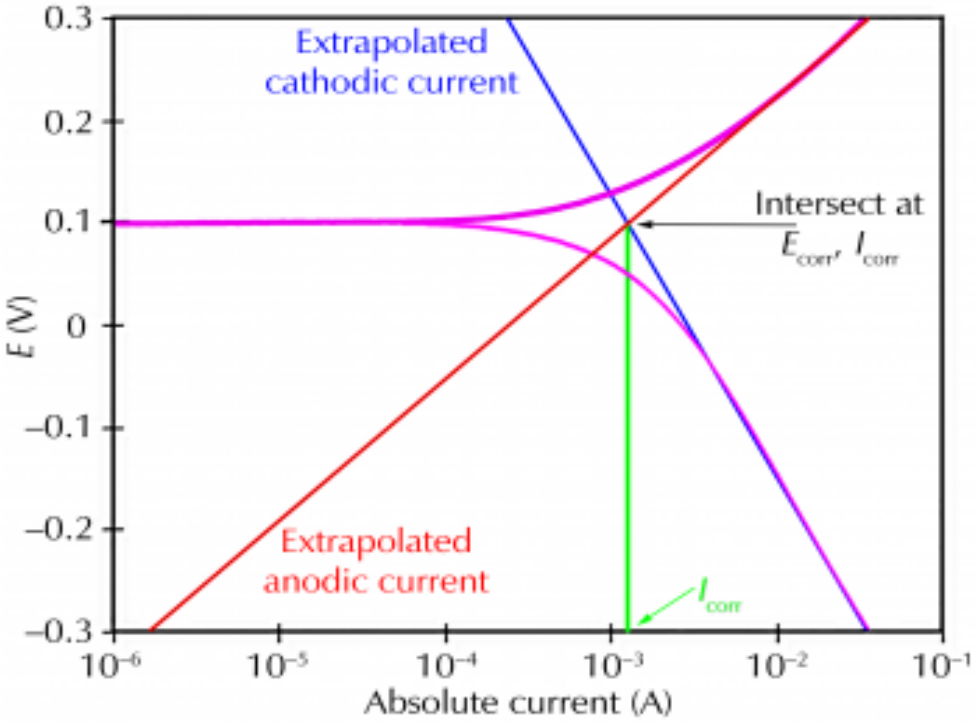

Figure 2.2. Polarization curve for a typical corrosion process showing classical Tafel plots [101].

2.7.2 Electrochemical impedance spectroscopy (EIS)

Electrochemical impedance spectroscopy (EIS) or simply impedance spectroscopy or AC impedance technique involves the application of a sinusoidal perturbation (either as potential or current) to the cell in a certain range of frequencies. If a sinusoidal potential excitation is applied to the cell, the measured response to this potential is an AC current signal, which can be analyzed as a sum of sinusoidal functions. The EIS techniques involves

non-destructive procedures at the OCP mode such that neither oxidation nor reduction reaction is forced to occur. This is due to the use of very small excitation amplitudes often in the range of 5–10 mV peak-to-peak, which causes minimal or no perturbations of the electrochemical test system [104]. The technique has proven to be advantageous for corrosion characterization of various oxide films on the metal surfaces and has been successfully utilized for corrosion studies in the recent years [105, 106]. Another usefulness of the EIS technique is the ability to distinguish the dielectric and electric properties of individual contributions of components under investigation and provides insight into the corrosion process occurring on the substrate surface [107, 108].

2.7.2.1 The theory of electrochemical impedance

A simple electrical circuit that contains resistance (R) as the circuit element that resists the flow of electrical current generally obeys the Ohm's law given by:

$$R = \frac{E}{I} \tag{2.10}$$

where R is the resistance, E is the voltage, and I is the current. Equation 2.10 is a generalization that is only applicable to an ideal resistor. Most real life electrical circuits contain or are better described with a more complex element known as impedance (Z). The impedance serves the same purpose of resisting the flow of electrical current like the resistance but without the limitations and oversimplifications such as non-frequency dependency of resistance values and in-phase relationship between current and voltage that are assumed in the construct of the Ohm's law. In an electrochemical cell, slow electrode kinetics, slow preceding chemical reactions, and slow diffusion can all impede electron flow, and can be considered analogous to the resistors, capacitors, and inductors that impede the

flow of electrons in an ac circuit. The total impedance in a circuit is the combined quantitative effect of all its resistors, capacitors, and inductors to the flow of electrons [104].

Electrochemical impedance theory describes the response of a circuit to an alternating current or voltage as a function of frequency. Electrochemical impedance is usually measured by applying an AC potential to an electrochemical cell and then measuring the AC current through the cell. The AC potential is a sinusoidal excitation signal of the form [100, 104, 107]:

$$E_t = E_o \sin(\omega t) \tag{2.11}$$

where E_t is the potential at time t, E_o is the amplitude of the signal, and ω is the radial frequency. The radial frequency ω (in radians/second) is related to the frequency f (in hertz) is:

$$\omega = 2\pi f \tag{2.12}$$

The response of electrochemical cell to the small excitation signals normally applied and measured in electrochemical impedance is pseudo linear. In this (pseudo-) system the current response to the sinusoidal potential is also a sinusoid at the same frequency but shifted in phase such that the current response can be expressed in an equation analogous to Equation 2.11 as [104]:

$$I_t = I_o \sin(\omega t + \phi) \tag{2.13}$$

where I_t is the current at time t, I_o is the current amplitude, φ is the phase angle (shift) between the potential and current. A similar expression to the Ohm's law can be established between the sinusoidal potential and current as [104]:

$$Z = \frac{E_t}{I_t} = \frac{E_o \sin(\omega t)}{I_o \sin(\omega t + \phi)} = Z_o \frac{\sin(\omega t)}{\sin(\omega t + \phi)} \tag{2.14}$$

where Z is the total impedance and Z_o is the impedance magnitude. By using Eulers relationship and vector analysis, Equation 2.14 can be expressed as [104]:

$$Z = Z_o(\cos\phi + j\sin\phi) = Z_o\cos\phi + jZ_o\sin\phi = Z_{re} + Z_{im}j \quad (2.15)$$

where $j = \sqrt{-1}$, Z_{re} and Z_{im} are the real and imaginary parts of the impedance respectively.

2.7.2.2 EIS spectra and equivalent circuits

The plots generated during the EIS measurements are collectively referred to as the EIS spectra. There are various ways of representing EIS results among them are the Nyquist and Bode plots. The Nyquist plot is the plot of imaginary part of the impedance (Z_{im}) against the real component (Z_{re}) such that the impedance is represented as a vector arrow of length |Z| inclined to the horizontal (Z_{re}) axis at an angle, φ (known as the phase angle) as shown in Figure 2.3. The vertical axis in the Nyquist plot is negative and each point on the plot corresponds to the impedance at one frequency. The lower values of Z_{re} correspond to higher frequencies while the higher values are points taken at lower frequencies. The phase angle φ can be expressed as the complex argument of the impedance as [104]:

$$\phi = \arg(Z) = \tan^{-1}\left(\frac{Z_{im}}{Z_{re}}\right) \quad (2.16)$$

The Nyquist plot in Figure 2.3 shows a semicircle, which is characteristic of a single "time constant" [104]. The frequency at which the impedance data are recorded and the variations in the phase angles over the range of frequency employed for the experimental measurements are not displayed on the Nyquist plot. For this reason, the Bode plots are often used in addition to the Nyquist plots to derive more parameters and information about the circuit [104]. The Bode plots comprise the plots of logarithm of frequency on the horizontal axis and both the absolute values of the impedance and the phase-shift on the vertical axis as shown in Figure 2.4.

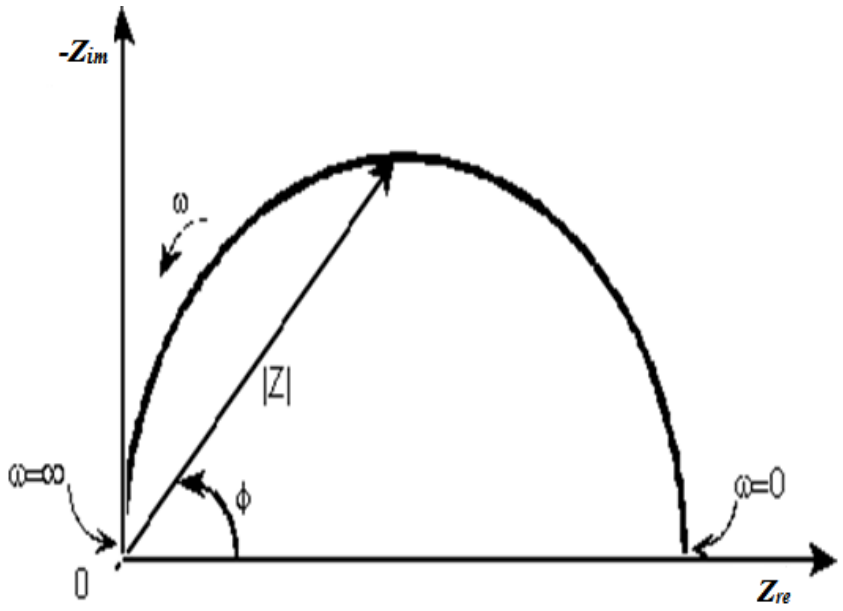

Figure 2.3. Typical Nyquist plot showing the essential components of the plot [104].

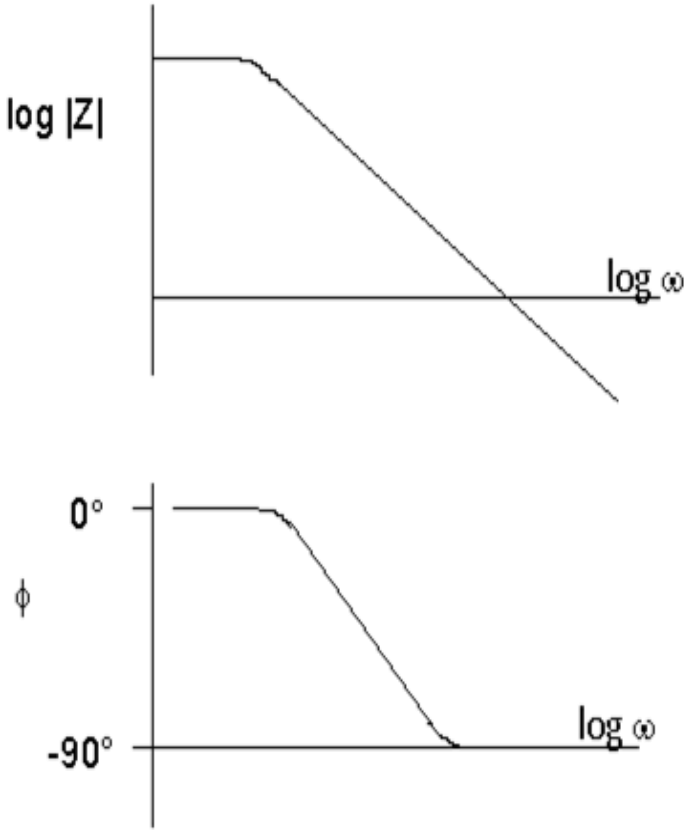

Figure 2.4. Typical Bode plots with one time constant showing the plots of logarithmic values of impedance magnitudes, and the phase angles against logarithmic frequency values [104].

Table 2.1. Basic circuit elements with their symbols and respective current-voltage and impedance equations.

Circuit element: symbol	Current-Voltage Equation	Impedance Equation
Resistor: 	$E = IR$	$Z = R + 0j$ ($j^2 = -1$)
Capacitor: 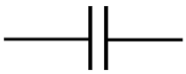	$I = C\, dE/dt$	$Z = 0 - j/\omega C$ ($\omega = 2\pi f$)
Inductor: 	$E = L\, di/dt$	$Z = 0 + j\omega L$

EIS spectra are usually analysed by fitting the experimental data into appropriate equivalent circuit model that provides adequate description of the processes that occurred on the electrode surface. The surface of an electrode immersed in electrolyte solution behaves like an electrical circuit in which circuit elements are interconnected in series or parallel [109]. Simple equivalent circuits often contain basic electrical elements like resistors, capacitors and inductors. The relationships between the current and voltage of each of these elements and their respective impedance values are listed in Table 2.1.

As shown in Table 2.1, the impedance of a resistor has no imaginary component, and the current through the resistor is in phase with the voltage, that is, the phase shift is zero degree. The impedance of a capacitor on the other hand has only the imaginary component, which is a function of both capacitance and frequency. The current through a capacitor is always 90 degrees out of phase with the voltage across it, while the current is leading the voltage. Because the impedance of a capacitor varies inversely with frequency, at high frequencies a capacitor acts as a short circuit with its impedance tending towards zero. At low frequencies (approaching dc) a capacitor acts as an open circuit while the impedance tends towards infinite. The inductor, just like a capacitor also has only imaginary part in its

impedance and the current through an inductor is always 90 degrees out of phase with the voltage drop across it, such that the current lags behind the voltage. Also, as the frequency increases, the impedance of an inductor increases. It acts as a short circuit at low frequencies and as a large impedance at high frequencies.

The electrode surface in typical electrochemical experiments often involves more complex physical and/or electrochemical phenomena that cannot be adequately described by simple circuit elements but rather a combination of two or more circuit elements. In practice, EIS spectra are often processed by constructing simple equivalent circuit models via approximate arrangements of circuit elements to make initial guesses and then iteratively fit the experimental data to the theoretical circuit model. Most potentiostats for EIS measurements are now equipped with sophisticated software programs that carry out these iterations and produce results within a short period of time. The closeness of the theoretical data to the experimental results is often adjudged based on some statistical error values produced as part of the iteration results.

Most of the real-world systems especially in corrosion studies do not give semi-circular Nyquist plots with the center on the horizontal axis. Instead, the usual observed plot corresponds to the arc of a circle whose center is below the real impedance (horizontal) axis. In an attempt to make an/a (near) accurate description of the response of such systems, the constant phase element (CPE) was introduced. The CPE is a non-intuitive circuit element that was invented to fit experimental EIS data that exhibit depressed semi-circular behaviour, which has been attributed to various phenomena including inhomogeneity of electrode surface [60, 110-113]. Though the physical origins of the CPE are controversial, Hirschorn et al. [110] had reported that the CPE behaviour may be attributed to the distribution of physical properties in films, in the direction normal to the electrode surface.

Jorcin et al. [114] had earlier reported that the CPE parameters are considered to arise from a distribution of time-constants along the surface of an electrode or in the direction normal to the electrode and the time-constants distributions result from distributions of physical properties including structure, reactivity, dielectric constants, and resistivity. The CPE behaviour therefore depends on the nature of the system being investigated. Electrochemical systems involving oxide films, metal/passive film interface, film/electrolyte interface etc. are better described with the CPE element [110, 115].

The CPE impedance is expressed in terms of the model parameters *n* and *Q* as [116, 117]:

$$Z_{CPE} = \frac{1}{Q(i\omega)^n} \tag{2.17}$$

where Q is the CPE constant (in $\Omega^{-1}S^{n}cm^{-2}$); $j^2 = -1$ is the imaginary number; ω is the angular frequency (in $rads^{-1}$); and n is a CPE exponent, which can be used as a gauge of the heterogeneity or roughness of the surface. The numerical values of n varies between -1 and 1 such that the CPE represents a resistance, when n = 0, a capacitance, when n = 1, an inductance, when n = −1, and a Warburg impedance, when n = 0.5 [58]. The phase angle of the CPE impedance is independent of the frequency and has a constant value of –(90*n*) degrees in accordance to the name – constant phase element. This implies that the phase angle of the CPE is 90^{o} only when *n* = 1, that is the CPE is a true capacitor. When n is close to 1.0, the CPE resembles a capacitor, but the phase angle is not exactly 90° but rather a constant value, somewhat less than 90° at all frequencies [118].

2.8 Basics of quantum chemical calculations

Quantum chemistry is the branch of chemistry that makes use of the principles of quantum mechanics to solve problems of chemical relevance ranging from molecular structural problems to chemical thermodynamics, reaction kinetics, reaction mechanisms, etc. Quantum mechanical models treat an electron as a wave-like material rather than a particle,

and provide approximate solutions to the Schrodinger wave equations (SWEs) leading to the prediction of some relevant properties of an electron or electronic system, and hence, provide explanations to the behaviour of the overall chemical system.

The Schrodinger wave equation (SWE), which is the mathematical formulation that forms the basis for obtaining nearly all molecular quantum chemical parameters, is given as:

$$\hat{\mathrm{H}}\psi = E\psi \tag{2.18}$$

where $\hat{\mathrm{H}}$ is the Hamiltonian, Ψ is the wave function, and E is the energy of the system. In mathematical concept, equations of the form in 2.18 are called the Eigen-equations, for which Ψ and E are more appropriately referred to as the Eigen-function and Eigen-value respectively. The general expression for the Hamiltonian, $\hat{\mathrm{H}}$ for a system with *i* number of particles can be expressed as:

$$\hat{\mathrm{H}} = -\sum_{i}^{particles} \frac{\nabla_i^2}{2m_i} + \sum_{i<j}^{particles} \sum \frac{q_i q_j}{r_{ij}} \tag{2.19}$$

where ∇_i^2, m_i, q_i and r_{ij} are the Laplacian operator acting on particle *i*, mass of particle *i*, charge of particle *i*, and distance between particles *i* and *j*, respectively. The first term is the kinetic energy of the particle within a wave formulation, while the second term is the energy due to Coulombic attraction or repulsion between particles. The Hamiltonian in Equation 2.19 is somewhat complex and therefore, nearly never used in any of the current computational chemistry software. The simplified form of Equation 2.19 resulting from the Born-Oppenheimer approximation, which assumes that the nuclear and electronic motions can be treated separately, is often used. Upon the Born-Oppenheimer approximation, Equation 2.18 becomes:

$$\hat{\mathrm{H}} = -\sum_{i}^{electrons} \frac{\nabla_i^2}{2m_i} - \sum_{i}^{nuclei} \sum_{j}^{electrons} \frac{Z_i}{r_{ij}} + \sum_{i<j}^{electrons} \frac{1}{r_{ij}} \tag{2.20}$$

where the first term here is the kinetic energy of the electrons only; the second term is the attraction of electrons to nuclei and the third term is the repulsion between electrons. The nuclear-nuclear repulsion term can be added to the energy obtained from Equation 2.20 at the end of the calculation [119].

2.8.1 The wave functions and the basis sets

The wave function, Ψ may be constructed in a number of ways, and the relative quality of the formulated wave functions may be assessed by the evaluation of the energy Eigen-value associated with each wave function. The wave function with the lowest energy is usually the most acceptable and presumably the best one to use for computing other properties of the system being studied by the application of appropriate operators. The Eigen-functions for a molecular system may be properly called the molecular orbitals (MOs) and the pure electronic energy (the Eigen-value) associated with each molecular orbital is the energy of the electron in that orbital [120, 121]. For systems with only one electron and one nucleus, the Schroedinger wave equation, with Born-Oppenheimer approximation has been solved exactly. The Eigen-functions that are determined in that instance are the familiar hydrogenic atomic orbitals, 1s, 2s, 2p, 3s, 3p, 3d, etc. These hydrogenic atomic orbitals (functions) may be useful in the construction of more complicated molecular orbitals. A guess wave function Ψ can be constructed as a linear combination of atomic wave functions, φ as [120]:

$$\psi = \sum_{i=1}^{N} a_i \varphi_i \tag{2.21}$$

where the set of N functions φ_i is called the 'basis set' and each has associated with it some coefficient a_i. This construction is known as the linear combination of atomic orbitals (LCAO) approach.

A basis set is a mathematical description of the orbitals in a system, or a set of functions used to describe the shape of the orbitals in the atoms present in a system [122, 123]. It is the set of mathematical functions from which the wave function, which is used for approximate theoretical calculation or modeling is constructed [120, 122]. Basis sets serve as sets of basic functional building blocks that can be stacked or added to have the features that are need for quantum chemical calculations. In this regard, a limited or countless number of basis sets can be added together to construct an approximate wave function for an atomic or molecular orbital [120, 122]. The selected mathematical functions are those that describe the radial and angular distributions of electron density [122, 124]. Molecular orbitals and the entire wave functions are created by taking linear combinations of radial and angular (basis) functions. Although it is possible to create basis sets from the scratch, most calculations are done using existing basis sets. The appropriateness of the chosen basis set for a particular type of calculation is an important factor in determining the accuracy of the quantum chemical calculation results [123]. More so, the smaller the basis set, the poorer the representation, and commonly, the less accurate the results. Computational time and accuracy are also influenced by the type of basis function because fewer basis functions will be required to achieve a given level of accuracy if a single, representative basis set is able to reproduce the unknown function properly [119].

The two types of basis functions commonly used in electronic structure calculations are the Slater-type orbitals (STO) and Gaussian-type orbitals (GTO) basis functions, which are subsequently shortened as the STFs and the GTFs (i.e. Slater-type functions and Gaussian-type functions respectively). The STFs represent the real situation for the electron density in the valence region and beyond, but fail to give a good representation around or near the nucleus. The STFs exhibits close resemblance to the hydrogenic atomic orbitals and many

earlier calculations were carried out using the STOs basis functions [120, 122]. The general mathematical expression for the STFs is [119, 120]:

$$\chi_{\zeta,n,l,m}(r,\theta,\phi) = NY_{l,m}(\theta,\phi)r^{n-1}e^{-\zeta r} \tag{2.22}$$

where N is a normalization constant, ζ is an exponent that can be chosen according to a simple set of rules developed by Slater, which depends among other things, on the atomic number, *n* is the principal quantum number for the valence orbital, $Y_{l,m}(\theta, \varphi)$ is the spherical harmonic function, which in turn depends on the angular momentum quantum numbers *l* and *m* [119, 120, 122, 125, 126].

The STOs have a number of attractive features, which include the exhibition of correct exponential decay with increasing *r*, the hydrogenic feature of the angular component, and presence of a cusp as the nucleus of the 1s orbital. Also, overlap integrals between two STOs as a function of interatomic distance are practically and readily computable. One of the major set-backs attributed to the STFs especially in the ab initio Hartree-Fock (HF) theory is the lack of analytical solution for the general four-index integral involved in the HF theory, and the subsequent somewhat rigid requirement that such integrals be solved by numerical methods. This unavoidably stiff condition and the complexity of the analytical solutions severely limit the usefulness of the STFs in molecular systems of any significant size. Nevertheless, high quality STO basis sets have been developed for atomic and diatomic calculations, where such limitations do not arise [120, 127].

The modification of the STO functional proposed by Boys [128] led to the introduction of the GTO functional, which contains the exponential $e^{-\beta r2}$, rather than the $e^{-\alpha r}$. This followed from the fact that all that is required for there to be an analytical solution of the general four-index integral formed from STO functions is that the radial decay of the STOs be changed from e^{-r} to e^{-r2}. In this regard, the AO-like functions are chosen to have the form

of a Gaussian function. The general functional form of the GTFs in the polar, Cartesian and normalized atom-centered Cartesians coordinates forms respectively are [119, 120, 123]:

$$\chi_{\zeta,n,l,m}(r,\theta,\phi) \;\; \alpha \;\; \mathrm{Y}_{\mathrm{l,m}}(\theta,\phi) r^{2n-2-l} e^{-\zeta r^2} \tag{2.23}$$

$$\chi_{\zeta,l_x,l_y,l_z}(x,y,z) = N x^{l_x} y^{l_y} z^{l_z} e^{-\zeta r^2} \tag{2.24}$$

$$\chi_{\zeta,l_x,l_y,l_z}(x,y,z) = \left(\frac{2\zeta}{\pi}\right)^{3/4} \left[\frac{(8\zeta)^{l_x+l_y+l_z} l_x! l_y! l_z!}{(2l_x)!(2l_y)!(2l_z)!}\right]^{1/2} x^{l_x} y^{l_y} z^{l_z} e^{-\zeta\left(x^2+y^2+z^2\right)} \tag{2.25}$$

where r^2 in Equations 2.23 and 2.24 has been replaced by $(x^2 + y^2 + z^2)$ in Equation 2.25, ξ is an exponent controlling the width of the GTO, and l_x, l_y, and l_z are non-negative integers that dictate the nature of the orbital in a Cartesian form. The sum of l_x, l_y, and l_z determines the type of orbital such that $l_x + l_y + l_z = 0$ implies a spherical symmetry (i.e. a *s*-type GTO), $l_x + l_y + l_z = 1$ implies an axial symmetry about a single Cartesian axis (i.e. *p*-type GTO), etc. [120].

The comparative behaviour of STOs and GTOs are shown in Figure 2.5. As shown in Figure 2.5, the STO shows the correct functional behavior near the nucleus, i.e. a cusp, and decays in the correct way at long distances, whereas, the GTO provides a relatively poor description of the atomic orbitals, it has a finite value at the nucleus and decays too quickly thereby underestimating long range interactions [129, 130]. The GTFs are however more useful for molecular systems because the resulting four-index integral can be solved analytically. The GTFs can be made to produce similar hydrogenic atomic orbitals obtainable from the STFs by adding many GTFs together to approximate the correct shape of the orbital near and far from the nucleus as in [119, 120]:

$$\chi_{\zeta,l_x,l_y,l_z}(x,y,z) = \sum_{a=1}^{n} c_a \phi_{\zeta,l_x,l_y,l_z}(x,y,z) \tag{2.26}$$

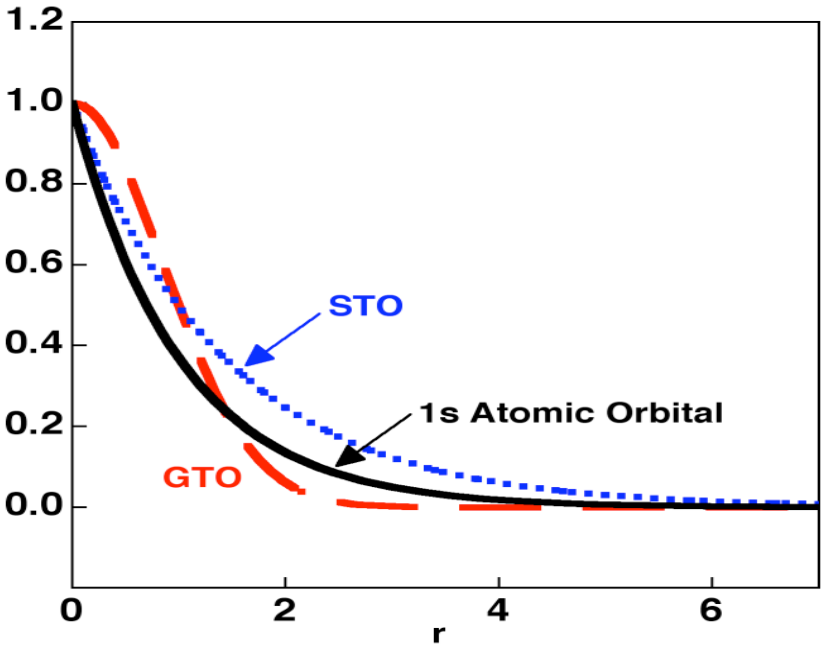

Figure 2.5. Comparison of the STF and GTF s-type atomic orbitals [129].

where *n* is the number of Gaussians used in the linear combination, and the coefficients *c* are chosen to optimize the shape of the basis function sum and ensure normalization [119, 120]. When a basis function is defined as a linear combination of GTFs, it is referred to as a 'contracted' basis function, and the individual GTFs from which it is formed are called the 'primitive' Gaussians. Thus, in a basis set of contracted GTOs, each basis function is defined by the contraction coefficients *c* and exponents ξ of each of its primitives. The 'degree of contraction' refers to the total number of primitives used to make all of the contracted functions. Contracted GTOs when used as basis functions continue to permit analytical evaluation of all of the four-index integrals [119, 120].

A systematic determination of the optimal contraction coefficients and exponents for an adequate representation of STOs by contracted GTOs was first carried out by Hehre, Stewart, and Pople [131] and established for a large number of atoms in the periodic table. Hehre et al. constructed a series of different basis sets for different values of *n* in Equation 2.26 (particularly *n* = 2–6) and called them the STO-*n*G basis sets, that is, 'Slater-Type Orbital

approximated by *n* Gaussians'. The more the number of Gaussian primitives employed (i.e. the larger the value of *n*), the more closely and accurately a contracted function can be made to mimic a particular STO. However, as *n* increases the four-index two-electron integral becomes increasingly complicated to evaluate. The optimum value of *n*=3 has been reported based on the acceptable speed and accuracy [120], and the STO-3G is generally known as a minimal or single-ζ basis set. Other more flexible forms of basis sets that have been developed over the years by decontracting the minimal basis set include the double-ζ, the triple-ζ or more generally the multiple-ζ basis sets. Examples of such basis sets are the correlation-consistent polarized core and valence multiple (double/triple/etc.) zeta basis sets such as cc-pCVDZ, cc-pCVTZ, etc. developed by Woon and Dunning [132, 133].

Since the core orbitals are relatively only weakly affected by chemical bonding compared to the valence orbitals, it is reasonable to associate more flexibility to the valence basis functions than the core basis functions. This had led to the introduction of the split valence' or 'valence-multiple-ζ' basis sets in which core orbitals continue to be represented by a single (contracted) basis function, while valence orbitals are split into arbitrarily many functions. The popular Pople type basis sets such as 3-21G, 6-21G, 4-31G, 6-31G, and 6-311G etc. are the most widely used split-valence basis set. Additional features that are often added to the Pople basis sets to improve accuracy in some cases are the polarization functions and the diffuse functions. The polarization functions are indicated by one or more asterisks symbols or using the orbital symbols in parenthesis. Examples include 6-31G* (or 6-31G(d)), which implies that a set of d-orbital primitives has been added to atoms other than hydrogen; and 6-31G** (or 6-31G(d,p)), which means that a set of *p* primitives has been added to hydrogen in addition to the d-orbital primitives on the higher atoms. These functions are called polarization functions because they give the wave function more flexibility to change shape [120].

Polarization functions are used because they often result in more accurate computed geometries and vibrational frequencies [123]. The diffuse functions can also be added to the Pople basis sets by using one or two plus signs such as in 6–31+G* or 6–31++G*. A single plus sign indicates that diffuse functions have been added to atoms other than hydrogen. The second plus sign indicates that diffuse functions are being used for all atoms including hydrogen. These diffuse functions are primitives with small exponents, thus describing the shape of the wave function far from the nucleus and they are more strongly recommended to be used for anions, which have larger electron density distributions. They are also used for describing interactions at long distances, such as van der Waals interactions [119, 120, 123].

2.8.2 Computational chemistry methods and models

In principle, QM can predict any property of an individual atom or molecule exactly. The fundamental postulates of quantum mechanics assert that microscopic systems are described by ‘wave functions’ that completely characterize the entire physical properties of the system and there is always a quantum mechanical ‘operator’ that corresponds to each physical observable. The quantum mechanical ‘operator’ can be applied to the wave function to predict the probability that the system will exhibit certain properties or values that relate to that observable [120, 123]. In practice, however, the QM equations have only been solved exactly for one electron systems. A myriad collection of methods has been developed towards the approximate solutions for multiple electron systems. The successful application of quantum mechanics to solving any chemical problem rests on using a “correct” approximation to obtaining appropriate quantum chemical parameters and closeness of the predicted data to the experimental results [120]. The success of a quantum chemical calculation therefore depends on finding good approximate solutions to the correct Schrodinger wave equation of the system being investigated. Therefore, approximate

solutions to the Schrodinger wave equations are very useful provided an adequate amount of sophistication is applied by the researcher towards choosing a valid approximation and judging the accuracy of the results obtained [119].

The Hamiltonian in Equation 2.20 is obviously complex for a system containing two or more particles. More so, the Schrodinger wave equation comprising the Hamiltonian in Equation 2.20 operating on the wave function of the form in Equation 2.21 cannot be solved exactly. Various approximation methods have been developed and implemented in different sophisticated computer software codes to aid speedy calculations of quantum chemical parameters. Depending on the accuracy wanted and the nature of the system being studied, useful information can be obtained for systems containing up to several thousand particles. One of the main problems in computational chemistry is selecting a suitable level of theory or method for a given problem, and ability to evaluate the quality of the obtained results [119]. The evolution of advanced computer algorithms and hardware, and the incorporation of theoretical quantum chemical models into well robust computer software programs have greatly enhanced the applications of quantum chemistry and/or theoretical/computational chemistry in solving chemical related problems. The use of quantum chemically derived parameters to describe the adsorption and corrosion inhibition behaviour of organic compounds has been well developed owing to the advancement in the computer hardware and software technologies.

2.8.2.1 Ab initio methods

Ab initio methods make use of pure theoretical principles to compute molecular and/or quantum chemical parameters. They do not include experimental data. The approximations involved in the ab initio methods are usually mathematical based, such as using a simpler mathematical expression that can represent a wave function, using a finite

basis set, and/or finding an approximate solution to the differential equations. Ab initio calculations use the correct Hamiltonian and do not use experimental data other than the values of the fundamental physical constants. However, ab initio calculations do not imply "100 % accuracy" since a number of approximations is always involved in the calculations.

The most common type of ab initio calculation is the Hartree Fock (HF) calculation that makes use of mainly the central field approximation, which does not include Coulombic electron-electron repulsion. The net effect of electron-electron repulsion is added in the calculation by integrating the repulsion term [123, 124]. One of the advantages of this method is that it breaks the many-electron Schrödinger equation into many simpler one-electron equations such that each one electron equation is solved to yield a single electron wave function, called an orbital, and the associated (orbital) energy. The orbital describes the behavior of an electron in the net field of all the other electrons [123].

The HF calculations involve the use of initial guess for the orbital coefficients from which a new set of orbital coefficients can be derived in an iterative procedure using energy minimization as the constraint. This iterative procedure is continued until the energy and orbital coefficients at a particular iteration step is the same as the one that follows. At this stage, the calculation is said to be converged [123]. HF orbitals can be constructed to reflect whether the overall electronic system is paired or unpaired by using the appropriate mode of HF model, that is, restricted HF (RHF) or unrestricted HF (UHF). The RHF method is applicable for the singlet spin system and consumes less CPU time because the same orbital spatial function is used for both α and β spin electrons in each pair [123]. The UHF on the other hand is used when a system contains unpaired electrons and it is described using two completely separate sets of orbitals for α and β electrons.

Simple HF calculations do not take the electron–electron repulsion effect into account. The effect of pairwise electron–electron interaction on the results obtained from HF

calculations can be considered by using the post-HF corrections. Some of the methods that complement HF calculations with electron-electron correlations include the Moller–Plesset perturbation theory (MPn, where n = 1 to 5, is the order of correction), the generalized valence bond (GVB) method, multi-configurational self-consistent field (MCSCF), configuration interaction (CI), and coupled cluster theory (CC) [123]. Each of these methods addresses the correlated calculation in a distinct manner, and each has its own level of accuracy.

In general, ab initio calculations give very good qualitative results and can yield increasingly accurate quantitative results as the molecules in question become smaller. The advantage of ab initio methods is that they eventually converge to the exact solution once all the approximations are made sufficiently small in magnitude. The overall relative but nonmonotonic trend of accuracy of results from HF based methods is [123]:

$$HF << MP2 < CISD \approx MP4 \approx CCSD < CCSD(T) < CCSDT < Full\ CI$$

One major disadvantage of ab initio methods is their computational expensiveness. They consume enormous amounts of computer CPU time, memory, and disk space. The HF method scales as N^4, where N is the number of basis functions. This means that a calculation for a system that contains as twice as many basis sets will take 16 (i.e. 2^4) times as long to complete. Correlated calculations often scale much worse and consume much more time [123].

2.8.2.2 Semiempirical methods

Semiempirical methods attempt to address the problem of computational expensiveness that limits the use of ab initio methods especially for large molecular systems. The development of semiempirical methods is to further ensure the achievement of the potentially critical role that theory could play in corroborating experimental facts on any number of

fronts such that, theoretical studies could also be carried out on (large) molecules that are practically (computationally) inaccessible by ab initio methods [123]. Semiempirical methods employ the HF theory as the framework but shorten the computational time by introducing further approximations particularly for the computation of the two electron (four-index) integrals, which is the most demanding step involved in an HF calculation [120].

In the semiempirical methods construct, the valence electrons are considered explicitly and the core electrons are accounted for by reducing the nuclear charge or introducing functions to model the combined repulsion due to the nuclei and core electrons. Furthermore, only a minimum basis sets are used to describe the valence electrons, while some of the two-electron integrals are also omitted. The neglected parts of the calculations are accounted for by using the parameterization approach. The parameters to be used in compensating for the gross omission of some parts (integrals) in the semiempirical models are obtained by fitting the results to experimental data or ab initio calculations [123].

The advantage of semiempirical calculations is that they are much faster than ab initio calculations. The disadvantage of semiempirical calculations is that the results can be erratic and fewer properties can be predicted reliably [120, 123]. If the molecule being computed is similar to molecules in the database used to parameterize the method, then the results may be very good via comparison. If the molecule being computed is significantly different from anything in the parameterization set, the results may be very poor [123].

The central assumption of semi-empirical methods is the zero differential overlap (ZDO) or neglect of differential overlap (NDO) approximation, which neglects all products of basis functions that depend on the same electron coordinates when located on different atoms. To compensate for these neglected differential overlaps, the remaining integrals are made into parameters and their values are assigned based on ab initio calculations or experimental data. The number of integrals neglected and the mode of parameterization

inform the various models derived from the semi-empirical methods [119]. These include the Huckel theory (HT), extended Huckel theory (EHT), neglect of diatomic differential overlap (NDDO), intermediate neglect of differential overlap (INDO), Zerner's INDO (ZINDO), symmetrically orthogonalized intermediate neglect of differential overlap (SINDO), partial retention of diatomic differential overlap (PRDDO), Fenske-Hall, typed neglect of differential overlap (TNDO), semi-ab initio method 1 (SAM1), complete neglect of differential overlap (CNDO), Pariser-Parr-Pople (PPP) model for conjugated π systems, modified intermediate neglect of differential overlap (MINDO) models, and modified neglect of differential overlap (modified NDDO) such as MNDO, AM1, PM3 and PM6 models [123].

2.8.2.3 Density functional theory (DFT) methods

DFT has become very popular and widely used in the recent years because it has been observed to be less computationally intensive than other methods with similar accuracy [119, 120, 123]. As a result, it is presently considered to be the most successful and also the most promising approach to compute the electronic structure of matter, including atoms, molecules, solids, nuclei, and quantum and classical fluids [134]. Statistical records placed the number of publications where the phrase “density functional theory” or “DFT” appeared in the title or abstract of Chemical Abstract search between 1990 and 1999 at above 10,000 publications with increasing relevance on yearly basis. This again confirmed the dominant use of DFT-based model chemistry in computational chemistry researches [134, 135]. The use of electron density in deriving ground-state properties is advantageous and lessens computational time because the integrals for Coulomb repulsion are only done over the electron density (a three-dimensional function). This implies that the DFT calculations scale only as N^3 making them to be faster than the HF calculations (which scale as N^4). The

accuracy of a DFT calculation depends on the type of functionals used such that better DFT functionals give results with accuracy similar to that of an MP2 calculation [123].

The original formulation of the DFT established by Hohenberg and Kohn [136] provides the ground state properties of a many-electron system from the electron density rather than the many-body wave function employed by the HF theory. In other words every ground-state property, and in particular the ground-state energy, is a functional of the electron density. The simple and practical method for carrying-out DFT calculations that retains the exact nature of the original DFT construct was later provided by Kohn and Sham [137].

The electron density is the central quantity in DFT, and it is defined as the multiple integral over the spin coordinates of all electrons and over all but one of the spatial variables as [119, 120]:

$$\rho(\vec{r}) = N \int ... \int \left| \Psi(\vec{x_1}, \vec{x_2}, ... \vec{x_N} \right|^2 d\vec{x_1}\, d\vec{x_2} ... d\vec{x_N} \qquad (2.27)$$

where $\rho(\vec{r})$ determines the probability of finding any of the N electrons within volume element $d\vec{x}$.

The probability (or electron) density, $\rho(\vec{r})$ needs to satisfy certain unique properties. These properties and their consequences are discussed in details elsewhere [137]. The mathematical proof of the first Hohenberg-Kohn theorem eventually established that the total energy (E[ρ]) associated with the electron density can be expressed as the sum of nuclear energy due to nuclei-electron attraction ($E_{Ne}[\rho]$), the kinetic energy of the electron (T[ρ]), and the energy term due to electron-electron repulsion ($E_{ee}[\rho]$), i.e. [134]:

$$E[\rho] = E_{Ne}[\rho] + T[\rho] + E_{ee}[\rho] \qquad (2.28)$$

The speed and accuracy of a DFT calculation depend on the type of functional and the basis set employed. Since basis sets are fundamental mathematical expressions that are

common to most computational chemistry methods, the distinctive trademark of the DFT methods are the functionals. There is a whole list of different functionals with varying advantages or disadvantages. Some of these functionals were developed from fundamental quantum mechanics and some were developed by parameterizing functions to best reproduce experimental results [123]. So many functionals have been developed till date. Among them are those that are based on only the electron exchange (without correlation terms) that is, the X-alpha (X_α) functionals. Others provide simplest approximation to the complete problem and developed based on the local density approximation (LDA) or local spin density approximation (LSDA) for high-spin systems [119]. An example is Vosko, Wilks and Nusair (VWN) functional. Examples of functionals that utilize the electron density and its gradient (gradient corrected functionals) include Becke correlation functional with Lee, Yang, Parr exchange (BLYP). Others are the more recent hybrid functionals such as Becke 3-parameter exchange with Lee, Yang, Parr correlation (B3LYP), Becke 3-parameter exchange with Perdew correlation (B3P86), Becke 3-parameter exchange with Perdew and Wang correlation, etc. [119, 120, 123].

2.8.2.4 Molecular mechanics methods

Even though semiempirical methods are practically useful for a number of large organic molecules, they still appear to be relatively computational-intensive for most biomolecular systems when compared to the molecular mechanics methods [119]. Molecular mechanics methods provide the means of modeling the behaviour of molecules that are too large to be subjected to effective semi-empirical treatment. Molecular mechanics avoids quantum mechanical theory completely, and therefore does not employ a wave function or total electron density in its construct [120]. The energy expression consists of the sum of simple classical equations with some associated constants called the force fields. The

constants in the equations are obtained either from spectroscopic data or ab initio calculations. These equations describe various aspects of the molecule, such as bond stretching, bond bending, torsions, electrostatic interactions, van der Waals forces, and hydrogen bonding [123]. Force fields differ in the number of terms in the energy expression, the complexity of those terms, and the way in which the constants were obtained. Since electrons are not explicitly included, electronic processes cannot be modeled [123].

Various terms that may be present in the energy expression include the valence terms for describing a single aspect of the molecular shape such as bond stretching, angle bending, ring inversion, or torsional motion; the cross terms for describing the relative effect of one type of motion of the molecule on the other types of motion [119, 120, 123]. A cross term commonly used is a stretch-bend term, which describes how equilibrium bond lengths tend to shift as bond angles are changed. Some force fields contain two or more valence terms, some have no cross terms, while some contain electrostatic functions that are based on Coulombs laws [123]. Common force field terms employ in most of the current molecular mechanics calculations include the harmonic force field terms for describing bond stretch and angle bend, cosine force field term for the torsion, Leonard-Jones force field term for van der Waals interactions, Coulomb force field term for electrostatic interactions, Taylor and Morse force field terms for the stretch-bend and bond stretch respectively. Each of these force field terms has unique mathematical expression for calculating the energy term [123].

A molecular mechanics force field may be parameterized for a specific class of molecules and any relevance of such force field will be found in describing other molecules that belong to the class used in the parameterization. Commonly used molecular mechanics force fields that have been implemented in different software packages include the assisted model building with energy refinement (AMBER), the chemistry at Harvard macromolecular mechanics (CHARMM), the consistent force field (CFF), the Carbohydrate hydroxyls

represented by external atoms (CHEAT), the DREIDING, the empirical conformational energy program for peptides (ECEPP), the empirical force field (EFF), the Gronigen molecular simulation (GROMOS), the molecular mechanics (MM), the Merck molecular force field (MMFF), the optimized potentials for liquid simulation (OPLS), the Tripos, the universal force field (UFF), etc. [123].

2.9 Molecular dynamics (MD) and Monte Carlo (MC) simulations

In the conventional molecular mechanics approach, the molecule is assumed to be quite small and characterized by fairly "stiff" molecular coordinates such that its "well" on the potential energy surface (PES) will be narrow and deep, and the range of structures it samples will all be fairly close to the so called minimum-energy structure. This idea may be hypothetically reasonable for a molecule with fairly "stiff" molecular coordinates. However, most real life chemical problems involving molecules and molecular phenomena are characterized by large molecules or bulk materials containing thousands of atoms. Such systems are characterized with 'loose' molecular coordinates and series of non-bonding interactions, having many loose degrees of freedom. In the real systems the probability distribution of possible structures is not compactly localized and the structure-less nature of such molecular systems must be taken into account in ensuring proper description of their properties.

The vast majority of experimental techniques measure molecular properties as averages, which may be either time averages or ensemble averages or, most typically, both. The aim of molecular dynamics and Monte Carlo computational techniques is to reproducing these aspects of molecular behaviour as accurately as possible [120] Computer simulations are generally carried out to gain better insights into understanding the properties of microscopic interactions between assemblies of molecules in order to complement the

observations from the macroscopic experimental findings. They are widely used to study the structure and dynamics of macromolecules. The two main families of simulation technique are the molecular dynamics (MD) and Monte Carlo (MC). Additionally, there is a whole range of hybrid techniques which combine features from both simulation techniques [138].

The mathematical theories, formulations and equations that form the basis of MD and MC simulations have been discussed in details in various sources [120, 138-147].

2.9.1 The use of MD and/or MC simulations in corrosion inhibition studies

The inhibition of metal corrosion by organic compounds (inhibitors) is generally believed to begin with the adsorption of the inhibitor molecules on the metal surface. The adsorption of organic compounds on the metal surface could be as result of electrostatic interactions between the charged organic (inhibitor) molecules and the oppositely charged metal surface. This mode of adsorption is known as the physical adsorption or physisorption [148, 149]. On the other hand, corrosion inhibitors may adsorb on metal surface by the sharing of electrons between some atomic entities or functional groups in the inhibitor molecule and some atomic orbitals in the metal [150]. A donor atom in the inhibitor molecule may donate its unshared electrons or pi-electrons to the appropriate vacant orbital(s), usually d-orbitals of the metal to form coordinate bond. This mode of adsorption is referred to as the chemical adsorption or chemisorption [151]. A proper investigation of the mode of adsorption of inhibitor molecules on metal surface is very crucial for proper understanding of the inhibition properties of organic compounds, and also in designing new corrosion inhibitors. Both modes of adsorption produce protective film on the metallic surface, which prevents the surface from direct exposure to corrosive medium.

Although, quantum chemically derived parameters such as the frontier molecular orbital energies and other derivable quantities have been successfully correlated with the

corrosion inhibition behaviour of organic compounds, however, instances have also been reported where quantum chemical parameters did not correlate sufficiently with the experimentally observed trend of corrosion inhibition potentials of some sets of organic compounds [84, 152]. It has also been proposed that quantum chemical calculations alone are not sufficient to provide theoretical explanations to the adsorption and inhibition behaviour of organic compounds [153, 154].

Theoretical models that will mimic the real experimental situations should be able to predict the actual interfacial interactions between the concerned metallic surface and inhibitor molecules. More recent studies that attempt to provide more in-depth investigations into the adsorption phenomena and corrosion inhibition properties of organic compounds have adopted the use of MD and/or MC simulations as modern tools for predicting the actual interfacial configuration (minimum energy configuration) of the interactions between organic molecules and bulk metal surface, as well as the associated adsorption and binding energies. The simulations also have the capability of predicting the mode of adsorption (physisorption or chemisorption) involved in the inhibition process.

A review of past studies in the use of MD and MC simulation techniques in corrosion inhibition researches identified the works of Obot and Gasem [155], in which MD simulations were used in conjunction with DFT quantum chemical calculations to substantiate the observed trend of the inhibition efficiencies of some pyrazine derivatives. Xia et al. had also employed MD simulations to investigate the relationship between the structure of some imidazole derivatives and their corrosion inhibition performances [156]. Cao et al. had successfully made use of MD simulations to study the interaction between the inhibitor molecules and Fe (1 0 0) surface and found a good correlation between experimental and theoretical results [157].

Kovacevic and Kokalj [158] had successfully investigated the adsorption of four azole molecules on Cu(111) and Al(111) surfaces by means of atomistic computer simulations based on density-functional theory and plane-wave pseudopotential method. Kokalj and Sebastijan [159] had provided a detailed description of the adsorption behaviour of neutral and dehydrogenated species of 3-amino-1,2,4-triazole, benzotriazole, and 1-hydroxybenzotriazole on Cu(111) surface, by using the atomistic computer simulations based on density-functional theory and plane-wave pseudopotential method. Guo et al. [67] had investigated the interactions of three triazole derivatives with Cu(111) substrates with the aid of the periodic slab model using density functional theory calculations. Tang et al. had utilized the MD simulations approach with the use of Fe (001) cleaved surface to reveal that molecules of 2-amino-5-phenyl-1,3,4-thiadiazole adsorb on the iron surface in the vertical manner with the adsorption of Cl^- and SO_4^{2-} electrolyte anions, and the higher negative interaction energy was observed in the SO_4^{2-} containing medium [91].

Obot and his co-workers had in various studies, proven the suitability of MC simulation technique for the description of adsorption characteristics of inhibitor molecules on metal surface. The lowest energy configuration and the associated energy parameters, including the total, average, van der Waals, electrostatic, intermolecular, adsorption, and deformation energies had been reported for the interactions of some 5-(phenylthio)-3H-pyrrole-4-carbonitriles with Fe (110) by using the MC simulation approach [160]. In a related study, MC simulations of the interactions between 2-(2-bromophenyl)-1H-benzimidazole and Fe (110) surface, and 2-(2-bromophenyl)-H-benzimidazole and Fe (110) surface produced the adsorption energies that correlated well with the trend of experimental inhibition efficiencies [161]. The most stable configuration and adsorption energies for the interaction of some amino acids with Cu (111)/50 H_2O interface had been reported in a study that was carried out with the aid of Metropolis MC simulations methodology in which the Condensed-phase

Optimized Molecular Potentials for Atomistic Simulation Studies (COMPASS) force field was employed [162]. The MC simulation approach had been used to calculate the equilibrium adsorption configurations of vinylimidazole and allylimidazole on Fe_2O_3 (0 1 0) surface and the results revealed that vinylimidazole inhibits steel corrosion better than allylimidazole in agreement with experimental findings [163].

Hence, previous studies in the last five years have strongly demonstrated the importance of MD and MC simulation techniques in proving better insights into the adsorption mechanisms of corrosion inhibitors on metal and metallic alloy surfaces.

2.10 Quinoxaline and its derivatives

As earlier stated under the problem statement (*vide supra* section 1.6), quinoxaline and its derivatives constitute an important class of nitrogen-containing heterocycles and exhibit a wide spectrum of applications. The unsubstituted quinoxaline is an hetero-aromatic compound with molecular formula $C_8H_6N_2$, and the molecular structure as shown in Figure 2.6. It comprises two six-membered aromatic rings – benzene and pyrazine fused together. It is therefore also referred to as benzopyrazine. In this section, some properties of quinoxaline, synthesis of quinoxalines, and their applications as corrosion inhibitors will be reviewed.

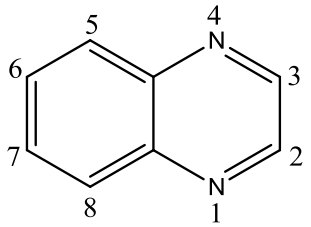

Figure 2.6. Molecular structure of quinoxaline

2.10.1 Some properties of quinoxaline

The parent quinoxaline molecule (Figure 2.6) is a colourless crystalline solid, soluble in water, and melts at 29-31℃ [164-166]. It is a weak base with pKa of 0.6. It is much more

basic than pyrazine (pKa 0.4) [165]. The second pKa of quinoxaline is -5.52, which implies that the molecule will only undergo significant di-protonation in a strong acidic medium [164]. Quinoxaline forms salts with acids and undergoes nitration under harsh conditions at 90 ℃ in the presence of concentrated nitric acid and oleum to give a mixture of 5-nitroquinoxaline (1.5 %) and 5,7-dinitroquinoxaline (24 %). Quinoxaline undergoes oxidation in the presence of the strong oxidizing agent, alkaline potassium permanganate to give pyrazine 2,3-dicarboxylic acid, while in the presence of peracid as oxidizing agent, quinoxaline di-N-oxide is formed [166-168].

A solution of quinoxaline in n-heptane exhibits UV-vis absorption spectra in the range of 304 – 375 nm with varying molar extinction coefficients. The chemical shifts (δ, ppm) of H-2/H-3 of quinoxaline have been reported to appear at 9.74 in $CDCl_3$, while the ^{13}CNMR peaks appear at C-2/C-3: 145.5, C-5/C-8: 129.8, C-6/C-7: 129.9, and C-4a/C-8a: 143.2 in $CDCl_3$ [164, 165].

2.10.2 Synthesis of quinoxalines

Quinoxalines are obtained by cyclocondensation of 1,2-diaminoarenes with 1,2-dicarbonyl compounds in the presence of a suitable substance as catalyst [165]. The general schematic equation for the synthesis of quinoxalines is given as:

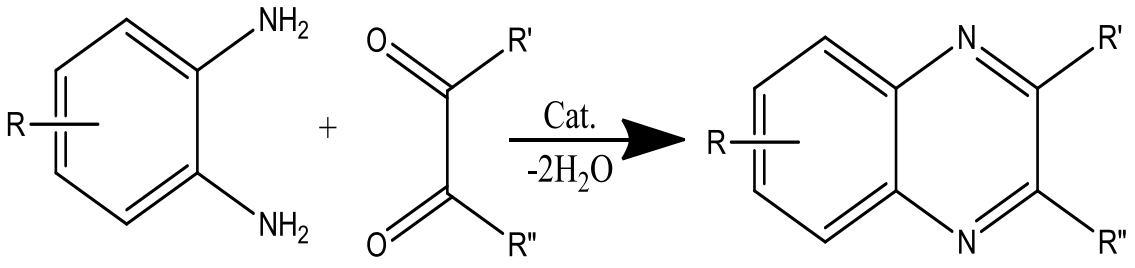

Scheme 1. Schematic equation for the synthesis of quinoxalines

Various catalysts have been designed towards continuous improved methods for the synthesis of quinoxalines. Some of the catalysts that have been successfully used in the synthesis of quinoxalines are aminosulfonic acid [169], MnO_2 [170], ceric ammonium nitrate [171], reusable polyaniline-sulfate salt catalyst [172], cupric sulfate pentahydrate [173], manganese octahedral molecular sieves [174], ionic liquid [TMPSA].HSO_4 (trimethyl-3-sulfopropylammonium) [175], $MnCl_2$ [176], Keggin-type W-heteropoly acid [177], NH_4Br [178, 179], $CuCl_2/O_2$ [178] etc. Apart from the reaction of 1,2-diaminoarenes with 1,2-carbonyl compounds, quinoxalines have also been successfully synthesised in the $SnCl_2$-promoted process involving the reaction of 2-nitroanilines, 1,2-dinitroarenes, or benzofuroxanes with 1,2-diketones. The $SnCl_2$ in the process acts both as a reducing agent and as a catalyst for cyclocondensation reaction [179]. Meshram et al. has also reported the effects of solvents and reaction time on the product yield when they synthesized various functionalized quinoxalines through the reactions of phenacyl bromides and diaminoarenes in the presence of 1,4-diazabicyclo[2,2,2]octane and atmospheric oxygen [180].

Factors that significantly influence the regioselectivity of quinoxaline formation include the electrophilicity of the C=O groups (on the di-carbonyl), the basicity of the $–NH_2$ functional groups (in the diamionoarene) and the reaction conditions such as pH and temperature [181].

2.10.3 Previous studies on quinoxalines as corrosion inhibitors

A number of studies have been reported on the use of quinoxalines as corrosion inhibitors. El-Ouali et al. [28] had studied the inhibition of steel corrosion in 1 M HCl by 2-phenylthieno(3, 2-b)quinoxaline using the weight-loss method and a maximum inhibition efficiency of 95 % was reported at 500 µM concentration. Zarrouk et al. [29] had reported the inhibition potentials of three functionalized quinoxalines namely, 2-(4-(2-ethoxy-2-oxoethyl)-

2-p-tolylquinoxalin-1(4H)-yl)acetate, 1-[4-acetyl-2-(4-chlorophenyl)quinoxalin-1(4H)-yl]acetone and 2-(4-methylphenyl)-1,4-dihydroquinoxaline for Cu in 2 M HNO_3 using the weight-loss and electrochemical techniques. In their study, Zarrouk and co-workers reported up to 92.7 % inhibition efficiency (from the EIS measurements) at 1000 µM concentration of 2-(4-(2-ethoxy-2-oxoethyl)-2-p-tolylquinoxalin-1(4H)-yl)acetate, and the inhibitors were found to act mainly as cathodic-type inhibitors. The three compounds were also observed to adsorb on Cu surface via the physical adsorption mechanism.

In another study, Abboud et al. [24] investigated the inhibition properties of 2,3-quinoxalinedione using both electrochemical and non-electrochemical techniques. The 2,3-quinoxalinedione was found to be a mixed-type inhibitor whose adsorption obeys the Langmuir adsorption isotherm. The inhibitor was observed to give 88 % (Tafel polarization measurement) inhibition efficiency at 1000 µM solution.

The corrosion inhibition potentials of acenaphtho[1,2-b]quinoxaline, indeno-1-one[2,3-b]quinoxaline, and 2,3-diphenylbenzoquinoxaline for MS in 0.5 M H_2SO_4 were reported in three separate studies carried out by Obot et al. [182] and Obot and Obi-Egbedi [12, 13] respectively using weight-loss method and quantum chemical calculations. The three compounds were found to exhibit inhibition efficiencies of 80, 81, and 99 % respectively (obtained from the weight-loss measurements) at 10 µM and 30 ^{o}C.

Furthermore, the study by Elayyachy et al. [183] compared the inhibition efficiencies of 2-[3-(2-oxo-2-phenylethylidene)-1,4-dihydroquinoxaline-2(1H)-ylidene]-1-phenylethanone and amino-2-aniline using both the weight-loss and electrochemical methods. It was observed that the quinoxaline derivative showed higher corrosion inhibition efficiency of up to 85 % at 298 K (from polarization measurements) for the C80 steel in 1 M HCl. Also, the corrosion inhibition activities of five quinoxaline derivatives, namely 3-methyl-2-phenylquinoxaline, 2,3-diphenylquinoxaline, 3-methyl-2(2‟‟hydroxyphenyl)quinoxaline, 3-phenyl-

2(2‟hydroxyphenyl)quinoxaline and 3-methyl-2(3‟-methoxy,4‟-hydroxyphenyl)quinoxaline for the corrosion in MS in 1 M H_2SO_4 was reported by Chitra et al. [184] using the weight-loss, gasometric and electrochemical methods.

Theoretical investigations of the prospective inhibition performances of the same set of compounds for the corrosion of Cu in acidic medium were reported by [185] using the quantum chemical calculations with the density functional theory method. The two studies revealed that the 3-methyl-2(3``-methoxy-4``-hydroxyphenyl)quinoxaline showed the best inhibition performance with the efficiency as high as 99 % (obtained from polarization method) at 1 mM concentration. All the compounds were found to be mixed-type inhibitors with predominantly cathodic inhibition activities [184].

Zarrok et al. [186] synthesized 3-methyl-1-propargylquinoxalin-2(1H)-one and investigated its inhibition potentials for carbon steel corrosion in 1 M HCl using both the weight-loss and electrochemical methods. The compound showed up to 91 % percentage inhibition efficiency (obtained from electrochemical methods), acted as a mixed-type inhibitor and adsorbed on the steel surface via competitive physical and chemical adsorption mechanisms as predicted by the Langmuir adsorption isotherm model. Adardour et al. [187] investigated the corrosion inhibition potentials of 3,7-dimethylquinoxalin-2(1H)-one and 3,7-dimethylquinoxalin-2(1H)-thione for MS in 1 M HCl using the weight-loss and electrochemical methods. It was observed that the inhibition potentials of the two compounds increased with increasing concentrations up to 86 % for the 3,7-dimethylquinoxalin-2(1H)-thione (obtained from weight-loss measurements) at 10000 µM and decreased thereafter.

More so, Elouali et al. [28] had studied the thermodynamics of steel corrosion in HCl solution in the presence of 2-phenylthieno(3,2-b)quinoxaline as corrosion inhibitor using the weight-loss method and quantum chemical calculations. An efficiency of 95 % was observed using 500 µM amount of the inhibitor at 308 K. The inhibition performances of quinoxaline,

2-chloroquinoxaline, 2-quinoxalinethiol, and 4-(quinoxalin-2-yl)phenol for MS in 1 M HCl were investigated by Fu et al. [188] using the weight-loss and electrochemical methods, as well as quantum chemical calculations and molecular dynamics simulation approaches. All the methods employed showed that the 4-(quinoxalin-2-yl)phenol exhibited the best inhibition potentials with 98 % inhibition efficiency at 1 mM concentration and 298 K (Tafel polarization results), and all the compounds are mixed-type inhibitors.

The present investigation therefore focuses on a different set of quinoxaline derivatives whose adsorption and corrosion inhibition properties have not been described anywhere in the literature. Extensive studies that involve various experimental techniques and theoretical methods were conducted in a bid to investigate for the first time, the adsorption of the selected compounds on MS in 1 M HCl solution and consequently their corrosion inhibition properties.

CHAPTER 3

MATERIALS AND METHODS

3.1 Experimental details

3.1.1 Materials, equipment, reagents and apparatus

3.1.1.1 MS (MS) sheets

The MS sheets used for the corrosion testing have the elemental composition (in weight percent) of Carbon (0.17 %), Manganese (0.46 %), Silicon (0.26 %), Sulphur (0.017 %), Phosphorus (0.019 %), and balance Fe. The choice of MS as the test material for this study is based on its wide industrial and structural applications [56, 189], which in turn are connected with its high strength to mass ratio and relatively low cost. Other special features of carbon steel and MS that support the choice of MS for this study have been highlighted in section 2.4.

3.1.1.2 Quinoxaline derivatives

The choice of quinoxaline derivatives as corrosion inhibitors in this study is premised on their documented anticorrosion activities and relative non-toxicity. Detailed literature review on the use of quinoxaline as corrosion inhibitors can be found in section 2.10.3 of this thesis. The presence of aromatic rings, pi-electrons and heteroatoms in the molecules of the compounds considered in this study portrays them as prospective efficient corrosion inhibitors. The quinoxaline derivatives investigated in this work were obtained from Vitas-M Laboratory, Ltd., Apeldoorn the Netherlands; Life Chemicals Inc., Munich, Germany; Enamine Ltd., New Jersey, United States of America, and ChemBridge Corporation, San Diego, United States of America. All the compounds are of high purity and were used without further purifications. The quinoxaline derivatives were divided into five groups based on some levels of similarity and specific variation in their molecular structure and substituent functional groups. Some relevant information about the quinoxaline derivatives and the acronyms with which they are referred are listed in Tables 3.1-3.5.

Table 3.1. GROUP I: Me-4-PQPB, Mt-4-PQPB, Mt-3-PQPB, and Oxo-1,3-PQPB

Structure	Source	Molecular formula and Name
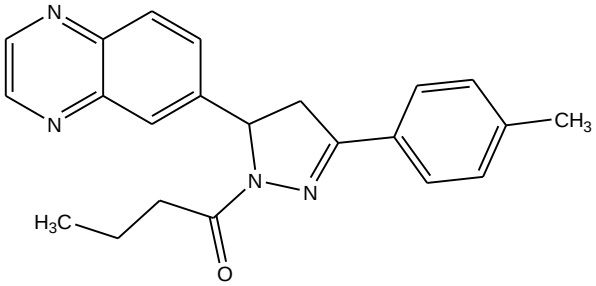 **Adopted acronym:** Me-4-PQPB	Life Chemicals Inc.	**Molecular formula:** $C_{22}H_{22}N_4O$ **Name:** 1-[3-(4-methylphenyl)-5-(quinoxalin-6-yl)-4,5-dihydropyrazol-1-yl]butan-1-one **Molecular mass:** 358.4363 g/mol
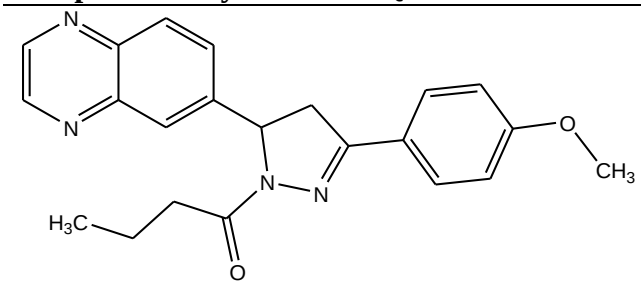 **Adopted acronym:** Mt-4-PQPB	Vitas-M Laboratory Ltd.	**Molecular formula:** $C_{22}H_{22}N_4O_2$ **Name:** 1-(3-(4-methoxyphenyl)-5-(quinoxalin-6-yl)-4,5-dihydro-1H-pyrazol-1-yl)butan-1-one **Molecular mass:** 374.4357 g/mol
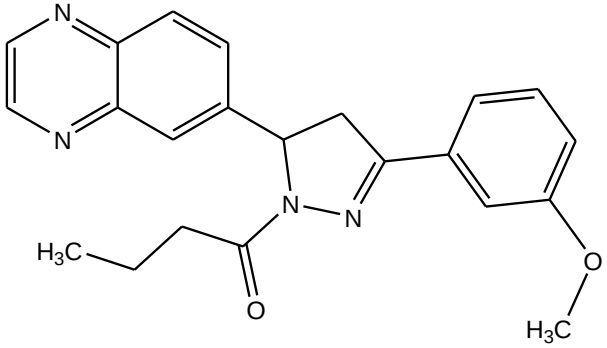 **Adopted acronym:** Mt-3-PQPB	Life Chemicals Inc.	**Molecular formula:** $C_{22}H_{22}N_4O_2$ **Name:**1-[3-(3-methoxyphenyl)-5-(quinoxalin-6-yl)-4,5-dihydropyrazol-1-yl]butan-1-one **Molecular mass:** 374.4357 g/mol
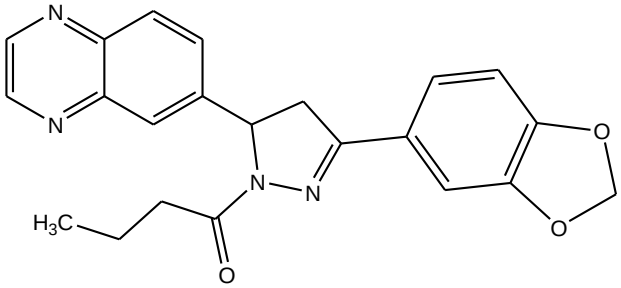 **Adopted acronym:** Oxo-1,3-PQPB	Vitas-M Laboratory Ltd.	**Molecular formula:** $C_{22}H_{20}N_4O_3$ **Name:**1-[3-(2H-1,3-benzodioxol-5-yl)-5-(quinoxalin-6-yl)-4,5-dihydropyrazol-1-yl]butan-1-one **Molecular mass:** 388.4192 g/mol

Table 3.2. GROUP II: PQDPB, PQDPP, and PPQDPE

Structure	Source	Molecular formula and Name
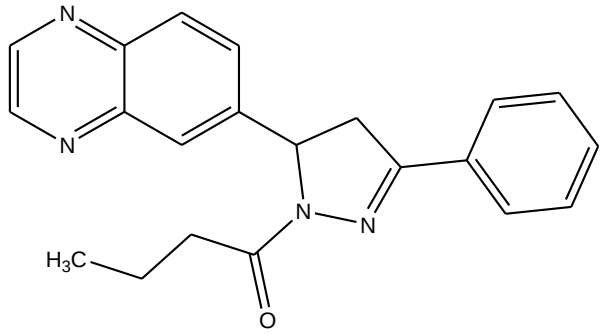 **Adopted acronym:** PQDPB	Vitas-M Laboratory, Ltd.	**Molecular formula:** $C_{21}H_{20}N_4O$ **Name:** 1-[3-phenyl-5-quinoxalin-6-yl-4,5-dihydropyrazol-1-yl]butan-1-one **Molecular mass:** 344.4097g/mol
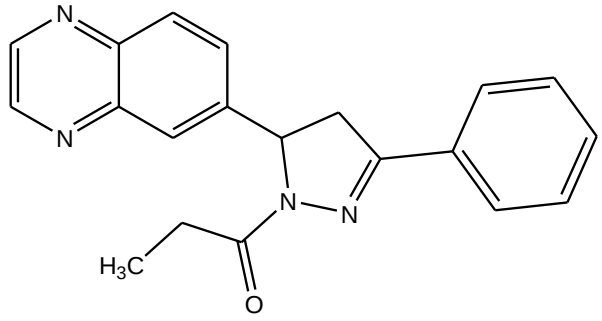 **Adopted acronym:** PQDPP	Vitas-M Laboratory Ltd.	**Molecular formula:** $C_{20}H_{18}N_4O$ **Name:** 1-(3-phenyl-5-(quinoxalin-6-yl)-4,5-dihydro-1H-pyrazol-1-yl)propan-1-one **Molecular mass:** 330.3831 g/mol
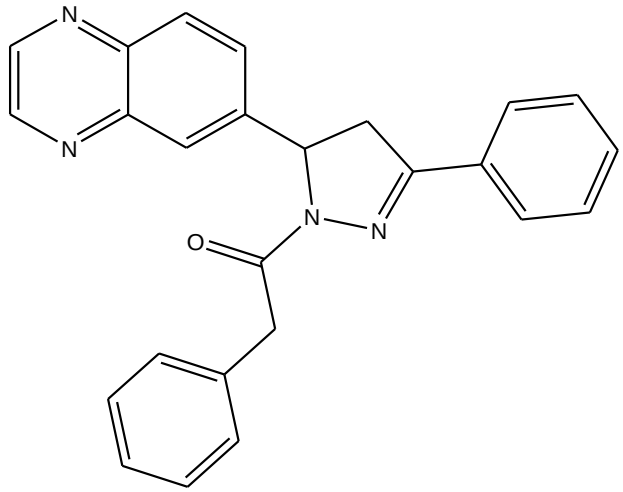 **Adopted acronym:** PPQDPE	Enamine Ltd.	**Molecular formula:** $C_{25}H_{20}N_4O$ **Name:** 2-phenyl-1-[3-phenyl-5-(quinoxalin-6-yl)-4,5-dihydropyrazol-1-yl]ethanone **Molecular mass:** 392.4525 g/mol

Table 3.3. Group III: MS-4-PQPP, MS-2-PQPP, and MS-3-PQPP

Structure	Source	Molecular formula and Name
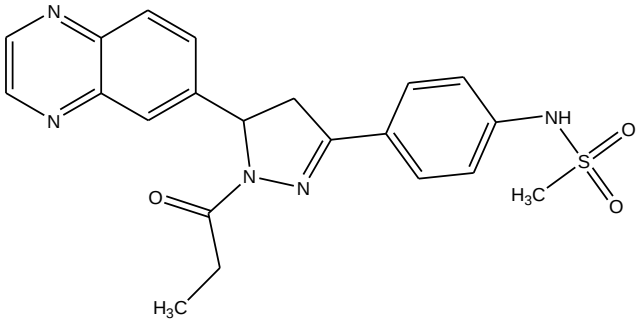 **Adopted acronym:** MS-4-PQPP	Life Chemicals Inc.	**Molecular formula:** $C_{21}H_{21}N_5O_3S$ **Name:** N-{4-[1-propanoyl-5-(quinoxalin-6-yl)-4,5-dihydropyrazol-3-yl]phenyl}methanesulfonamide **Molecular mass:** 423.488 g/mol
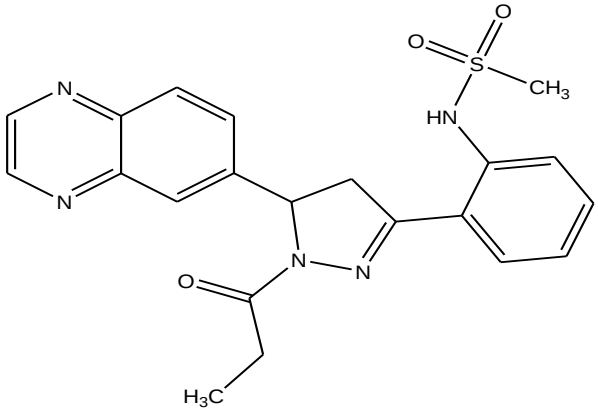 **Adopted acronym:** MS-2-PQPP	Vitas-M Laboratory Ltd.	**Molecular formula:** $C_{21}H_{21}N_5O_3S$ **Name:** N-(2-(1-propanoyl-5-(quinoxalin-6-yl)-4,5-dihydro-1H-pyrazol-3-yl)phenyl)methanesulfonamide **Molecular mass:** 423.488 g/mol
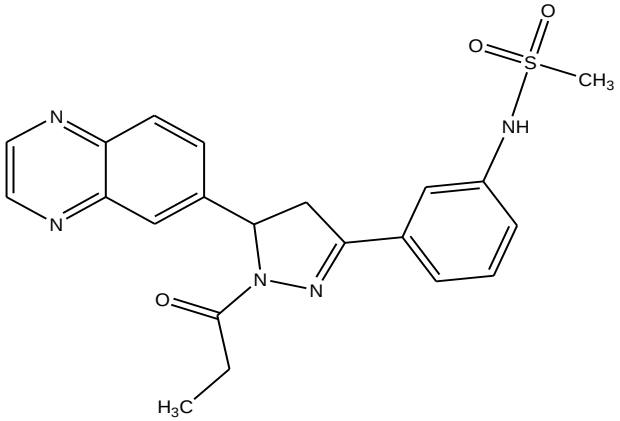 **Adopted acronym:** MS-3-PQPP	Vitas-M Laboratory, Ltd.	**Molecular formula:** $C_{21}H_{21}N_5O_3S$ **Name:** N-(3-(1-propanoyl-5-(quinoxalin-6-yl)-4,5-dihydro-1H-pyrazol-3-yl)phenyl)methanesulfonamide **Molecular mass:** 423.488 g/mol

Table 3.4. Group IV: MS-4-PQPMS, MS-3-PQPMS, and MS-2-PQPMS

Structure	Source	Molecular formula and Name
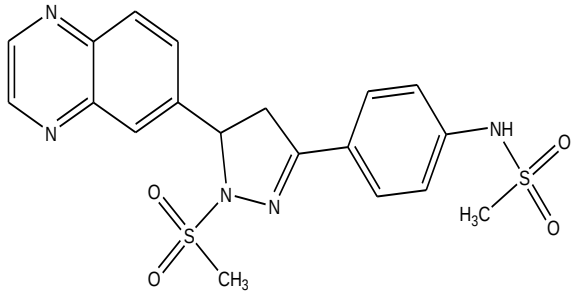	Enamine Ltd.	**Molecular formula:** $C_{19}H_{19}N_5O_4S_2$ **Name:** N-(4-(1-(methanelsulfonyl)-5-(quinoxalin-6-yl)-4,5-dihydro-1H-pyrazol-3-yl)phenyl)methanesulfonamide **Molecular mass:** 445.515 g/mol
Adopted acronym: MS-4-PQPMS		
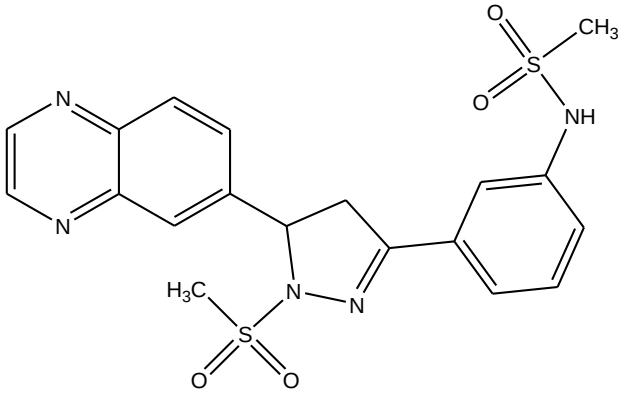	Vitas-M Laboratory Ltd.	**Molecular formula:** $C_{19}H_{19}N_5O_4S_2$ **Name:** N-{3-[1-(methylsulfonyl)-5-(quinoxalin-6-yl)-4,5-dihydro-1H-pyrazol-3-yl]phenyl}methanesulfonamide **Molecular mass:** 445.515 g/mol
Adopted acronym: MS-3-PQPMS		
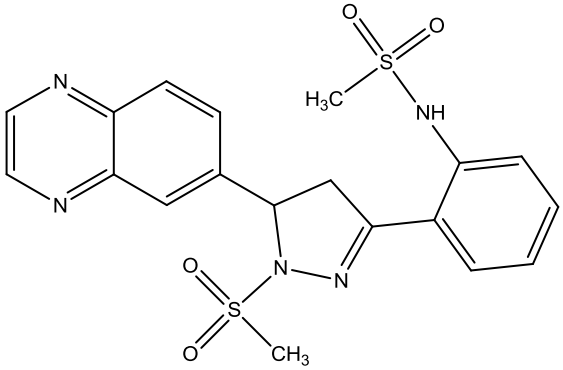	Life Chemicals Inc.	**Molecular formula:** $C_{19}H_{19}N_5O_4S_2$ **Name:** N-(2-(1-(methanesulfonyl)-5-(quinoxalin-6-yl)-4,5-dihydro-1H-pyrazol-3-yl)phenyl)methanesulfonamide **Molecular mass:** 445.515 g/mol
Adopted acronym: MS-2-PQPMS		

Table 3.5. Group V: Mt-3-PQPP, Cl-4-PQPP, MS-4-PQPA, and MS-2-PQPA

Structure	Source	Molecular formula and Name
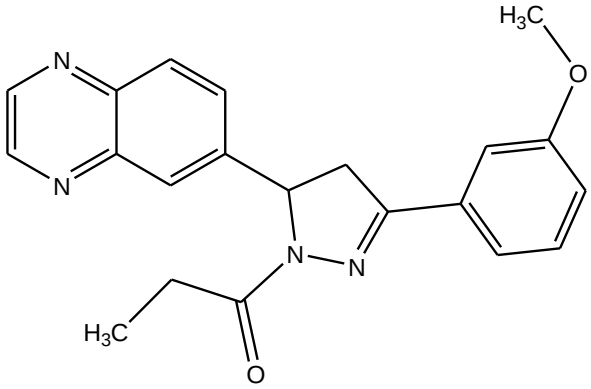 **Adopted acronym:** Mt-3-PQPP	Vitas-M Laboratory, Ltd.	**Molecular formula:** $C_{21}H_{20}N_4O_2$ **Name:** 1-[3-(3-methoxyphenyl)-5-(quinoxalin-6-yl)-4,5-dihydropyrazol-1-yl]propan-1-one **Molecular mass:** 360.4091 g/mol
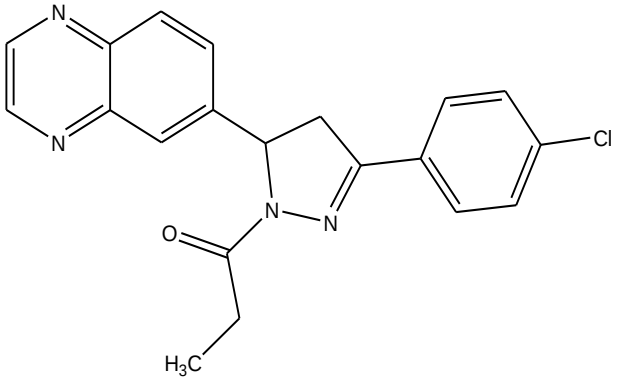 **Adopted acronym:** Cl-4-PQPP	Life Chemicals Inc.	**Molecular formula:** $C_{20}H_{17}ClN_4O$ **Name:** 1-(3-(4-chlorophenyl)-5-(quinoxalin-6-yl)-4,5-dihydro-1H-pyrazol-1-yl)propan-1-one **Molecular mass:** 364.828 g/mol
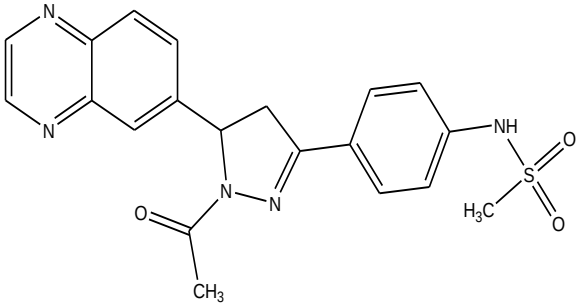 **Adopted acronym:** MS-4-PQPA	ChemBridge Corporation	**Molecular formula:** $C_{20}H_{19}N_5O_3S$ **Name:** N-{4-[1-acetyl-5-(quinoxalin-6-yl)-4,5-dihydropyrazol-3-yl]phenyl}methanesulfonamide **Molecular mass:** 409.462 g/mol
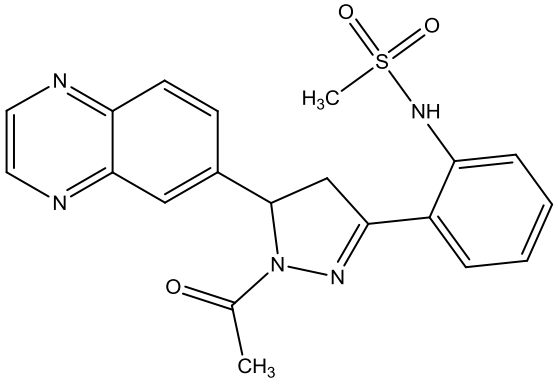 **Adopted acronym:** MS-2-PQPA	Vitas-M Laboratory, Ltd.	**Molecular formula:** $C_{20}H_{19}N_5O_3S$ **Name:** N-{2-[1-acetyl-5-(quinoxalin-5-yl)-4,5-dihydropyrazol-3-yl]phenyl}methanesulfonamide **Molecular mass:** 409.462 g/mol

3.1.1.3 Other chemicals, reagents and accessories

The hydrochloric acid used for the experiment has an assay of 32 % and was obtained from Promark chemicals, South Africa. The analytical reagent (AR) grade acetone with 99.5 % assay was obtained from Sigma Aldrich, South Africa. Epoxy resin and catalyst were obtained from Davidson Fibreglass, Pretoria, Gauteng, South Africa. Distilled water was used throughout the experiments.

3.1.1.4 Equipment and apparatus

Basic laboratory apparatus used for the experiments include a 2000 mL volumetric flask, 50 mL volumetric flasks, 100 mL beakers, 20 mL sample bottles, glass funnel, spatula, pipettes and pipette fillers. The two Autolab galvanostat/potentiostat (PGSTAT) 302N pieces of equipment used for all the electrochemical studies were acquired from Metrohm Eco Chemie, Utrecht, the Netherlands and Metrohm SA, Pretoria, Gauteng, South Africa. The Ag/AgCl in 3 M KCl reference electrode (RE), the platinum rod counter electrode (CE), and the glass cell used for electrochemical studies were obtained from and Metrohm SA, Pretoria, Gauteng, South Africa.

The Fourier transform infrared (FTIR) spectrophotometer (Cary 600 series FTIR) was obtained from Agilent Technology, California, the United States of America. The two UV-visible spectrophotometers used in this work are the Cary series UV-vis spectrometer obtained from Agilent Technology, California, the United States of America, and the UviLine 9400 obtained from SCHOTT Instruments, SWISS Laboratory, Midrand, Gauteng, South Africa. The SHIMADZU AY 220 analytical weighing balance obtained from SHIMADZU Corporation, Philippines was used for all the weighing. The silico rubber moulds, and the Struers MD Piano 220 (size: 200 dia) and Struers LaboPol-1 were obtained from IMP

Scientific & Precision (PTY) Ltd. Boksburg, Gauteng, South Africa. The pictures of some of the equipment used are shown in Figures 3.1-3.4.

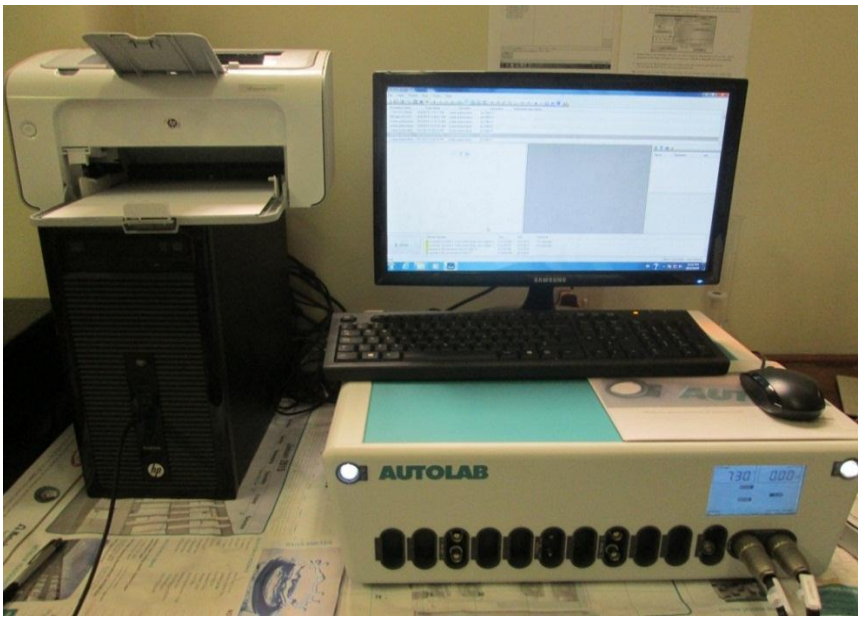

Figure 3.1. The Autolab PGSTAT 302 N used for electrochemical studies.

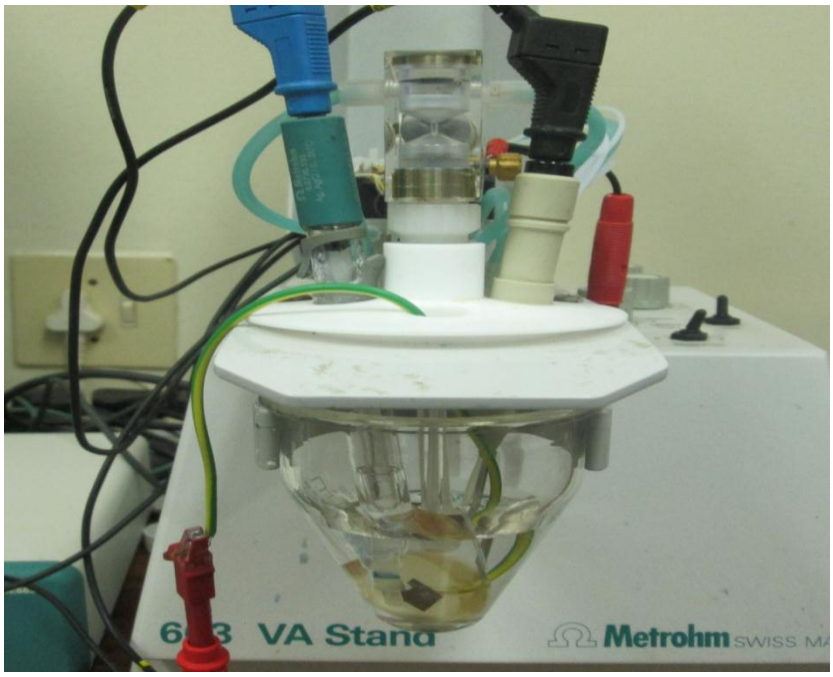

Figure 3.2. Typical set-up of the electrochemical experiment showing the electrochemical glass cell and electrodes.

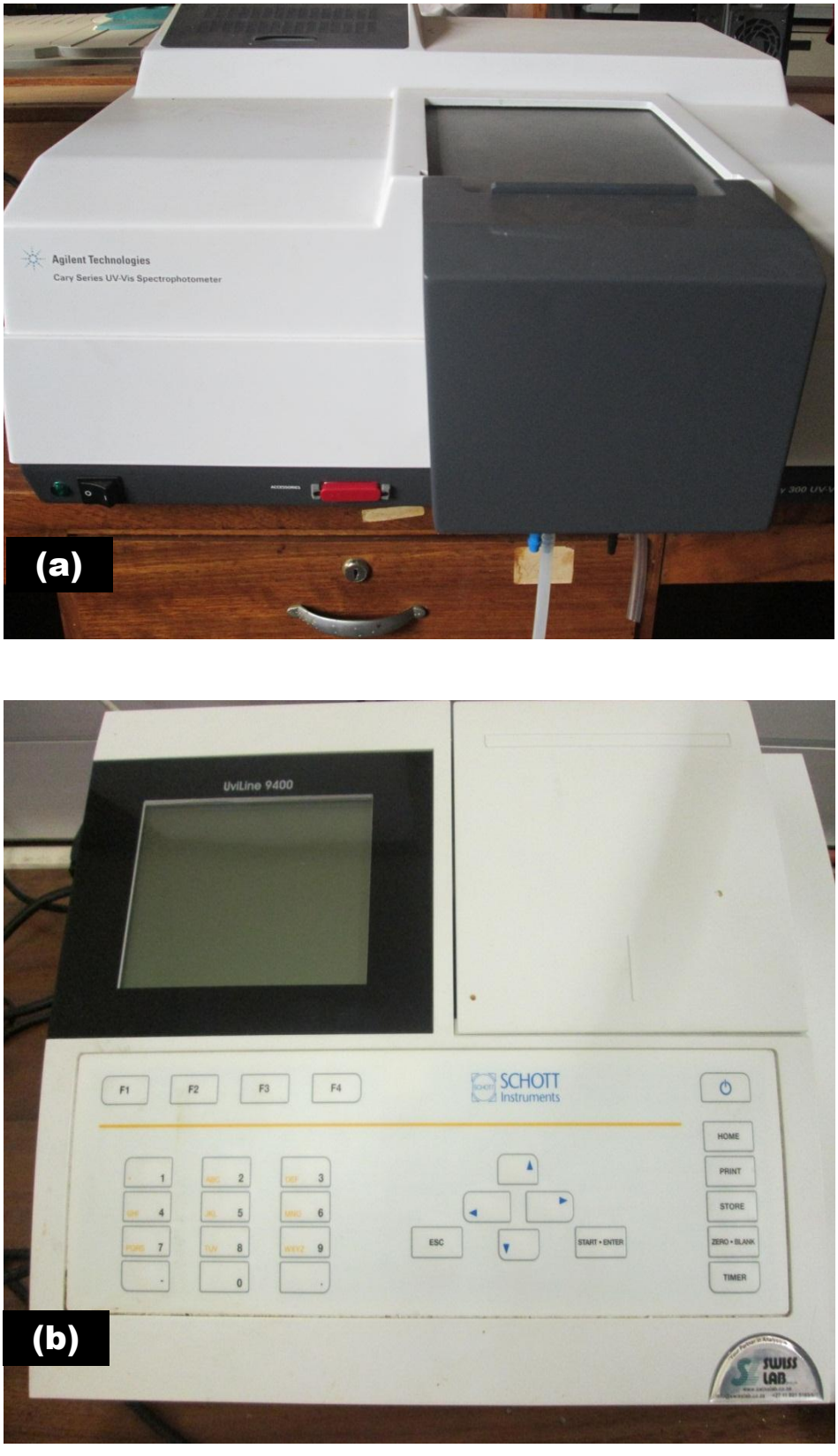

Figure 3.3. The UV-Vis spectrophotometers (a) Cary UV-Vis, and (b) UViLine 9400 used for the UV-Vis studies.

Figure 3.4. The Struers LaboPol-1equipment used for pre-surface cleaning.

3.1.2 MS working electrode: pre-treatment and surface preparation

For the purpose of electrochemical studies, MS sheets were cut into 1 cm × 1 cm dimension, glued to a connecting wire using aluminium foil tape, and embedded in a silico-rubber mould or holder using epoxy resin. A few drops of catalyst were added to the resin to facilitate setting or solidification. A representative picture of the MS working electrodes (WEs) used for the experiments is shown in Figure 3.5. An exposed surface area of 1 cm^2 was ensured for the MS working electrode (WE) to maintain uniform contact area for electrochemical reactions. The MS surface was mechanically abraded on Struers MD Piano 220 (size: 200 dia) mounted on Struers LaboPol-1 machine to remove traces of epoxy resin from the surface. The surface was then ground with SiC paper of graded grit sizes ranging from 600 to 1200 to ensure a relatively polished surface free of initial corrosion products or rusts. The MS surface was then washed with water, degreased in acetone and then washed

with water again, before finally dried with clean white towel paper. The surface pre-treated MS specimens were used immediately for the electrochemical experiments.

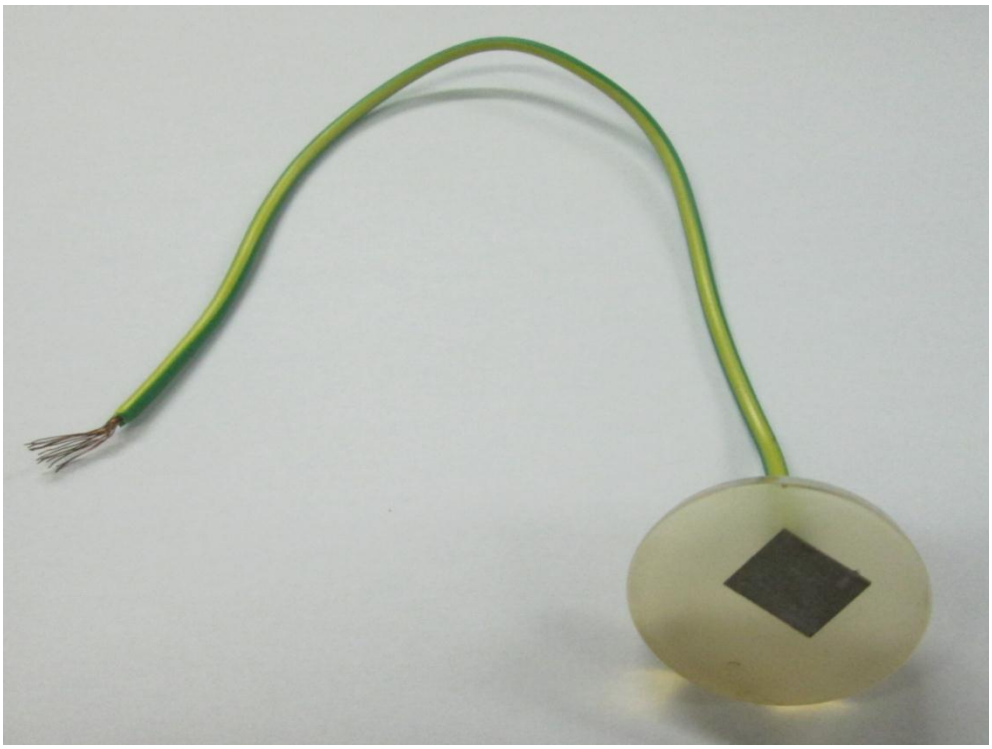

Figure 3.5. The picture of a typical MS (WE) used for the experiments.

3.1.3 Aggressive solutions and electrolytes

The aggressive solution of 1 M HCl (pH = 0) was prepared by diluting 196.50 mL the 32% AR grade HCl with distilled water and make up to 2000 mL. HCl is one of the two most commonly used acids in industrial environments. It is relatively cheap and readily available in the market. This informed its choice as the test corrosive medium for this study. Some industrial applications of HCl, other acids being used, and the behaviour of carbon steel or MS in acidic environments have been presented in section 2.4. Even though the HCl solutions used in many industrial processes may not be up to 1 M concentration, the choice of 1 M HCl for this study is to mimic a more punitive aggressive environment for testing the protective efficacy of the selected corrosion inhibitors. Various concentrations: 5, 10, 20, 40, 60, 80, and

100 ppm of the inhibitors were prepared by carefully weighing the appropriate amounts of each quinoxaline derivative and dissolve in 50 mL volumetric flask using 1 M HCl solution. A carefully measured 20 mL solution of 1 M HCl was used as the electrolyte for the blank experiment (without the inhibitor). Similarly, 20 mL solutions that contain various concentrations of test compounds (the quinoxaline derivatives) were used as electrolytes for the inhibitor containing electrolytes.

3.1.4 Electrochemical measurements

All electrochemical measurements were carried out on the Autolab PGSTAT 302N equipped with a three-electrode electrochemical cell system and driven by the general purpose electrochemical system (GPES) software and Frequency response analyzer (FRA) software. The Nova 1.10.1.9 software was used in some cases. Some of the adopted steps for the electrochemical set-up and measurements have been previously described in the literature [57, 90, 112, 190-193]. A Ag/AgCl in 3 M KCl electrode was used as the reference electrode (RE), a platinum rod was used as the counter electrode (CE), while a MS sample obtained as described in section 3.1.2 was used as the working electrode (WE). The RE, CE and WE are all immersed in the electrolyte such that the WE is close to the RE as much as possible in order to minimize voltage (IR) drop, and the electrochemical cell is connected to the potentiostat. The typical electrochemical set-up is shown in Figure 3.2 above.

After the immersion of the MS (WE) in the aggressive solution, a period of 30 minutes was allowed for the electrochemical system to reach the steady open circuit potential (OCP) before carrying out the electrochemical measurements. This period has been adjudged to be sufficient for OCP stabilization for an electrochemical system consisting of MS in acidic medium [57, 60, 90, 148, 191, 193-199].

Tafel curves were obtained by sweeping the potential up to ±100 mV with respect to the E_{corr} [200, 201] at the scan rate of 1 mV/s [201-204]**.** This potential range is enough to provide sufficiently linear Tafel regions as Tafel curves are known to be obtained when the potential is drifted away from the E_{corr} by up to ±50 to ±100 mV [36]. The electrochemical impedance spectroscopic (EIS) measurements were conducted at the OCP by analyzing the frequency response of the electrochemical system in the range of 100 kHz to 100 mHz at 5 mV peak-to-peak amplitude using the AC-signal [193].

All electrochemical experiments were conducted under aerated unstirred conditions at 303 K. Corrosion inhibition efficiency (% IE_p) was calculated from the polarization experiment as [60, 191, 196, 197, 205-208]:

$$\%IE_P = 100\left(\frac{i_{corr}^0 - i_{corr}}{i_{corr}}\right) \tag{3.1}$$

where i_{corr}^0 and i_{corr} are corrosion current densities in the absence and presence of inhibitors respectively.

For the impedance experiment, corrosion inhibition efficiency (% IE_I) was calculated using the equation [60, 191, 194, 196, 197, 205-208]:

$$\%IE_I = 100\left(\frac{R_{ct} - R_{ct}^0}{R_{ct}}\right) \tag{3.2}$$

where R_{ct}^0 and R_{ct} are the charge transfer resistances without and with various concentrations of inhibitors respectively.

The surface coverage (θ) is related to the percentage inhibition efficiency (%*IE*) as [209]:

$$\theta = \frac{\%IE}{100} \tag{3.3}$$

3.1.5 UV-vis spectroscopic studies

The ultraviolet-visible (UV-vis) spectroscopy is a well-known characterization technique that is suitable to differentiate between two different solutions based on their characteristic absorption of monochromatic light. The UV-vis spectroscopy is a simple and direct conventional technique that is often used provide quick information about possible transformation or otherwise that might have occurred in a reaction system over time. Each chemical species has its characteristic absorbance maximum called the wavelength of maximum absorption (λ_{max}). According to Beer-Lambert law, the absorbance of a chemical species is proportional to its concentration. A change in the position of the absorption maximum (λ_{max}) and/or change in the value of absorbance indicate(s) the introduction, formation, or presence of new specie(s) in the solution and a subsequent change in the composition of the solution. The UV-vis absorption is therefore suitable for the identification of the presence of metal-organic complex species in solution when a metal is immersed in an organic solution.

The UV-vis spectroscopic technique is often used in corrosion inhibition studies to inform the formation inhibitor-metal complex [24, 57, 60, 210]. In order to confirm the possibility of the formation of inhibitor-Fe complex, UV–vis absorption spectra of 1 M HCl solutions containing 100 ppm of each quinoxaline derivative were recorded before and after 3 hours of MS immersion.

3.1.6 Quantum chemical calculations

Geometry optimizations and vibrational frequency calculations were carried out on the neutral and singly protonated forms of the studied quinoxaline derivatives without symmetry constraint using the density functional theory (DFT) method. The essence of the vibrational frequency calculations was to ensure that the optimized geometry correspond to true energy

minimum in the potential well when there is no imaginary frequency. The force constant calculation is also necessary to obtain the zero-point energy corrected thermodynamic quantities required for the calculations of proton affinity. The B3LYP/6-31G(d) model chemistry employed in this study comprises the Becke's three parameter exchange functional [211] combined with Lee-Yang-Parr correlation functional for the electrons correlations [212, 213] and the Pople type basis set 6-31G(d). The B3LYP functional has been widely used in literature in conjunction with different Pople's basis sets to produce satisfactory geometries at relatively less computational cost [214-217].

The initial molecular structures of the compounds were modeled with the GaussView 5.0, while the geometry optimizations and force constant calculations were carried out using the Gaussian 09W version D.01 software [218]. All the possible sites of protonation were considered for the singly protonated species in order to identify the most favourable site of protonation. The reason for considering the protonated species is premised on the possibility of these compounds to undergo protonation in acidic medium such that the protonated species could take part in the corrosion inhibition process. All the calculations were carried out in the gas phase.

The frontier molecular orbital (FMO) energy parameters including the highest occupied molecular orbital (HOMO) and lowest unoccupied molecular orbital (LUMO) energies were obtained for both the neutral and protonated forms of the inhibitor molecules. According to the Koopmans' theorem [219], the E_{HOMO} is related to the ionization potential (I) as $I = -E_{HOMO}$, while the E_{LUMO} is related to the electron affinity (A) as $A = -E_{LUMO}$. Chemical potential, μ, Absolute hardness, η and absolute electronegativity, χ were calculated using the respective equations [119, 220]:

$$\mu = -\frac{1}{2}(I + A) \tag{3.4}$$

$$\eta = \frac{1}{2}(I - A) \tag{3.5}$$

$$\chi = \frac{1}{2}(I + A) \tag{3.6}$$

Other global reactivity parameters including the electrophilicity index (ω), global electron donating power, (ω^-) global electron withdrawing power, (ω^+) and net electrophilicity ($\omega^{\pm}$) were also calculated using the respective equations [119, 220]:

$$\omega = \frac{\mu^2}{2\eta} \tag{3.7}$$

$$\omega^- = \frac{(3I + A)^2}{16(I - A)} \tag{3.8}$$

$$\omega^+ = \frac{(I + 3A)^2}{16(I - A)} \tag{3.9}$$

$$\omega^{\pm} = \omega^+ - (-\omega^-) = \omega^+ + \omega^- \tag{3.10}$$

The fraction of electrons transferred (ΔN) from the inhibitor (donating) molecule to the metallic (Fe) atom (acceptor) was calculated according to the equation [221]:

$$\Delta N = \frac{\chi_{Fe} - \chi_{inh}}{2(\eta_{Fe} + \eta_{inh})} \tag{3.11}$$

where χ_{Fe} and η_{inh} denote the electronegativity and hardness of iron and inhibitor respectively. A value of 7 eV/mol was used for the χ_{Fe}, while η_{Fe} was equated to 0 eV/mol for bulk Fe atom in line with the Pearson's electronegativity scale [222]. The total energy change (ΔE_T) that accompanies charge transfer from a donor molecule (the inhibitor) to the acceptor molecule/atom (Fe) was calculated according to the approximation made by Gomez et al. [223]:

$$\Delta E_T = \frac{-\eta}{4} \tag{3.12}$$

where η is the chemical hardness of the inhibitor molecule. Equation 3.12 suggests that if both forward and back-donation of charges between donor and acceptor molecules do occur, the energy change is directly proportional to the hardness of the inhibitor molecule [223].

In order to predict the active sites in the inhibitor molecule that are most likely to exhibit interactions with the metal atom and facilitate the adsorption process, it is necessary to estimate the local reactivity indices. The Fukui functions (f (**r**)) have been successfully used to analyze the active atomic sites in the inhibitor molecules that are most likely to interact with the metal atom or ion during the adsorption and corrosion inhibition process [223, 224]. The Fukui functions (f (**r**)) indicate the change in the electron density of a N electron system upon addition or removal of an electron [225]. The Fukui function, f^+ (**r**) that governs nucleophilic attacks is the change in electron density of a N electron system when an electron is added to the system leading to a N+1 electron species. It is a measure of the tendency of a molecule to accept an electron from a donor species. The site with a higher value of f^+ (**r**) is considered to be more susceptible to attacks by nucleophiles, making it to be locally more electrophilic. The Fukui function, f^- (**r**) is the change in electron density of a N electron system when an electron is removed from the system leading to a N-1 electron system. It rules on the electrophilic attacks, and it is a measure of the tendency of a molecule to donate an electron to an acceptor species [119, 212, 226]. The site with a higher value of f^- (**r**) is considered to be more susceptible to attacks by electrophiles, making it to be locally more nucleophilic.

The atom condensed Fukui functions using the Mulliken population analysis (MPA) and the finite difference (FD) approximations approach introduced by Yang and Mortier [227] were calculated from the equations:

$$f_k^+ = \rho_{k(N+1)}(r) - \rho_{k(N)}(r) \qquad (3.13)$$

$$f_k^- = \rho_{k(N)}(r) - \rho_{k(N-1)}(r) \quad (3.14)$$

where $\rho_{k(N+1)}$, $\rho_{k(N)}$ and $\rho_{k(N-1)}$ are the electron densities of the k^{th} atom in a molecule with N+1 electrons, N electrons and N-1 electrons respectively. Electron density values were approximated by Mulliken gross charges obtained from geometry optimizations. The graphical representations of the electron density distribution for the Fukui indices f^+ and f^- were visualized with the aid of the Multiwfn software [228, 229].

3.1.7 Molecular dynamics (MD) and Monte Carlo (MC) simulations

Molecular dynamic (MD) or Monte Carlo (MC) simulations were carried out to model the adsorption behaviour of the studied quinoxaline derivatives on MS (iron) surface. The simulations were used to compute the binding or adsorption energies of the lowest configuration interactions between the inhibitors molecules and clean iron surface.

Molecular dynamic simulations were carried out for GROUPs I, III-V by using the forcite module in the Material Studio software 7.0 from BIOVIA-Accelrys, USA. The simulations were carried out with Fe (110) crystal with a slab of 5 Å. The Fe (110) plane was enlarged to a (10 × 10) supercell to provide a large surface for the interaction of the inhibitors. After that, a vacuum slab with 30 Å thickness was built above the Fe (110) plane. The MD simulations were performed in NVT canonical ensemble at 298K with a time step of 1.0 fs and a total simulation time of 500 ps using Anderson thermostat. The interaction energy (E_{int}) of molecules with Fe surface was obtained using the equation:

$$E_{int} = E_{total} - (E_{surface} + E_{molecule}) \quad (3.15)$$

where E_{total} is the total energy of the molecules and the metal surface system; $E_{surface}$ is defined as the energy of metal surface without adsorption of molecules and $E_{molecule}$ is the energy of the isolated molecule of quinoxaline derivatives.

The binding energy is the negative of the interaction energy and is given as:

$E_{binding} = -E_{int}$ (3.16)

Monte Carlo simulations were carried out on GROUP II by using the adsorption locator code implemented in the Material Studio 7.0 software from BIOVIA-Accelrys, USA. The adsorption phenomenon and adsorption energy of the interaction between the inhibitor molecules and clean iron surface were simulated in the presence of water molecules. The simulation was carried out in a simulation box (29.78 Å × 29.78 Å × 58.10 Å) with periodic boundary conditions in order to simulate a representative part of an interface devoid of any arbitrary boundary effects. The Fe (110) plane was then enlarged to a (12 × 12) supercell. After that, a vacuum slab with 50 Å thickness was built above the Fe (110) plane. The inhibitor molecules along with 100 molecules of water were used for the simulations in each case. The use of the water molecules is important since electrochemical corrosion inhibition process takes place in aqueous solution. Although, in-vaccuo simulations have also been documented to produce acceptable results.

The Fe(110) surface was used for the simulations because it provides adequate representation of the Fe surface with sufficient stability and moderate atom density [188, 230, 231]. The Fe(110) plane has been successfully applied in the literature to describe the interactions between inhibitor molecules and Fe surface [188, 191, 230-237].

The condensed-phase optimized molecular potentials for atomistic simulation studies (COMPASS) force field was used to optimize the structures of all components of the system of interest. The COMPASS force field is an ab initio force field that enables accurate and simultaneous predictions of gas-phase properties (structural, conformational, vibrational, etc.) and condensed-phase (equation of state, cohesive energies, interaction energies, etc.) for a broad range of organic molecules, inorganic molecules and metals [238-242].

CHAPTER 4

RESULTS AND DISCUSSION

4.1 GROUP I: Me-4-PQPB, Mt-4-PQPB, Mt-3-PQPB, and Oxo-1,3-PQPB

GROUP I comprises four quinoxaline derivatives as listed in Table 3.1. These compounds have similar structural skeletons and differ only in the type and position of the substituent group attached to the phenyl ring. The compounds were investigated for their adsorption and corrosion inhibition properties on MS in 1 M HCl using both experimental and theoretical methods. Tafel plots, electrochemical impedance spectroscopic (EIS), FTIR, and UV-Vis studies were carried out to describe the corrosion inhibition potentials and adsorption mechanisms of the studied compounds. Quantum chemical calculations were also carried out to provide corroborative theoretical explanations to the experimental observations.

It is important to state that the results of the studies conducted on Me-4-PQPB, Mt-4-PQPB, Mt-3-PQPB, and Oxo-1,3-PQPB have been published in a peer-reviewed journal and the following sections of results and discussion on this set of compounds essentially refer to the published article [243].

4.1.1 Electrochemical studies

4.1.1.1 Tafel plots

The Tafel curves for MS in 1 M HCl without and with various concentrations of the Me-4-PQPB and Mt-4-PQPB are shown in Figure 4.1, while the Tafel plots for the other two compounds are shown in Figure AI-1 (Appendix I). The values of electrochemical parameters including the corrosion potential (E_{corr}), corrosion current density (i_{corr}), anodic and cathodic Tafel slopes (β_a and β_c respectively) obtained from the extrapolations of the polarization curves are listed in Table 4.1. It is clear from Figure 4.1. that the Tafel curves shifted to lower corrosion current density regions in the presence of inhibitors when compared to the uninhibited system.

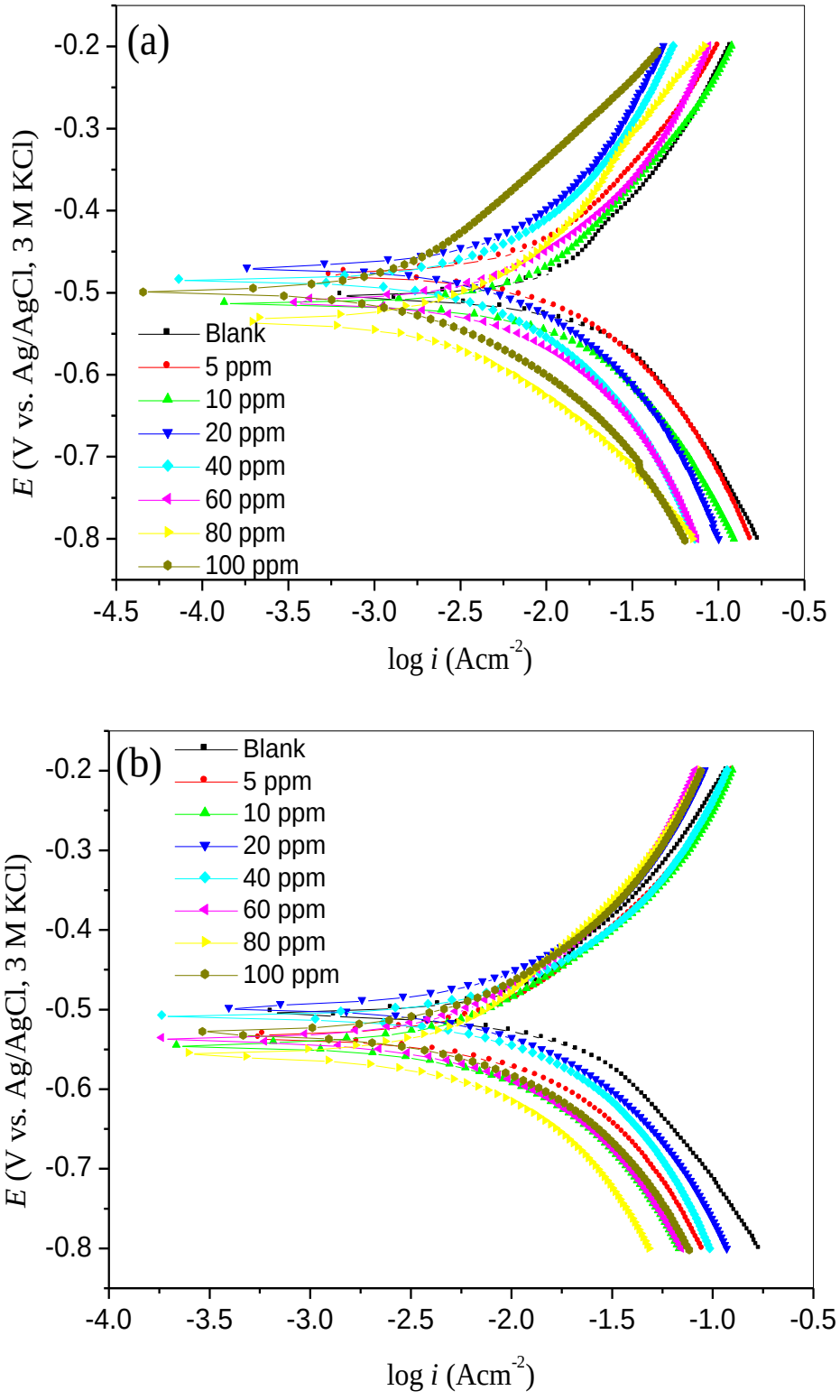

Figure 4.1. Tafel plots for MS in 1 M HCl without and with various concentrations of (a) Me-4-PQPB, and (b) Mt-4-PQPB.

Similar pattern of Tafel curves obtained for the four compounds suggests that the four compounds used as corrosion inhibitors exhibited similar inhibition mechanism. As reported in Table 4.1, the E_{corr} values are observed to shift to more positive values in most cases of the inhibitor concentrations when compared to the value for the uninhibited system. An inhibitor can be classified as cathodic, anodic or mixed type inhibitor based on the displacement of E_{corr} of inhibited system compared to the uninhibited one. A shift in E_{corr} greater than 85 mV relative to the E_{corr} of the blank is attributed to anodic or cathodic type inhibitor [244, 245]. The maximum shift in E_{corr} value in the present study is 54 mV, suggesting that the compounds are mixed-type inhibitors [202]. In other words, the compounds inhibit both the anodic and cathodic half reactions associated with corrosion process.

As shown in Table 4.1, the Tafel slopes, β_a and β_c change with the concentration of the inhibitors. The change in Tafel slopes has been reported to be due to a number of factors, which include the composition of the working electrode, concentration of the electrolyte, scan rate, and charge transfer coefficient [246]. De Souza and Spinelli [247] had reported the change in β_a for MS in acidic medium with varying concentration of caffeic acid inhibitor and have attributed the observations to the possible occurrence of the redox complexation process involving Fe(II) and Fe(III) complexes of the inhibitor, which in turn is affected by the pH of the medium and concentration of the inhibitor.

The values of β_a and β_c can also be used to corroborate the inference deducible from the displacement of E_{corr} in classifying the inhibiting effects of a compound as cathodic, anodic or mixed-type. The results in Table 4.1 show that the values of both β_a and β_c vary with inhibitor concentration. Though the variation of the Tafel slopes with concentration (Table 4.1) does not follow a definite trend, the results indicate that the addition of the inhibitors informs change in the values of both β_a and β_c, indicating that the rate of rate of both half-reactions inhibition varies with concentration of the inhibitors [244]. The overall

Table 4.1. Tafel parameters and percentage inhibition efficiency for the corrosion of MS in 1 M HCl containing different concentrations of inhibitors.

Inhibitor	*Conc.* (ppm)	$-E_{corr}$ (mV)	β_a (mV/dec)	β_c (mV/dec)	i_{corr} (mA/cm^2)	$\%IE_P$ (%)
Blank	-	504	133	246	9.87	
Me-4-PQPB	5	476	88	103	3.93	60.19
	10	474	87	119	3.62	63.28
	20	468	102	122	2.69	72.76
	40	484	101	111	2.21	77.61
	60	517	73	88	2.14	78.34
	80	533	127	127	1.94	80.34
	100	497	99	150	1.06	89.27
Mt-4-PQPB	5	506	108	143	5.55	43.74
	10	543	125	141	3.40	59.48
	20	480	112	134	3.72	62.24
	40	483	116	123	3.63	63.20
	60	536	118	145	3.54	64.10
	80	485	115	124	3.29	66.62
	100	528	112	126	3.15	68.08
Mt-3-PQPB	5	454	125	156	4.57	53.65
	10	505	131	150	3.91	60.36
	20	474	116	149	3.74	62.14
	40	470	96	148	3.70	62.51
	60	482	100	171	3.36	65.98
	80	483	104	168	3.21	67.42
	100	478	95	167	3.01	69.51
Oxo-1,3-PQPB	5	450	128	132	4.79	51.42
	10	486	102	172	4.34	55.96
	20	504	120	165	3.87	60.79
	40	462	118	153	3.75	62.02
	60	472	94	107	3.39	65.64
	80	461	106	155	3.22	67.35
	100	470	108	157	3.12	68.40

magnitude of the difference in β_a and β_c values compared to the blank results revealed that the inhibition effects of the studied compounds are cathodic-dominating since the changes in β_c values are more significant than the changes in βa values [117, 248]. The results obtained from the PDP study show that the corrosion current density decreases with increase in inhibitor concentration leading to an increase in inhibition efficiency. This might be due to

the interactions of inhibitor molecules with the steel surface. This reduces the area of active surface involved in corrosion [249]. The order of increasing inhibition efficiency of the studied compounds 100 ppm is Mt-4-PQPB < Oxo-1,3-PQPB < Mt-3-PQPB < Me-4-PQPB.

4.1.1.2 EIS measurements

The EIS measurements were conducted at the OCP after 1800 s of MS immersion in each aggressive medium. The representative Nyquist and Bode plots for MS in 1 M HCl without and with various concentrations of the studied compounds are in Figures 4.2 and 4.3 respectively for both Me-4-PQPB and Mt-4-PQPB. The EIS spectra for the other two compounds are shown in Figures AI-2 and AI-3 (Appendix 1). The Nyquist plots show a single depressed capacitive arc over the frequency range studied. More so, the Bode plots show a single peak in the plots of phase angle against frequency. This is an indication that the dissolution of MS is controlled by a single charge transfer process [250], and that the process is characterized by a single relaxation time constant. The imperfect semicircular nature of the Nyquist plots is a common observation for solid electrodes and is often referred to as the frequency dispersion of interfacial impedance which is commonly attributed to different factors such as surface roughness, impurities, discontinuity in the electrode, adsorption of inhibitor and inhomogeneity of the electrode surface [190, 250].

It is clear from Figure 4.2 that as the inhibitor concentration increases, the radius of the capacitive arc increases for all the four compounds. The impedance spectra were fitted into the equivalent circuit of the form $R_s(Q_{dl}R_{ct})$ in which the R_s was shorted by the constant phase element (CPE) which is placed in parallel to the R_{ct} as shown in Figure 4.4. The introduction of CPE into the circuit was necessitated by the prospective non-ideal capacitive behaviour of the electrode/electrolyte systems investigated in the present study, which promises to produce

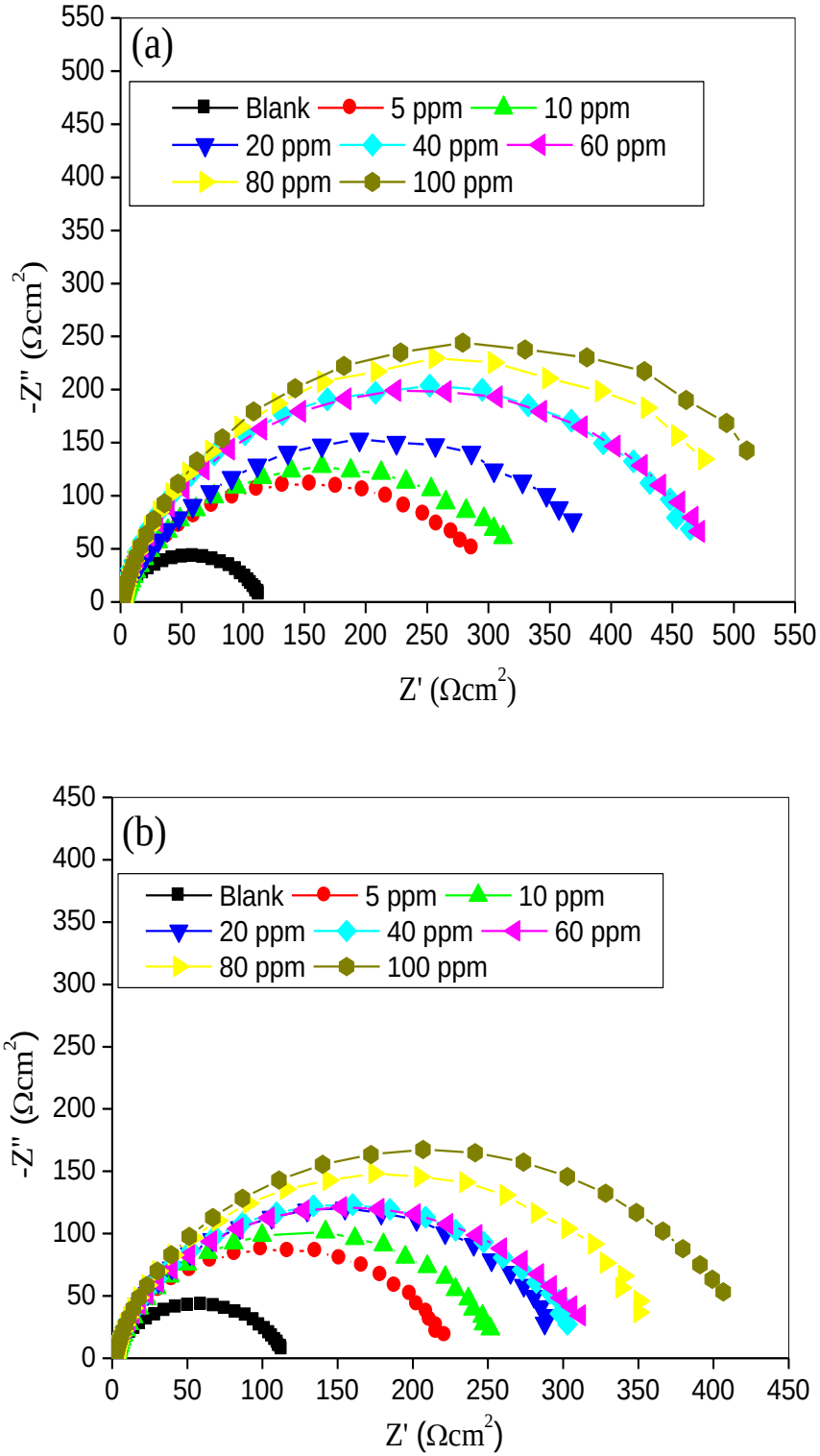

Figure 4.2. Nyquist plots for MS in 1 M HCl without and with various concentrations of (a) Me-4-PQPB, and (b) Mt-4-PQPB

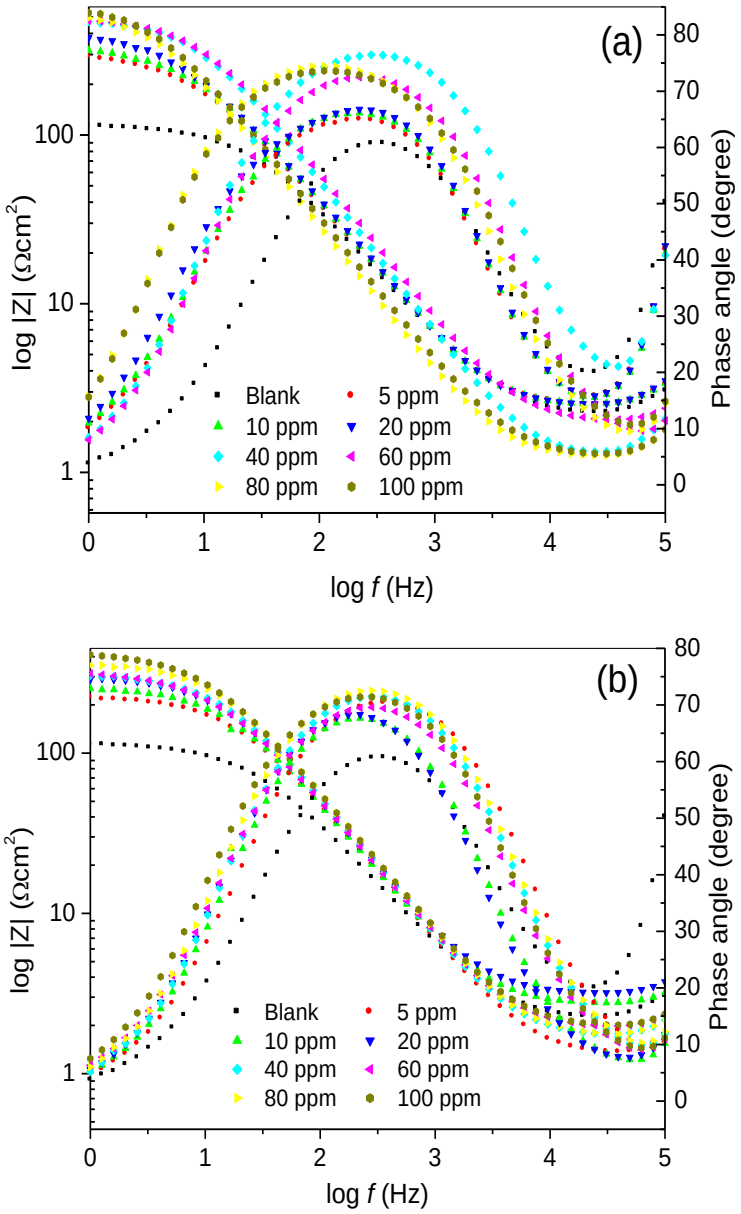

Figure 4.3. Bode plots for MS in 1 M HCl without and with various concentrations of (a) Me-4-PQPB, and (b) Mt-4-PQPB

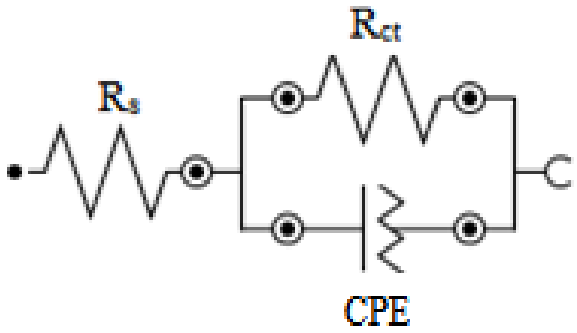

Figure 4.4. Equivalent circuit for the EIS experiment.

a more accurate fit.

Some relevant electrochemical parameters derived from the EIS measurements are listed in Table 4.2. The inhibition efficiencies derived from the EIS measurements are in close agreement with those obtained from the Tafel analyses. The data in Table 4.2 clearly reveal that the inhibitor molecules bring about a change in the electrical interface between the corrosive medium and the steel surface due to adsorption of inhibitors on MS surface. This leads to increase in the values of R_{ct} as the inhibitor concentration increases and hence an increase in inhibition efficiency. The values of the proportionality constant, Q do not show a uniform trend with change in inhibitor concentrations but the values of Q in the presence of inhibitors are lower than that of the uninhibited system, which suggests the adsorption of insulating layer on MS surface. The increase in the value of *n* (the gauge of inhomogeneity) in the presence of the inhibitors compared to the blank system also indicates the increase in inhomogeneity of the MS surface due to the adsorption of the inhibitor molecules, which leads to decrease in the exposed area of the active surface required for corrosion reaction [117].

The magnitude of the values of the phase angle ($|\theta|$) and slope ($|S|$) of the linear portion of log|Z| vs log *f* (at intermediate frequencies) are often used to explain the formation and nature of adsorbed film on electrode surface. The $|\theta|$ and $|S|$ are equal to 90 and 1 respectively for an ideal capacitor [117]. The closeness of these values to the thresholds for an ideal capacitor suggests the formation of adsorbed film on the electrode surface. The values of $|\theta|$ and $|S|$ as listed in Table 4.2 reveal that $|\theta|$ and $|S|$ are closer to 90 and 1 respectively in the presence of the inhibitors compared to the blank system. These relatively close values of $|\theta|$ and $|S|$ to that of ideal capacitor may be due to the formation of adsorbed film (of the inhibitor molecules) on the steel surface.

Table 4.2. EIS parameters and percentage inhibition efficiency for the corrosion of MS in 1 M HCl containing different concentrations of inhibitors.

Inhibitor	*Conc.* (ppm)	R_s (Ω/cm^2)	Q, Y_o ($\Omega^{-1}S^n cm^{-2}$)	n	R_{ct} (Ω/cm^2)	$\lvert\Theta\rvert$ (Degree)	$\lvert S\rvert$	$\%IE_I$ (%)
Blank	-	1.95	145.40	0.80	115.30	60.74	0.69	
Me-4-PQPB	5	2.28	126.90	0.82	300.50	65.00	0.77	61.63
	10	2.30	116.50	0.83	332.00	66.17	0.78	65.27
	20	2.28	119.80	0.82	402.00	66.75	0.79	71.32
	40	1.19	55.64	0.90	478.00	76.46	0.89	75.88
	60	1.98	55.92	0.88	486.00	72.49	0.85	78.74
	80	1.24	109.90	0.89	539.00	74.46	0.85	78.61
	100	1.25	105.80	0.88	589.00	73.63	0.83	80.42
Mt-4-PQPB	5	1.30	70.82	0.88	218.60	70.38	0.83	47.26
	10	2.70	73.37	0.88	250.90	67.66	0.81	54.04
	20	3.13	65.49	0.88	292.80	68.31	0.82	60.62
	40	1.70	61.98	0.88	302.3	71.52	0.85	61.86
	60	1.90	70.68	0.87	308.20	69.59	0.83	62.59
	80	1.71	56.62	0.89	357.00	72.55	0.86	67.70
	100	1.93	61.41	0.88	412.00	71.42	0.82	72.01
Mt-3-PQPB	5	1.72	68.32	0.88	241.80	70.15	0.84	52.32
	10	1.61	63.30	0.88	292.50	71.07	0.84	60.58
	20	2.16	107.4	0.85	270.30	67.34	0.80	61.78
	40	2.16	102.10	0.85	305.10	68.12	0.81	62.21
	60	3.43	76.77	0.86	341.00	67.88	0.81	66.19
	80	3.00	61.21	0.86	365.00	68.86	0.82	68.41
	100	2.99	59.41	0.87	380.00	69.13	0.79	69.66
Oxo-1,3-PQPB	5	1.72	68.32	0.88	241.80	70.15	0.84	52.32
	10	1.69	68.72	0.87	254.00	69.96	0.83	54.60
	20	2.59	89.90	0.84	294.20	66.79	0.80	60.81
	40	2.75	85.21	0.84	320.00	67.30	0.81	63.97
	60	2.46	65.68	0.88	336.00	70.91	0.85	65.68
	80	2.73	82.01	0.85	358.00	68.77	0.82	67.79
	100	2.72	79.80	0.86	365.00	68.89	0.79	68.41

4.1.2 Adsorption isotherms

The inhibition of metal corrosion by organic molecules is usually as a result of adsorption of the inhibitor molecule on the metal surface. The adsorption of an inhibitor on a metal surface depends on factors such as electronic properties, nature of metal surface, temperature, steric effect and varying degrees of surface-site activity [68]. The adsorption of

inhibitor on metal/solution interface may occur through the displacement of water molecules by the inhibitor molecules [251], which can be depicted by the hypothetical chemical equation:

$$Inh_{(sol)} + x\,H_2O_{(ads)} \leftrightarrow Inh_{(ads)} + x\,H_2O_{(sol)} \quad (4.1)$$

where, x (the mole ratio) is the number of water molecules replaced by one molecule of the inhibitor. The surface coverage, θ was calculated from the percentage inhibition efficiency (θ = %IE/100) using the data from both the polarization and EIS measurements at various concentrations of the inhibitors.

The data were subjected to various adsorption isotherm models including the Langmuir, Frumkin, Temkin, and Freundlich isotherms, but the Langmuir adsorption isotherm was found to give the best representation of the experimental data judging by the linearity of the isotherms and the near unity values of the correlation coefficient (R^2). The linear form of the Langmuir adsorption isotherm can be expressed as:

$$\frac{C_{inh}}{\theta} = \frac{1}{K_{ads}} + C_{inh} \quad (4.2)$$

where C_{inh} is the concentration of the inhibitor and K_{ads} is the equilibrium constant of the adsorption process. The isotherm plots of C_{inh}/θ *vs* C_{inh} are presented in Figure 4.5 in which straight lines with strong linear correlation coefficients of almost unity (R^2 = 0.99) are observed. The change in free energy of adsorption (ΔG_{ads}) was calculated from the relation:

$$\Delta G_{ads} = -RT \ln(55.5 K_{ads}) \quad (4.3)$$

where R is gas constant, T is absolute temperature and the constant 55.5 is the molar concentration of water.

The values of K_{ads} and ΔG_{ads} derived from the isotherms are listed in Table 4.3. The high values obtained for the K_{ads} as presented in Table 3 suggest strong adsorption of the

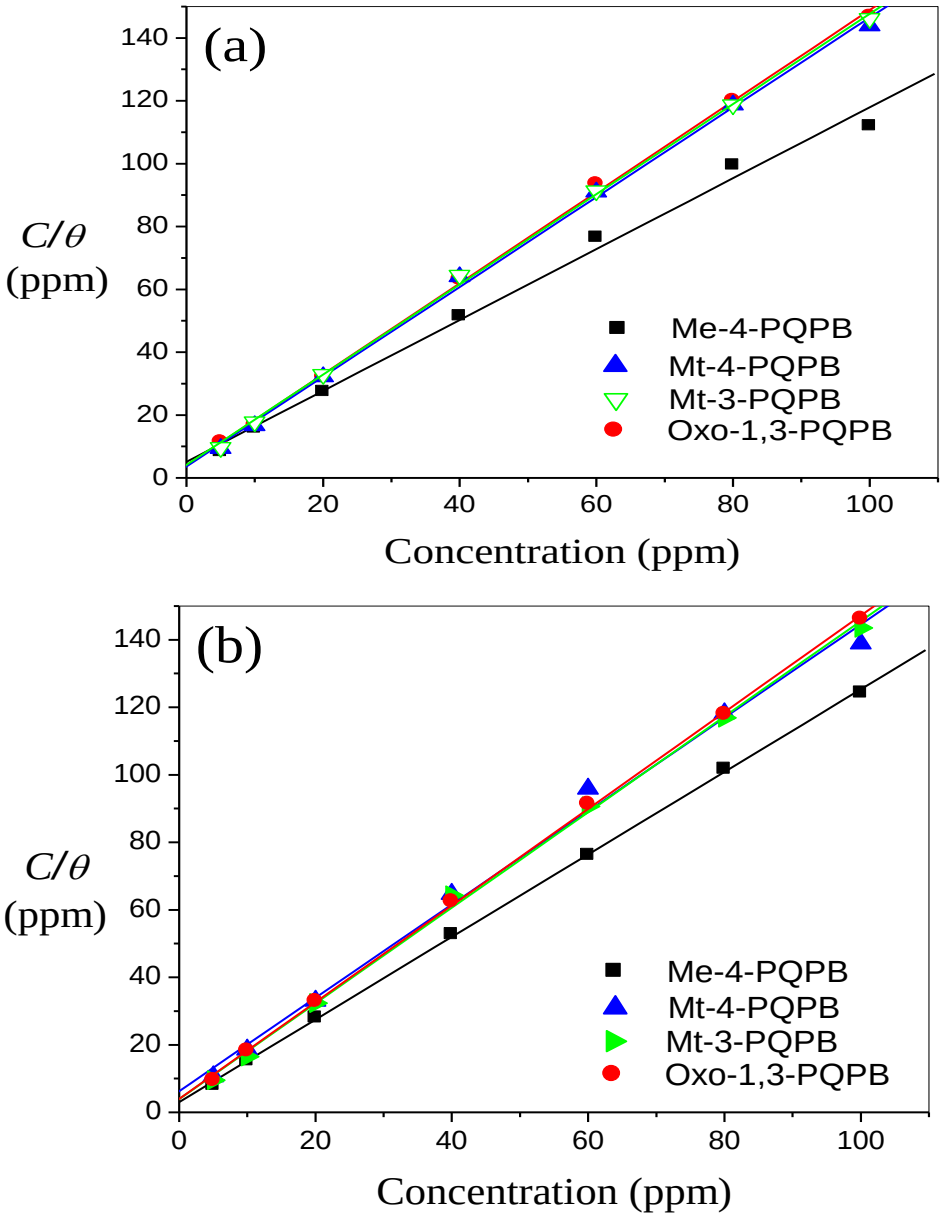

Figure 4.5. Langmuir adsorption isotherm plots for the studied inhibitors on MS surface in 1 M HCl (a) polarization and (b) EIS data.

inhibitors on MS surface. The values of ΔG_{ads} around -20 $kJmol^{-1}$ or less negative have been attributed to electrostatic interactions between the charged adsorbate molecules and the charged metal surface, also known as physisorption, while values around -40 *kJ/mol* or more negative values involve charge sharing or charge transfer from organic molecules to the metal surface to form coordinate bond, which is also referred to as chemisorption [190].

The results obtained for ΔG_{ads} as shown in Table 4.3 are all negative and have large magnitudes, which suggest that the inhibitors adsorb spontaneously on the MS surface. The values obtained for ΔG_{ads} lie between the thresholds for the classification of adsorption processes implying that the adsorption mechanisms of the studied inhibitors on MS surface involve both physisorption and chemisorption processes. This can further be inferred to be predominantly chemisorption because the values tend more towards the chemisorption indicator. In this study, the chemisorption mechanism is proposed between the studied inhibitors and MS surface and it is attributed to the possibility of charge sharing or charge transfer from the donor atoms and/or aromatic moieties around the inhibitor molecules to the vacant d-orbitals of iron.

Table 4.3. Equilibrium adsorption constant and change in free energy for the adsorption of the inhibitors on MS surface.

	Polarization		EIS	
Inhibitor	K_{ads} ($x10^{-4}$)	ΔG_{ads} (kJ/mol)	K_{ads} ($x10^{-4}$)	ΔG_{ads} (kJ/mol)
Me-4-PQPB	6.95	-38.20	11.71	-39.52
Mt-4-PQPB	9.44	-38.97	5.95	-37.81
Mt-3-PQPB	10.20	-39.17	9.42	-38.97
Oxo-1,3-PQPB	9.28	-38.93	9.77	-39.06

4.1.3 Spectroscopic analysis

FTIR and UV-Vis spectra of the pure inhibitors and the resulting solutions after 3 h of MS immersion were recorded. The FTIR spectra of Me-4-PQPB and Mt-4-PQPB and their resulting solutions after MS immersion are shown in Figure 4.6, while others are shown in Figure AI-4 (Appendix I). The bands corresponding to the stretching of aromatic C–H bonds are observed beyond 3000 cm^{-1}, while a group of bands between 1000 and 1500 cm^{-1} characteristics of the aromatic C–C stretching are also observed for all the studied compounds. The stretching frequencies of the carbonyl (C=O) were observed at around 1600

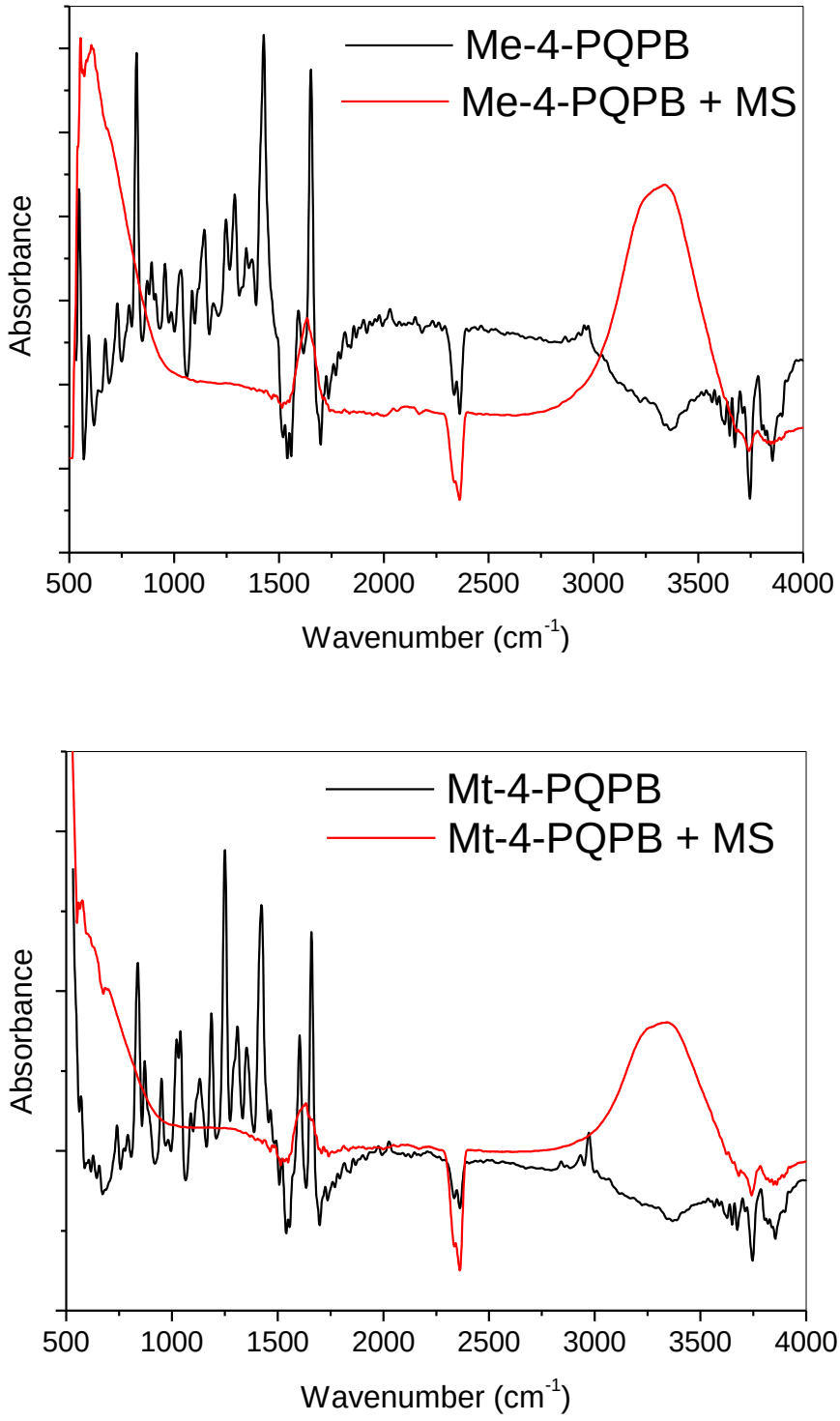

Figure 4.6. FTIR spectra of Me-4-PQPB and Mt-4-PQPB before and after MS immersion.

cm^{-1} with the stretching frequencies of C–N appearing close to it at relatively lower wavenumber. A remarkable difference between the FTIR spectra of the pure compounds and the resulting solution after MS immersion suggests that some chemical interactions have taken place between the inhibitor molecules and the prominent component of the steel, that is, Fe.

The UV-vis spectra of the inhibitors in acid solutions were compared with the resulting solutions after 3 h of MS immersion and the spectra are shown in Figure 4.7 (for Me-4-PQPB and Mt-4-PQPB) and Figure AI-5 (Appendix I) for Mt-3-PQPB and Oxo-1,3-PQPB. The UV-vis spectra of quinoxalines are known to show multiple absorption bands usually between 200 nm and 500 nm corresponding to $n\rightarrow\pi^*$, $\pi\rightarrow\pi^*$ transitions and intramolecular charge transfers (ICT) [252, 253]. The UV-vis spectra of the studied inhibitors have similar absorption characteristics with three maxima appearing around 210 nm, 250 nm and 300 nm. Me-4-PQPB showed absorption peaks at 205, 244, and 291 nm with additional one as a shoulder at 339 nm. Mt-4-PQPB showed absorption maxima at 208, 244, and 298 nm. Mt-3-PQPB exhibited light absorption with distinct peaks at 205, 243, and 298 nm. Oxo-1,3-PQPB showed absorption peaks at 208, 241, 272, and 320 nm. The bands at around or below 210 nm and 250 nm generally have higher absorbances for all the inhibitors. Upon MS immersion in the inhibitor solutions, the UV-vis spectra of the studied compounds showed some obvious changes as indicated below:

i. Me-4-PQPB: the peaks at 205 and 244 nm slightly red-shifted to 208 and 251 nm respectively, while the peak at 291 nm disappeared completely and the one at 339 nm became a mere shoulder.
ii. Mt-4-PQPB: all the peaks exhibited slight blue-shift such that the peaks at 208, 244, and 298 nm now appeared at 206, 241, and 290 nm respectively.

iii. Oxo-1,3-PQPB: the peaks at 208 and 320 nm both underwent bathochromic shift and appeared at 212 and 326 nm respectively, while the peak at 241 became a mere shoulder, and the peak at 272 nm had disappeared completely.

These notable changes in the absorption spectra of the inhibitors upon MS immersion suggest the occurrence of chemical interaction between the inhibitor molecules and Fe.

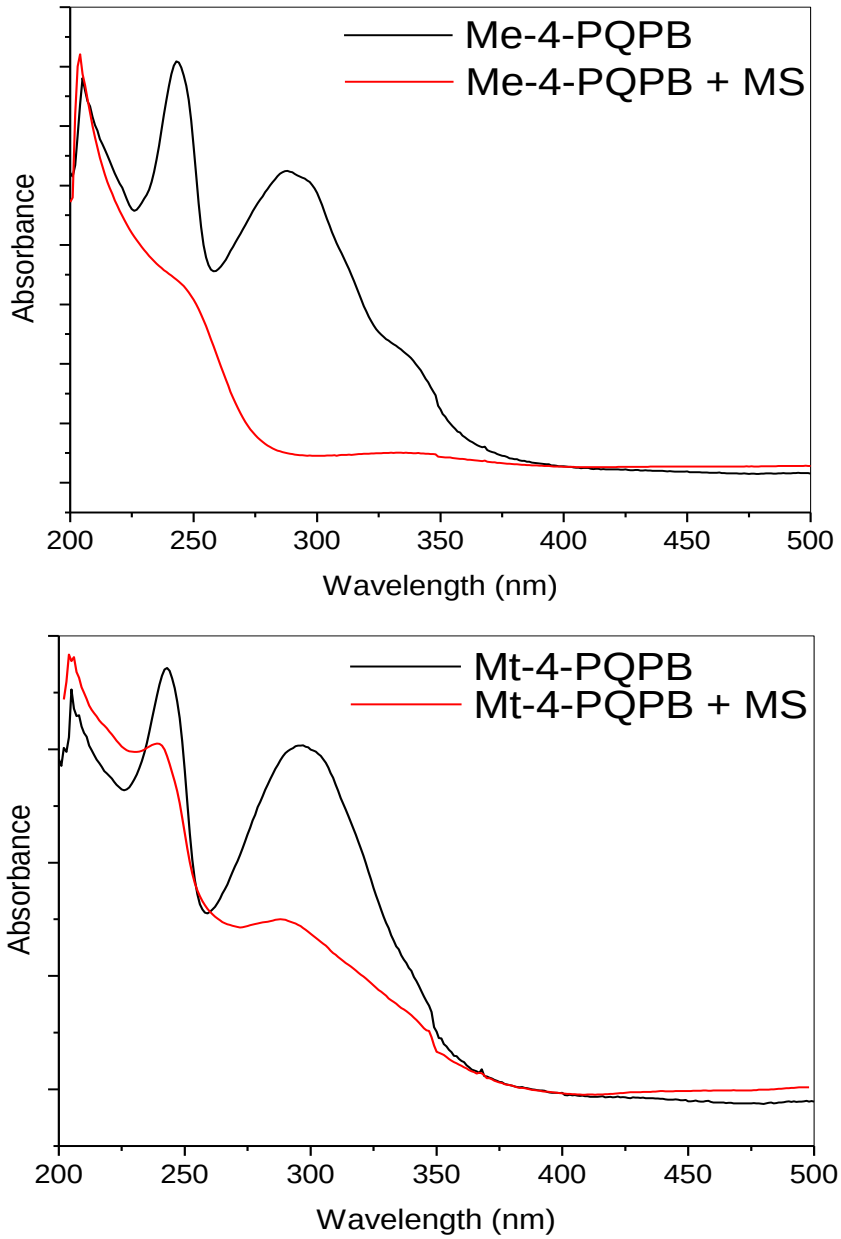

Figure 4.7. UV-vis spectra of Me-4-PQPB and Mt-4-PQPB before and after MS immersion.

4.1.4 Quantum chemical calculations

In order to investigate the relationship between inhibition efficiency and molecular reactivity at microscopic level, and to further explain the mechanism of inhibition based on molecular structural parameters, quantum chemical calculations were carried out on the studied inhibitors. The gas phase optimized molecular structures of the neutral and most stable protonated forms of the inhibitors are shown in Figure 4.8. Adsorption of an inhibitor molecule on a metal surface as well as its corrosion inhibition potential can be discussed on the basis of donor-acceptor interactions between the molecular orbitals of the inhibitor and the electronic orbitals of the metal atom.

According to the frontier molecular orbital (FMO) theory, the energy of the highest occupied molecular orbital (E_{HOMO}) is often associated with the electron donating ability of the molecule, while the energy of the lowest unoccupied molecular orbital (E_{LUMO}) is associated with the electron accepting ability of the molecule. A high value of the E_{HOMO} for a molecule implies a relatively less stable orbital and indicates the tendency of the molecule to donate electrons to the appropriate vacant d-orbital of the metal atom. On the other hand, a low value of E_{LUMO} for a molecule indicates the relative tendency of the molecule to accept electrons from metallic orbital during back-donation. The energy gap (ΔE), which is the difference between E_{LUMO} and E_{HOMO} is a measure of reactivity of a molecule. A low value of ΔE usually implies high reactivity.

In a simple relation, the inhibition efficiency is expected to be high for a molecule with a high E_{HOMO}, a low E_{LUMO} and a low ΔE [254]. In a more detailed investigation, other reactivity parameters most of which are derivatives of the FMO parameters are sometimes used to support experimental results. Some quantum chemical parameters were calculated for the neutral and the most stable protonated forms of the studied inhibitors and the results are presented in Tables 4.4, 4.5 and 4.6. Proton affinities (*PA*, kcal/mol) of the inhibitors

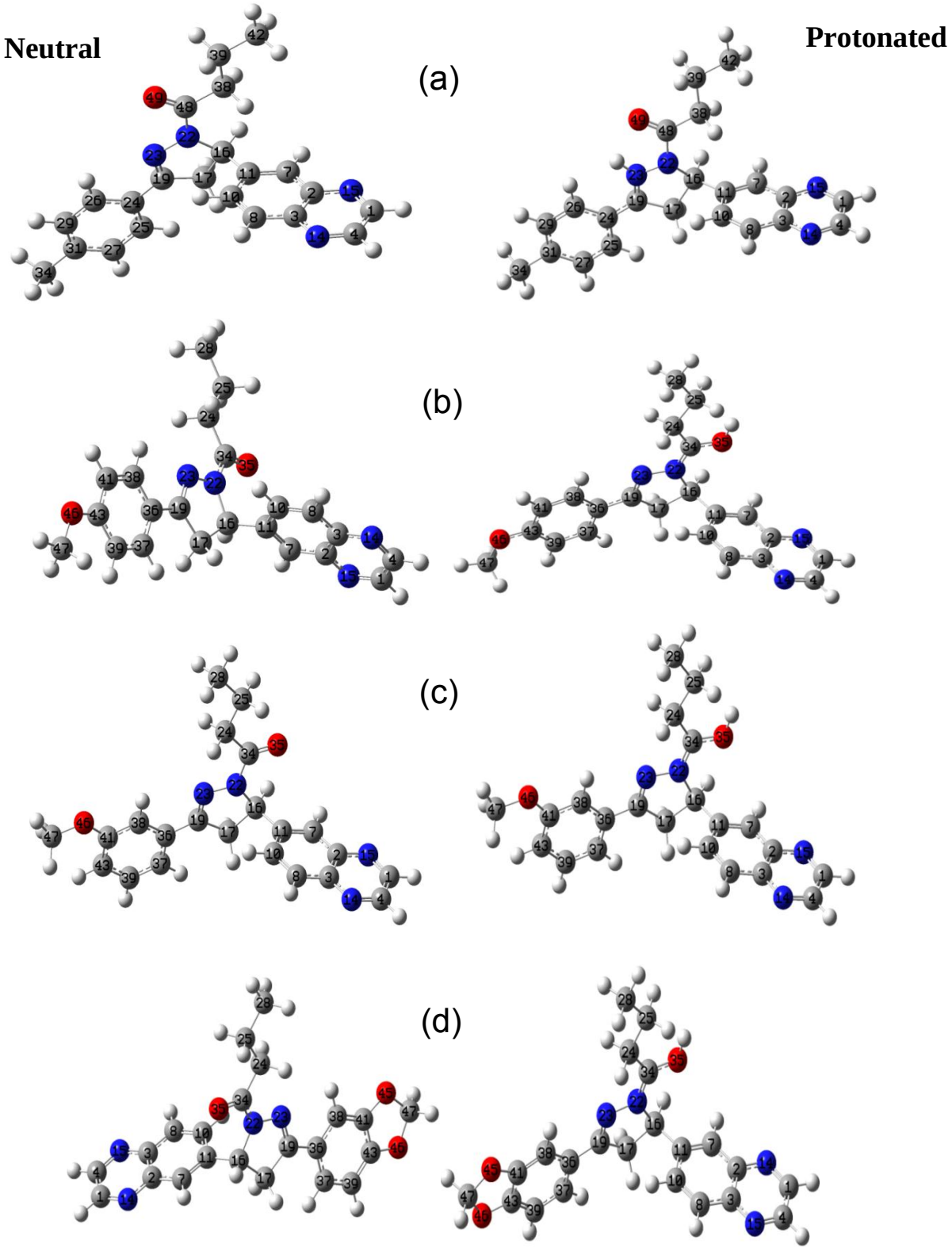

Figure 4.8. Gas phase optimized structures of the neutral and the most stable protonated forms of (a) Me-4-PQPB, (b) Mt-4-PQPB, (c) Mt-3-PQPB and (d) Oxo-1,3-PQPB at B3LYP/6-31G* level of theory.

were calculated as the difference between the total energy of the most stable protonated and neutral species and reported in Table 4.4. The values of the E_{HOMO}, E_{LUMO}, and ΔE ($E_{LUMO} - E_{HOMO}$) for both the neutral and most stable protonated forms of the studied compounds are also listed in Table 4.4.

The most stable protonated form of Me-4-PQPB corresponds to the species in which the proton is coordinately bonded to the N–23 atom, a N-atom on the dihydropyrazolyl ring, which was found to be more stable than the O–49 (carbonyl oxygen) protonated form by 3.64 kcal/mol. On the other hand, the most stable protonated forms of Mt-4-PQPB and Oxo-1,3-PQPB correspond to the species in which the proton is coordinately bonded to the O–35 (the carbonyl oxygen) atom, which were found be more stable than their respective N–15 (quinoxaline N-atom) protonated forms by 0.50 and 1.70 kcal/mol respectively. The protonated forms of Mt-3-PQPB at N-15, a quinoxaline nitrogen atom and O-35, the carbonyl oxygen atom have nearly the same energies. Hence, the O-35 protonated species was considered. The values of *PA* are high for the four inhibitors which imply that the inhibitors are susceptible to proton attack in acidic medium. The values of the E_{LUMO} of the protonated species are in the order Me-4-PQPB < Mt-3-PQPB < Oxo-1,3-PQPB < Mt-4-PQPB, which is in agreement with the order of inhibition efficiency at 100 ppm (*vide supra* experimental results). Me-4-PQPB has the least value of ΔE, which suggests highest reactivity and

Table 4.4. Total energy (*TE*), E_{HOMO}, E_{LUMO}, ΔE and *PA* the neutral and protonated forms of the inhibitors in the gas phase at B3LYP/6-31G* level of theory.

	Neutral				Protonated				
Inh	*TE* (Hartree)	E_{HOMO} (eV)	E_{LUMO} (eV)	ΔE (eV)	*TE* (Hartree)	E_{HOMO} (eV)	E_{LUMO} (eV)	ΔE (eV)	PA (kcal/mol)
Me-4-PQPB	-1145.82	-5.69	-2.14	3.55	-1146.21	-9.21	-6.04	3.17	240.65
Mt-4-PQPB	-1221.04	-5.55	-1.87	3.93	-1221.41	-8.84	-5.08	3.76	236.57
Mt-3-PQPB	-1221.04	-5.81	-1.88	3.93	-1221.41	-8.79	-5.26	3.53	235.47
Oxo-1,3-PQPB	-1295.04	-5.56	-1.89	3.67	-1295.42	-8.57	-5.17	3.40	235.56

inhibition efficiency in agreement with the experimental observations.

The HOMO and LUMO electron density isosurfaces of the neutral and protonated species of Me-4-PQPB and Mt-4-PQPB are shown in Figure 4.9, while the corresponding images for Mt-3-PQPB and Oxo-1,3-PQPB are shown in Figure AI-6 (Appendix I). In the neutral species, the HOMO of the inhibitors are localized on the phenyldihydropyrazolyl units and extended to their respective methyl/methoxy/dioxo substituents. The carbonyl functional groups are also involved in the HOMO. The LUMO surfaces of the neutral molecules are essentially localized on the quinoxaline units. The alkyl chain of the butanone unit is not involved in the electron density distributions of the HOMO and the LUMO. This suggests the strong π-characters of the HOMO surfaces of the molecules.

It can be inferred that the adsorption of the inhibitor molecules may be through the donation of π-electrons to the unoccupied d-orbitals of iron to form a coordinate bond, and also acceptance of electrons from the filled d-orbitals of Fe atom into the unoccupied molecular orbitals of the inhibitor in a retro-donation process. As shown in Figure 4.9, there is evidence of re-distribution of HOMO and LUMO electronic surfaces upon protonation. It is important to mention the remarkable differences in the HOMO and LUMO surfaces of the protonated Mt-4-PQPB and Mt-3-PQPB despite their similar molecular formulas and protonation pattern. This is attributed to the difference in electron-donating effect of the methoxy group on the phenyl ring which is in position 4 in Mt-4-PQPB and 3 in Mt-3-PQPB. This might the major reason for the different inhibition efficiencies exhibited by these molecules as observed from the experiments.

Quantum chemical parameters for the neutral and most stable protonated forms of the compounds were derived based on relevant equations already defined in section 3.1.7, and the results are listed in Table 4.5. It is obvious from the results in Table 4.5 that the values of electron affinity (*A*) for the protonated species are in the order Me-4-PQPB > Mt-3-PQPB >

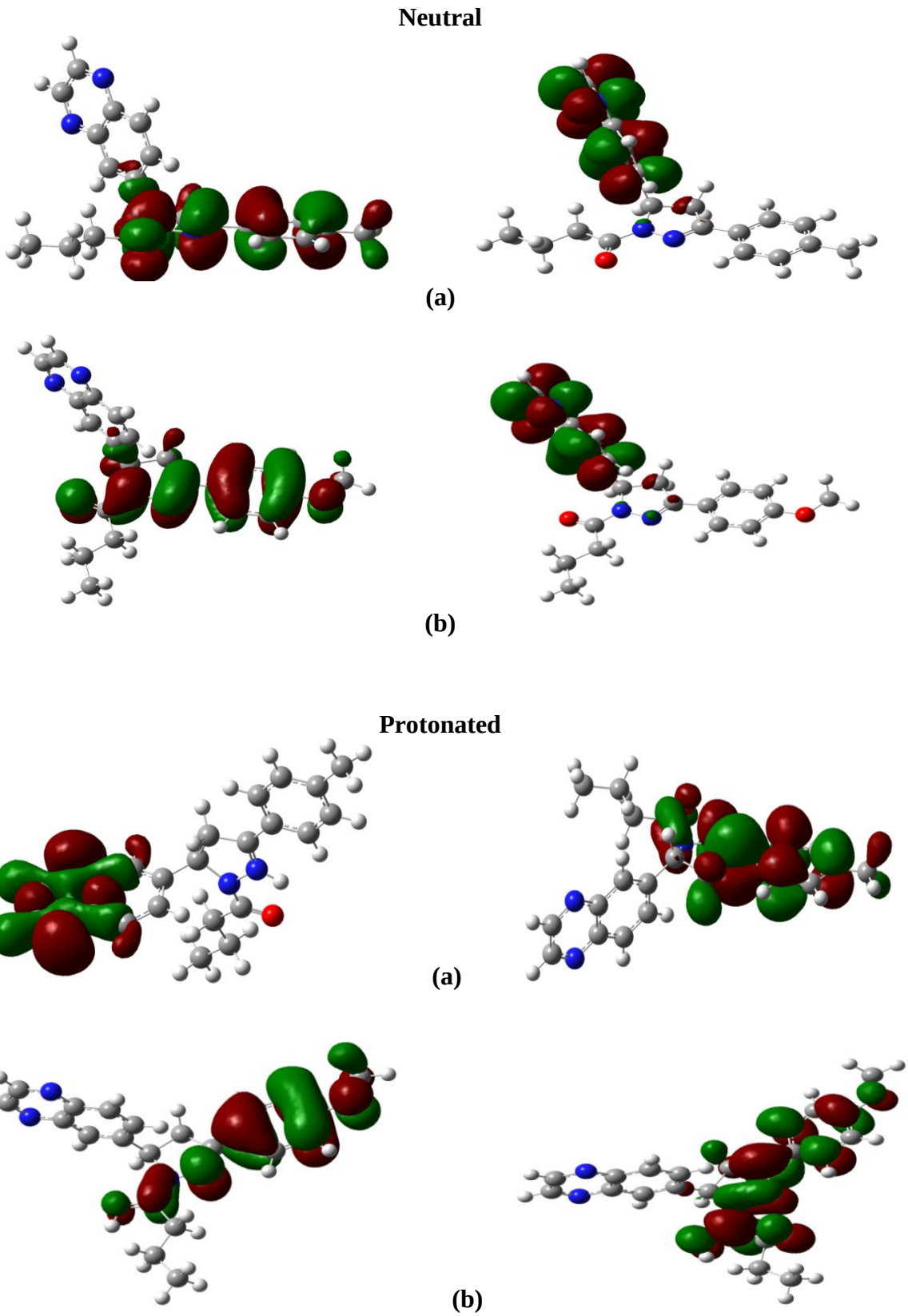

Figure 4.9. HOMO (left-hand side) and LUMO (right-hand side) electron density isosurfaces of the neutral and protonated forms of (a) Me-4-PQPB, and (b) Mt-4-PQPB.

Oxo-1,3-PQPB > Mt-4-PQPB, which agrees with the experimentally observed order of inhibition efficiencies. Me-4-PQPB has the highest value of χ and the least value of η, which implies that this compound has the highest tendency to retain its own electrons or attract electrons from electron-donating species, and also highest reactivity based on the hard-soft acid and base (HSAB) concept in association with the values of η. These observations support the highest inhibition efficiency of Me-4-PQPB as observed from the experimental results. The chemical potential (μ), which is a versatile reactivity index may either inform the trend of the propensity of the neutral inhibitor molecules to react directly with iron or undergo prospective transformation such as protonation before inhibiting the corrosion

Table 4.5. *I*, *A*, μ, η and χ for the neutral and protonated forms of the inhibitors in gas phase at B3LYP/6-31G* level of theory.

	Neutral					Protonated				
Inh	*I*	*A*	μ	η	χ	*I*	*A*	μ	η	χ
Me-4-PQPB	5.69	2.14	-3.92	1.78	3.92	9.21	6.04	-7.62	1.58	7.62
Mt-4-PQPB	5.55	1.87	-3.71	1.84	3.71	8.84	5.08	-6.96	1.88	6.96
Mt-3-PQPB	5.81	1.88	-3.84	1.96	3.84	8.79	5.26	-7.02	1.76	7.02
Oxo-1,3-PQPB	5.56	1.89	-3.72	1.84	3.72	8.57	5.17	-6.87	1.70	6.87

process. The decreasing order of the magnitudes of the values of the chemical potential for the neutral inhibitor molecules is Me-4-PQPB > Me-3-PQPB > Oxo-1,3-PQPB > Mt-4-PQPB, which is in agreement with the observed order of inhibition efficiencies. Although the values of μ for the protonated species do not agree perfectly with the experimentally observed trend of inhibition efficiencies, the still revealed that Me-4-PQPB and Mt-3-PQPB have higher reactivity than Mt-4-PQPB and Oxo-1,3-PQPB, with Me-4-PQPB having the highest magnitude of μ, which again is in support of its highest inhibition efficiency.

Other global reactivity parameters including the electrophilicity index (ω), global electron donating power, (ω^-) global electron withdrawing power, (ω^+) and net electrophilicity ($\omega^\pm$) were also calculated for the neutral and most stable protonated species of the studied inhibitors and the results are presented in Table 4.6. The values of ω, ω^-, and ω^+ obtained for the protonated inhibitor molecules agree with the observed inhibition efficiency (at 100 ppm) in the order Me-4-PQPB > Mt-3-PQPB > Oxo-1,3-PQPB > Mt-4-PQPB. The trend of these parameters cannot be generalized from the results obtained for the neutral inhibitor molecules. This observation is in support the assumption that in acidic media, the most stable protonated forms of the inhibitors may be responsible for the interaction with the MS surface. Similar observation had been reported on related compounds in literature [223].

The values of the fraction of electrons transferred (ΔN) from the inhibitor (donating) molecule to the metallic (Fe) atom (acceptor) were also calculated for the neutral and protonated species and the results are listed in Table 4.6. The values of ΔN for the neutral forms of the studied inhibitors are all positive, suggesting that the forward transfer of electrons from the inhibitor molecules to appropriate vacant orbitals of iron is a favourable process. However, the values of ΔN for the protonated species are negative for both Me-4-PQPB and Mt-3-PQPB, while those of Mt-4-PQPB and Oxo-1,3-PQPB are positive, suggesting that back-donation from occupied orbitals of iron to the protonated inhibitor molecules is predominant in the case of Me-4-PQPB and Mt-3-PQPB, while forward donation from protonated inhibitor molecules to iron is predominant in the case of Mt-4-PQPB and Oxo-1,3-PQPB. These assumptions do not totally preclude the possibility of opposing process in each case.

The correlations of the calculated quantum chemical parameters with experimental inhibition efficiencies suggest the possibility of the involvement of both the neutral and protonated forms of the studied compounds in the adsorption and corrosion inhibition

activities. This assumption is based on the fact that a quantum of parameters for both species do correlate with the observed results, while some do not, and this is an indication of the

Table 4.6. ω, ω^-, ω^+, $\omega^\pm$, ΔN and ΔE_T for the neutral and protonated forms of the inhibitors in gas phase at B3LYP/6-31G* level of theory.

	Neutral						Protonated					
Inh	ω	ω^-	ω^+	$\omega^\pm$	ΔN	ΔE_T	ω	ω^-	ω^+	$\omega^\pm$	ΔN	ΔE_T
Me-4-PQPB	8.64	6.50	2.58	9.08	0.87	-0.44	36.68	22.35	14.73	37.08	-0.20	-0.40
Mt-4-PQPB	7.48	5.82	2.11	7.94	0.89	-0.46	25.77	16.60	9.64	26.24	0.01	-0.47
Mt-3-PQPB	7.52	5.93	2.08	8.02	0.80	-0.49	27.96	17.71	10.69	28.40	-0.01	-0.44
Oxo-1,3-PQPB	7.56	5.87	2.15	1.84	0.89	-0.46	27.76	17.53	10.66	1.70	0.04	-0.42

complexity of the adsorption phenomena involving the studied inhibitor molecules and MS. However, the protonated species are characterized with more quantum chemical parameters that are in accord with the experimental observations than the neutral species.

In order to predict the local atomic sites in the inhibitor molecules that might be involved in adsorption and interactions with the metallic iron during the corrosion inhibition process, the Fukui indices for the neutral and the most stable protonated forms of the inhibitor molecules were calculated and the resulting graphical images of the corresponding electron density surfaces are shown in Figure 4.10 for both Me-4-PQPB and Mt-4-PQPB. Graphical representations of the Fukui functions for the neutral and protonated forms of Mt-3-PQPB and Oxo-1,3-PQPB are shown in Figure AI-7 (Appendix I).

It is obvious from the Fukui functions that the prominent sites for electrophilic attacks in the neutral inhibitor molecules are generally the N-22 and N-23 (in the pyrazolyl ring) and O-35 (oxygen of the carbonyl functional group) atoms. In the case of Me-4-PQPB, f_k^- is extended to the C-19 atom (on the pyrazolyl ring) and also slightly condensed on C-31 atom

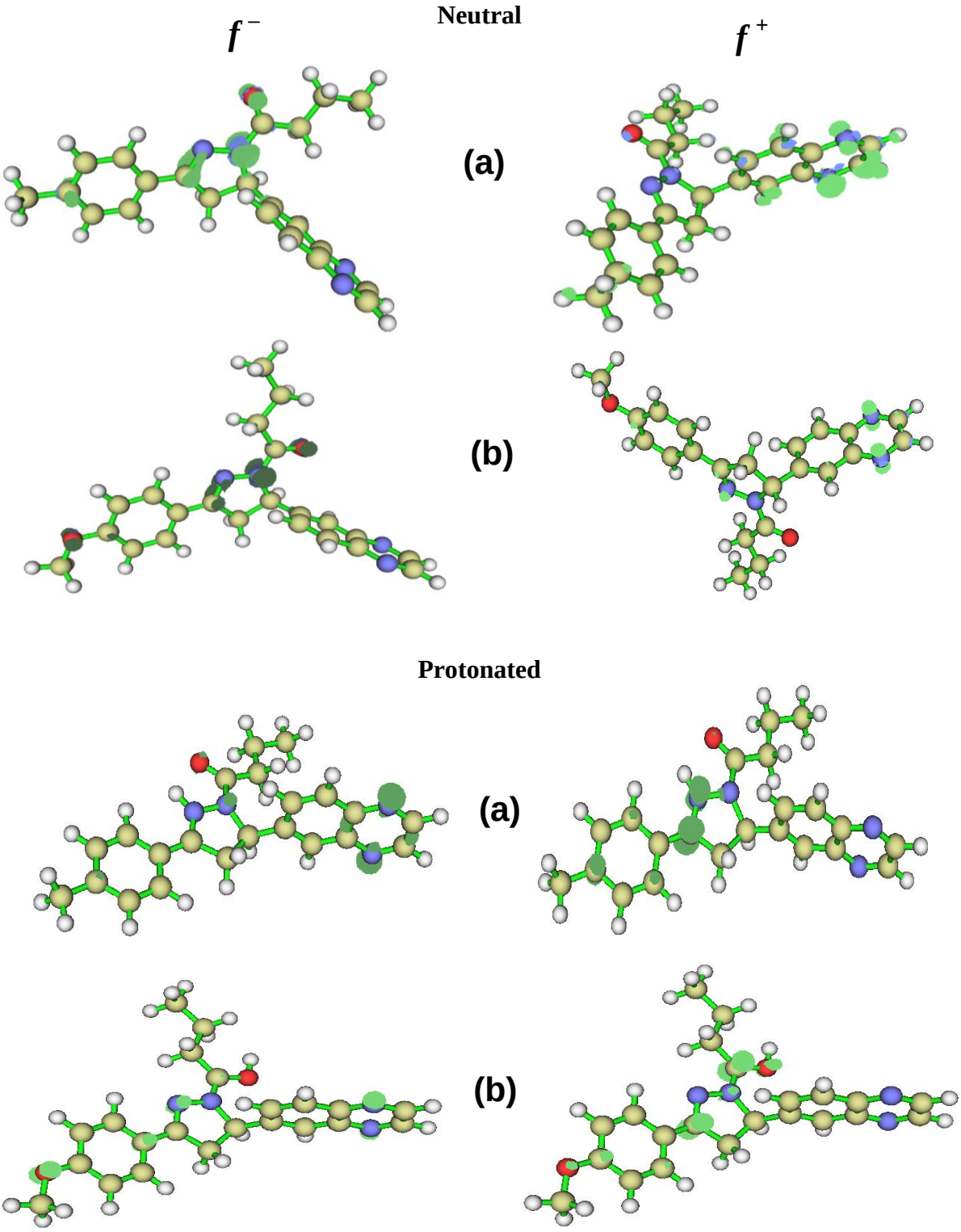

Figure 4.10. Fukui indices, f_k^- and f_k^+ for the neutral and protonated forms of (a) Me-4-PQPB, and (b) Mt-4-PQPB (*Isosurface = 0.007*).

(on the phenyl ring). The O-46 atom (of the alkoxy group) also exhibits a good nucleophilic character in Mt-4-PQPB and this is slightly extended to C-43 atom (of the phenyl ring). The O-46 atom (of the alkoxy group) in Mt-3-PQPB however did not appear to be a good nucleophilic site but the f_k^- value is relatively more condensed on C-43 atom (of the phenyl ring). The f_k^- value is more condensed on the O-46 atom than O-45 atom (in the dioxo-group) for Oxo-1,3-PQPB, while the C-19 (of the pyrazole ring), C-37 and C-43 atoms (both of the phenyl rings) also display slight nucleophilicity.

The results obtained for the Fukui index, f_k^+ that is associated with nucleophilic attacks reveal that the atomic sites in the molecules that are susceptible to attacks by electron rich species reside prominently on the quinoxaline ring, especially the N-14 and N-15 atoms. This is not unexpected because a quinoxaline unit has been identified to possess a highly electron-deficient nucleus and hence promises to be a good electron acceptor due to the presence of electron-withdrawing nitrogen atoms in the ring [255]. The nucleophilic nature of the atoms around the dihydropyrazolyl ring and the electrophilic nature of the atoms in the quinoxaline ring are in agreement with the established trend of chemical reactivity of heterocyclic compounds in which five membered ring heterocycles are regarded as π-excessive and their six-membered ring counterpart as π-deficient [256]. The extended electronic distribution observed for the f_k^+ of Oxo-1,3-PQPB at the same isosurface value could not be explained.

The f_k^- and f_k^+ for the protonated forms of the inhibitors reflect nearly opposite electron distributions compared to the Fukui indices of the neutral species. The atoms around the quinoxaline ring, especially the N-14 and N-15 atoms become more nucleophilic with larger values of the f_k^- than those in the dihydropyrazolyl ring. On the other hand, the f_k^+ values for the electrophilic atoms now appear greater on the atoms along the dihydropyrazolyl ring, the phenyl ring and the carbonyl functional groups. This may be due to the fact that the

protonation sites in the inhibitor molecules (N-23 and O-35 atoms) are generally closer to the dihydropyrazolyl ring leading to reduction in electron density in those vicinities thereby making the atoms to be more electrophilic than those around the quinoxaline ring.

4.1.5 Molecular dynamic (MD) simulations

The most stable configurations for the adsorption of the studied quinoxaline derivatives on Fe(110) surface are shown in Figure 4.11. The configurations in Figure 4.11 revealed that all the inhibitor molecules lie flat on the Fe surface, which propels strong interactions between the inhibitor molecules and the Fe. Some relevant energy parameters obtained from the simulations are listed in Table 4.7. The Me-4-PQPB/Fe(110) system has the least (most negative) total energy, which could be an indication of higher stability of this system relative to the others, and this is in accord with its highest experimental inhibition efficiency. The total energy of the Mt-3-PQPB/Fe(110) system ranks second most negative, which is also in agreement with the order of the experimental inhibition efficiency. The total energies of Mt-4-PQPB/Fe(110) and Oxo-1,3-PQPB/Fe(110) systems are very close, and this again goes in line with their similar inhibition strength observed from the experiments, and also their similar reactivity as implied from some of the quantum chemically derived reactivity indices.

However, the adsorption and deformation energies of these systems do not agree with the experimental observations. This disagreement between the simulated adsorption energies and the experimental observations may be possible because the construct of the MD simulation employed in this study only models non-covalent interactions between inhibitor molecules and Fe(110) substrate. Meanwhile, experimental data provided evidence of mixed physisorption and chemisorption.

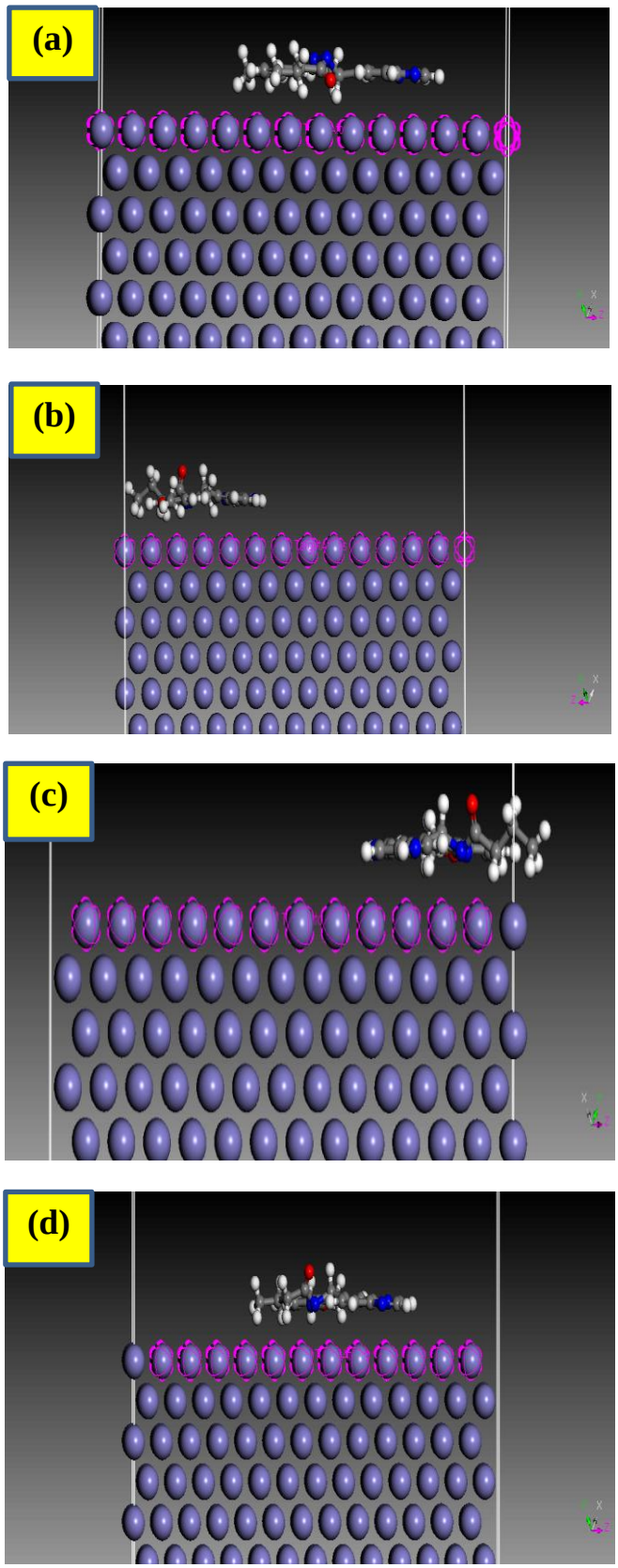

Figure 4.11. The most stable adsorption configuration of Me-4-PQPB, Mt-4-PQPB, Mt-3-PQPB and Oxo-1,3-PQPB on Fe (110) surface.

Table 4.7. Energy parameters obtained from the simulations of the adsorption of Me-4-PQPB, Mt-4-PQPB, Mt-3-PQPB and Oxo-1,3-PQPB on Fe (110) surface (in kJ/mol).

Inhibitors	Total Energy	Adsorption energy	Rigid adsorption energy	Deformation energy	dE_{ad}/dN_i
Me-4-PQPB	-591.32	-830.12	-878.69	48.56	-830.12
Mt-4-PQPB	-562.70	-852.75	-886.11	33.35	-852.75
Mt-3-PQPB	-572.48	-851.84	-884.91	33.07	-851.84
Oxo-1,3-PQPB	-561.29	-858.95	-899.83	40.88	-858.95

4.1.6 Proposed mechanism of adsorption and inhibition

Corrosion inhibition ability of organic inhibitors is usually as a result of the formation of protective film on the metal surface. The adsorption behaviour may be physisorption, chemisorption or a combination both. Based on the results obtained from the electrochemical experiments, spectroscopy measurements and quantum chemical calculations, the following possible adsorption and inhibition mechanisms can be proposed for the studied inhibitor molecules.

(i) The inhibitor molecules can readily be protonated in acid solution as in:

$$Inh + H_3O^+ \rightleftharpoons InhH^+ + H_2O \quad (4.4)$$

This protonated species can be adsorbed on the steel surface via electrostatic interactions, i.e. physisorption mechanism. There is possibility that the steel surface will be saturated with positive charges, but the presence of negatively charged Cl^- ions near the positively charged steel surface will facilitate the adsorption of the protonated inhibitor [257-259].

(ii) The inhibitors may adsorb on MS surface via chemisorption mechanism that involves the formation of coordinate bond via the transfer of the lone pair of electrons on the N and/or O atoms in the inhibitor molecule to the appropriate vacant orbitals of Fe. The chemical

adsorption can also be driven by donor-acceptor interactions between the π-electrons in the aromatic moieties of the inhibitor molecules and the vacant d-orbitals of the Fe [257, 258].

(iii) There could be formation of Fe^{2+} due to initial dissolution of MS in the corrosive medium. The inhibitor molecules can readily bind with the Fe^{2+} ions to form metal/inhibitor complex, which may adsorb on the steel surface via electrostatic interactions (physisorption) to inhibit further dissolution of the steel in acid solution, that is [258, 260, 261]:

$$Fe \rightleftharpoons Fe^{2+} + 2e^{-} \quad (4.5)$$

$$Fe^{2+} + Inh \rightleftharpoons [Fe\text{---}Inh]^{2+} \quad (4.6)$$

4.2 GROUP II: PQDPB, PQDPP, and PPQDPE

Group II comprises three compounds as listed in Table 3.2. These compounds have similar molecular framework consisting of 4,5-dihydro-1H-pyrazol-5-yl group as a substituent on the quinoxaline ring. The 4,5-dihydro-1H-pyrazol-5-yl substituent is also substituted by a carbonyl and phenyl groups on positions 1 and 3 of the pyrazole ring respectively. Therefore, the (GROUP II) compounds have common "nucleus", and differ only in the chain of the carbonyl group attached to the first nitrogen atom of the dihydropyrazole ring, that is, butyl (in PQDPB), propyl (in PQDPP) and phenylethyl (in PPQDPE). Therefore, the effects of electronic and steric hindrance of the substituent carbonyl functional groups on the protection efficacies of the compounds were investigated.

It is important to mention that the essential parts of the results of the studies conducted on PQDPB, PQDPP, and PPQDPE have been published in a peer-reviewed journal article and the following sections of results and discussion on this set of compounds reflect the contents of the published article [191].

4.2.1 Electrochemical studies

4.2.1.1 Tafel plots

Tafel curves were obtained for MS in 1 M HCl without and with various concentrations of the inhibitors and the results are presented in Figure 4.12. The Tafel curves in Figure 4.12 exhibit similar behaviour for the three inhibitors as well as for 1 M HCl blank system. This suggests that the mechanism of inhibition is the same for all the inhibitors studied in this work, and that addition of inhibitors does not cause significant change in the corrosion mechanism. There is apparent shift in both the anodic and cathodic arms of the polarization curves towards lower current density in the presence of the inhibitor molecules as compared to the uninhibited blank system. This implies that both the anodic and cathodic reactions associated with steel corrosion in 1 M HCl are inhibited. In other words, the studied compounds reduce the rate of anodic dissolution of MS in 1 M HCl and also retard the rate of cathodic H^+ ions reduction or hydrogen gas evolution.

The shift in the polarization curves in the direction of lower current density is also more pronounced at higher concentrations of the inhibitors, which suggests that the corrosion rate decreases with increasing concentrations of the studied inhibitors. There is an obvious shift in the polarization curve of PQDPB at 100 ppm towards a nobler potential relative to the blank and lower concentrations of the inhibitor. Similar observations are found in the case of PQDPP at 80 ppm and 100 ppm. The polarization curve of PPQDPE at 80 ppm also appeared at a nobler potential compared to the lower concentrations of the inhibitors, while at 100 ppm the curve appeared at a potential that is even nobler than the blank system. The distinct shifts in the polarization curves to the more anodic potentials at higher concentrations especially 80 and 100 ppm are clear indications enhanced inhibition efficiency of these compounds at high concentrations.

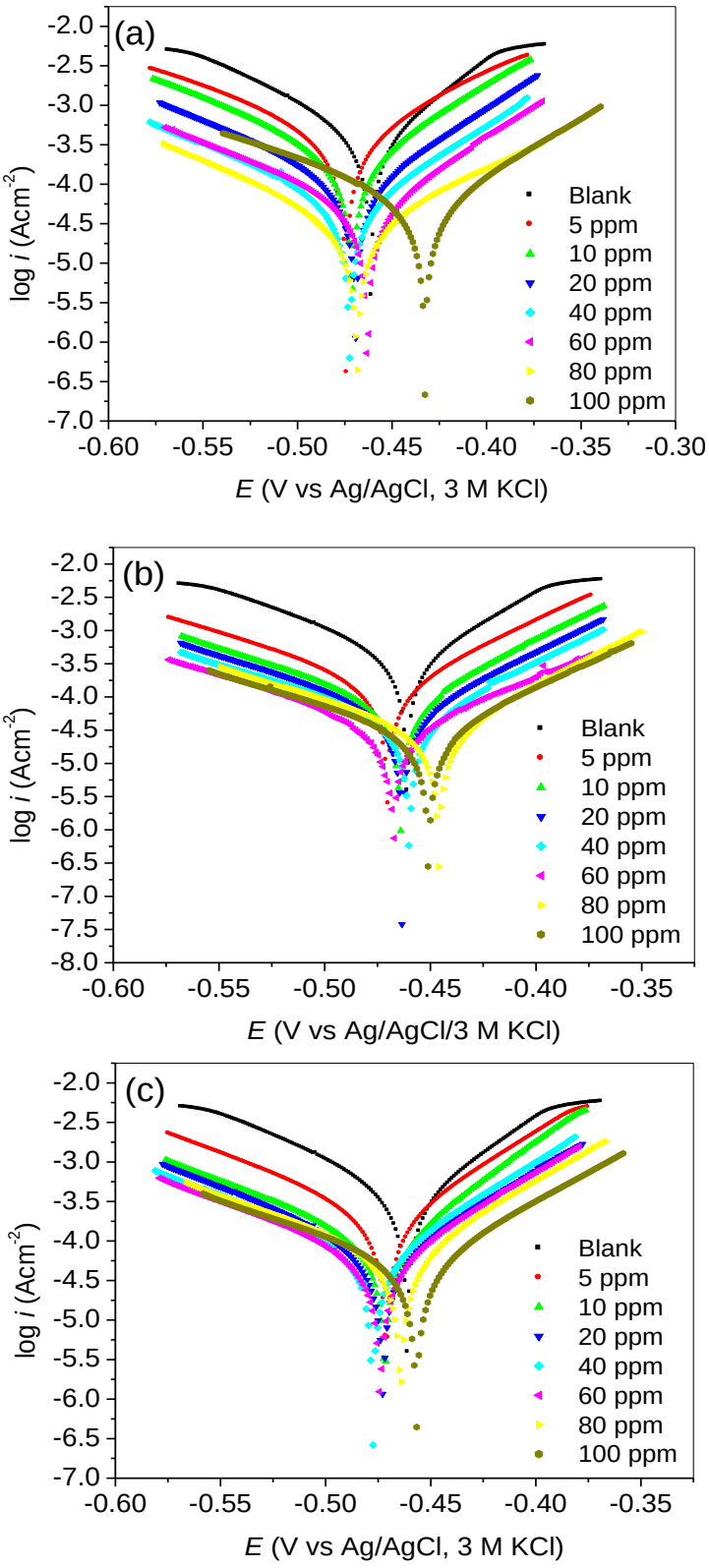

Figure 4.12. Tafel plots for MS in 1 M HCl without and with various concentrations of (a) PQDPB, (b) PQDPP, and (c) PPQDPE.

Tafel parameters including E_{corr}, i_{corr}, β_a and β_c derived by extrapolating the linear Tafel regions of the anodic and cathodic sections of the curves to the E_{corr} are listed in Table 4.8. The shift in E_{corr} obtained in the present study at various concentrations of the inhibitors does not follow a definite pattern. However, the maximum value of the shift in E_{corr} between the blank and the inhibitor-containing systems is 27.94 mV (less than 85 mV), which suggests that the studied compounds are mixed-type inhibitors. The i_{corr} decreases with increase in concentration of the inhibitors leading to increase in inhibition efficiency ($\%IE_P$). The order of inhibition efficiency of the three inhibitors at lower concentrations (5 ppm to 20 ppm) is PQDPP > PPQDPE > PQDPB, while the order of inhibition efficiency at higher concentrations (40 ppm to 100 ppm) is PQDPP > PQDPB > PPQDPE. The higher inhibition efficiency of PQDPB compared to PPQDPE at higher concentrations was attributed to the possibility of multiple protonation of available basic sites in PQDPB in the acid. A more detailed theoretical explanation in support of this possibility is discussed in the later sections (*vide infra*, quantum chemical calculations).

4.2.1.2 EIS measurements

The representative Nyquist and Bode plots of MS in 1 M HCl without and with various concentrations of PQDPB are shown in Figures 4.13. The corresponding plots for PQDPP and PPQDPE are shown in Figures AII-1 and AII-2 (Appendix II) respectively. The Nyquist plots show a single depressed capacitive arc over the frequency range studied. The Nyquist plots exhibit oval semicircular shapes, which are commonly observed for solid electrodes as a result of frequency dispersion of interfacial impedance. This feature is usually attributed to different factors such as surface roughness, impurities, discontinuity in the electrode, adsorption of inhibitor and inhomogeneity of the electrode surface [251]. Similarity in the shapes of these plots for the uninhibited and inhibited systems implies that the inhibitors reduce the corrosion rate without changing the corrosion mechanism [251, 262]. The results

Table 4.8. Tafel parameters and percentage inhibition efficiency for the corrosion of MS in 1 M HCl without and with inhibitors.

Compound	*Conc.* (ppm)	$-E_{corr}$ (mV)	i_{corr} (μA/cm^2)	β_a (mV/dec)	β_c (mV/dec)	$\%IE_P$
Blank	-	460.60	420.41	89.34	65.27	-
PQDPB	5	473.92	318.04	121.71	93.35	24.35
	10	471.17	204.04	98.82	74.51	51.47
	20	469.37	95.54	94.30	70.91	77.28
	40	472.61	58.86	102.28	75.33	86.00
	60	463.02	51.34	106.11	69.16	87.79
	80	468.58	45.66	104.91	101.61	89.14
	100	432.66	42.00	121.08	80.66	90.01
PQDPP	5	469.67	142.10	101.77	72.94	66.20
	10	464.22	79.32	102.92	65.56	81.13
	20	463.42	60.71	102.34	70.44	85.56
	40	459.97	48.85	112.90	70.42	88.38
	60	467.36	39.51	110.61	94.39	90.60
	80	446.17	37.67	110.27	65.41	91.04
	100	450.87	27.45	119.37	74.27	93.47
PPQDPE	5	470.64	213.82	94.11	64.98	49.14
	10	471.86	88.78	95.49	55.10	78.88
	20	472.59	77.22	96.20	74.00	81.63
	40	477.38	68.50	96.53	67.12	83.71
	60	474.03	59.22	103.56	67.08	85.91
	80	464.31	56.67	116.62	69.49	86.52
	100	456.85	48.14	127.29	74.49	88.55

also reveal that MS dissolution in the studied aggressive media is controlled by a single charge transfer process [192, 250]. The Nyquist plots exhibit large capacitive loops at high frequencies and this is usually associated with charge transfer process and electrical double layer [7, 263-265]. The diameter of the capacitive loop of the Nyquist plot in the presence of inhibitor is larger than that for the uninhibited system and increases with increase in concentration of the inhibitors. This implies that the inhibitors protect the steel surface against acid attack and the protection is enhanced at higher concentration of inhibitors.

The high frequency intercept with the real axis on the Nyquist plots corresponds to the solution resistance (R_s), while the low frequency intercept with the real axis is ascribed to the

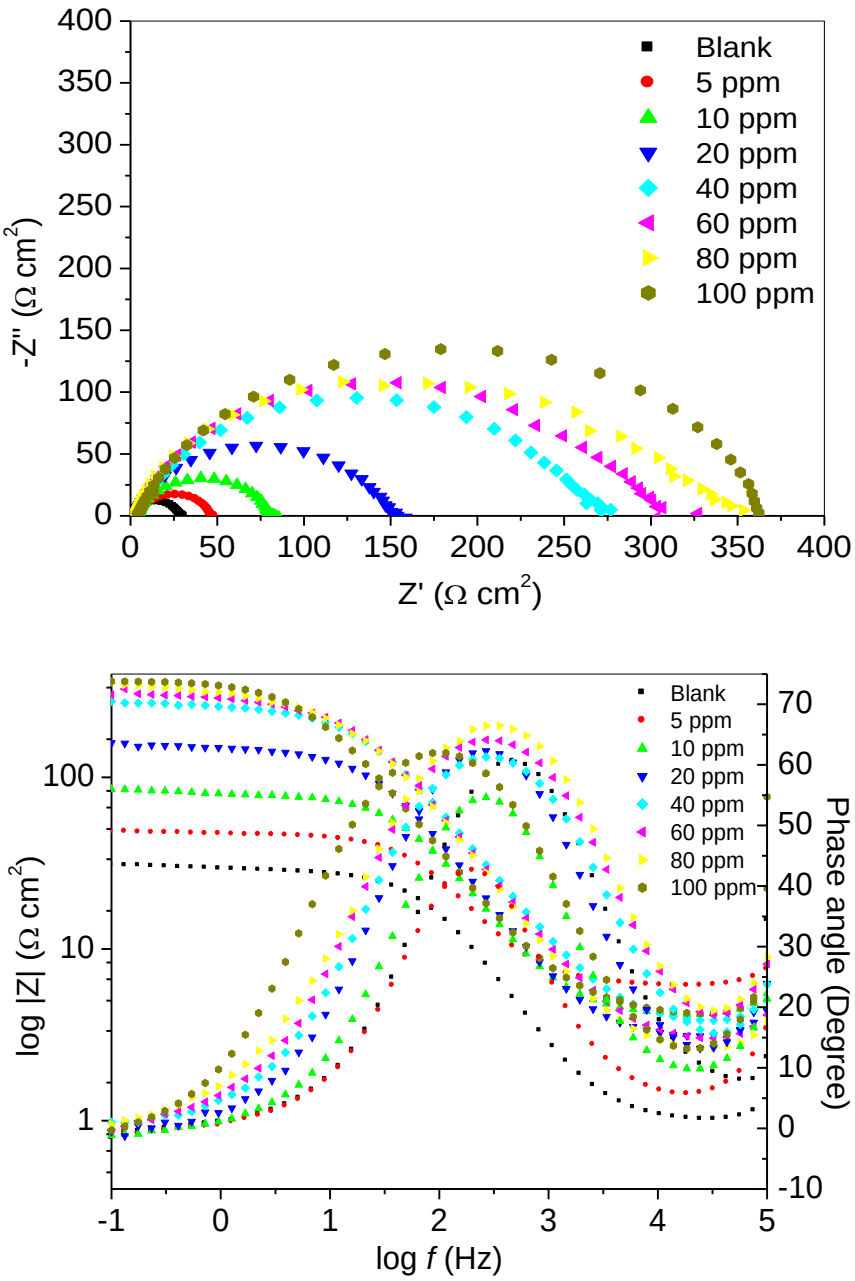

Figure 4.13. Nyquist plots and Bode plots for MS in 1 M HCl without and with various concentrations of PQDPB.

sum of the solution resistance (R_s) and the charge transfer resistance (R_{ct}), such that R_{ct} = *Z`(low freq) – Z`(high freq).* Electrochemical impedance kinetic parameters were obtained by fitting the impedance spectra to the equivalent circuit model $R_s(Q_{dl}R_{ct})$ (previously shown in Figure 4.4) and the results of the fitting and simulation analyses are listed in Table 4.9. Solution resistance is a significant factor in the impedance of an electrochemical cell and it is

the characteristic of the cell. The values obtained for R_s (Table 4.9) are generally higher for the inhibitors-containing electrochemical systems compared to the blank acid solution. This implies that the solution conductivity is reduced by the addition of the inhibitors. The R_s values do not show any regular pattern with increasing concentration of the inhibitors because the geometry of the area through which the current is transported in the systems may not be the same.

The values of Y_o are lower in the presence of inhibitors compared to that of uninhibited blank system. This can be attributed to gradual displacement of water molecules by inhibitor molecules at metal/solution interface leading to formation of protective layer on

Table 4.9. EIS parameters and percentage inhibition efficiency for the corrosion of MS in 1 M HCl without and with inhibitors.

Compound	*Conc.* (ppm)	R_s (Ωcm^2)	R_{ct} (Ωcm^2)	Y_o ($\mu Ss^n cm^{-2}$)	*n*	$\lvert\Theta\rvert$ (Degree)	$\lvert S\rvert$	$\%IE_I$
Blank	-	1.01	28.20	157	0.893	60.59	0.64	-
PQDPB	5	6.18	40.90	128.00	0.877	42.56	0.53	31.05
	10	4.14	77.20	98.30	0.867	54.63	0.65	63.47
	20	3.02	148.00	88.90	0.856	62.30	0.74	80.90
	40	2.83	263.00	76.20	0.842	61.30	0.72	89.28
	60	2.76	297.00	77.40	0.820	64.14	0.75	90.50
	80	5.37	349.88	65.40	0.834	66.48	0.76	91.94
	100	4.10	362.00	138.00	0.812	61.96	0.74	92.21
PQDPP	5	2.65	100.00	89.30	0.869	61.48	0.70	71.80
	10	3.46	178.00	75.40	0.857	62.89	0.74	84.16
	20	2.86	250.00	66.40	0.851	65.66	0.76	88.72
	40	2.37	321.00	81.30	0.822	66.48	0.76	91.21
	60	3.00	444.00	75.80	0.834	67.44	0.80	93.65
	80	3.35	457.79	63.70	0.856	68.92	0.82	93.84
	100	3.18	560.64	61.90	0.847	69.06	0.82	94.97
PPQDPE	5	2.06	63.00	107.00	0.872	60.17	0.65	55.24
	10	2.09	93.80	106.00	0.845	61.51	0.66	69.94
	20	2.08	166.00	84.20	0.835	63.75	0.68	83.01
	40	3.24	199.00	97.10	0.822	62.55	0.75	85.83
	60	2.05	215.00	87.30	0.803	63.39	0.68	86.88
	80	3.74	216.92	85.80	0.836	65.52	0.77	87.00
	100	2.45	297.16	88.00	0.825	65.52	0.77	90.51

the steel surface [68, 263, 266]. The values of the CPE exponent, *n* are reduced by the addition of inhibitors. This suggests that the surface inhomogeneity of the electrode increases in the presence of the inhibitors, which again is an indication of adsorption of the inhibitors on the steel surface [263]. The near unity values of *n* imply that the CPE in each case resembles a capacity and the steel/solution interface can be said to exhibit some capacitive characteristics [79, 113].

The increased values of R_{ct} with increasing concentration of the inhibitors can be attributed to coverage of the active surface/sites of the metal that may be involved in charge transfer process. The values of $\%IE_I$ (inhibition efficiency from impedance experiment) also increase with increase in concentration of inhibitors, with PQDPP having the highest inhibition efficiency of 94.97 % at 100 ppm. The values of the percentage inhibition efficiency obtained from the polarization and EIS measurements are comparable as the mean difference between the values of $\%IE_I$ and $\%IE_P$ (inhibition efficiencies from impedance and polarization studies respectively) is between 3.0 – 5.4 % and the trend of $\%IE_I$ for the three inhibitors is the same as that observed from the polarization studies.

The values of $|\theta|$ and $|S|$ are greater than those of the blank system especially at high concentrations. The values of $|\theta|$ and $|S|$ are closer to 90 degree and 1 respectively in the presence of PQDPP, which suggests that the molecules of the compound adsorbed as protective film on the steel surface and exhibits some capacitive behaviour. The protective film also shields the steel from direct acid attack. A comparison of the values of $|\theta|$ and $|S|$ for PQDPB and PPQDPE suggests that the latter only forms effective and/or capacitive protective film on the steel surface at higher concentrations (above 10 ppm), while the latter appears to cover the steel surface more effectively over the entire concentration range.

4.2.2 Adsorption isotherms

The displacement of water molecules from the MS/solution interface as well as the adsorption of the inhibitor molecules at the interface was investigated by subjecting the experimental data to various adsorption isotherms including Langmuir, Frumkin and Temkin. Only the Langmuir and Frumkin isotherms gave satisfactory fits with $R^2 > 0.9$ especially with the EIS data. However, thermodynamic and interaction parameters were calculated for the studied molecules based on the slopes and intercepts obtained from the Frumkin adsorption isotherms. The preference for the Frumkin adsorption isotherm is partly due its more realistic consideration of the real properties of a two-dimensional surface state of the adsorption layer, which in a way takes the surface molecular area of the adsorbed molecules and their intermolecular interactions into consideration [267]. The data from the EIS measurements were subjected to the linearized Frumkin adsorption isotherm of the form:

$$\ln\left[\frac{\theta}{C(1-\theta)}\right] = \ln K_{ads} + 2a\theta \tag{4.7}$$

where θ is the degree of surface coverage ($\theta = \%IE_I/100$), C is the concentration of the inhibitor, K_{ads} is the equilibrium constant of the adsorption process and a is the interaction parameter, which predicts the nature of interaction (attraction, repulsion or none) that exists between the adsorbed species.

As reported in literature [268], a value of $a > 0$ implies an attraction between the adsorbed species, a value of $a < 0$ is an indication of repulsion between the adsorbed species, while a value of $a = 0$ implies lack of interaction between the adsorbed species. The Frumkin adsorption plots for the studied compounds are shown in Figure 4.14. The results obtained for the interaction parameter, a, equilibrium constant of adsorption, K_{ads} and change in Gibb's free energy of adsorption, ΔG_{ads} are listed in Table 4.10 The values of the interaction parameter obtained for the studied inhibitors are all greater than zero, which connotes

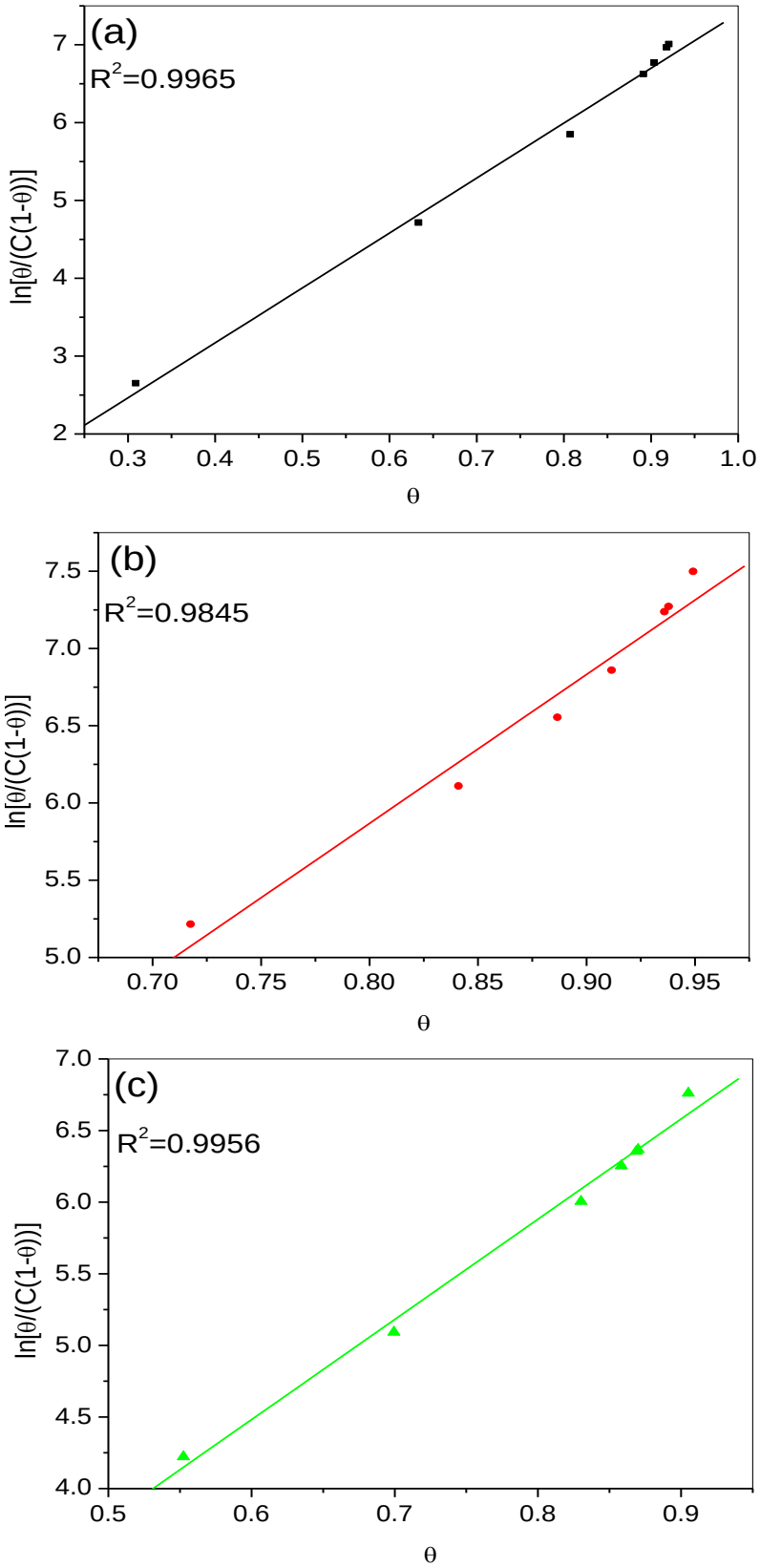

Figure 4.14. Frumkin isotherm plots for MS corrosion in 1 M HCl in the presence of various concentrations of (a) PQDPB, (b) PQDPP and (c) PPQDPE.

Table 4.10. Thermodynamics and interaction parameters for the adsorption of the studied compounds on MS in 1 M HCl at 303.15 K.

Inhibitor	a	K_{ads} (x10^{-5})	$-\Delta G_{ads}$ (kJ/mol)
PQDPB	3.530	2.44	41.38
PQDPP	4.818	20.82	46.79
PPQDPE	3.499	2.96	41.87

attraction between the adsorbed inhibitor species. Adsorption of the inhibitors on steel surface is spontaneous as inferred from the negative values of ΔG_{ads}. The values of ΔG_{ads} obtained for the studied compounds are beyond the threshold associated with chemisorption. In other words, the adsorption process of the studied compounds on MS surface is mainly characterized by chemisorption processes [6, 269, 270].

4.2.3 Quantum chemical calculations

Geometry optimizations of the molecular structures of the three inhibitors were carried out in the gas phase without symmetry constraint. Both ab initio Hartree Fock (HF) and density functional theory (DFT) methods were used in order to ensure adequate explanation of the inhibition properties of the molecules in terms of their molecular and electronic structures. The resulting optimized geometries were confirmed to be of energy minima with the absence of imaginary frequency in the vibrational and force constant calculations. Since the molecules contain multiple donor sites with varying degree of basicity, calculations were also carried out on the protonated forms of the molecules to investigate the possibility of the molecules being protonated in the acid and the likelihood of the steel corrosion being inhibited by the protonated species.

4.2.3.1 Neutral species

The optimized structures of the neutral forms of the three compounds obtained at B3LYP/6-31G(d) level of theory are shown in Figure 4.15. The corresponding optimized structures obtained at HF/6-31G(d) level are shown in Figure AII-3 (Appendix II). Numbering labels are put on only the atoms referenced during the discussion of the results. Relevant quantum chemical parameters of the optimized structures are listed in Table 4.11. The trends of the properties obtained using HF and DFT methods are the same, though the magnitudes of most of the parameters differ (Table 4.11). The difference in the quantitative values of the parameters obtained using the two models is not unexpected as the levels of approximations employed in the two methods are not the same. For instance, HF/6-31G(d) assigned a partial double bond to the supposed saturated bond between N22 and C45 and seems to overestimate some of the electronic properties.

The ability of each inhibitor molecule to adsorb on the steel surface is explained based on possible donor-acceptor relationship between the inhibitor molecule and iron. Graphical surfaces of HOMO and LUMO of the studied compounds are shown in Figure 4.16. The HOMO surfaces of the three compounds are similar and are distributed along the 3-phenyl-4,5-dihydropyrazole unit, extending to their carbonyl functional groups. Their LUMO surfaces are also similar, being localized mainly on the quinoxaline ring. The E_{HOMO}, the E_{LUMO}, and the energy gap, $\Delta E_{L\text{-}H}$ were calculated and utilized to explain the relative propensity of each inhibitor molecule to donate and/or accept electron(s) to/from the appropriate orbitals of iron atom [163].

The results of the quantum chemical parameters presented in Table 4.11 show that apart from the total energy (E_T) and molecular weight (M wt.), most of the other parameters obtained for PQDPB and PPQDPE are amazingly close in magnitudes despite the large difference in their molecular weights. This may inform why the trend of their experimental

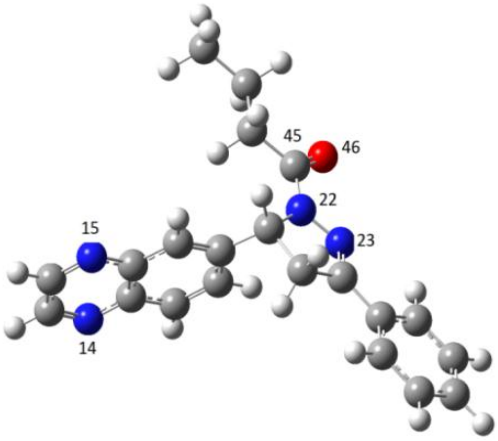

PQDPB

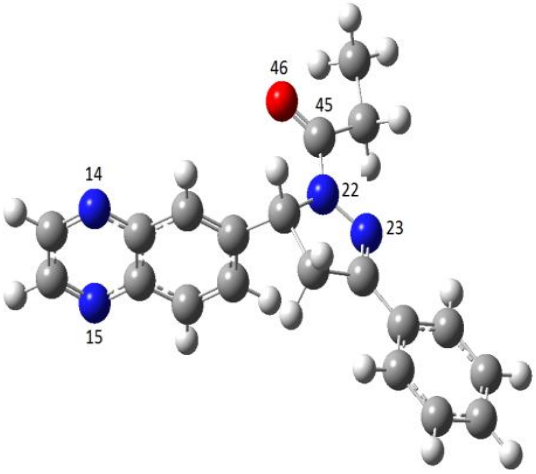

PQDPP

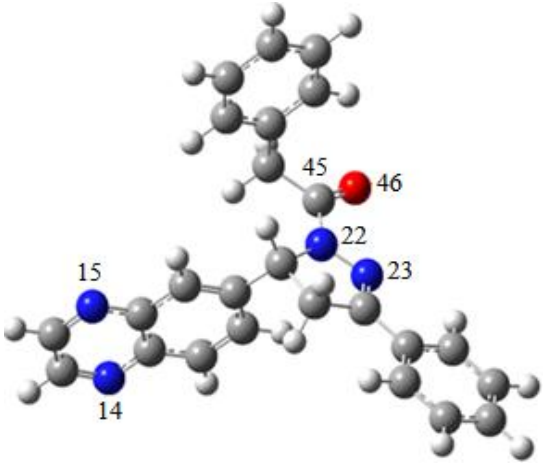

PPDQPE

Figure 4.15. Gas phase optimized structures of the neutral form of the compounds at B3LYP/6-31G(d) level of theory.

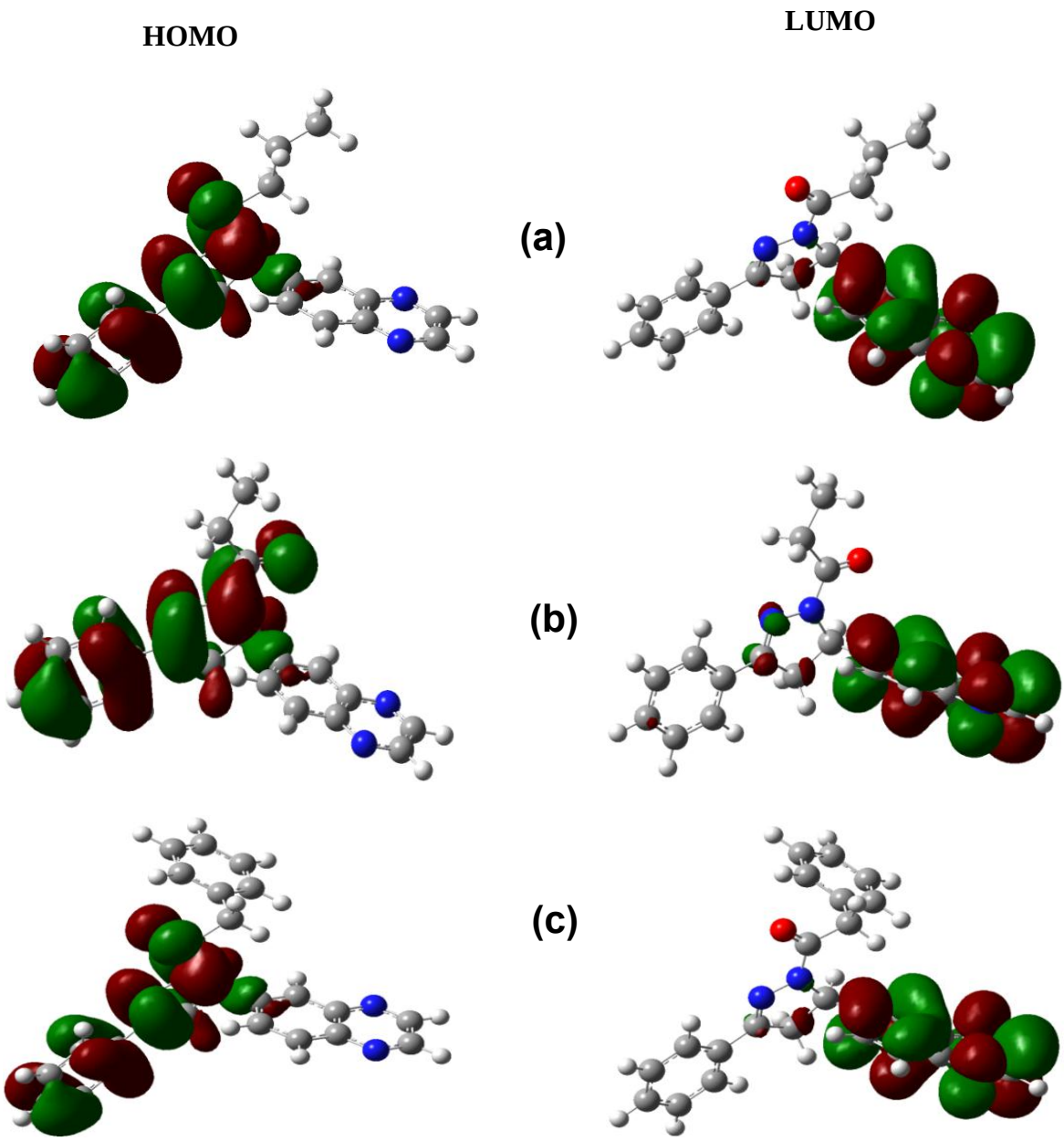

Figure 4.16. HOMO and LUMO electron density isosurfaces of the neutral form of (a) PQDPB, (b) PQDPP and (c) PPQDPE at B3LYP/6-31G(d) level.

%IE was not consistent at lower and higher concentrations. As mentioned earlier (*vide supra* electrochemical studies), PPQDPE shows better inhibition efficiency than PQDPB at lower concentrations but the trend is reversed at higher concentrations. The results obtained for the number of electrons transferred (ΔN) are listed in Table 4.11. The values of ΔN in Table 4.11

are in agreement with Lukovits's study [271] but the trend is not consistent with the experimental inhibition efficiency.

The dipole moments of the studied inhibitor molecules are also calculated and reported in Table 4.11. There is dissenting opinion in the use of dipole moment as a descriptor for inhibition performance. Some authors are of the opinion that an increase in dipole moment leads to decrease in inhibition efficiency with the explanation that low values of dipole moment will favour accumulation of the inhibitor in the surface layer. In another view, some authors believe that high dipole moment will enhance inhibition efficiency due to increased dipole-dipole interactions between the inhibitor molecules and the metal surface [89, 272-274]. The trend of the dipole moment values for the three inhibitors as shown in Table 4.11 is

Table 4.11. Gas phase quantum chemical parameters of PQDPB, PQDPP and PPQDPE at HF/6-31G(d) and B3LYP/6-31G(d).

	HF/6-31G(d)			B3LYP/6-31G(d)		
Parameter	PQDPB	PQDPP	PPQDPE	PQDPB	PQDPP	PPQDPE
E_T *(eV)*	-1099.54	-1060.51	-1251.01	-1106.50	-1067.20	-1258.93
E_{LUMO} *(eV)*	1.71	2.00	1.70	-2.16	-1.92	-2.17
E_{HOMO} *(eV)*	-8.30	-8.41	-8.32	-5.80	-5.86	-5.84
ΔE_{L-H} *(eV)*	10.01	10.41	10.02	3.64	3.94	3.67
A (eV)	-1.71	-2.00	-1.70	2.16	1.92	2.17
I (eV)	8.30	8.41	8.32	5.80	5.86	5.84
χ *(eV)*	3.30	3.20	3.31	3.98	3.89	4.00
η *(eV)*	5.00	5.20	5.01	1.82	1.97	1.84
ΔN	0.37	0.36	0.37	0.83	0.79	0.82
Dipole moment (Debye)	5.32	4.38	5.38	4.60	3.96	4.66
M wt. (g/mol)	344.16	330.15	392.16	344.16	330.15	392.16

in line with the opinion of the authors that believe in increasing inhibition performance with decreasing dipole moment [90, 275, 276].

The Fukui functions f^+ and f^- associated with the nucleophilic and electrophilic attacks respectively were calculated. Graphical representations of these functions for PQDPB are shown in Figure 4.17. Corresponding electron density isosurfaces of these functions for PQDPP and PPQDPE are shown in Figure AII-4 (Appendix II). The three inhibitors have many sites that are susceptible to nucleophilic and electrophilic attacks and can facilitate their adsorption onto MS surface. Atoms in quinoxaline rings are essentially susceptible to nucleophilic attacks, while the carbonyl oxygen atoms and nitrogen atoms in dihydropyrazole rings are mainly susceptible to electrophilic attacks.

The quantum chemical parameters in Table 4.11 do not provide adequate justifications to the experimentally observed trends of %*IE*. For instance, highest value of $\Delta E_{L\text{-}H}$ and η obtained for PQDPP do not correspond with its highest value of experimental %*IE*. Since these compounds have a number of donor atoms or basic sites, there is a chance that one or more of these sites is/are protonated in the acid such that the steel corrosion is inhibited by the protonated species. This informed further calculations on the protonated species of the inhibitors.

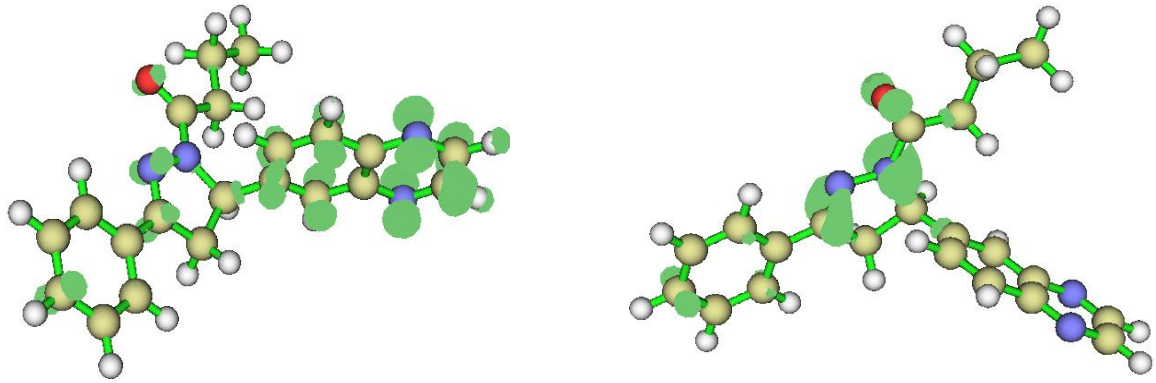

Figure 4.17. Fukui functions, f^+ *and* f^- (left and right-hand sides respectively) for the neutral form of PQDPB (*Isosurface = 0.003 and 0.005 for* f^+ *and* f^- *respectively*).

4.2.3.2 Protonated species

The compounds were protonated singly at N14, N15, N22, N23 and O46. Gas phase geometry optimizations and frequency calculations were carried out on each mono-protonated species at B3LYP/6-31G(d). Since N22 is a saturated nitrogen atom, protonation of this atom was not favourable as it leads to the cleavage of N22–C45 bond. The most preferred site of protonation in each molecule was determined based on gas phase proton affinity (*PA*) and basicity (*GB*) values. Each compound was treated as a potential base with one prospective basic site. Protonation reaction at a particular donor site in a neutral molecule, B can be written as:

$$B + H^+ \rightleftharpoons BH^+ \quad (4.8)$$

Gas phase proton affinity (*PA*) for Equation 4.8 was calculated as the negative value of the difference in enthalpies of product and reactants, expressed as [277-280]:

$$PA = -\Delta H = -\left[H_{gas}(BH^+) - (H_{gas}(B) + H_{gas}(H^+))\right] \quad (4.9)$$

where H_{gas} is the enthalpy at 298.15 K labeled in Gaussian output for frequency calculations as the sum of electronic and thermal enthalpies. Since H^+ is monatomic specie, the only non-zero contribution to its enthalpy is the translational energy ($3/2RT$ = 3.720 kJ/mol). Gas phase basicity of each prospective site of protonation was also calculated as the negative change in Gibbs free energy of the protonation reaction in Equation 4.8 as [278]:

$$GB = -\Delta G = G_{gas}(B) + G_{gas}(H^+) - G_{gas}(BH^+) \quad (4.10)$$

where G_{gas} is the free energy at 298.15 K labelled in Gaussian output for force constant calculations as sum of electronic and thermal free energies. $G_{gas}(H^+)$ is defined as:

$$G_{gas}(H^+) = 3/2RT + TS(H^+) \quad (4.11)$$

where $S(H^+)$ was taken to be 108.95 J/mol/K [278, 279]. Absolute values of *PA* and *GB* and their respective relative values (Δ*PA* and Δ*GB*) calculated at 298.15 K using the B3LYP/6-31G(d) method are listed in Table 4.12. The results in Table 4.12 show that the most probable sites of protonation are: N23 in PQDPB, N14 in PQDPP and O46 in PPQDPE. More so, there is a chance of multiple protonation in some cases where Δ*PA* and Δ*GB* are close to that of the

Table 4.12. Proton affinity (*PA*) and gas-phase basicity (*GB*) for PQDPB, PQDPP and PPQDPE at B3LYP/6-31G(d) level.

	PA (kJ/mol)/Protonation site				*GB* (kJ/mol)/Protonation site			
Compound	N14	N15	N23	O46	N14	N15	N23	O46
PQDPB	926.59 (-39.46)	924.12 (-41.92)	966.04 (0)	954.24 (-11.80)	958.93 (-42.13)	956.88 (-44.18)	1001.06 (0)	985.50 (-15.56)
PQDPP	949.06 (0)	942.36 (-6.69)	939.81 (-9.25)	942.40 (-6.65)	980.27 (0)	975.92 (-4.35)	972.61 (-7.66)	973.83 (-6.44)
PPQDPE	918.39 (-52.55)	916.38 (-54.56)	959.22 (-11.72)	970.94 (0)	954.12 (-48.95)	953.07 (-50.00)	996.75 (-6.32)	1003.07 (0)

In parentheses: Δ*PA* = *PA* (less stable) – *PA* (most stable); Δ*GB* = *GB* (less stable) – *GB* (most stable)

most preferred site of protonation.

For instance, PQDPB may as well be protonated at O46, PQDPP may be protonated at all sites, while PPQDPE may also be protonated at N23 under favourable conditions. Again, PQDPB and PPQDPE exhibit similar behaviour in terms of preferred sites of protonation as both can readily be protonated at N23 and O46, though the selectivity of the most preferred site is reversed. It is observed that PPQDPE has a better chance of getting doubly protonated than PQDPB. There is therefore a possibility of this compound getting doubly protonated at lower concentrations (5 ppm to 20 ppm), making it to exhibit higher inhibition efficiencies at

these concentrations than PQDPB. However, when PQDPB happens to be double protonated (especially at higher concentrations: 40 ppm to 100 ppm), it shows better inhibition potential than PPQDPE.

For further investigation, relative reactivity of the most stable protonated species was examined using the FMO parameters. The HOMO and LUMO graphical surfaces of the most stable protonated species are shown in Figure AII-5 (Appendix II) and the corresponding relevant quantum chemical parameters are listed in Table 4.13. The results in Table 4.13 show that PQDPP- $H^{+}_{(N14)}$ has the highest E_{HOMO}, E_{LUMO} and the lowest ΔE_{L-H} when compared with PQDPB-$H^{+}_{(N23)}$ and PPQDPE-$H^{+}_{(O46)}$.The trends of these parameters are:

E_{HOMO}: PQDPP-$H^{+}_{(N14)}$ > PQDPB-$H^{+}_{(N23)}$ ≥ PPQDPE-$H^{+}_{(O46)}$

E_{LUMO}: PQDPP-$H^{+}_{(N14)}$ < PQDPB-$H^{+}_{(N23)}$ < PPQDPE-$H^{+}_{(O46)}$

ΔE_{L-H}: PQDPP-$H^{+}_{(N14)}$ < PQDPB-$H^{+}_{(N23)}$ < PPQDPE-$H^{+}_{(O46)}$

Table 4.13. Quantum chemical parameters for the most stable protonated species: PQDPB-H^{+}, PQDPP-H^{+} and PPQDPE-H^{+}.

	B3LYP/6-31G(d)		
Parameter	PQDPB	PQDPP	PPQDPE
E_T (eV)	-1106.88	-1067.57	-1259.31
E_{LUMO} (eV)	-6.20	-7.05	-5.17
E_{HOMO} (eV)	-9.25	-8.35	-9.28
ΔE_{L-H} (eV)	3.05	1.30	4.11
A (eV)	6.20	7.05	5.17
I (eV)	9.25	8.35	9.28
χ (eV)	7.72	7.70	7.22
η (eV)	1.52	0.65	3.61
ΔN	-0.24	-0.54	-0.03
Dipole moment (Debye)	8.31	12.90	3.61

These trends are in perfect support of PQDPP as the most efficient inhibitor (*cf.* experimental %*IE* values). PQDPP-$H^{+}_{(N14)}$ also has the least value of chemical hardness (η), which also supports its high reactivity and enhanced inhibition performance. The negative value of ΔN for the protonated species is due to their higher electronegativity than atomic iron. This suggests back-donation from the *d*-orbitals of iron to the vacant π-molecular orbitals of the protonated inhibitor molecule. The values of ΔN suggest that PQDPP-$H^{+}_{(N14)}$ has the highest tendency to receive electrons from the metal during retro-donation and the trend supports experimentally observed inhibition performances. The trend of the dipole moments of the protonated species is in line with previous reports that believe that the higher the dipole moment the higher the inhibition efficiency.

The Fukui indices of the protonated inhibitors are also calculated and the graphical electron density surfaces are presented in Figure 4.18 for PQDPB. The graphical electron density isosurfaces for the Fukui functions of PQDPP and PPQDPE are shown in Figure AII-6 (Appendix II). The prospective sites for nucleophilic and electrophilic attacks are clearly marked by the change in electron density upon addition or removal of electron from the respective most stable protonated species.

The f^{+} sites for PQDPB are mainly found on a N-atom and a C-atom on the pyrazole ring, and also on some C-atoms on the phenyl ring directly attached to the pyrazole ring. The O-atom of the carbonyl group is only slightly susceptible to nucleophilic attack. The f^{-} sites are essentially located on the N-atoms and aromatic π-electron regions of the quinoxaline ring and also on a N-atom of the pyrazole ring.

The f^{+} sites for PQDPP are mainly found on a N-atoms and aromatic π-electron regions of the quinoxaline ring, while the f^{-} sites are essentially located on a N-atom and π-electron regions of the pyrazole ring and also on the O-atom of the carbonyl group and π-electron regions of the phenyl group directly attached to the pyrazole ring. In the case of

PPQDPE, the f^+ sites are mainly located on the C-atoms of the pyrazole ring and the phenyl group directly attached to it. The O-atom of the carbonyl group and some of its C-atoms also showed some propensities for nucleophilic attacks. The f^- sites for PPQDPE are mainly found on the N-atoms of the quinoxaline ring and slightly extended to the N-atom and C-atoms of the pyrazole ring and the phenyl group directly attached to it respectively.

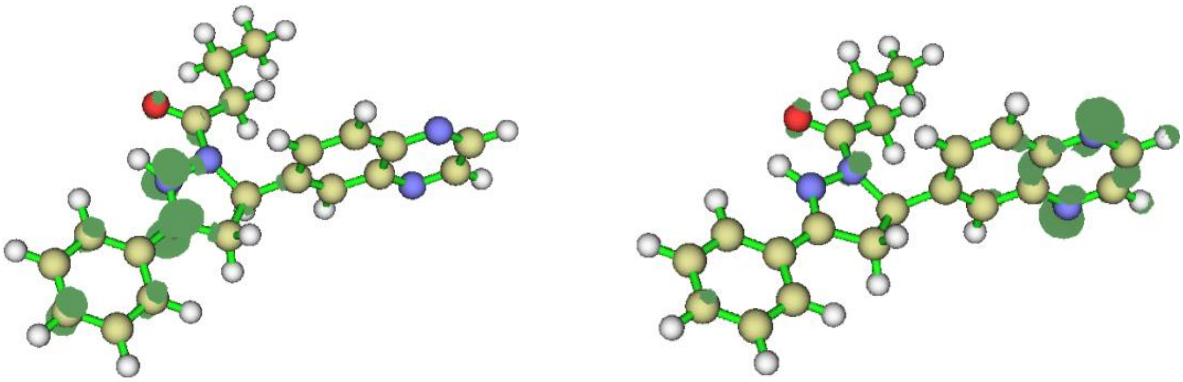

Figure 4.18. Fukui functions, f^+ and f^- (left and right-hand sides respectively) for the most stable protonated form of PQDPB (*Isosurface = 0.003 and 0.005 for f^+ & f^- respectively*).

4.2.4 Monte Carlo simulations results

The adsorption of the studied inhibitor molecules (PQDPB, PQDPP, and PPQDPE) on Fe(110) surface in the presence of 100 water molecules was simulated using Monte Carlo simulations and the most stable configurations are shown in Figure 4.19. Some energy parameters or adsorption descriptors associated with the most stable configuration in each case are listed in Table 4.14. The parameters include total energy of the substrate–adsorbate configuration, which is defined as the sum of the energies of the adsorbate components, the rigid adsorption energy, and the deformation energy. The substrate energy (i.e., Fe(110) surface) is taken as zero. Moreover, adsorption energy is the energy released (or required) when the relaxed adsorbate component was adsorbed on the substrate. The adsorption energy is defined as the sum of the rigid adsorption energy and the deformation energy for the adsorbate component. The rigid adsorption energy reports the energy released (or required)

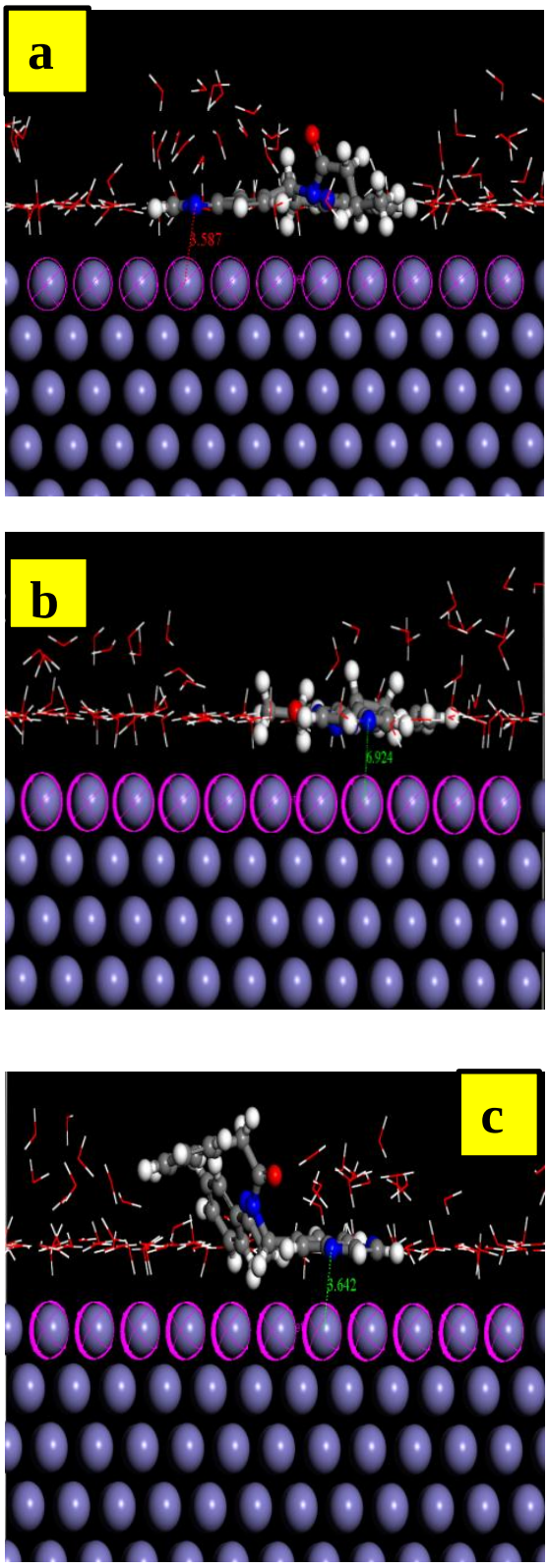

Figure 4.19. The most stable (low energy) configuration for the adsorption of (a) PQDPB, (b) PQDPP , and (c) PPQDPE on Fe (110)/100 H_2O interface obtained through the Monte Carlo simulations.

when the un-relaxed adsorbate component (before the geometry optimization step) was adsorbed on the substrate. The deformation energy is the energy released when the adsorbed adsorbate component was relaxed on the substrate surface. Finally, the differential parameter, dE_{ad}/dN_i is the energy change associated with the most stable configuration of a substrate–adsorbate system when one of the adsorbate components is removed from the system.

From Figure 4.19, it is evident that PQDPP which exhibited the strongest interaction and by extension highest inhibition efficiency lies almost flat or nearly parallel on the Fe(110) surface leading to a stronger interaction. PQDPB and PPQDPE had various slanting angle of deviations as they interact with the iron surface. This leads to reduced interactions with the iron surface. The results in Table 4.14 show that PQDPP/Fe(110) system has the highest magnitudes of the total energy, the adsorption energy and the rigid adsorption energy. This is in agreement with its highest inhibition efficiency among the three inhibitors studied in this work. The magnitudes of the adsorption energies of the studied inhibitors on iron surface increase in the order: PQDPP > PQDPB > PPQDPE. Highest negative adsorption energy indicates the system with the most stable and stronger adsorption [281, 282].

The change in energy, dE_{ad}/dN_i upon change in the number of inhibitor or water molecules also showed that PQDPP undergoes higher stabilization upon addition/removal of inhibitor molecule(s) compared to PQDPB and PPQPE, while PQDPB shows slightly better stabilization upon change in system components than PPQDPE. In all cases, the change in adsorption energies upon change in the number of inhibitor molecules is far higher than that of water molecules. This suggests that the inhibitor molecules have better tendency of displacing water molecules from iron surface and adsorbing on the surface to form stable adsorption layer of the inhibitor molecules, which can protect the iron from aqueous corrosion.

Table 4.14. Energy parameters of the lowest configurations obtained from the Monte Carlo simulations of the adsorption of PQDPB, PQDPP and PPQDPE on Fe (110)/100H_2O interface (in kJ/mol).

Systems	Total Energy	Adsorption energy	Rigid adsorption energy	Deformation energy	dE_{ad}/dN_i Inhibitors	dE_{ad}/dN_i H2O
Fe(110)/PQDPB/100 H_2O	-6381.69	-6651.97	-6942.97	290.96	-777.09	-27.78
Fe(110)/PQDPP/100 H_2O	-6514.32	-6815.53	-7146.90	331.33	-833.41	-54.81
Fe(110)/PPQDPE/100 H_2O	-6374.70	-6649.76	-6950.46	300.66	-691.03	-26.28

4.2.5 Inhibition activity of the studied inhibitors and carbonyl reactivity

Since the three inhibitors studied in the present work only differ in chain of the carbonyl groups, it may be necessary to consider possible correlations between the trends of inhibition efficiency and carbonyl reactivity. The reactivity of carbonyl group arises from the electronegativity of oxygen atom and the resulting polarization of the carbon-oxygen double bond. Aldehydes are generally known to be more reactive than ketones on the basis of electronic and steric effects [283]. In other words, short-chain carbonyls are more reactive than long-chain carbonyls. More so, aliphatic carbonyls are more reactive than aromatic carbonyls because the electron-donating resonance effect of the aromatic ring in aromatic carbonyls makes the carbonyl group less electrophilic than the carbonyl group of an aliphatic carbonyl [283]. The results obtained for the *% IE* of the studied inhibitors agree with the trend of reactivity of carbonyl compounds. PQDPP with the shortest carbonyl chain length is the most efficient inhibitor of MS corrosion in 1 M HCl.

4.3 GROUP III: MS-2-PQPP, MS-3-PQPP and MS-4-PQPP

Group III comprises three quinoxaline derivatives as listed in Table 3.3. These compounds have the same molecular formula, functional groups, and similar molecular structures. These compounds only differ in the position of the sulphonamide group that is

directly attached to the phenyl group, which in turn is attached to the N-atom (at position 3) of the pyrazole ring. Therefore, the effect of relative position of the sulphonamide group on the adsorption and corrosion inhibition properties of these compounds was investigated. The presence of multiple pi-electron rings and/or units and heteroatoms portrays these compounds as prospective efficient corrosion inhibitors.

4.3.1 Electrochemical studies

4.3.1.1 Tafel plots

Tafel curves were obtained for MS in 1 M HCl without and with various concentrations of MS-4-PQPP, MS-2-PQPP, and MS-3-PQPP and the results are presented in Figure 4.20. The curves shift towards lower current density region in the presence of the inhibitors compared to the blank acid medium. This suggests that the studied compounds reduce the corrosion current and therefore reduce the corrosion rate. The polarization curves also exhibit some shifts in potential towards more anodic or cathodic regions than the acid blank. The direction of the shift is not uniform as it varies with concentrations of the inhibitors. This suggests that the inhibitors affect both the anodic and cathodic corrosion reactions. The shift in the polarization curves in the direction of lower current density is also more pronounced at higher concentrations of the inhibitors, which suggests that the corrosion rate decreases with increasing concentrations of the inhibitors. All the studied compounds showed obvious shift in the polarization curves towards more positive values at higher concentrations, especially at 80 ppm and/or 100 ppm. This is an indication of increased ability of the compounds to inhibition acid corrosion of MS [284].

Tafel parameters obtained from Figure 4.20 are listed in Table 4.15. The shift in E_{corr} between the inhibitor containing system and the blank is generally less than the threshold

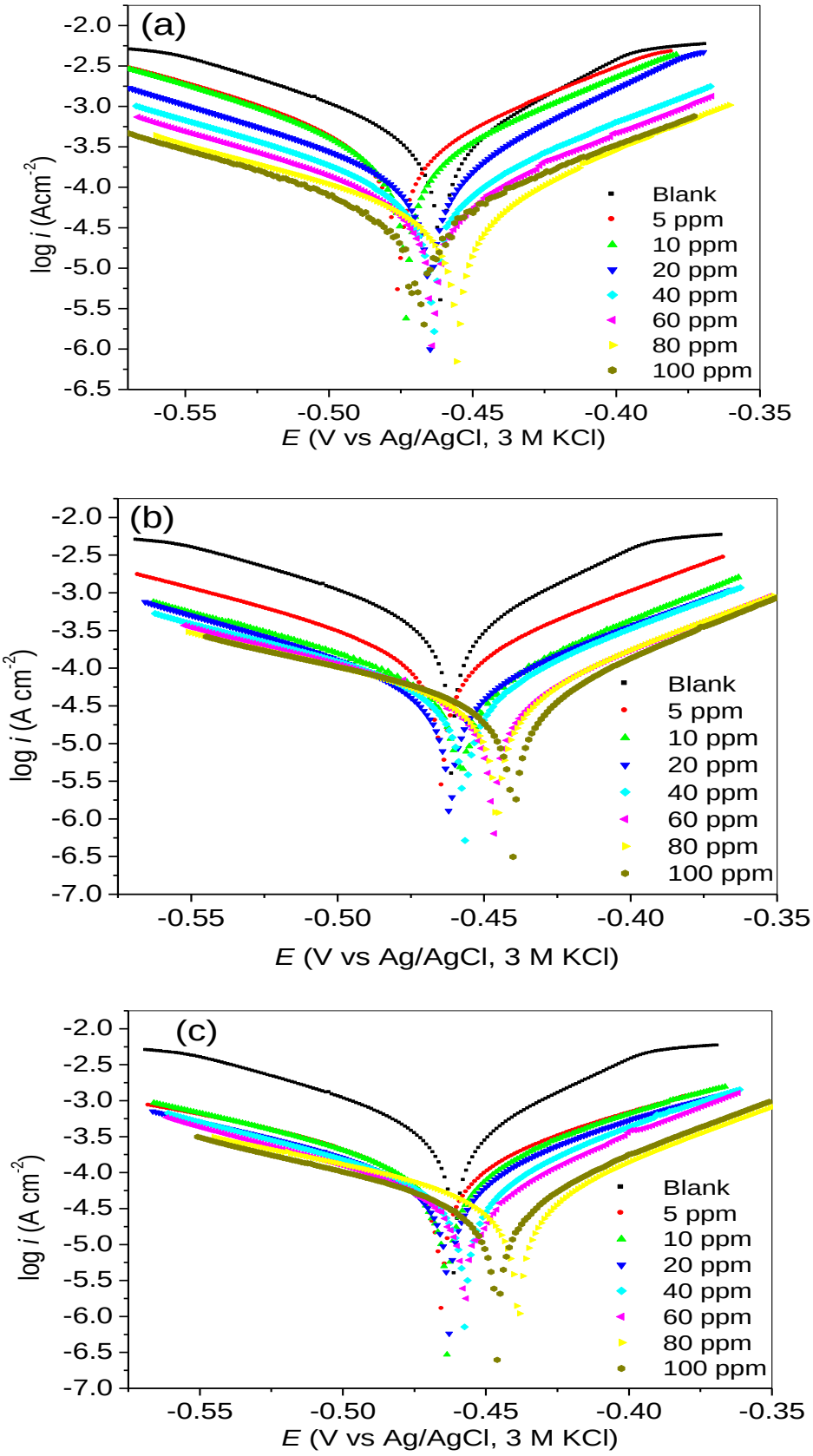

Figure 4.20. Tafel plots for MS in 1 M HCl without and with various concentrations of (a) MS-2-PQPP, (b) MS-3-PQPP, and (c) MS-4-PQPP.

value of 85 mV for all the studied compounds, which implies that the studied compounds are mixed-type inhibitors. They inhibit both the anodic MS dissolution and cathodic hydrogen gas evolution reactions associated with the corrosion process. The E_{corr} values for MS-2-PQPP shift slightly towards more cathodic regions at 5 ppm to 80 ppm concentrations compared to the blank, while the shift in E_{corr} is slightly more anodic than the blank at 100 ppm. The polarization curves for MS-3-PQPP exhibit slightly cathodic shift at 5 ppm and 20 ppm, but appear at more anodic regions at higher concentrations (40 ppm – 100 ppm). MS-4-PQPP on the other hand shows slightly cathodic shifts in E_{corr} at lower concentrations (5 ppm to 20 ppm) and more anodic shifts. The corrosion current density, i_{corr} decreases with increase

Table 4.15. Tafel parameters and percentage inhibition efficiency for the corrosion of MS in 1 M HCl without and with inhibitors.

Compound	*Conc.* (ppm)	- E_{corr} (mV)	i_{corr} (μA/cm^2)	β_a (mV/dec)	β_c (mV/dec)	$\%IE_P$
Blank	-	460.60	420.41	89.34	65.27	-
	5	475.46	318.55	93.84	77.90	24.19
	10	473.01	251.66	88.54	75.81	40.11
MS-2-PQPP	20	464.90	137.89	96.81	59.76	67.20
	40	463.73	95.73	101.36	76.51	77.22
	60	463.72	70.20	102.01	76.58	83.29
	80	468.43	50.11	105.91	81.71	88.08
	100	455.35	51.34	116.70	71.85	87.78
	5	463.98	142.63	97.59	73.44	66.06
	10	457.67	62.37	97.00	67.40	85.16
MS-3-PQPP	20	461.61	54.87	91.42	74.03	86.94
	40	456.72	55.71	111.01	71.14	86.74
	60	446.76	40.69	112.77	70.54	90.32
	80	445.78	42.57	126.68	70.87	89.87
	100	440.36	41.35	137.58	68.03	90.16
	5	465.03	148.12	130.50	95.46	64.75
	10	463.62	120.81	114.64	84.47	71.25
MS-4-PQPP	20	462.93	98.12	121.64	83.28	76.65
	40	457.26	70.76	110.17	71.31	83.16
	60	457.30	50.36	99.82	67.95	88.02
	80	436.70	46.39	130.28	71.25	88.96
	100	446.57	41.50	122.28	68.82	90.12

in concentration of the inhibitors leading to increase in $\%IE_P$.

The $\%IE_P$ of MS-2-PQPP increases from 24.19 % at 5 ppm up to 88.08 % at 80 ppm. Further increase in concentration does not show any significant effect on inhibition efficiency. The increase in inhibition efficiency with increasing concentration may be attributed to increase in the number of adsorbed molecules of the inhibitor on the steel surface. The number of molecules that adsorb on the active sites on the MS surface increase with increasing concentration of the inhibitor, leading to an increase in surface coverage, and consequently, increase in inhibition efficiency.

The trend of the inhibition performance of MS-3-PQPP is such that there is an apparent increase in inhibition efficiency as the concentration of the inhibitor increases from 5 ppm to 10 ppm. The values of the $\%IE_P$ at 20 ppm and 40 ppm are nearly the same. A maximum value of 90.32 % was obtained at 60 ppm. Further increase in concentration above this value does not seem to have noticeable effect on inhibition efficiency. The $\%IE_P$ of MS-4-PQPP increases continuously as the concentration increases from 5 ppm to 100 ppm.

Based on the maximum value of $\%IE_P$ obtained for each compound within the concentration range (5 ppm – 100 ppm), it can be concluded that the order of corrosion inhibition ability of the studied compounds is MS-3-PQPP > MS-4-PQPP > MS-2-PQPP. The variation of the $\%IE_P$ with concentration is depicted in Figure 4.21 in which the comparative trend of $\%IE_P$ for the studied compounds as well as the critical concentration for highest inhibitive effect for each compound is readily envisioned. It is apparent from Figure 4.21 that the $\%IE_P$ of MS-2-PQPP reaches maximum at 80 ppm, while that of MS-3-PQPP attains a plateau at 60 ppm, and that of MS-4-PQPP starts to approach inundation at 60 ppm. It is also noteworthy that the E_{corr} and β_a values at (or within) the identified critical concentration for the studied compounds are remarkably different from their corresponding values at the preceding concentrations. This may have something to do with change in electrochemical

behaviour of the system at these concentrations due to the presence of some new species such as protonated inhibitor molecules. The effect of this development on the corrosion inhibition process is more pronounced on the anodic MS dissolution reaction.

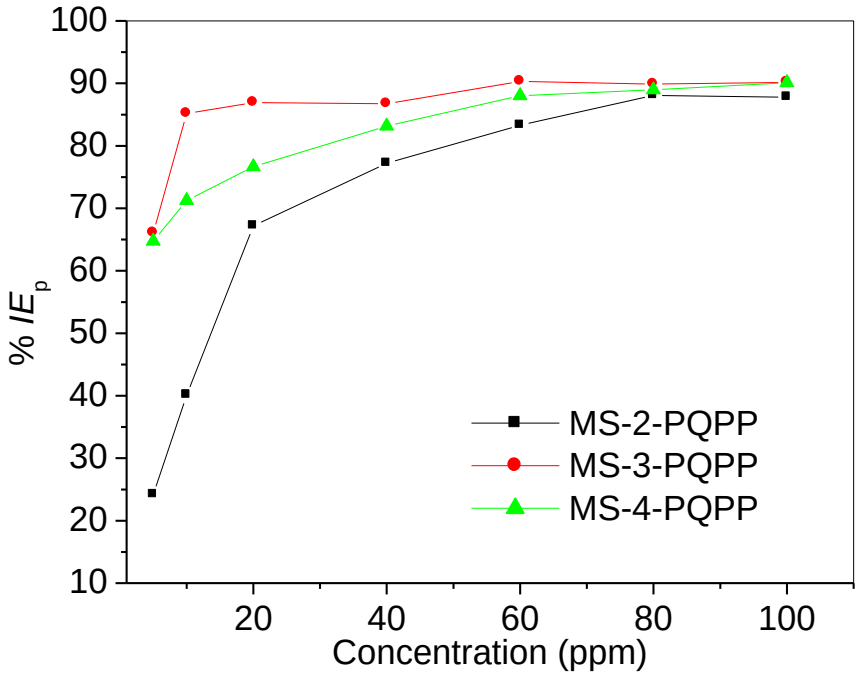

Figure 4.21. Variation of *%IE*$_P$ with concentrations of the studied inhibitors.

4.3.1.2 EIS measurements

The EIS measurements were carried out on the studied compounds at the same concentration range in order to support the results obtained from the Tafel analyses. The Nyquist and Bode plots for MS in 1 M HCl in the absence and presence of various concentrations of MS-2-PQPP are shown in Figure 4.22, while the corresponding plots for MS-3-PQPP and MS-4-PQPP are shown in Figures AIII-1 and AIII-2 (Appendix III) respectively. The plots show similar behaviour in the absence and presence of the inhibitors, which suggests that the inhibition of steel corrosion in the acid by the studied compounds does not alter the mechanism of the corrosion process [8, 90, 285].

The Nyquist plots show single depressed semicircles corresponding to one time constant in the Bode plots. The depression of a Nyquist semicircle is attributed to frequency

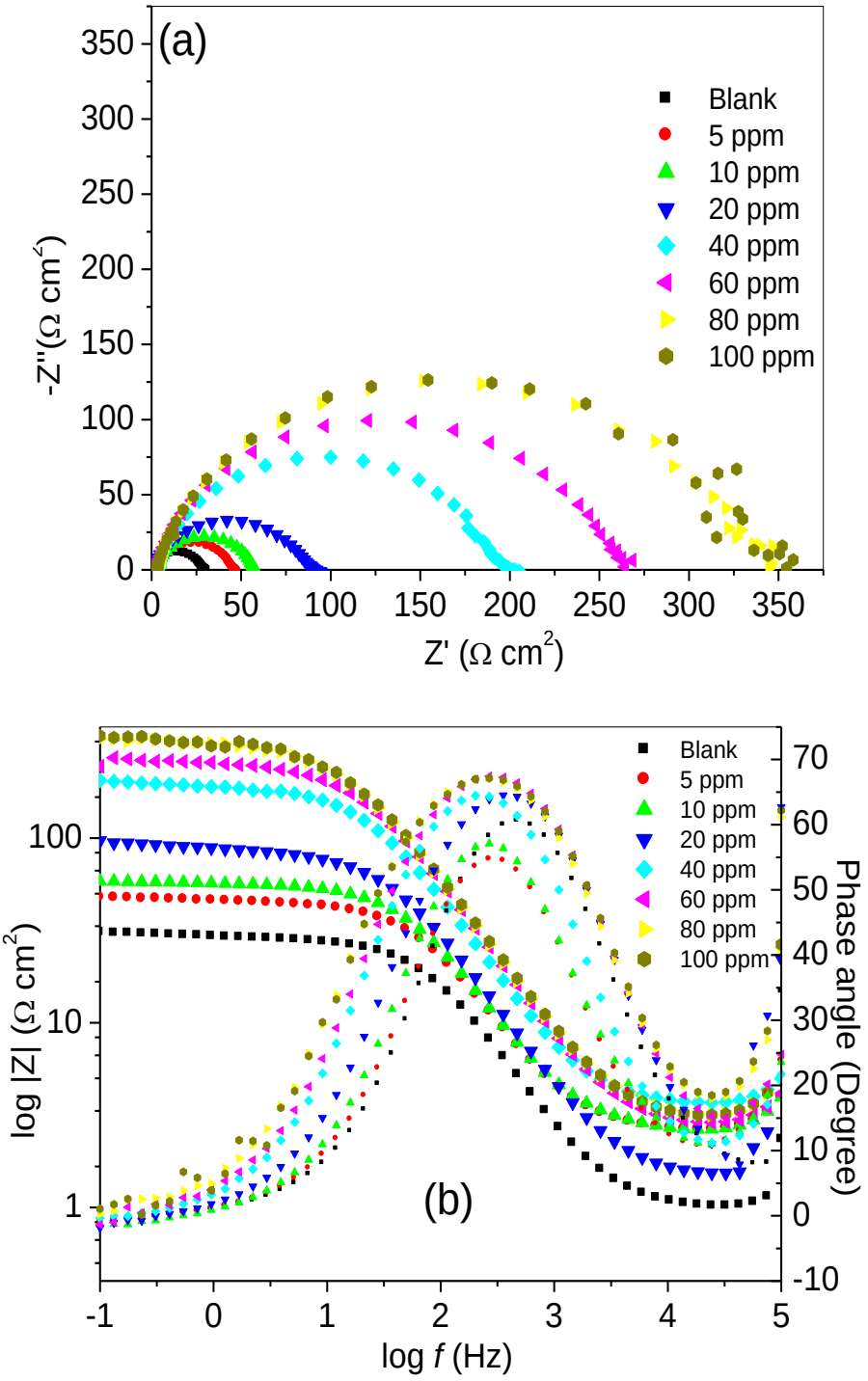

Figure 4.22. Nyquist (a) and Bode (b) plots for MS in 1 M HCl without and with various concentrations of MS-2-PQPP.

dispersion effects that may result from roughness of the electrode surface and/or other forms of interfacial phenomena [286, 287]. The depressed one time constant semi-circular Nyquist profiles show capacitive behaviour at low frequencies, which suggests that the corrosion of

MS in the studied media is essentially controlled by a single charge transfer process. The diameters of the Nyquist semicircles in the presence of the inhibitors are generally larger than that of the uninhibited system and these diameters increase with increasing concentration of each of the studied inhibitors. This implies that the impedance of the MS/electrolyte system is larger in the presence of the inhibitors, and increases with increase in concentration. This suggests that the rate of MS dissolution in the acid is impeded by the studied inhibitors and the extent of retardation of the steel dissolution increases with increasing inhibitor concentration.

The EIS spectra were fitted to the equivalent circuit model of the form in Figure 4.4. The values of electrochemical parameters obtained from the EIS spectra are presented in Table 4.16. The results show that the R_{ct} increases with increasing concentration of the inhibitors, which implies that the resistance of the steel/electrolyte systems to the transfer of charges associated with corrosion process increases with increasing concentration of the inhibitors. This may be due to decrease in the exposed/active surface/sites of the metal that may be involved in corrosion based charge transfer process [3].

The percentage inhibition efficiency ($\%IE_I$) also increases with increase in inhibitor concentration. A maximum value of $\%IE_I$ is attained at certain concentration for each compound. Similar observations were also recorded from the polarization experiments. The values of the constant phase element (CPE), Y_0 do not follow a definite pattern but they are generally lower for the inhibited systems than the uninhibited one, which indicates that the molecules of the studied compounds adsorbed on the steel surface to form a protective layer. In most cases, values of Y_0 at higher concentrations of the inhibitors are also lower than at lower concentrations, though the trends cannot be generalized for all the studied compounds over the entire concentration range. The values of the CPE exponent, n are close to unity, which implies that the electrode/electrolyte systems considered in the present study have

Table 4.16. EIS parameters and percentage inhibition efficiency for the corrosion of MS in 1 M HCl without and with various concentrations of the inhibitors.

Compound	*Conc.* (ppm)	R_s (Ωcm^2)	R_{ct} (Ωcm^2)	Y_o ($\mu Ss^n cm^{-2}$)	*n*	$\|\theta\|$ (Degree)	$\|S\|$	$\%IE_I$
Blank	-	1.01	28.20	157	0.893	60.59	0.64	-
MS-2-PQPP	5	2.65	42.6	124	0.886	54.68	0.66	34.04
	10	2.67	54.6	124	0.880	57.12	0.70	48.53
	20	1.51	86.8	110.0	0.873	64.52	0.72	67.51
	40	3.64	190	71.9	0.877	64.45	0.78	85.21
	60	2.76	255	61.6	0.869	67.45	0.79	88.98
	80	2.89	337	67.6	0.848	67.08	0.79	91.66
	100	2.93	332	69.9	0.847	67.12	0.79	91.54
MS-3-PQPP	5	3.04	125	78.8	0.878	63.10	0.76	77.52
	10	2.66	259	62.1	0.883	68.90	0.82	89.15
	20	3.18	302	54.2	0.891	69.24	0.83	90.70
	40	3.48	304	58.4	0.868	67.27	0.80	90.76
	60	3.06	431	59.1	0.862	69.38	0.82	93.48
	80	2.99	428	57.1	0.855	68.86	0.81	93.44
	100	2.17	459	57.5	0.867	71.74	0.84	93.88
MS-4-PQPP	5	19.6	134	77.7	0.878	42.60	0.53	79.03
	10	14.6	161	70.3	0.887	49.44	0.61	82.55
	20	17.3	196	63.1	0.879	49.24	0.60	85.66
	40	7.35	255	61.8	0.888	61.75	0.76	88.98
	60	2.14	325	57.5	0.884	71.42	0.84	91.35
	80	2.96	431	68.8	0.863	69.41	0.82	93.48
	100	2.91	436	66.0	0.861	69.86	0.83	93.56

mainly capacitive characteristics. The values of *n* are also indicative of the degree of heterogeneity of the electrode surface. The relatively lower values of *n* for the inhibited systems compared to the acid blank indicates that the steel surface shows less inhomogeneity in the presence of the inhibitors due to the adsorbed inhibitor molecules, which homogeneously covered the surface.

The magnitude of the maximum phase angle, $|\theta|$ and the magnitude of the slope of the linear portion (intermediate frequencies) of the Bode impedance modulus, $|S|$ are also listed in Table 4.16. The results show that $|\theta|$ is closer to 90^0, while $|S|$ is closer to 1 at higher concentrations of the inhibitors compared to the blank system. These observations are true

over the entire concentration range for MS-3-PQPP. This suggests that the electrode/electrolyte interface behaves closer to an ideal capacitor at higher concentrations of the inhibitors. This also implies that the inhibitor molecules adsorbed on the steel surface to for a protective film with some levels of capacitive characteristics. Although, such inferences cannot be drawn from the values of $|\theta|$ and/or $|S|$ at lower concentrations of MS-2-PQPP and MS-4-PQPP as some of these values are lesser than that of the uninhibited acid system. This however does not rule out the formation of adsorbed film on the steel surface at those concentrations but might imply that the behaviour of the electrode/electrolyte interface is farther from ideal capacitor compared to the blank. The consistently higher values of these parameters for MS-3-PQPP over the entire concentration range are also in support of its higher inhibition efficiency than MS-2-PQPP and MS-4-PQPP.

4.3.2 Adsorption isotherms

The experimental data were found to fit into the Langmuir adsorption isotherm and the plots are shown in Figure 4.23. The adsorption isotherms exhibit linear plots with correlation coefficient (R^2) values of 1.000. The near unity values of the slopes i.e. 0.98 (MS-2-PQPP), 1.06 (MS-3-PQPP), and 1.05 (MS-4-PQPP) also support the conformation of the experimental data with the Langmuir adsorption isotherm.

The adsorption parameters such as the K_{ads} and ΔG_{ads} were calculated and listed in Table 4.17. The high values of K_{ads} obtained for the studied compounds imply that the displacement of water molecules from the steel/acid interface by the inhibitor molecules, and consequently the adsorption of the inhibitor molecules on the steel surface is a favourable process, and the compounds adsorb strongly on MS surface. The negative values of ΔG_{ads} also suggest spontaneous adsorption of the inhibitor molecules on the steel surface. It can be inferred from the range of values of ΔG_{ads} in Table 4.17 that the mode of adsorption of

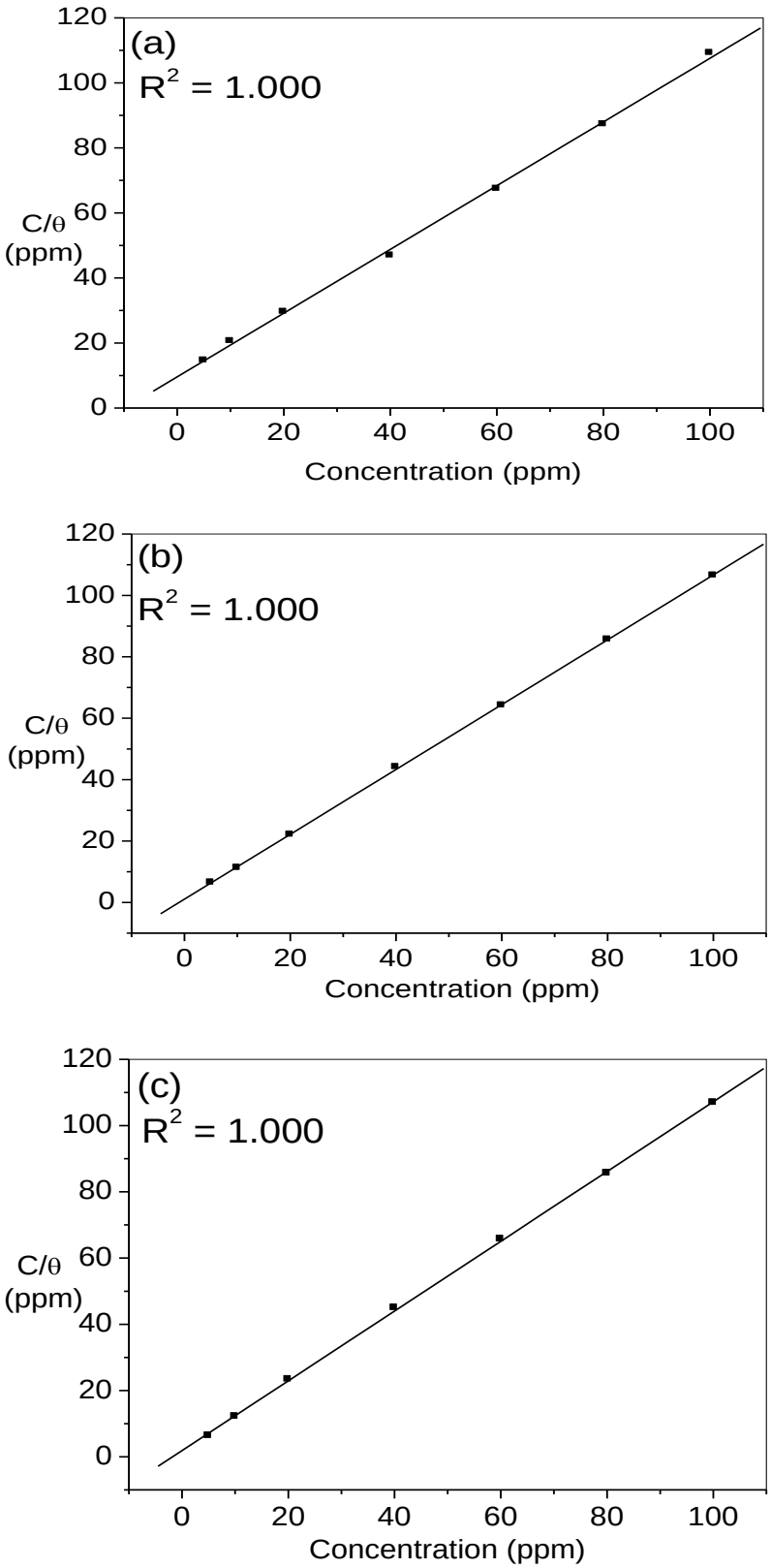

Figure 4.23. Langmuir adsorption isotherms for (a) MS-2-PQPP, (b) MS-3-PQPP, and (c) MS-4-PQPP on MS in 1 M HCl. (*Experimental data were taken from the EIS measurements*).

MS-2-PQPP involves competitive physisorption and chemisorption, while MS-3-PQPP and MS-4-PQPP adsorb on MS in 1 M HCl by chemisorption mechanism. The trend of the values of K_{ads} and ΔG_{ads} is such that MS-3-PQPP > MS-4-PQPP > MS-2-PQPP, which is the same as the relative order of the *%IE*.

Table 4.17. Thermodynamic parameters for the adsorption of the studied compounds on MS in 1 M HCl at 303.15 K.

Inhibitor	K_{ads} (x10^3)	$-\Delta G_{ads}$ (kJ/mol)
MS-2-PQPP	44.15	37.08
MS-3-PQPP	397.80	42.62
MS-4-PQPP	226.20	41.20

4.3.3 UV-vis spectroscopic analyses

UV-vis spectroscopic analyses were carried out on the solutions of the studied inhibitor molecules and the resulting solutions after MS immersion for 3 hours and the spectra are shown in Figure 4.24. The most prominent absorption band in the UV-vis spectra the three compounds appears at 200 nm – 201 nm and this band is due to n → π* transition. MS-2-PQPP also shows a shoulder-like band of lower absorbance at 219 nm, while MS-3-PQPP and MS-4-PQPP both show absorption bands at 239 nm and 300 nm – 301 nm due to π → π* transitions and intramolecular charge transfers (ICT) respectively. After MS immersion, MS-2-PQPP shows a new band at 336 nm and the absorbances are generally higher than without the steel immersion. The major difference in the UV-vis spectra of the solutions of MS-3-PQPP and MS-4-PQPP after MS immersion is the increase in absorbance of the bands at 200 nm – 201 nm. The observed changes in the absorption spectra of the studied compounds after MS immersion suggest the occurrence of chemical interactions between the inhibitor molecules and Fe leading to the formation of Fe-inhibitor complexes.

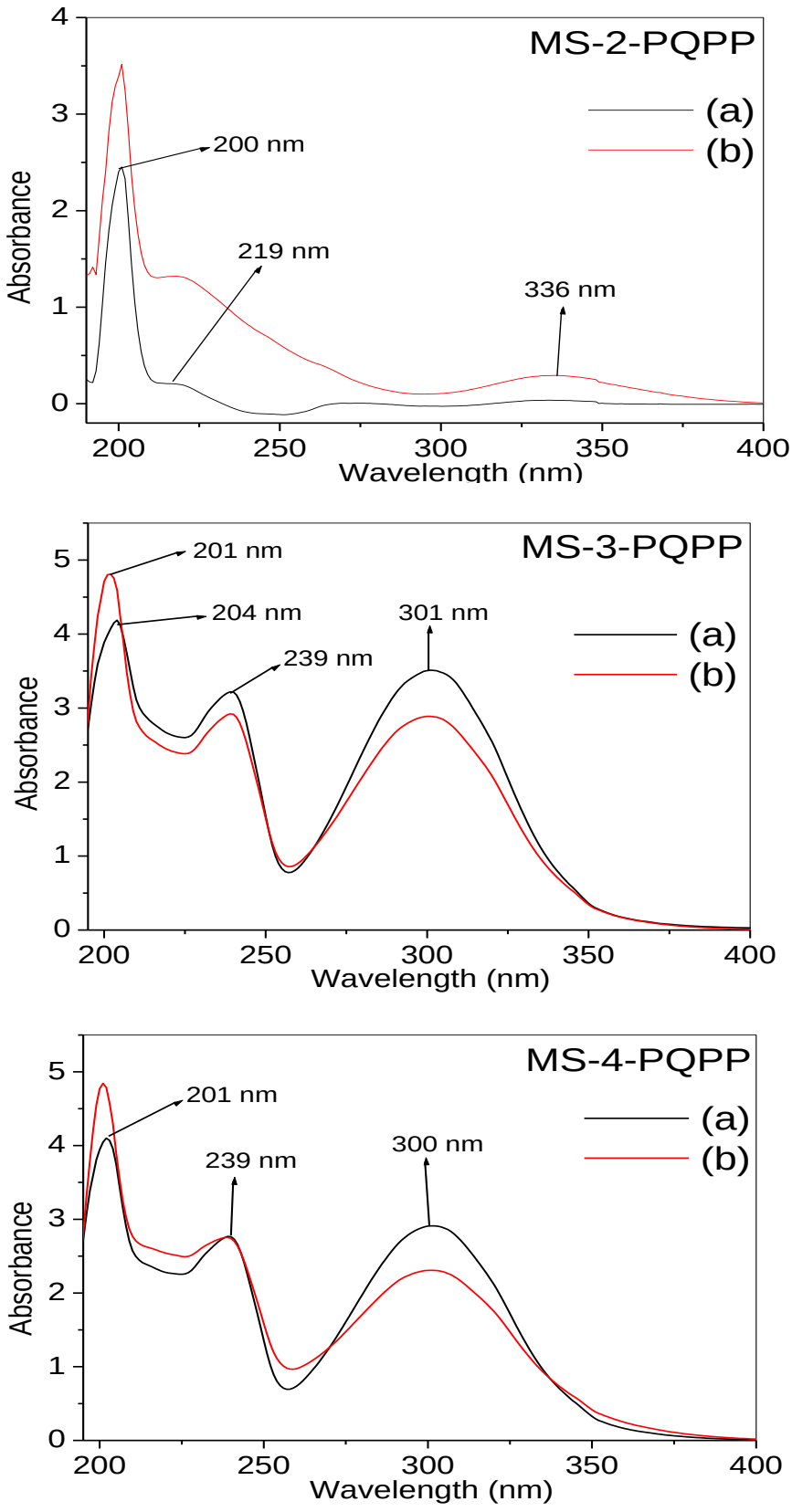

Figure 4.24. UV-vis spectra of the acidic solutions of studied inhibitors **(a)** before, and **(b)** after MS immersion.

4.3.4 Quantum chemical calculations

4.3.4.1 Neutral species

Quantum chemical calculations were performed on the neutral forms of the studied molecules using the B3LYP/6-31G(d) model. Full geometry optimizations and frequency calculations were carried out in the gas phase without geometry constraint and the optimized structures corresponding to the true energy minima (confirmed by the absence of imaginary frequency in the force constant calculations) of the neutral molecules are shown in Figure 4.25. The electron density distributions for the HOMO and LUMO are also shown in Figure 4.26.

The HOMO of all the molecules comprises both π- and σ- type orbitals, but essentially dominated by π-type molecular orbitals. The HOMO electron density is distributed oven the entire pyrazole and phenyl rings. The N-atom of the methanesulphonamido group and the O-atom of the carbonyl functional group in each case are also involved in the HOMO electron density distributions. This suggests that prospective interactions of the studied molecules with MS via the donation of high energy π-electrons to the vacant d-orbitals of Fe will occur predominantly around the pyrazole and phenyl rings. The HOMO orbitals around the N-atom of the methanesulphonamido group and the carbonyl O-atom are σ-type, indicating that these groups can interact with vacant p-orbitals of Fe. The S- and O-atoms of the sulphonamido group are not involved in the HOMO electron density distributions.

The LUMO electron density distributions on the other hand are mainly found on the quinoxaline rings of the molecules and they are π-type orbitals. Some distinctive salient features are observed in the LUMO of MS-3-PQPP. Apart from the atoms in the quinoxaline ring, the sp^2 N-atom of the pyrazole ring and the C-atoms adjoining the pyrazole and phenyl rings in MS-3-PQPP are also involved in the LUMO electron density surface of the molecule. Some of the C-atoms in the phenyl ring especially those around the sulphonamido groups

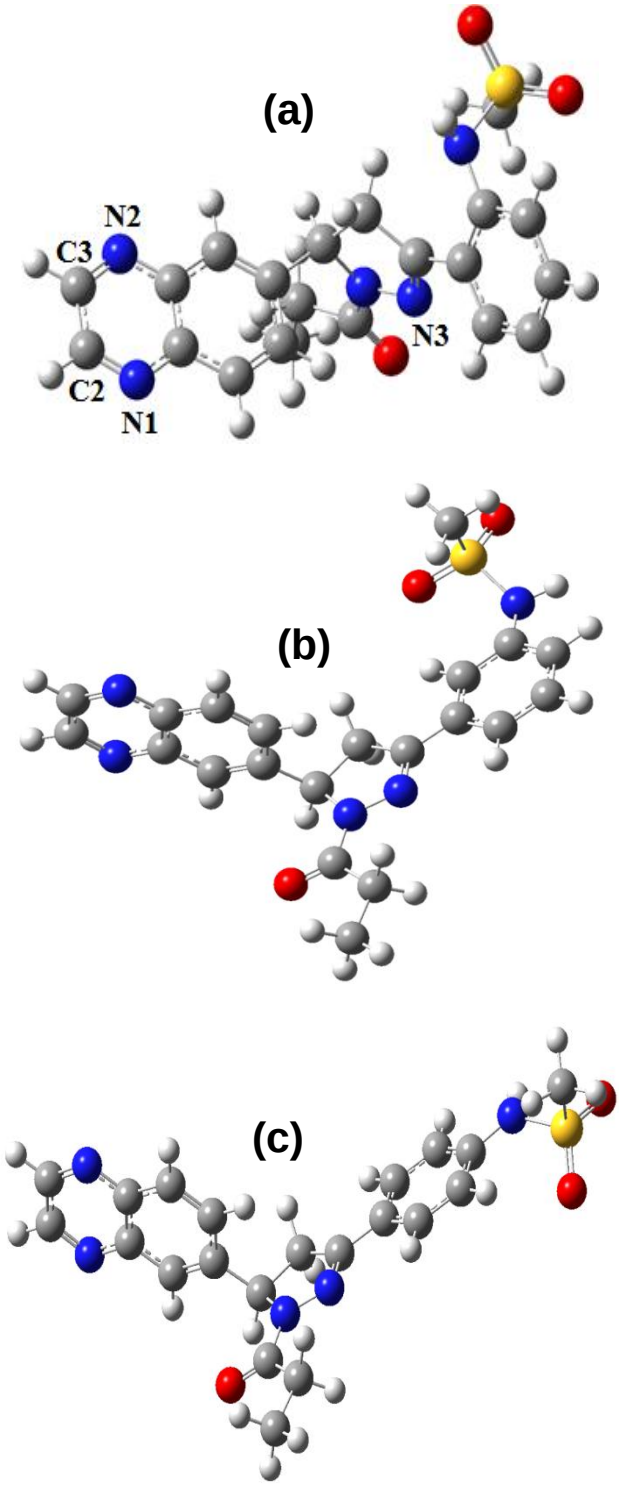

Figure 4.25. Optimized structures of neutral molecules of (a) MS-2-PQPP, (b) MS-3-PQPP, and (c) MS-4-PQPP at B3LYP/6-31G(d) level of theory. (*Selected atomic labels in (a) were used for the purpose of discussion of results later on in this section and section 4.3.5.*2).

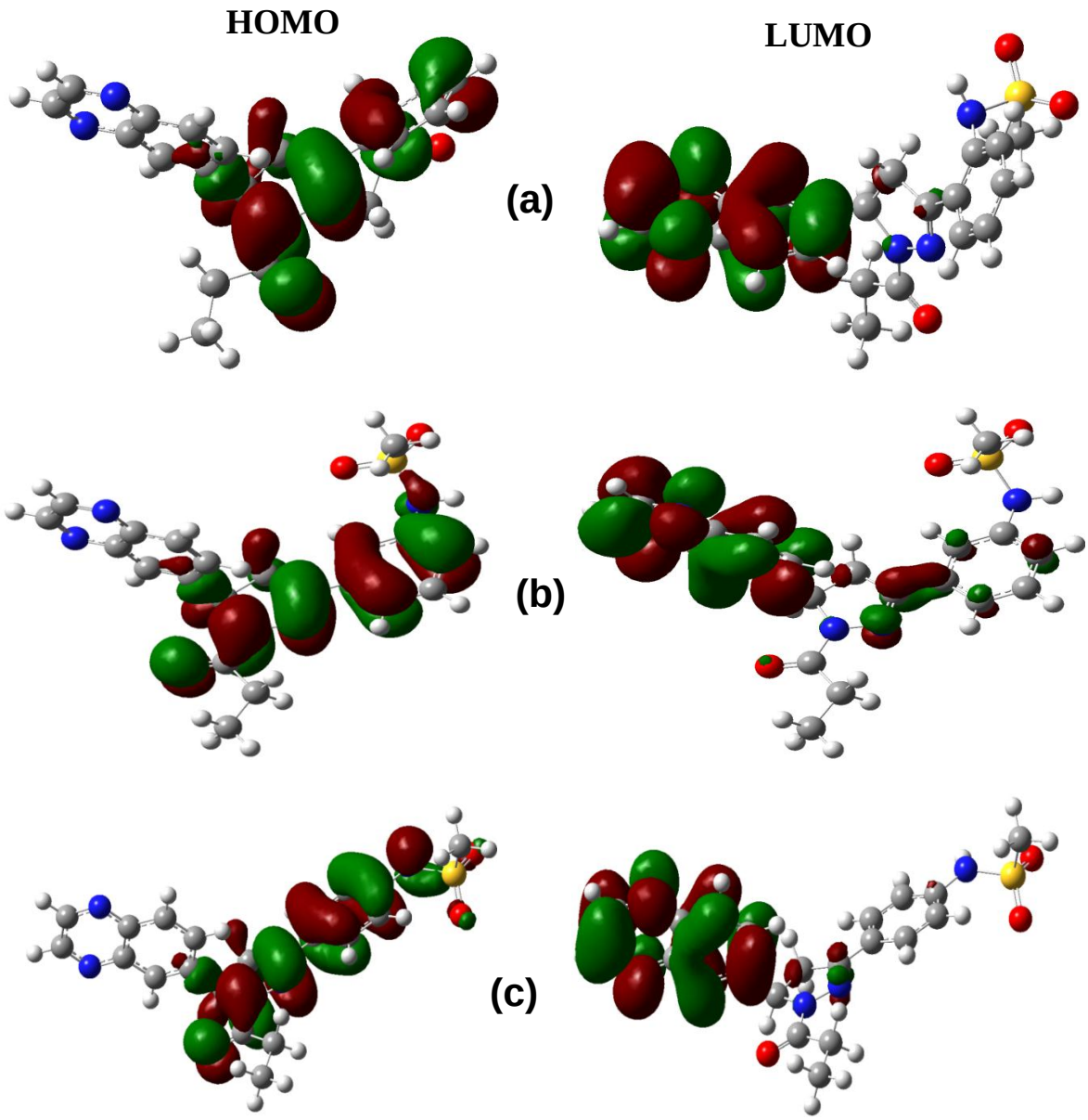

Figure 4.26. HOMO and LUMO electron density isosurfaces of (a) MS-2-PQPP, (b) MS-3-PQPP, and (c) MS-4-PQPP at B3LYP/6-31G(d) level of theory.

also contribute to the LUMO electron density distributions in MS-3-PQPP. These observations suggest that the position of the sulphonamido group (i.e. position 3 on the phenyl ring) in this molecule favours the interactions of the compound with MS via retro-donation from the metal.

Selected quantum chemical parameters of the studied molecules are listed in Table 4.18. The values of the E_{LUMO} for the studied compounds revealed that MS-2-PQPP has the least value of E_{LUMO}, which implies that it has the highest relative tendency to receive electrons from the appropriate filled orbitals of the metal. This suggests that MS-2-PQPP should have the highest inhibition performance, which however is contrary to experimental observations. The trend of the E_{LUMO} is such that MS-2-PQPP < MS-4-PQPP < MS-3-PQPP, which does not support the order of experimentally observed %IE. The values of the E_{HOMO} on the other hand suggest that MS-4-PQPP with the highest E_{HOMO} should have the highest tendency to donate its HOMO electrons to the appropriate vacant orbitals of the metal thereby making it a potentially better inhibitor than MS-3-PQP and MS-2-PQPP. This again does not totally describe the observed trend of the inhibition performances of the molecules. It can be inferred that the FMO energies do not provide adequate justifications to the relative performance of the studied molecules as corrosion inhibitors. This may be due to the complex nature of the adsorption process involved in the experiment but could not be represented in the quantum chemical modelling. Other quantum chemical parameters are

Table 4.18. Quantum chemical parameters for the neutral molecules of: MS-2-PQPP, (b) MS-3-PQPP, and (c) MS-4-PQPP at B3LYP/6-31G(d) level of theory.

Parameter	MS-2-PQPP	MS-3-PQPP	MS-4-PQPP
E_{LUMO} *(eV)*	-2.243	-1.942	-1.946
E_{HOMO} *(eV)*	-6.124	-5.983	-5.734
$\Delta E_{L\text{-}H}$ *(eV)*	3.881	4.041	3.789
χ *(eV)*	4.183	3.963	3.840
η *(eV)*	1.941	2.020	1.894
ΔN	0.726	0.752	0.834
Dipole moment (Debye)	3.816	5.493	4.505

somewhat derived from the frontier molecular orbital energies and as a result do not also explain what was observed in the experiment. The values of ΔN for these molecules are generally less than 3.6, suggesting that the inhibition efficiency will increase with increasing electron-donating ability of the molecules in accordance to Lukovit's proposition [271]. The decreasing order of the dipole moments of the compounds is MS-3-PQPP > MS-4-PQPP > MS-2-PQPP, which is in agreement with the observed trend of inhibition performances. The high dipole moment of MS-3-PQPP is assumed to enhance its inhibition performance by promoting dipole-dipole interactions between the inhibitor molecules and the steel surface. Similar observations have been reported in the literature [89, 272-274] and also reported earlier in this thesis (*vide supra* section 4.2.4.1).

The Fukui indices were computed for the neutral molecules of the compounds. The atomic sites for nucleophilic (f^+) and electrophilic (f^-) attacks are shown in Figure 4.27. It is apparent from the f^+ electron density surfaces that the prospective interactions of a negatively charged metallic surface with the inhibitor molecules will occur mainly through the N-atoms and the aromatic centre (C2=C3) in the quinoxaline ring, the sp^2 N-atom (N3) in the pyrazole ring, and the π-electron centre between the C-atoms adjoining the pyrazole and phenyl rings. Some of the C-atoms (in the phenyl ring) especially those in the neighbourhood of the methanesulphonamido group might be prospective sites for nucleophilic attacks. The most probable sites for electrophilic attacks are shown from the f^- graphical images include the two N-atoms in the pyrazole ring, the carbonyl oxygen, the π-electron centres on the phenyl ring around the point of attachment of the methanesulphonamido group. These observations suggest that in acidic medium where a positively charged metallic surface overlaid with negatively charged chloride ions (from HCl solution) is present, the studied inhibitors will interact essentially through the quinoxaline ring. On the other hand, positively charged metallic surface or ions can bind to the inhibitor molecules via the pyrazole ring.

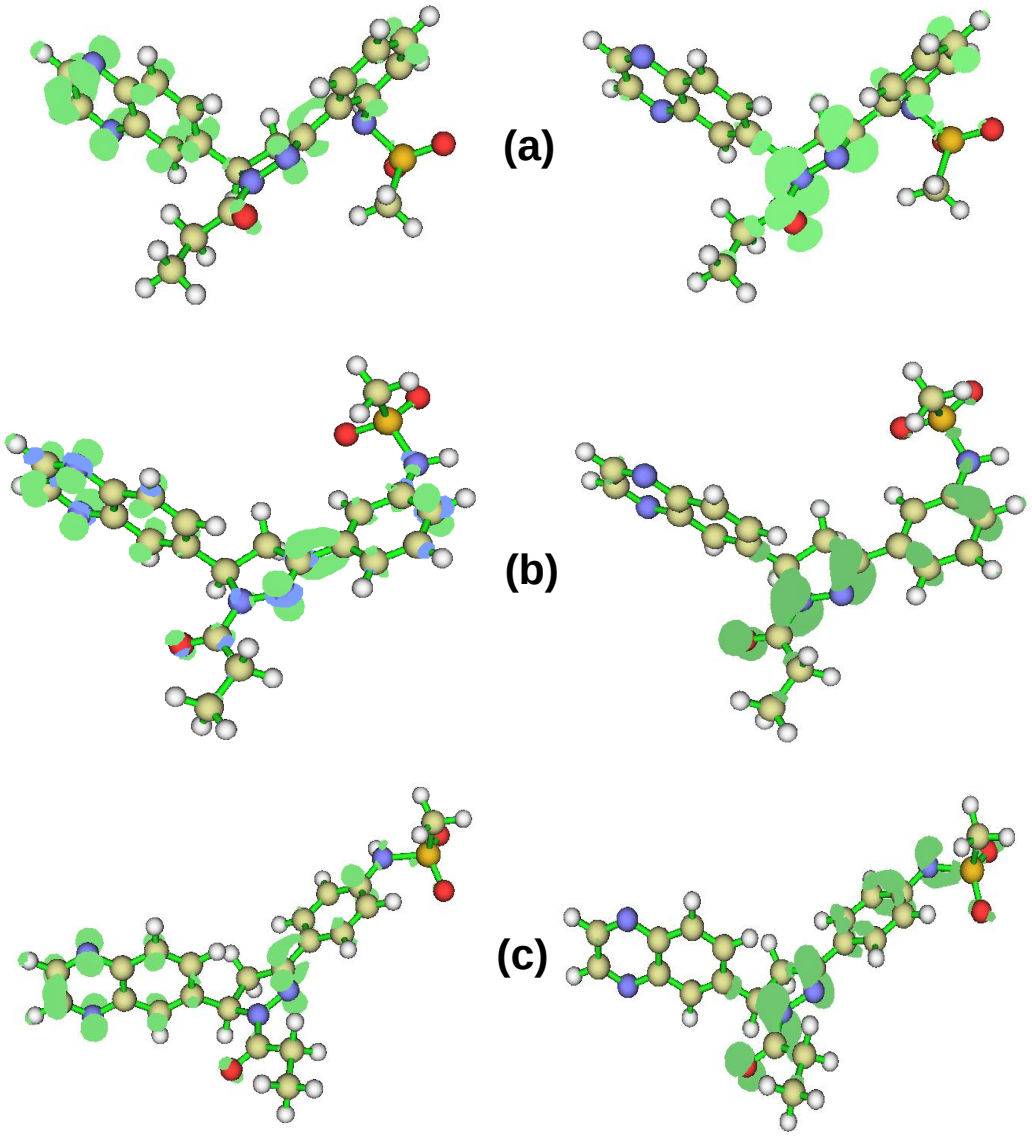

Figure 4.27. Fukui functions, f^+ and f^- (left- and right-hand sides respectively) for the neutral forms of (a) MS-2-PQPP, (b) MS-3-PQPP, and (c) MS-4-PQPP (*Isosurface = 0.003*).

4.3.4.2 Protonated species

Since the studied compounds possess prospective sites of protonation, the proton affinity (PA) and gas-phase basicity (GB) of the donor sites were calculated as described earlier in section 4.2.4.2 of this thesis and the results are listed in Table 4.19. Addition of a proton to an inhibitor will make it to be relatively electron deficient and will increase its propensity to accept electrons from an electron-rich centre. The most probable sites of protonation in the studied compounds were identified as the carbonyl oxygen (O1) in MS-2-

PQPP, the sp^2 nitrogen (labelled N3 in Figure 4.25) of the pyrazole ring in MS-3-PQPP, and the nitrogen atom on the quinoxaline ring (labelled N2). The three most prospective sites of protonation were reported for each molecule and it can be seen from the results in Table 4.19 that MS-3-PQPP has better chance of multiple protonation and/or presence of protonated species at different sites due to relatively close values of PA (and GB) for N1, N2 and O1 compared to MS-4-PQPP and MS-2-PQPP. Therefore, the higher inhibition performance of MS-3-PQPP compared to MS-4-PQPP and MS-2-PQPP might be due to the presence of various protonated species that might participate in the adsorption process. This will increase the electron-accepting tendency of this molecule, such that its inhibition potential is enhanced by retro-donation from the metal.

Analyses of the relative reactivity of the various possible protonated species of these studied compounds were carried out and some of the quantum chemically derived reactivity indices are listed in Table 4.20. Since MS-2-PQPP only has the tendency of protonation at N3, the reactivity of the MS-2-PQPP-H^+_{N3} species can be compared with those of MS-3-PQPP- H^+_{O1}, MS-3-PQPP- H^+_{N1}, and MS-3-PQPP- H^+_{N2} (for MS-3-PQPP), and MS-4-PQPP-

Table 4.19. Proton affinity (PA) and gas-phase basicity (GB) of the sites of protonation in MS-2-PQPP, MS-3-PQPP, and MS-4-PQPP at B3LYP/6-31G(d) level of theory.

	PA (kJ/mol)/Protonation site			*GB* (kJ/mol)/Protonation site		
Compound	N1	N2	N3/O1*	N1	N2	N3/O1*
MS-2-PQPP	920.12 (-46.57)	922.53 (-44.15)	966.68 (0)	950.36 (-46.18)	952.66 (-43.88)	996.54 (0)
MS-3-PQPP	932.24 (-6.61)	925.94 (-12.90)	938.85* (0)	965.95 (-6.93)	962.56 (-10.33)	972.89* (0)
MS-4-PQPP	942.19 (-7.41)	949.61 (0)	923.04 (-26.56)	973.77 (-4.69)	978.46 (0)	954.29 (-24.18)

In parentheses: ΔPA = *PA* (less stable) – *PA* (most stable); ΔGB = *GB* (less stable) – *GB* (most stable)

*N3 or O1, and the most stable protonated form of MS-2-PQPP is the protonated specie at N3, while that of MS-3-PQPP is the specie protonated at O1.

H^+_{N1} and MS-4-PQPP- H^+_{N2} (for MS-4-PQPP). The results in Table 4.20 are for the most stable protonated species only (in each case). However, it was observed that the E_{LUMO} values (not listed the Table 4.20) for MS-3-PQPP-H^+_{N1} and MS-3-PQPP- H^+_{N2}, which are also prospective species of MS-3-PQPP in acidic solution are -7.131 eV and -7.184 eV respectively, which favour electron acceptance from the metal during back donation better than those of MS-4-PQPP-H^+_{N1} and MS-4-PQPP-H^+_{N2} (-7.017 eV and -6.962 eV respectively) and MS-2-PQPP-H^+_{N3} (-6.085 eV). This trend of E_{LUMO} of possible protonated species in acidic medium agrees with the observed trend of inhibition performance of the studied compounds, suggesting that protonated species play very active role in the corrosion inhibition properties of the studied compounds, even though adsorption of some molecules of neutral species cannot be completely ruled during the complex adsorption process in the bulk electrochemical system.

Table 4.20. Quantum chemical parameters for the most stable protonated forms of MS-2-PQPP, MS-3-PQPP, and MS-4-PQPP at B3LYP/6-31G(d) level of theory.

Parameter	MS-2-PQPP-$H^+_{(N3)}$	MS-3-PQPP- $H^+_{(O1)}$	MS-4-PQPP- $H^+_{(N2)}$
E_{LUMO} *(eV)*	-6.085	-5.323	-6.962
E_{HOMO} *(eV)*	-9.246	-8.948	-7.947
$\Delta E_{L\text{-}H}$ *(eV)*	3.160	3.626	0.985
χ *(eV)*	7.665	7.136	7.455
η *(eV)*	1.580	1.813	0.493
ΔN	-0.210	-0.037	-0.462
Dipole moment (Debye)	4.011	7.772	21.714

4.3.5 Molecular dynamic (MD) simulations

The lowest configurations for the adsorption of the studied inhibitor molecules on Fe (110) surface were obtained from MD simulations and these are shown in Figure 4.28. The

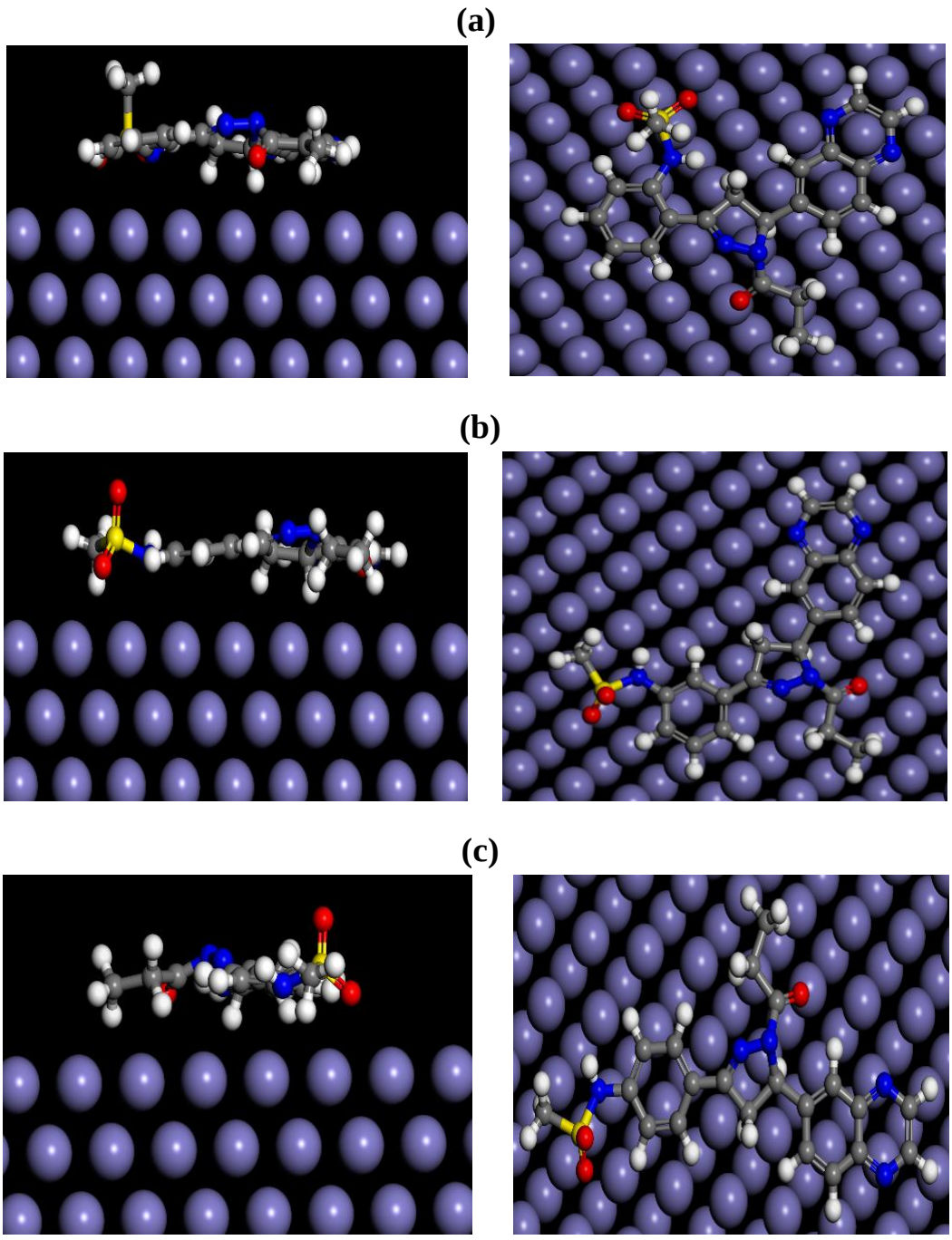

Figure 4.28. Side and top views of the low adsorption energy configurations of (a) MS-2-PQPP, (b) MS-3-PQPP and (c) MS-4-PQPP interactions with Fe (110) using molecular dynamics simulations.

inhibitor molecules adopt parallel or flat orientation on the Fe surface, which support optimum interactions between the inhibitor molecules and the metallic substrate. The methyl group of the methanesulphonamido substituent appear to be sticking out the surface of the Fe

in the case of MS-2-PQPP, which might reduce the degree of interactions between the inhibitor molecule and the Fe atoms compared to the level of interactions found in MS-3-PQPP/Fe (110) and MS-4-PQPP/Fe(110) systems. The associated energy parameters obtained from the simulations are listed in Table 4.21. The results show that the other of binding energies of the inhibitor/Fe(110) systems is MS-3-PQPP/Fe(110) > MS-4-PQPP/Fe(110) > MS-2-PQPP/Fe(110), which is in agreement with the trend of the experimentally observed inhibition strengths of the studied compounds.

Table 4.21. Selected energy parameters for the most stable configurations of the adsorption of the studied inhibitors on Fe (110) surface (in kJ/mol)

System	Interaction energy	Binding energy
Fe (110) + MS-2-PQPP	-976.908	976.908
Fe (110) + MS-3-PQPP	-1113.337	1113.337
Fe (110) + MS-4-PQPP	-1095.693	1095.693

4.4 GROUP IV: MS-2-PQPMS, MS-3-PQPMS, and MS-4-PQPMS

Group IV comprises three quinoxaline derivatives as shown in Table 3.4. The compounds have two sulphonamide groups, one directly attached to the N-atom (at position 1) of the pyrazole ring, and the other directly attached to the phenyl group, which in turn is directly bonded to the N-atom (at position 3) of the pyrazole ring. They differ only in the position of the sulphonamide group that is directly attached to the phenyl group and the effects of relative position of this second sulphonamide group on the adsorption and corrosion inhibition properties of these compounds were investigated.

4.4.1 Electrochemical studies

4.4.1.1 Tafel plots

The Tafel curves for MS in 1 M HCl without and with various concentrations of MS-4-PQPP, MS-2-PQPP, and MS-3-PQPP are shown in Figure 4.29. The curves show relative shifts towards the lower current density regions in the presence of the inhibitors compared to

the blank, and these shifts are more apparent at the anodic than the cathodic arms of the curves. This suggests that the studied compounds reduce the corrosion current density and thereby retard the corrosion rate. The curves also reveal that the studied inhibitors retard both the anodic and cathodic half- reactions, with more prominent effects on the anodic MS dissolution [288]. The similar features of the Tafel curves in the absence and presence of the inhibitors suggests that the inhibitors reduced the corrosion rate without affecting the mechanism of the corrosion reaction [191, 243, 289]. It is important to highlight the relative shift in the Tafel plots along the potential axis. In relation to the Tafel curve for the blank, the curves for MS-2-PQPMS appear at slightly more cathodic points at lower concentrations, and later shifted to a faintly more anodic point at 40 ppm, after which there is a more apparent anodic shift and the potential then appears stable from 60 ppm to 100 ppm. The Tafel curves for MS-3-PQPMS show a slight cathodic shift compared to the blank only at 40 ppm, while the curves emerge at marginally more anodic potentials at other concentrations. The Tafel curves for MS-4-PQPMS however appear generally at somewhat more anodic potentials than the blank.

Tafel parameters for the studied compounds are listed in Table 4.22. The results show that the shift in E_{corr} upon addition of the studied inhibitors when compared to the blank is generally less 85 mV, suggesting that the studied compounds act as mixed-type inhibitors [60, 202]. Besides, the variation in the E_{corr} seems negligible with the maximum shift of about ± 17 mV. This observation suggests that the addition of the studied inhibitors does not, or, only weakly perturb the MS electrode surface [290]. Such a small shift in the E_{corr} can also been attributed to the geometric blocking of the active sites on the steel surface by the inhibitor molecules [157, 291]. The values of the Tafel slopes, β_a and β_c appear to vary with concentrations of the inhibitors, though without a simple definite pattern. However, the values of β_a and β_c in the presence of the inhibitors are generally higher than those of the

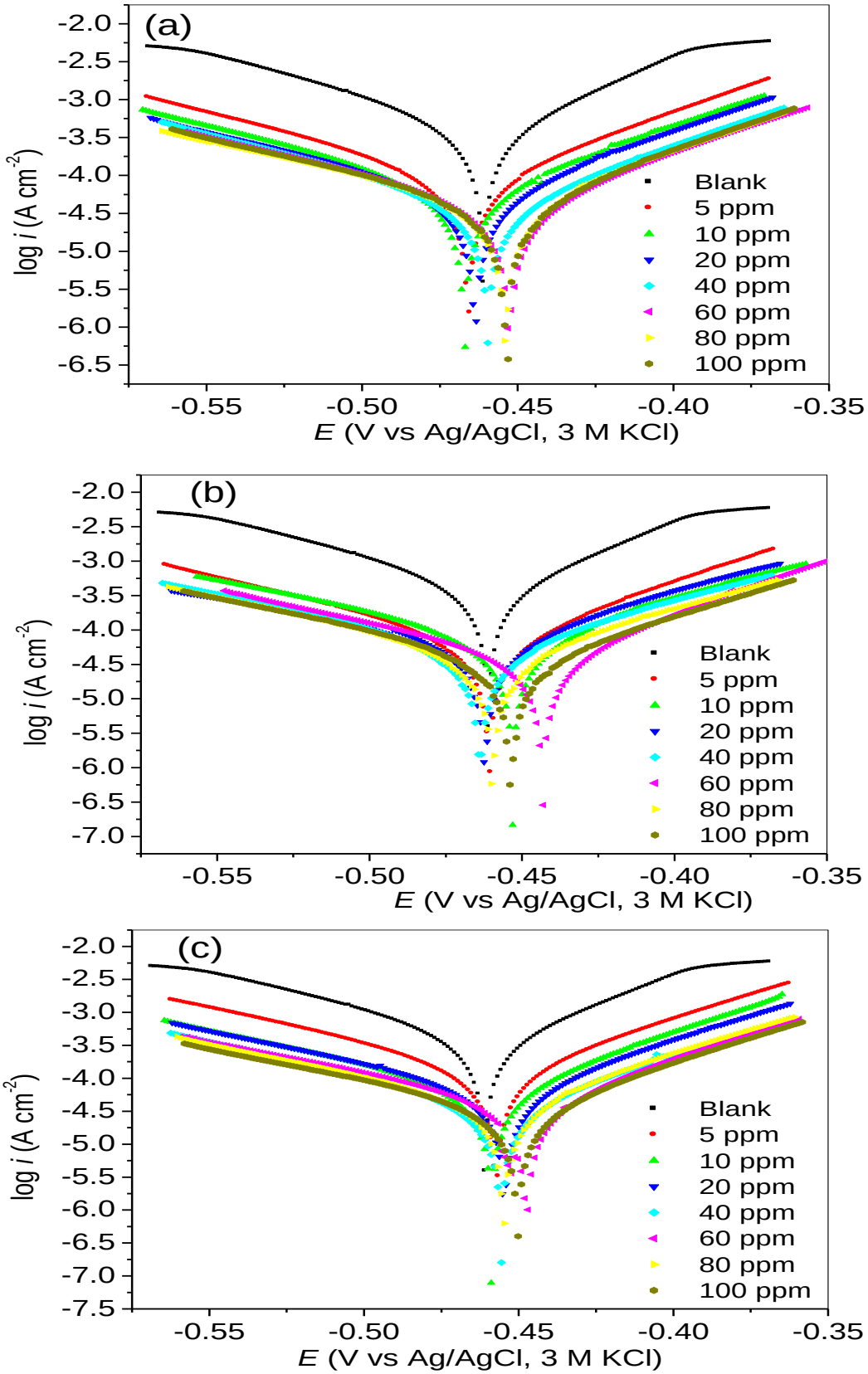

Figure 4.29. Tafel plots for MS in 1 M HCl without and with various concentrations of (a) MS-2-PQPMS, (b) MS-3-PQPMS, and (c) MS-4-PQPMS.

Table 4.22. Tafel parameters and percentage inhibition efficiency for the corrosion of MS in 1 M HCl without and with inhibitors.

Compound	*Conc.* (ppm)	$-E_{corr}$ (mV)	i_{corr} (μA/cm^2)	β_a (mV/dec)	β_c (mV/dec)	$\%IE_P$
Blank	-	460.60	420.41	89.34	65.27	-
	5	465.56	89.66	94.52	73.95	78.66
	10	467.08	64.91	96.26	74.48	84.55
MS-2-PQPMS	20	461.70	59.02	106.98	76.13	85.96
	40	459.43	42.86	98.11	75.83	89.80
	60	452.64	42.62	111.11	74.89	89.86
	80	453.96	45.89	120.66	77.68	89.08
	100	453.77	45.36	114.33	74.23	89.20
	5	460.43	69.86	97.47	70.14	83.38
	10	455.11	55.91	96.89	62.17	86.70
MS-3-PQPMS	20	451.55	62.18	111.60	74.69	86.23
	40	463.79	61.68	115.64	95.61	85.32
	60	443.09	42.83	115.71	67.38	89.81
	80	459.91	48.15	111.61	91.19	88.54
	100	454.09	41.20	109.76	84.44	90.20
	5	456.99	131.53	96.36	71.75	68.70
	10	458.81	70.27	104.07	67.77	83.28
MS-4-PQPMS	20	454.72	69.87	109.05	71.62	83.37
	40	455.70	44.17	104.41	75.84	89.49
	60	447.36	45.38	115.74	70.34	89.20
	80	454.99	45.19	110.94	73.80	89.25
	100	450.79	38.47	115.60	72.06	90.84

blank. The variation in the values of the Tafels slopes with change in the concentration of the inhibitors also seems more apparent for the β_a than β_c. These observations suggest the formation of some inhibitor complexes of Fe in the low and higher oxidation states on the MS electrode surface [243, 247], and also corroborate the more inhibitive actions of the compounds on the anodic reaction than the cathodic one.

The values of the i_{corr} decrease with increasing concentrations of the inhibitors, leading to increase in $\%IE_P$. This implies that the studied compounds inhibit MS corrosion in the acid possibly via the formation of adsorbed film of the inhibitor molecules on the steel surface. The $\%IE_P$ of MS-2-PQPMS increases with increasing concentration of the inhibitor from

78.66 % at 5 ppm up to 89.86 % at 60 ppm. Further increase in concentration beyond this point does not make any significant difference in the value of $\%IE_P$. It is noteworthy that the values of $\%IE_P$ appears seemingly constant from 40 ppm to 100 ppm. In other words, the values of the $\%IE_P$ within this concentration range are not significantly different within the limit of experimental errors.

The $\%IE_P$ for MS-3-PQPMS increases from 83.38 % at 5 ppm to 90.20 % at 100 ppm. The values of $\%IE_P$ between 60 ppm and 100 ppm are very close. The $\%IE_P$ for MS-4-PQPMS ranges from 68.70 % at 5 ppm to 90.84 % at 100 ppm. It is obvious that the values of $\%IE_P$ remain relatively the same between 40 ppm and 100 ppm.

The overall performance based on the average values of $\%IE_P$ within the concentration range considered in this work is MS-3-PQPMS (87.17 %) > MS-2-PQPMS (86.73 %) > MS-4-PQPMS (84.88 %).

4.4.1.2 EIS measurements

The Nyquist and Bode plots for MS in 1 M HCl in the absence and presence of various concentrations of MS-2-PQPMS are shown in Figures 4.30. The same plots are shown in Figures AIV-1 and AIV-2 (Appendix IV) for MS-3-PQPMS and MS-4-PQPMS respectively. The plots show similar behaviour in the absence and presence of the inhibitors, suggesting that addition of the compounds to the corrosive acid medium does not change the corrosion mechanism [8, 90, 285]. The Nyquist plots show single depressed semicircles with their centres below the real impedance axis over the frequency range studied. The Bode plots show single time constant, which implies that the corrosion process involves single charge transfer reaction.

The diameters of the Nyquist semicircles in the presence of the inhibitors are generally larger than that of the uninhibited system indicating larger electrochemical impedance for the

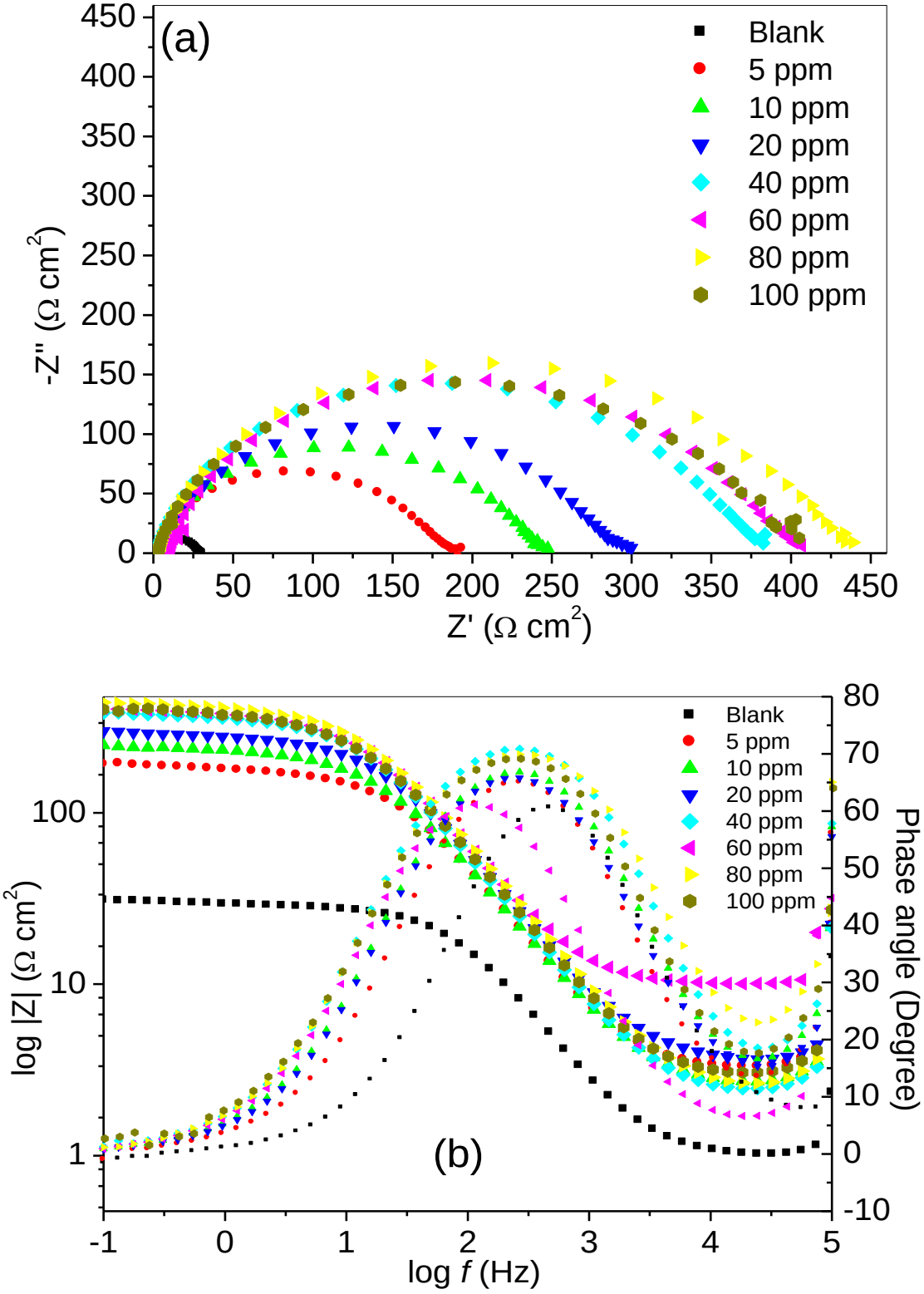

Figure 4.30. Nyquist (a) and Bode (b) plots for MS in 1 M HCl without and with various concentrations of MS-2-PQPMS.

MS/electrolyte system in presence of the inhibitors than the uninhibited blank system. The larger impedance in the presence of inhibitors is an indication of anticorrosion characteristics of the studied compounds. The EIS spectra were fitted to the $R_s(R_{ct}Q)$ equivalent circuit model and the predicted EIS spectra data are presented in Table 4.23. The R_s values at various concentrations of the inhibitors do not show a uniform trend, but the values are generally larger for the inhibitor-containing systems than the blank, suggesting that the relative conductivity of the electrochemical system is reduced by the inhibitor molecules. This can be attributed to the reduction in the number of migrating ions in the system as a result of the adsorption of the inhibitor molecules on the steel surface. This also reduces the steel dissolution in the acid [191].

The R_{ct} values are higher for the inhibitor-containing systems than the blank, which implies that the resistance of the steel/electrolyte systems to the charge transfer process is enhanced by the inhibitor molecules. These observations are attributable to the formation of protective film of the inhibitor molecules on the steel surface. The protective film of the inhibitor reduces direct contact of the steel with the aggressive acid solution. All the studied compounds show appreciable values of $\%IE_I$ even at the lowest concentration of 5 ppm. The $\%IE_I$ values for MS-2-PQPMS increases from 84.21 % (at 5 ppm) to a maximum value of 93.93 % (at 80 ppm), while the values for MS-3-PQPMS range from 87.73 % to 93.39 % (i.e. 5 ppm to 100 ppm), and the $\%IE_I$ values for MS-4-PQPMS range from 69.25 % (at 5 ppm) to 94.00 % (at 100 ppm). All the studied compounds showed $\%IE_I$ of about 93 % at 40 ppm. Based on the average values of $\%IE_I$ over the studied concentration range, it can be inferred that the order of inhibition efficiency of the compounds follows: MS-3-PQPMS (91.31 %) > MS-2-PQPMS (90.44 %) > MS-4-PQPMS (88.24 %), which is in agreement with the results obtained from the polarization measurements.

Table 4.23. EIS parameters and percentage inhibition efficiency for the corrosion of MS in 1 M HCl without and with various concentrations of the inhibitors.

Compound	*Conc.* (ppm)	R_s (Ωcm^2)	R_{ct} (Ωcm^2)	Y_o ($\mu Ss^n cm^{-2}$)	*N*	$\lvert\Theta\rvert$ (Degree)	$\lvert S\rvert$	$\%IE_I$
Blank	-	1.01	28.20	157	0.893	60.59	0.64	-
MS-2-PQPMS	5	3.17	178.00	71.98	0.874	65.00	0.77	84.21
	10	2.54	234.00	80.85	0.856	66.83	0.78	87.99
	20	3.48	282.00	66.75	0.854	65.80	0.78	90.04
	40	2.28	365.00	61.56	0.874	70.86	0.83	92.30
	60	2.43	378.00	57.82	0.868	61.08	0.76	92.57
	80	2.33	420.00	60.00	0.854	69.91	0.81	93.30
	100	2.80	384.00	64.90	0.861	69.37	0.82	92.68
MS-3-PQPMS	5	2.26	229.00	63.24	0.876	66.96	0.79	87.73
	10	3.07	247.00	71.63	0.864	52.03	0.64	88.62
	20	2.18	293.00	61.80	0.869	57.24	0.72	90.41
	40	3.20	401.00	54.66	0.875	54.42	0.67	92.99
	60	2.85	395.00	55.67	0.873	70.17	0.83	92.89
	80	2.51	409.00	67.47	0.855	69.67	0.82	93.13
	100	2.52	425.00	64.50	0.857	69.91	0.82	93.39
MS-4-PQPMS	5	2.96	91.39	92.84	0.895	61.79	0.75	69.25
	10	1.98	214.00	67.38	0.869	68.82	0.79	86.87
	20	2.74	256.00	68.93	0.872	67.70	0.80	89.02
	40	2.38	387.00	50.28	0.885	71.81	0.84	92.74
	60	2.59	393.00	56.88	0.872	70.41	0.82	92.85
	80	2.68	398.00	61.72	0.876	70.81	0.83	92.94
	100	2.41	468.00	59.06	0.869	71.39	0.84	94.00

The values of Y_0 (in Table 4.23) do not follow a uniform trend but lower values are generally recorded for the inhibitor-containing systems compared to the blank, which indicates that the molecules of the studied compounds adsorbed on the steel surface to form a protective layer. The values of the CPE exponent, *n* are close to unity, which implies that the electrode interface exhibits pseudocapacitive behaviour. The relatively lower values of *n* for the inhibitor-containing systems compared to the blank is an indication of a more homogeneous surface of the MS electrode, which is adequately covered by the adsorbed inhibitor molecules.

The values of $|\theta|$ and $|S|$ are also listed in Table 4.23 and results show that $|\theta|$ is closer to 90^0, while $|S|$ is closer to 1 in the presence of the inhibitors compared to the blank. Though the values of $|\theta|$ at some concentrations (10 ppm – 40 ppm) of MS-3-PQPMS are lower than that of blank, the corresponding values of $|S|$ for this compound at the same concentrations are still closer to unity than the value for the blank. These observations suggest that the electrode/electrolyte interface behaves closer to an ideal capacitor in the presence of the inhibitors than the blank. This also implies that the inhibitor molecules adsorbed on the steel surface to form a protective film with some levels of capacitive characteristics. Similar observations were reported for the GROUP III compounds (*vide supra* Section 4.3.1.2).

4.4.2 Adsorption isotherms

The experimental data were found to suitably fit the Langmuir adsorption isotherm model as the plots of C/θ versus C (Figure 4.31) show straight lines with correlation coefficient (R^2) values of 1.000. The near unity values of the slopes i.e. 1.07 (MS-2-PQPMS), 1.07 (MS-3-PQPMS), and 1.05 (MS-4-PQPMS) also support the conformation of the experimental data with the Langmuir adsorption isotherm.

The values of K_{ads} and ΔG_{ads} obtained from the Langmuir isotherms are listed in Table 4.24. The high values of K_{ads} imply that the adsorption of the inhibitor molecules on the steel surface and the displacement of water molecules is a favourable process. It can also be inferred that the inhibitors adsorb strongly on the steel surface. The negative values of ΔG_{ads} connote spontaneous adsorption of the inhibitor molecules on the steel surface. The magnitudes of ΔG_{ads} obtained for the studied compounds are greater than 40 kJ/mol, suggesting the adsorption of these compounds on MS surface in 1 M HCl proceeds via chemisorption mechanism. The magnitudes of the values of K_{ads} and ΔG_{ads} for the studied

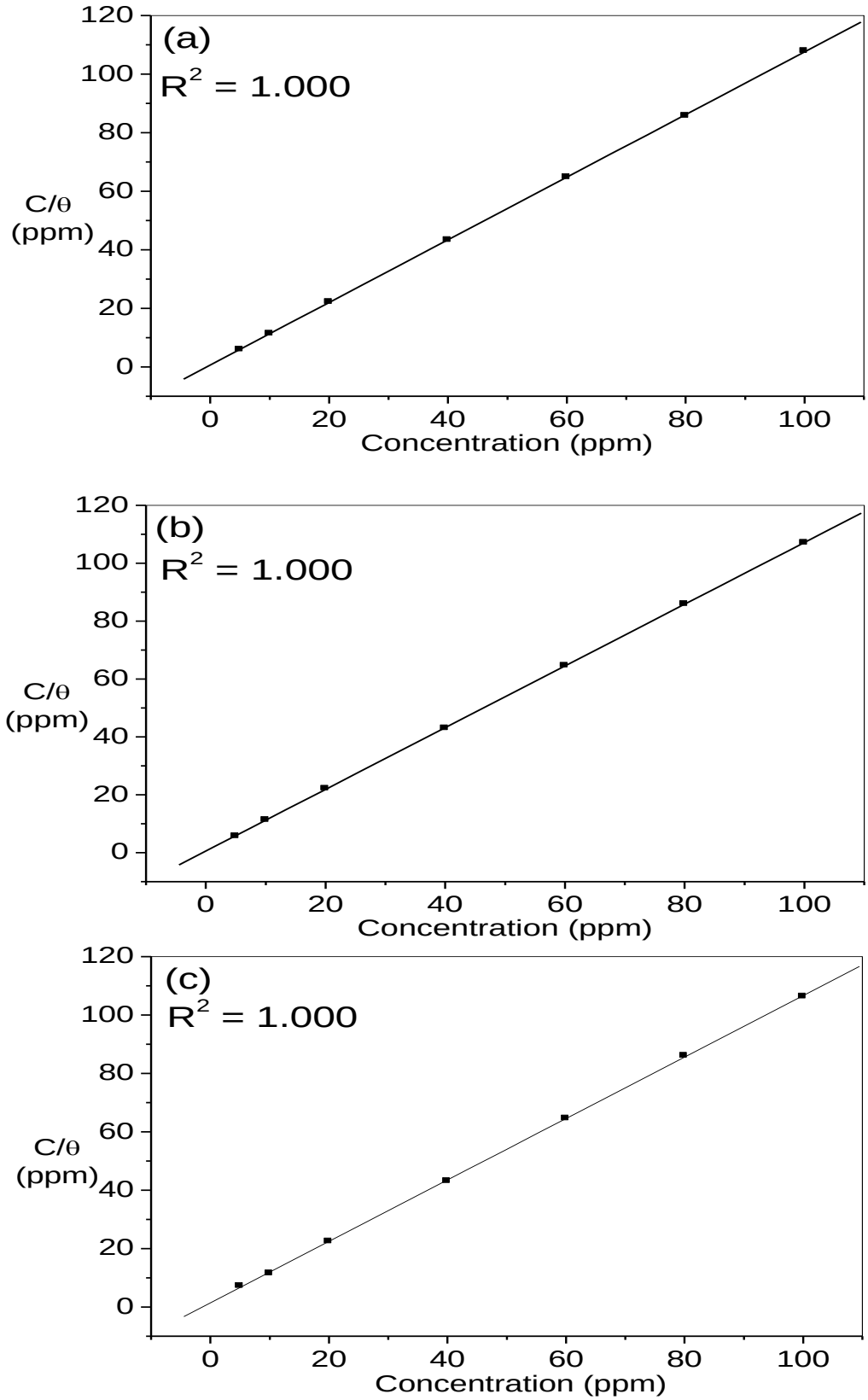

Figure 4.31. Langmuir adsorption isotherms for (a) MS-2-PQPMS, (b) MS-3-PQPMS, and (c) MS-4-PQPMS on MS in 1 M HCl. (*Experimental data were taken from the EIS measurements*).

compounds follow the trend: MS-3-PQPMS > MS-2-PQPMS > MS-4-PQPMS, which is the same as the relative order of the *%IE*.

Table 4.24. Thermodynamic parameters for the adsorption of the studied compounds on MS in 1 M HCl at 303.15 K.

Inhibitor	K_{ads} (x10^3)	$-\Delta G_{ads}$ (kJ/mol)
MS-2-PQPMS	692.90	44.02
MS-3-PQPMS	791.10	44.35
MS-4-PQPMS	311.69	42.01

4.4.3 UV-vis spectroscopic analyses

UV-vis spectroscopic analyses were carried out on the solutions of the studied inhibitor molecules and the resulting solutions after MS immersion for 3 hours. The recorded UV-vis spectra are shown in Figure 4.32. MS-2-PQPMS and MS-3-PQPMS show multiple light absorption bands at 208 nm – 209 nm, 240 nm, 273 nm, and 327 nm – 329 nm, which are due to n→π*, π→π* transitions, and intramolecular charge transfers (ICT). MS-4-PQPMS shows bands at 206 nm, 242 nm and 285 nm, which can also be attributed to n→π*, π→π* transitions, and intramolecular charge transfers (ICT) respectively.

Upon MS immersion, MS-2-PQPMS shows additional band at 230 nm, while the band at 240 nm is red-shifted to 244 nm, and those at 273 nm and 327 nm are blue-shifted to 271 nm and 323 nm respectively. For MS-3-PQPMS, the bands at 208 nm and 329 nm shifted to longer wavelengths, appearing at 211 nm and 332 nm respectively, while the one at 273 nm broadens to a shoulder-like band. The band at 206 nm in the UV-vis spectrum of MS-4-PQPMS red-shifted to 210 nm after MS immersion. The spectra of the resulting solutions after MS immersion generally showed higher absorbances than those before steel immersions. All these observations point at the possible interactions between Fe and the inhibitor molecules and formation of Fe-inhibitor complexes.

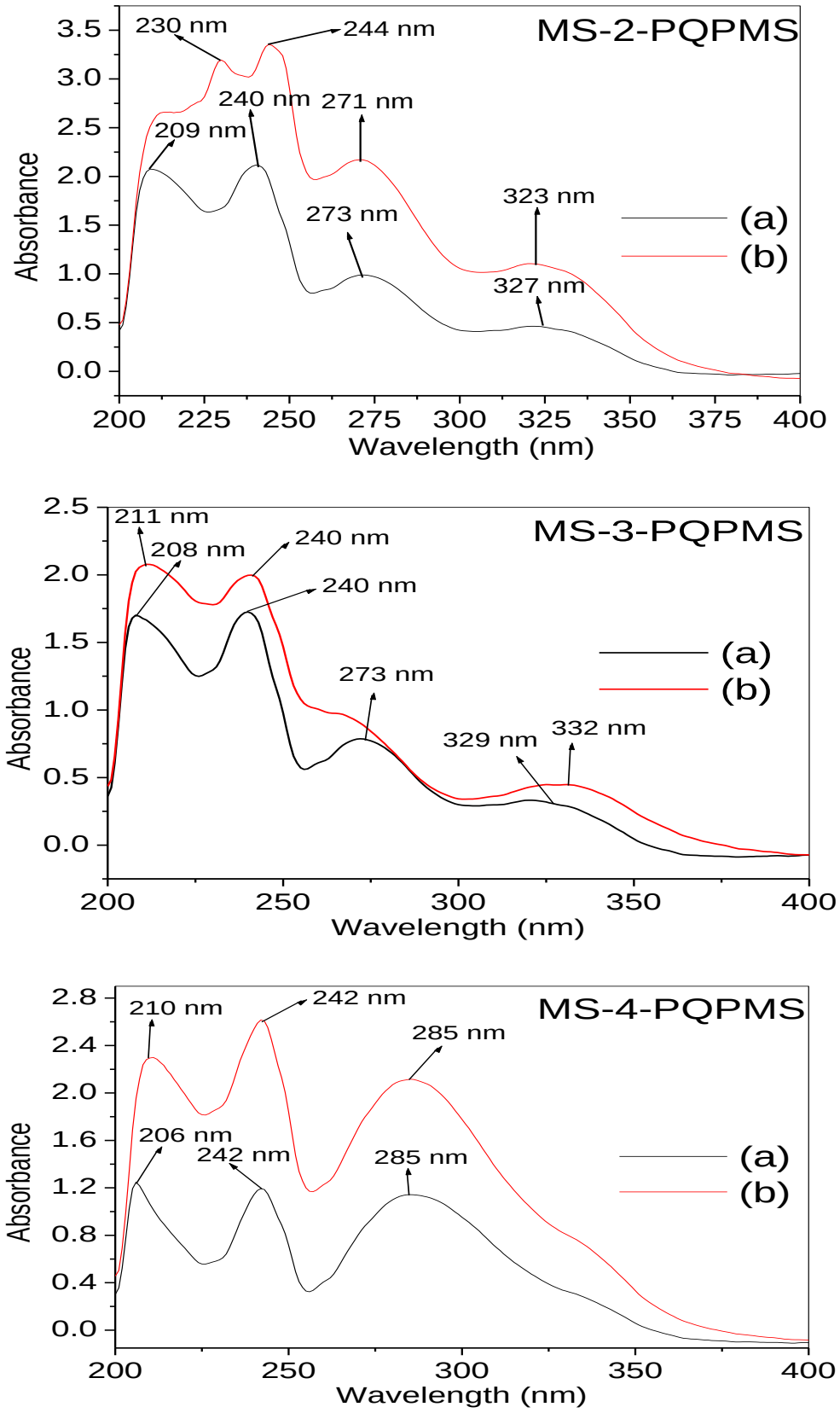

Figure 4.32. UV-vis spectra of the acidic solutions of studied inhibitors **(a)** before, and **(b)** after MS immersion.

4.4.4 Quantum chemical calculations

4.4.4.1 Neutral species

The optimized structures of the neutral molecules of the studied compounds are shown in Figure 4.33. The optimized structures correspond to the true energy minima in the potential well and this was confirmed by the absence of imaginary frequency in the force constant calculations. The corresponding HOMO and LUMO electron density isosurfaces are shown in Figure 4.34. The HOMO electron density is essentially distributed over the entire pyrazole and phenyl rings, while the LUMO comprises mainly the atoms and π-electron systems in the quinoxaline ring. It is also apparent that the O-atoms of the methanesulphonamido group attached to the N-atom of the pyrazole ring also contribute to the HOMO, although the S-atom of the group does not make significant contribution to the HOMO. Apart from the quinoxaline ring, the LUMO of MS-2-PQPMS is slightly extended to the sp^2 N-atom of the pyrazole ring, while that of MS-3-PQPMS involves the π-electron centre of the C=C group adjoining the pyrazole to the phenyl ring, as well as the sp^2 atom of the pyrazole ring and the C-atom of the phenyl ring adjacent to the methanesulphonamido group.

Some reactivity parameters of the neutral molecules were calculated in an attempt to relate them with the observed trend of the %IE of the molecules and the results are listed in Table 4.25. The E_{LUMO} values for the neutral molecules are in the order MS-3-PQPMS < MS-4-PQPMS < MS-2-PQPMS, which is not in total agreement with the observed order of inhibition performance of the molecules but is in support of the highest inhibition performance of MS-3-PQPMS. The E_{HOMO} values also do not correlate with the experimentally observed trend of %IE. Therefore, other parameters derived from the frontier molecular orbital energies might as well not provide adequate description of the order of inhibition performances of the studied compounds. It is however noteworthy that the

electronegativity (χ) values follow the trend: MS-3-PQPMS > MS-2-PQPMS > MS-4-PQPMS, which is in

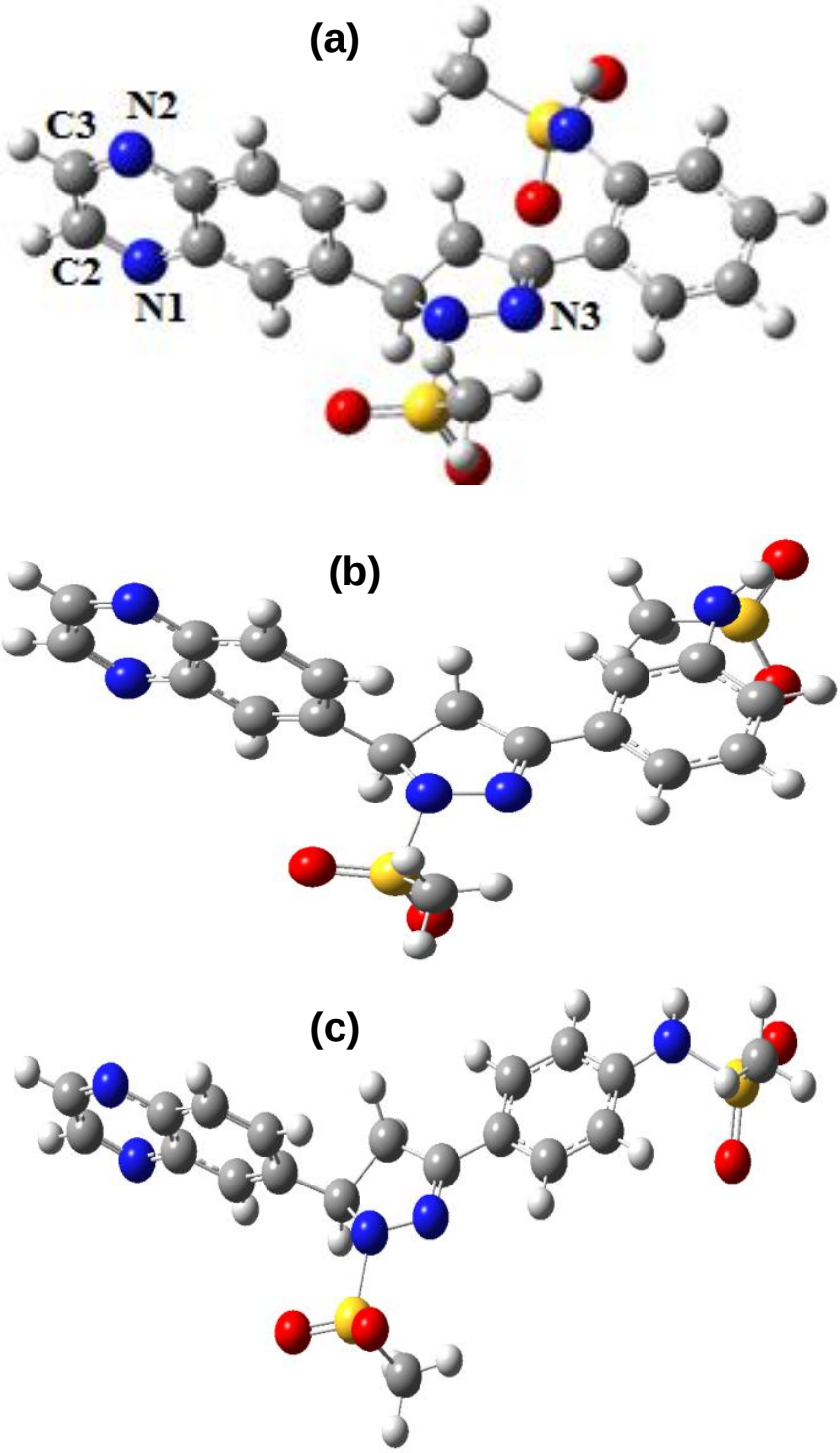

Figure 4.33. Optimized structures of neutral molecules of (a) MS-2-PQPMS, (b) MS-3-PQPMS, and (c) MS-4-PQPMS at B3LYP/6-31G(d) level of theory. (*Atom numbering in (a) were used to refer to the position of the atoms in the discussion of results*).

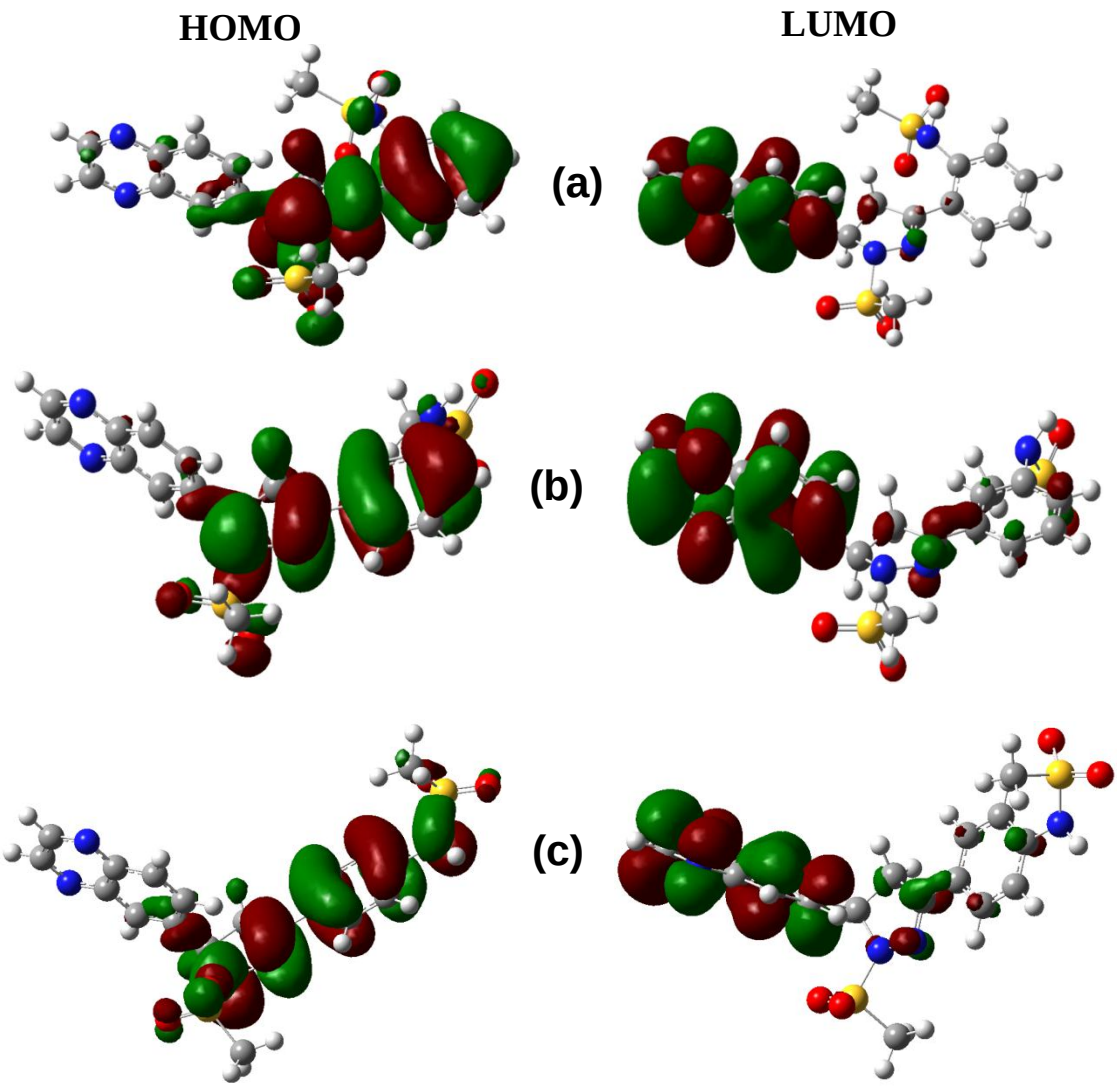

Figure 4.34. HOMO and LUMO electron density isosurfaces of (a) MS-2-PQPMS, (b) MS-3-PQPMS, and (c) MS-4-PQPMS at B3LYP/6-31G(d) level of theory.

agreement with the observed inhibition potential. This observation suggests that the strength of corrosion inhibition of these molecules is somewhat in relation with the relative ability of each molecule to attract electrons from the metal in a retro-donation mechanism during the donor-acceptor interactions that leads to the adsorption of the inhibitor molecules on the steel surface.

The values of ΔN for all the three compounds are less than 3.6, suggesting that the inhibition efficiency of these molecules may increase with increasing electron-donating ability of the molecules. In corollary to this inference, and since ΔN is a measure of number of electrons transferred from the inhibitor molecule to the metal, the relative values of ΔN, i.e. MS-3-PQPMS < MS-2-PQPMS < MS-4-PQPMS may imply that the molecule with the least electron-donating ability, or perhaps highest electron-acceptance capacity has the highest inhibition efficiency and the observed results of %IE from the experiments do align with the values of ΔN in this respect. No direct correlation could be made of the values of the dipole moment of the neutral molecules with the observed %IE. This observation is not unpopular in corrosion inhibition studies as earlier highlighted in some previous sections of this thesis.

Investigations of the prominent atomic sites or centres for nucleophilic and electrophilic attacks that might occur during the donor-acceptor interactions between the inhibitor molecules and MS were carried out using the Fukui functions. The Fukui indices f^+ and f^- associated with the centres for nucleophilic and electrophilic attacks respectively in the inhibitor molecules were calculated and visualized as graphical images in Figure 4.35. The

Table 4.25. Quantum chemical parameters for the neutral molecules of MS-2-PQPMS, MS-3-PQPMS, and MS-4-PQPMS at B3LYP/6-31G(d) level of theory.

Parameter	MS-2-PQPMS	MS-3-PQPMS	MS-4-PQPMS
E_{LUMO} *(eV)*	-1.974	-2.051	-1.981
E_{HOMO} *(eV)*	-6.329	-6.444	-6.004
$\Delta E_{L\text{-}H}$ *(eV)*	4.355	4.393	4.023
χ *(eV)*	4.152	4.248	3.993
η *(eV)*	2.178	2.196	2.012
ΔN	0.654	0.626	0.748
Dipole moment (Debye)	5.930	3.641	1.049

prominent sites for nucleophilic attack are found on the quinoxaline ring, involving the two N-atoms in the ring and the π-electron centre around the C2=C3 group in the quinoxaline ring. Other prospective sites for nucleophilic attack in the molecules include the sp^2 N-atom in the pyrazole ring and the π-electron centre between the two C-atoms connecting the pyrazole and phenyl rings. One or two C-atoms on the phenyl ring might also be involved in nucleophilic attacks, indicating the electron deficient attributes of some C-atoms in the phenyl ring especially the one that is directly attached to the methanesulphonamido group.

The electron density distributions for f^- for the studied compounds reveal that the most prominent sites for electrophilic attacks are the N-atoms of the pyrazole ring. In MS-2-PQPMS, the phenyl C-atom attached to the methanesulphonamido group and the one at beta

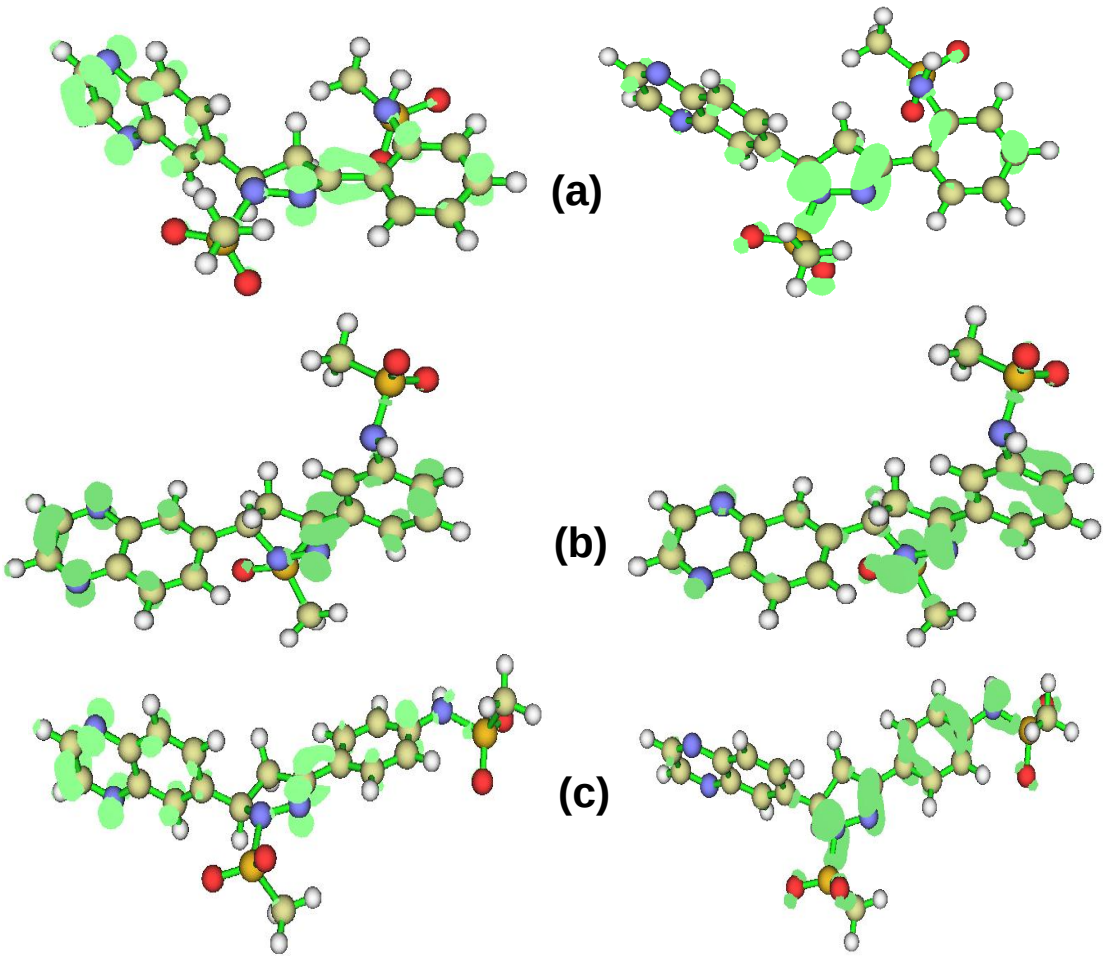

Figure 4.35. Fukui functions, f^+ (left-hand side) and f^- (right-hand side) for (a) MS-2-PQPMS, (b) MS-3-PQPMS, and (c) MS-4-PQPMS. (*Isosurface = 0.003*).

position to it might also be involved in electrophilic attacks. Similarly in MS-3-PQPMS and MS-4-PQPMS, the π-electron centres around the C-atoms in the phenyl ring, especially the one directly attached to the methanesulphonamido group and the one at alpha position relative to it may also participate in electrophilic attacks. The N, O, and S heteroatoms of the methanesulphonamido groups in the studied molecules do not appear to be promising sites for nucleophilic and electronic attacks but rather tune the electronic properties of the atoms or groups or centres around them.

4.4.4.2 Protonated species

Since the studied molecules contain prospective sites for protonation in acidic medium, theoretical investigations of the propensity of these sites to protonation and the most probable sites of protonation in each molecule were conducted. Proton affinity (PA) and gas-phase basicity (GB) were calculated as discussed in the earlier parts of this thesis and the results are presented in Table 4.26. The values of PA and GB for MS-2-PQPMS indicate that the N3-atom (i.e. the sp^2 N-atom in the pyrazole ring) is the most probable site of protonation. However, the N1 and N2 on the quinoxaline ring may also under protonation as their PA and GB values are close to that of N3. This suggests the possibility of having different protonated species of this molecule in acidic medium. The prominent site of protonation in MS-3-PQPMS is the N1-atom of the quinoxaline ring, followed by the N2 atom, and the N3-atom may not be favourably protonated. The most promising site of protonation in MS-4-PQPMS is N1, followed by N2 and N3.

Attempts were made to correlate the reactivity indices of prospective protonated species with the observed %IE of the studied molecules. The quantum chemical reactivity parameters of the most stable protonated species are listed in Table 4.27. The results show that MS-3-PQPMS-$H^+_{(N1)}$ (the most probable protonated form of MS-3- PQPMS) has a higher E_{HOMO}, a

lower E_{LUMO}, and a lower ΔE_{L-H} than MS-2-PQPMS-$H^+_{(N3)}$ (the most probable protonated form of MS-2-PQPMS), which supports its higher inhibition performance observed in the

Table 4.26. Proton affinity (PA) and gas-phase basicity (GB) of the sites of protonation in MS-2-PQPMS, MS-3-PQPMS, and MS-4-PQPMS at B3LYP/6-31G(d) level of theory.

	PA (kJ/mol)/Protonation site			*GB* (kJ/mol)/Protonation site		
Compound	N1	N2	N3	N1	N2	N3
MS-2-PQPMS	947.12 (-1.16)	940.87 (-7.40)	948.28 (0)	978.79 (-2.04)	973.05 (-7.78)	980.83 (0)
MS-3-PQPMS	945.57 (0)	943.14 (-2.42)	929.86 (-15.74)	976.50 (0)	973.66 (-2.84)	959.58 (-16.93)
MS-4-PQPMS	947.57 (0)	944.76 (-2.81)	935.19 (-12.39)	982.99 (0)	980.76 (-2.23)	971.10 (-11.89)

In parentheses: ΔPA = *PA* (less stable) – *PA* (most stable); ΔGB = *GB* (less stable) – *GB* (most stable)

Table 4.27. Quantum chemical parameters for the most stable protonated forms of (a) MS-2-PQPMS, MS-3-PQPMS, and MS-4-PQPMS at B3LYP/6-31G(d) level of theory.

Parameter	MS-2-PQPMS-$H^+_{(N3)}$	MS-3-PQPMS-$H^+_{(N1)}$	MS-4-PQPMS-$H^+_{(N1)}$
E_{LUMO} *(eV)*	-6.123	-6.971	-6.971
E_{HOMO} *(eV)*	-9.216	-8.280	-8.041
ΔE_{L-H} *(eV)*	3.093	1.309	1.070
χ *(eV)*	7.670	7.625	7.506
η *(eV)*	1.547	0.654	0.535
ΔN	-0.217	-0.478	-0.473
Dipole moment (Debye)	6.501	15.592	19.579

experimental studies. The higher inhibition strength of MS-2-PQPMS compared to MS-4-PQPMS cannot be directly correlated with the quantum chemical parameters in Table 4.27. However, since MS-2-PQPMS has a chance of getting protonated at three different sites, there is possibility of having different protonated species in the acid i.e. MS-2-PQPMS-$H^+_{(N1)}$, MS-2-PQPMS-$H^+_{(N2)}$ and MS-2-PQPMS-$H^+_{(N3)}$. It was observed (but not shown in

Table 4.27) that other possible protonated species of MS-2-PQPMS, i.e. MS-2-PQPMS-$H^{+}_{(N1)}$ and MS-2-PQPMS-$H^{+}_{(N2)}$ have lower E_{LUMO}: -7.0211 eV and -7.065 eV respectively, and higher electronegativity, χ: 7.833 eV and 7.815 eV than all the prospective protonated species of MS-4-PQPMS i.e. MS-4-PQPMS-$H^{+}_{(N1)}$ (Table 4.27) and MS-4-PQPMS-$H^{+}_{(N2)}$ (E_{LUMO} = -7.004 eV, χ = 7.501 eV), indicating that the protonated species of MS-2-PQPMS have better propensity for electron acceptance than those of MS-4-PQPMS and this might contribute to the higher inhibition performance of MS-2-PQPMS than MS-4-PQPMS.

4.4.5 Molecular dynamic (MD) simulations

The interactions of the studied (GROUP IV) compounds with clean Fe (110) surface were modelled with MD simulations and the respective lowest energy configurations of the inhibitor/Fe (110) systems are shown in Figure 4.36. All the three compounds adopt flat orientation during the interactions with Fe (110) surface indicating that the heteroatoms and pi-electrons in the inhibitor molecules will interact optimally with the atomic Fe. The interaction and binding energies for the inhibitor/Fe (110) systems are listed Table 4.28. The order of the binding energies is MS-3-PQPMS/Fe (110) > MS-2-PQPMS/Fe (110) > MS-4-PQPMS/Fe (110), which is in agreement with the order of inhibition efficiencies recorded from the experiments.

Table 4.28. Selected energy parameters for the adsorption of the studied inhibitors on Fe (110) surface (in kJ/mol)

System	Interaction energy	Binding energy
Fe (110) + MS-2-PQPMS	-868.230	868.230
Fe (110) + MS-3-PQPMS	-877.046	877.046
Fe (110) + MS-4-PQPMS	-846.833	846.833

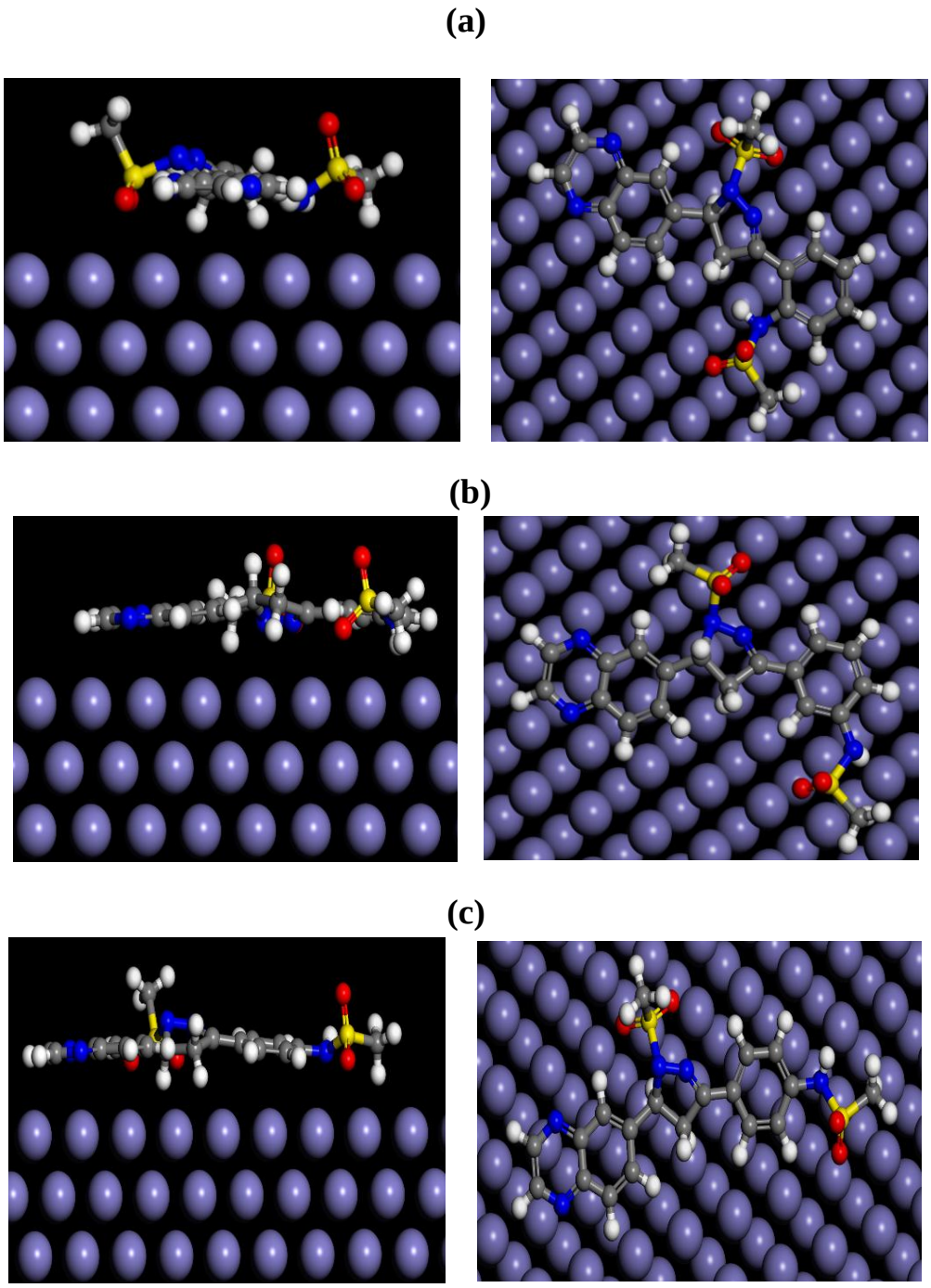

Figure 4.36. Side (left hand side) and top (right hand side) views of the most stable configurations of (a) MS-2-PQPMS, (b) MS-3-PQPMS and (c) MS-4-PQPMS interactions with Fe (110) using molecular dynamics simulations.

4.5 GROUP V: Mt-3-PQPP, Cl-4-PQPP, MS-2-PQPA, and MS-4-PQPA

The Group V comprises four compounds as listed in Table 3.5. All the four compounds have the 5-(quinoxalin-6-yl)-4,5-dihydropyrazol-1-yl group, however, Mt-3-PQPP and Cl-4-PQPP both have a propanol group attached to position 1 on the pyrazole ring and only differ in the functional groups and the position of the functional groups attached to the phenyl ring, i.e. 3-methoxyphenyl (for Mt-3-PQPP) and 4-chlorophenyl (for Cl-4-PQPP). On the other hand, MS-2-PQPA and MS-4-PQPA are similar, as they both contain an ethanol group attached to the position 1 on the pyrazole ring and a methanesulfonamido group attached to the phenyl ring, and only differ in the position of the methanesulfonamido group that is directly attached to the phenyl ring. Therefore, comparative adsorption and corrosion inhibition behaviour of these compounds is better explained by comparing Mt-3-PQPP and Cl-4-PQPP separately, and MS-2-PQPA and MS-4-PQPA separately.

An “inter-group” comparison can also be made by comparing the anticorrosion properties of Mt-3-PQPP and Cl-4-PQPP with PQDPP (in Group II) in which the phenyl group has no substituent. In this regard, the effect of methoxy and chloro substituents on the corrosion inhibition potentials of PQDPP can be investigated. Another “cross-group" comparison can also be established by comparing the adsorption and inhibition characteristics of MS-2-PQPA and MS-4-PQPA MS-2-PQPP and MS-4-PQPP respectively (in Group III) in order to investigate the effect of chain length of the carbonyl functional group on the adsorption and corrosion inhibition properties. The molecular structures, formulas and weights of Mt-3-PQPP, Cl-4-PQPP, MS-2-PQPA, and MS-4-PQPA compounds are already listed in Table 3.5.

4.5.1 Electrochemical studies

4.5.1.1 Tafel plots

The representative Tafel plots for the corrosion of MS in 1 M HCl without and with various concentrations of the GROUP V compounds are shown in Figure 4.37 for Mt-3-PQPP and MS-2-PQPA. The Tafel curves for the other two compounds shown similar patterns and are shown in Figure AV-1 (Appendix V). The curves clearly exhibit lower current density in the presence of the inhibitors compared to the blank, indicating that the studied compounds reduce the corrosion current density for MS in 1 M HCl and thereby reduce the corrosion rate.

An apparent feature of the polarization curves in the presence of Mt-3-PQPP is the parallel anodic lines of successively lower current density with increasing concentration of the inhibitor. The polarization curves for all the four compounds show nearly parallel anodic and cathodic lines with similar current-potential profiles. These observations imply that the studied compounds inhibit steel corrosion by merely adsorbing on the active sites for the anodic and cathodic half-reactions associated with the corrosion process without changing the mechanism of corrosion. The adsorbed inhibitor molecules decrease the surface area available for the corrosion reactions thereby reducing the corrosion rate [292-294].

The current-potential curves for the inhibitors appear at relatively more cathodic or anodic potentials compared to the blank indicating that the adsorption of the inhibitor molecules on the steel surface modifies the propensity of MS to corrosion reaction. The polarization curves for Mt-3-PQPP, Cl-4-PQPP, and MS-2-PQPA shift to more anodic potentials relative to the blank at higher concentrations (80 ppm and 100 ppm) of the inhibitors, while the Tafel curves for MS-4-PQPA over the entire concentration range (except at 10 ppm) appear at farther anodic potentials than the blank.

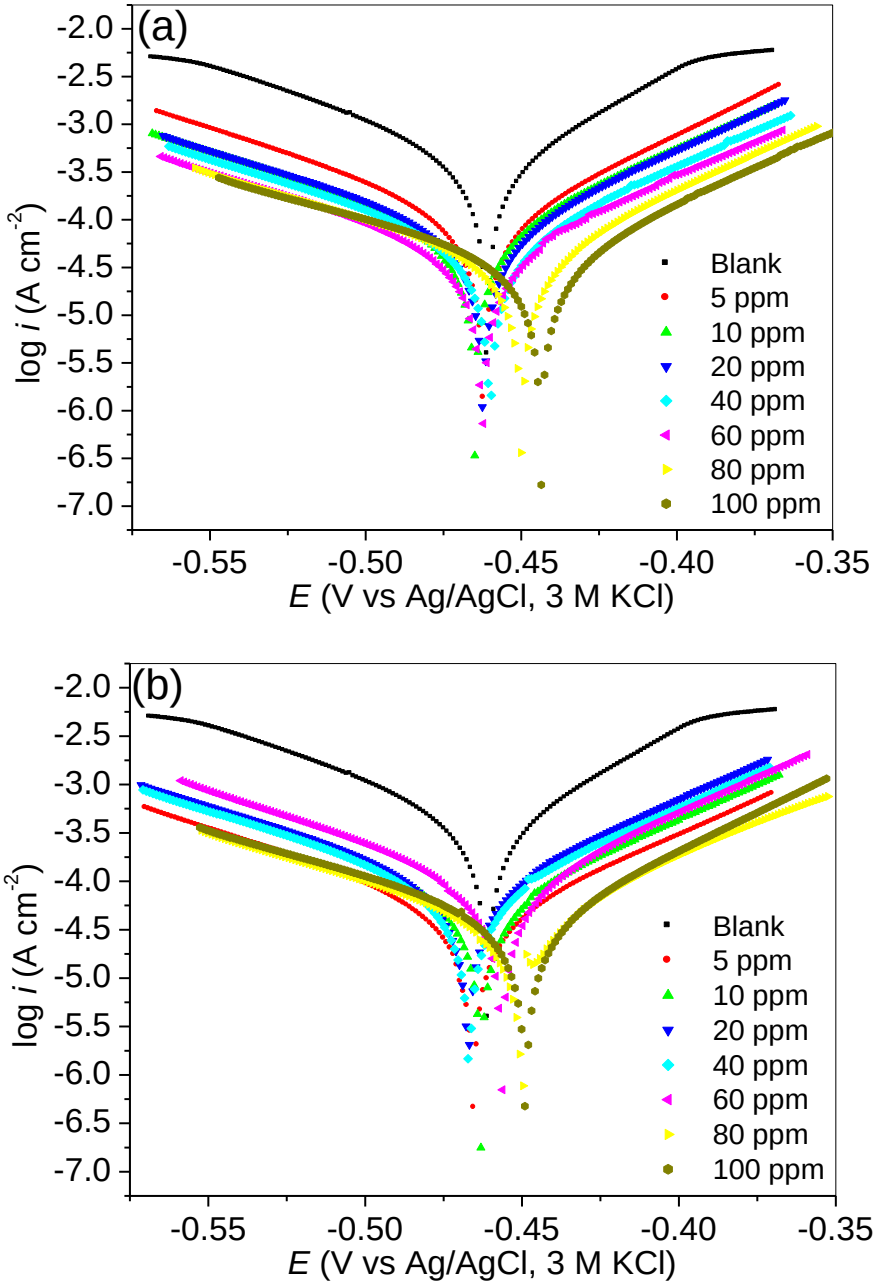

Figure 4.37. Tafel plots for MS in 1 M HCl without and with various concentrations of (a) Mt-3-PQPP and (b) MS-2-PQPA.

Tafel parameters obtained for the compounds are listed in Table 4.29 for both Mt-3-PQPP and MS-2-PQPA. Table AV-1 (Appendix V) shows the complete list of Tafel parameters for the four compounds. The relative shift in E_{corr} for all the studied compounds (compared to the blank) over the entire concentration range is not up to 85 mV indicating that the compounds inhibit both anodic MS dissolution and cathodic hydrogen gas evolution

reactions of the corrosion process and are thus mixed-type inhibitors. The small shift in potentials observed for these compounds may also infer non-perturbative or weakly perturbative adsorption of the inhibitors on the MS electrode surface [290], and the geometric blocking of the active sites on the steel surface by the inhibitor molecules [291, 295]. A comparison of the E_{corr} values for Mt-3-PQPP and Cl-4-PQPP reveals that the former exhibits nobler anodic potentials than the latter and this is attributed to the presence of the highly electron-donating $–OCH_3$ group in Mt-3-PQPP, which promotes its adsorption on the steel surface via effective forward charge donation from the inhibitor to the appropriate vacant orbitals of the metal.

The values of the Tafel slopes, β_a and β_c are not significantly affected by the addition of the inhibitors, which also suggests that the inhibitors do not alter the mechanism of corrosion reaction. The possible reasons for the slight deviations of the Tafel slopes of the inhibitor-containing systems from the blank values have been discussed in the previous section (*vide supra* Section 4.1.1.2). It is noteworthy that the slight change in the values of β_a and β_c at various concentrations of the inhibitors appear more apparent for the anodic reactions than the corresponding cathodic counterpart at the same concentration. This suggests that the inhibitive effects of the studied compounds are more effective on the anodic MS dissolution than the cathodic hydrogen evolution reaction.

The i_{corr} values for Mt-3-PQPP decrease with increasing concentration of the inhibitor, while those of Cl-4-PQPP decrease to a minimum at 60 ppm, and later increases. The i_{corr} values for MS-2-PQPA do not give a uniform trend with change in concentration, those of MS-4-PQPA decrease with increasing concentration and reach a minimum at 80 ppm. As expected from the i_{corr} values, the $\%IE_P$ of Mt-3-PQPP increases with increasing concentration, while the $\%IE_P$ of Cl-4-PQPP reaches an optimum value at 60 ppm and

Table 4.29. Tafel parameters and percentage inhibition efficiency for the corrosion of MS in 1 M HCl without and with inhibitors.

Compound	*Conc.* (ppm)	$-E_{corr}$ (mV)	i_{corr} (μA/cm^2)	β_a (mV/dec)	β_c (mV/dec)	$\%IE_P$
Blank	-	460.60	420.41	89.34	65.27	-
Mt-3-PQPP	5	461.81	95.25	89.20	68.01	77.34
	10	464.85	73.30	100.05	72.61	82.56
	20	462.23	72.53	101.48	70.28	82.75
	40	460.05	55.78	101.31	71.90	86.73
	60	462.49	45.46	104.27	75.70	89.19
	80	449.97	41.78	117.85	69.82	90.06
	100	443.66	40.85	132.42	72.42	90.28
MS-2-PQPA	5	465.04	45.25	93.78	78.28	89.24
	10	463.06	68.29	95.54	76.14	83.76
	20	467.18	89.35	99.18	73.79	78.75
	40	466.87	79.20	99.37	76.04	81.16
	60	456.37	92.02	96.05	72.85	78.11
	80	450.02	47.57	128.98	79.52	88.68
	100	448.86	45.53	119.50	70.83	89.17

decreases thereafter. This was not observed for Mt-3-PQPP over the range of concentrations studied.

Although, the reason(s) for the undulating $\%IE_P$ for MS-2-PQPA could not be verified as at the time of writing this report, the behaviour might be due to the position of the methanesulphanamido group on the phenyl ring (position 2), which may have irregular contributions to the intermolecular steric repulsions depending on the orientations of the inhibitor molecules relative to each other. The $\%IE_P$ for MS-4-PQPA increases with increasing concentration and attained the highest value 89.81 % at 80 ppm. The values of $\%IE_P$ for MS-4-PQPA between 60 ppm and 100 ppm are not significantly different.

4.5.1.2 EIS measurements

The Nyquist and Bode plots for MS in 1 M HCl without and with various concentrations of Mt-3-PQPP and MS-2-PQPA are shown in Figures 4.38 and 4.39 respectively. The same plots for Cl-4-PQPP and MS-4-PQPA are shown in Figures AV-2 and

AV-3 (Appendix V) respectively. The Nyquist plots show single depressed semicircles corresponding to one time constant in the Bode plots. This suggests that the dissolution of MS electrode in the studied electrolytes is controlled by a single charge transfer process. The depression of the Nyquist semicircles is a common characteristics of solid electrodes and has been explained in the previous sections (*vide infra* Sections 4.3.1.2 and 4.4.1.2). Both the Nyquist and Bode plots in the absence and presence of the inhibitors show similar features indicating that the compounds inhibit the corrosion reaction without changing the mechanism of the process.

The diameters of the Nyquist semicircles in the presence of the inhibitors are generally larger than that of the blank. This also corresponds to the higher impedance modulus at intermediate to low frequency regions of the Bode impedance plots, and the observed broadening of single time constant maximum in the Bode phase angle plots of the inhibitor-containing systems. These observations suggest the formation of the protective film of the inhibitor molecules on the steel surface [296, 297].

The electrochemical parameters obtained from the fit and simulation analyses of the impedance spectra using the simple $R_s(R_{ct}Q)$ equivalent circuit are shown in Table 4.30 for Mt-3-PQPP and MS-2-PQPA. A complete list of the EIS parameters for the four compounds is contained in Table A5-2 (Appendix 5). The values of R_s do not form a definite trend with increasing concentration of the inhibitors, but it clear that the values are higher in the presence of the inhibitors than the blank suggesting relatively low conductivity media in the presence of the inhibitors.

The R_{ct} values for Mt-3-PQPP increase with increasing concentration corresponding to increasing values of $\%IE_I$. The values of R_{ct} and $\%IE_I$ also increase with increasing

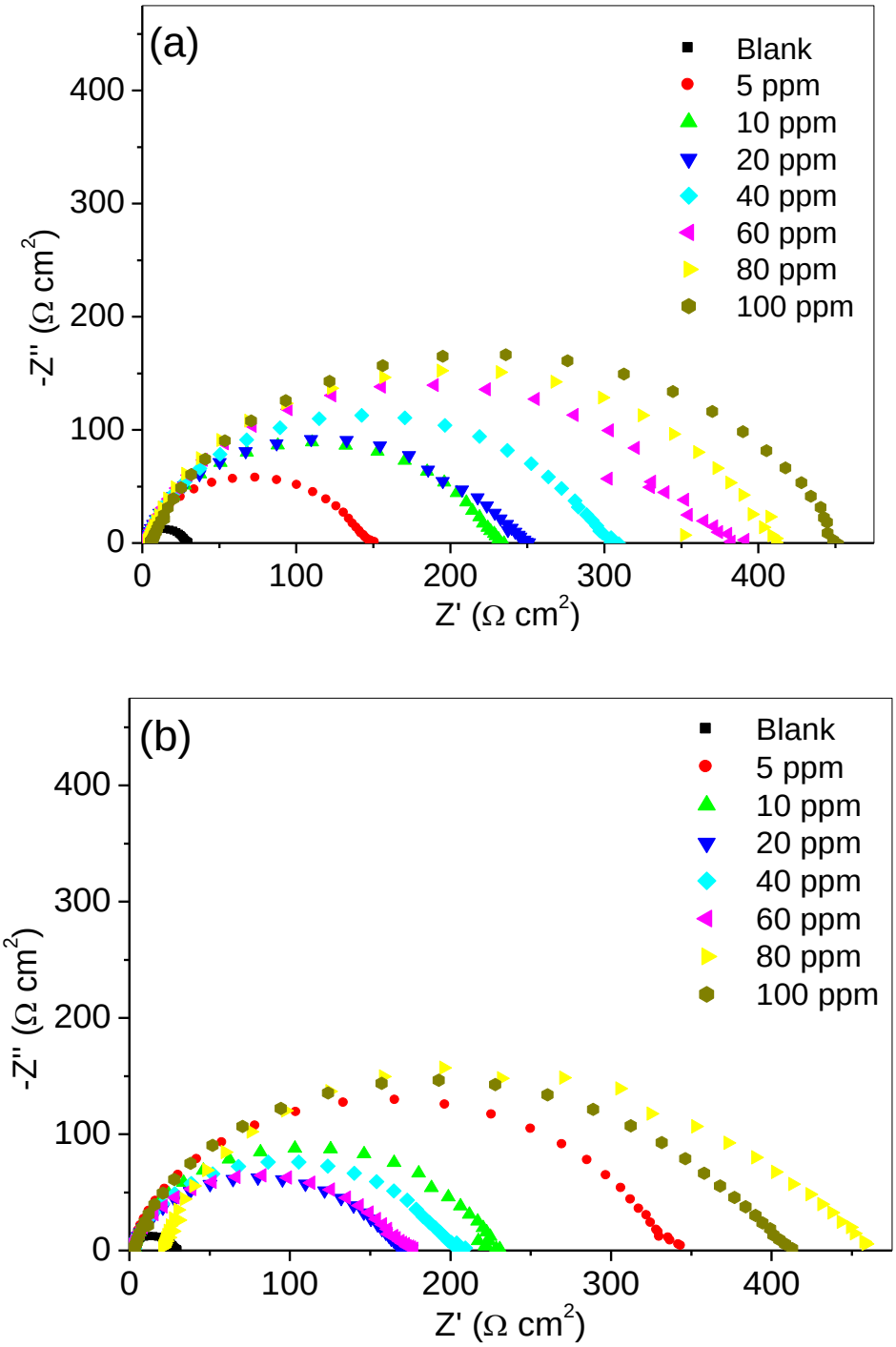

Figure 4.38. Nyquist plots for MS in 1 M HCl without and with various concentrations of the inhibitors (a) Mt-3-PQPP and (b) MS-2-PQPA.

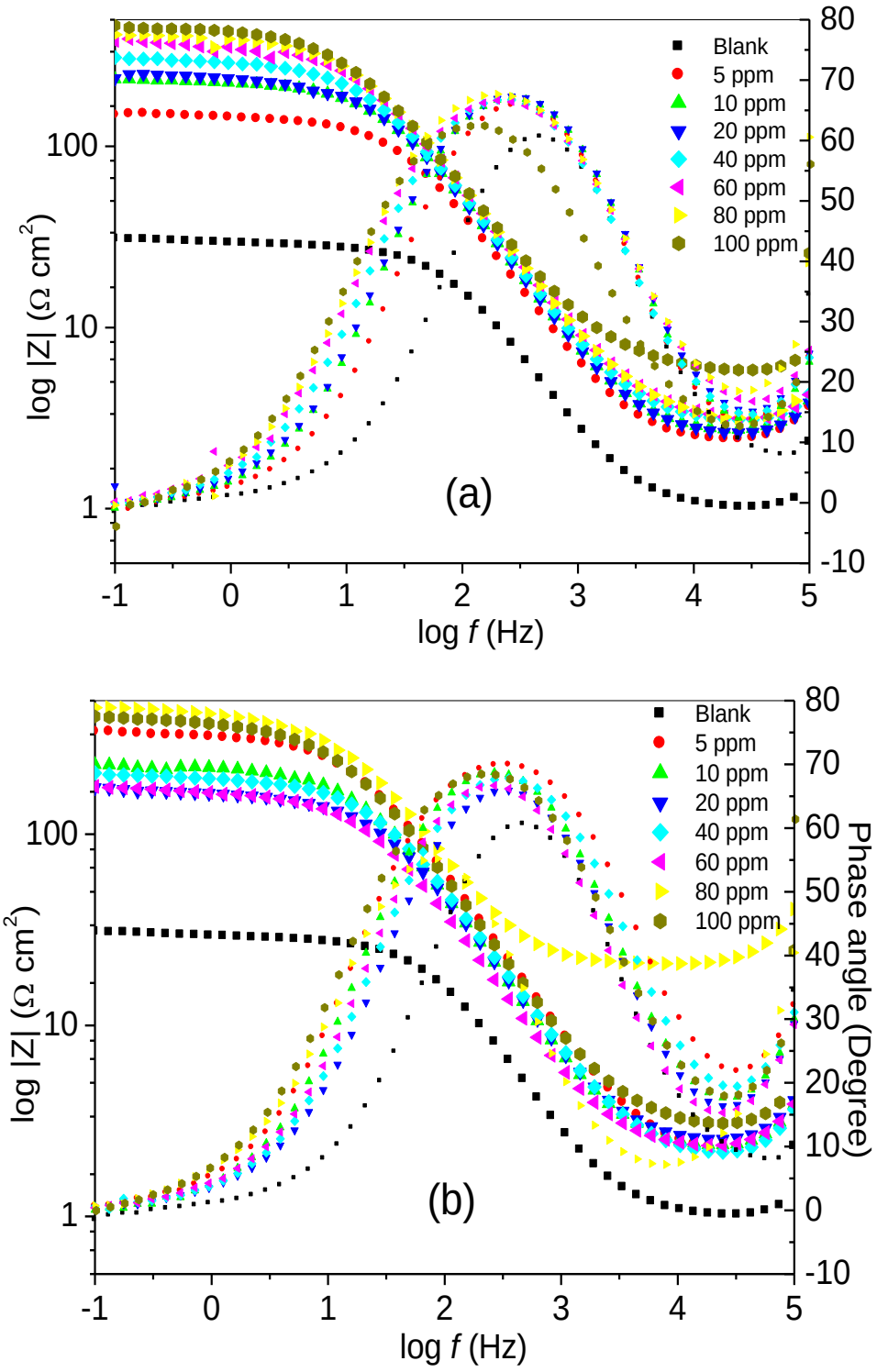

Figure 4.39. Bode plots for MS in 1 M HCl without and with various concentrations of the inhibitors (a) Mt-3-PQPP, and (b) MS-2-PQPA.

concentration of Cl-4-PQPP and attained a maximum value at 60 ppm. Further increase in concentration did not reflect noticeable change in the value of R_{ct}. The trend of the values of $\%IE_I$ for Cl-4-PQPP is the same as that observed from the Tafel analyses. As observed from the Tafel plots, irregular trend in the values of $\%IE_I$ for MS-2-PQPA are also observed from the EIS measurements.

MS-4-PQPA also shows increasing $\%IE_I$ with increasing concentration and affords a maximum value of $\%IE_I$ (93.02 %) at 80 ppm. The values of the CPE exponent, *n* are closer to unity, indicating that the MS/electrolyte systems investigated in this study have pseudo-capacitive behaviour. The magnitudes of *n* are slightly lower for the inhibitor containing systems suggesting higher degree of homogeneity of the electrode surface than the blank. This observation has been recounted for other compounds reported in this thesis (*vide infra* GROUPS III and IV). The values of $|\Theta|$ and $|S|$ obtained for the studied compounds also reveal pseudo capacitive behaviour and corroborate the suggested formation of the

Table 4.30. EIS parameters and percentage inhibition efficiency for the corrosion of MS in 1 M HCl without and with various concentrations of the inhibitors.

Compound	*Conc.* (ppm)	R_s (Ωcm^2)	R_{ct} (Ωcm^2)	Y_o ($\mu S s^n cm^{-2}$)	*n*	$\|\Theta\|$ (Degree)	$\|S\|$	$\%IE_I$
Blank	-	1.01	28.20	157	0.893	60.59	0.64	-
	5	2.36	143	72.9	0.884	65.79	0.76	80.28
	10	2.64	225	65.4	0.875	67.10	0.79	87.47
Mt-3-PQPP	20	2.52	236	69.0	0.869	67.33	0.79	88.05
	40	2.98	294	70.5	0.859	66.72	0.80	90.41
	60	2.98	363	71.4	0.842	66.60	0.79	92.23
	80	2.95	399	69.8	0.846	67.66	0.80	92.93
	100	5.68	447	79.1	0.824	62.67	0.76	93.69
	5	2.05	330	58.2	0.862	69.91	0.80	91.46
	10	2.25	222	70.3	0.875	68.71	0.80	87.30
MS-2-PQPA	20	2.41	163	74.2	0.867	65.90	0.75	82.70
	40	2.03	196	70.2	0.866	67.82	0.78	85.61
	60	2.27	165	88.4	0.874	66.68	0.79	82.91
	80	21.0	415	55.9	0.864	55.18	0.67	93.20
	100	2.86	391	67.3	0.853	68.69	0.81	92.79

adsorbed film of the inhibitor molecules on the steel surface thereby protecting the surface from direct exposure to the acid.

Based on the values of *%IE* over the entire concentration range, it can be inferred that the trends of $\%IE_P$ for the studied compounds are Mt-3-PQPP > Cl-4-PQPP, and MS-2-PQPA > MS-4-PQPP. It is important to mention that the comparison of *%IE* values for MS-2-PQPA and MS-4-PQPA is somewhat complicated due the irregular trend of the *%IE* values for MS-2-PQPP, and the deduction of the trend for these two compounds was based on the average value and may not be an absolute rank of the strength of inhibition performance of the compounds.

A comparison of the overall inhibition performances of Mt-3-PQPP and Cl-4-PQPP compared to PQDPP (in Group II) reveals that Mt-3-PQPP shows higher inhibition efficiency than PQDPP at lower concentrations (5 ppm and 10 ppm), while Cl-4-PQPP shows lower inhibition potential than PQDPP. This implies that the $–OCH_3$ group in Mt-3-PQPP and the chloro group in Cl-4-PQPP both affect the adsorption and inhibition characteristics of the compounds. On the other hand, MS-2-PQPA shows higher (average) inhibition efficiency than MS-2-PQPP (Group III), while MS-4-PQPA shows lower (average) inhibition efficiency than MS-4-PQPP. The effect of carbonyl chain length on the inhibition efficiency that was investigated in Group III is also brought forward here. However, the relationship is not a simple one due to the possible complexity of the adsorption process especially in a case like these compounds where multiple prospective protonation sites are available.

4.5.2 Adsorption isotherms

The adsorptions of Mt-3-PQPP, Cl-4-PQPP, MS-2-PQPA, and MS-4-PQPA were found to obey the Langmuir adsorption isotherm. The representative adsorption isotherms for the compounds are shown for Mt-3-PQPP and MS-2-PQPA in Figure 4.40. Langmuir

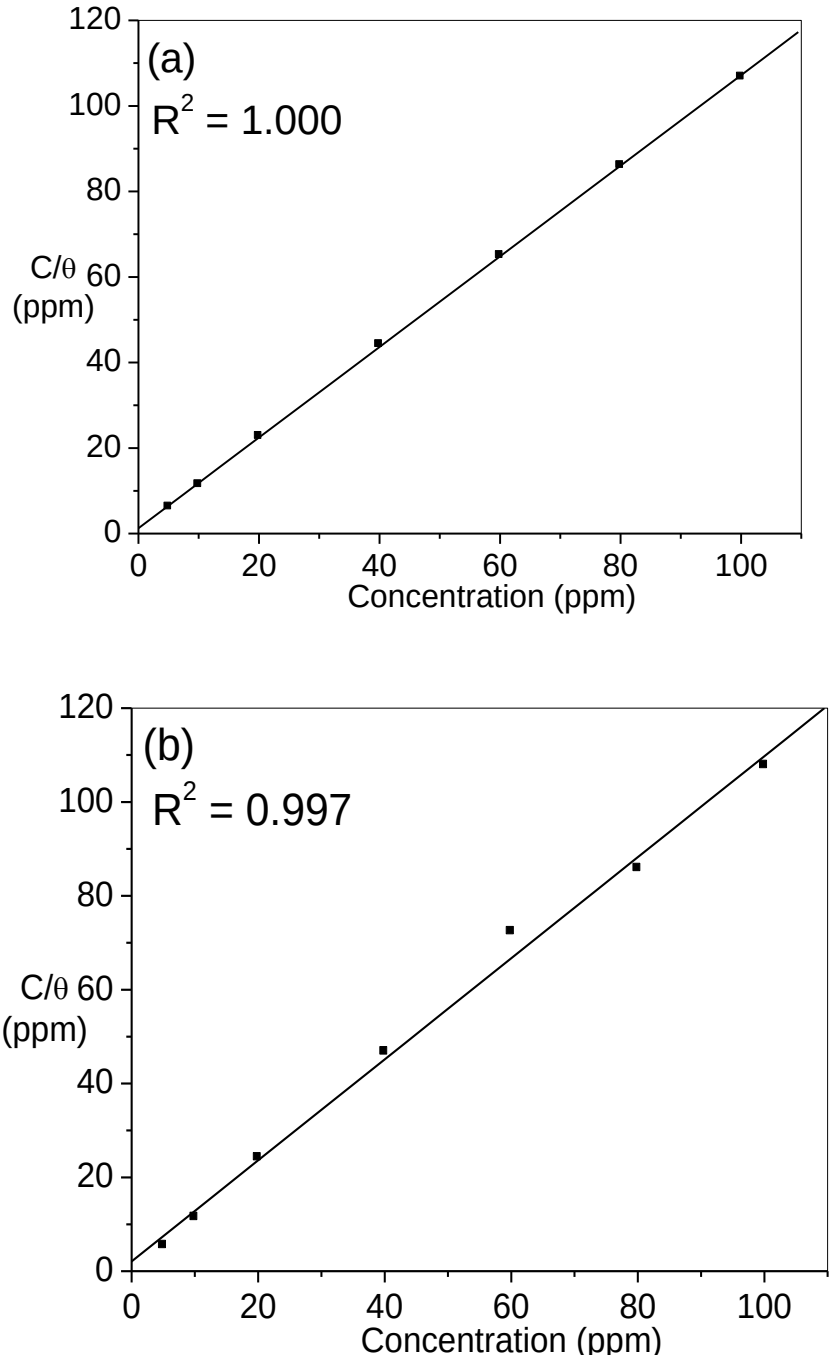

Figure 4.40. Langmuir adsorption isotherms for (a) Mt-3-PQPP, and (c) MS-2-PQPA on MS in 1 M HCl (*Experimental data were taken from the EIS measurements*).

adsorption isotherms for Cl-4-PQPP and MS-4-PQPA are displayed in Figure AV-4 (Appendix V). All the plots are linear with R^2 values of almost unity. The slopes of the straight lines are also near unity in accordance to the simple Langmuir adsorption isotherm model.

The thermodynamic parameters for the adsorption process are listed in Table 4.31. The large values of K_{ads} are indications of strong adsorption of the studied compounds on the steel surface. The negative values of ΔG_{ads} imply spontaneous adsorption process. The values of ΔG_{ads} for Mt-3-PQPP, MS-2-PQPA, and MS-4-PQPA suggest that the adsorption of these compounds on MS proceed via chemisorption mechanism, while the value of ΔG_{ads} for Cl-4-PQPP suggests that it adsorbs on the steel surface via competitive physisorption and chemisorption mechanisms. It is also inferrable from the values of ΔG_{ads} for MS-2-PQPA and MS-4-PQPA that the adsorption of the former is less spontaneous than the latter.

Table 4.31. Thermodynamic parameters for the adsorption of the studied compounds on MS in 1 M HCl at 303.15 K.

Inhibitor	K_{ads} ($x10^3$)	$-\Delta G_{ads}$ (kJ/mol)
Mt-3-PQPP	285.56	41.78
Cl-4-PQPP	88.35	38.83
MS-2-PQPA	195.53	40.83
MS-4-PQPA	278.13	41.80

4.5.3 UV-vis spectroscopic analyses

The UV-vis spectra for Mt-3-PQPP and MS-2-PQPA before and after MS immersion for 3 hours are shown in Figure 4.41. The spectra for Cl-4-PQPP and MS-4-PQPA are shown in Figure AV-5 (Appendix V). The absorption spectrum of Mt-3-PQPP before MS immersion show bands at 210 nm, 239 nm and 288 nm corresponding to n→π*, π→π* transitions and intramolecular charge transfers (ICT) respectively. The absorption spectrum of Cl-4-PQPP shows a maximum at 200 nm corresponding to n→π* transition and a low absorbance peak at 285 nm due to π→π* transition.

The spectrum of MS-2-PQPA shows two maxima at 206 nm and 239 nm corresponding to n→π* and π→π* transitions respectively. MS-4-PQPA shows bands at 211 nm, 242 nm,

and 302 nm, which also correspond to n→π*, π→π* transitions and intramolecular charge transfers (ICT) respectively. Apparent changes in the absorption spectra of these compounds were observed after MS immersion. The band at 210 nm in Mt-3-PQPP became a shoulder with lower absorbance. The band at 285 nm in Cl-4-PQPP disappeared and the solution shows higher absorbance. MS-2-PQPA also shows higher absorbance upon MS immersion and the feature of the spectrum is completely changed. For MS-4-PQPA, the bands at 211 nm and 302 nm red-shifted and blue-shifted respectively to 214 nm and 288 nm. The observed changes in the spectra after MS immersion may be as a result of interactions between the inhibitor molecules and MS, and perhaps due to the formation of Fe-inhibitor complexes.

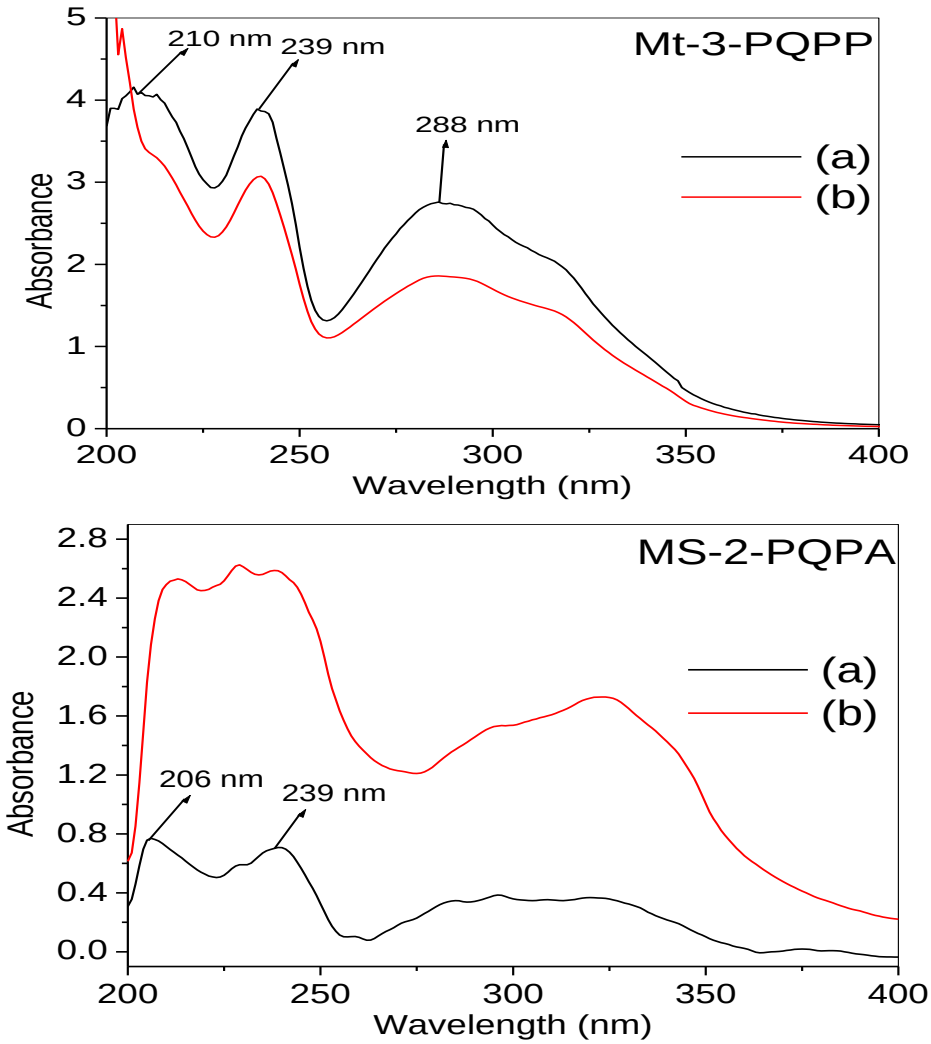

Figure 4.41. UV-vis spectra of the acidic solutions of Mt-3-PQPP and MS-2-PQPA **(a)** before, and **(b)** after MS immersion.

4.5.4 Quantum chemical calculations

4.5.4.1 Neutral species

The optimized structures of the neutral molecules of Mt-3-PQPP and MS-2-PQPA and their respective HOMO and LUMO electron density isosurfaces are shown in Figure 4.42. The optimized structures, HOMO and LUMO of Cl-4-PQPP and MS-2-PQPA are shown in Figure AV-7 (Appendix V). The optimized structures correspond to the true energy minima in the potential well as confirmed by the absence of imaginary frequency in the force constant calculations.

The HOMOs of all the four compounds are essentially distributed over the entire pyrazole and phenyl rings. The O-atom of the carbonyl functional group is also involved in the HOMO in all the compounds. The HOMO of Mt-3-PQPP is also extended to the O-atom of the methoxy substituent on the phenyl ring, confirming the electron-donating ability of this group. The HOMO of Cl-4-PQPP also involves the Cl-substituent on the phenyl ring, suggesting that the Cl-substituent at this position has some electron-donating effects. The apparent difference between the electron distributions in the HOMOs of MS-2-PQPP and MS-3-PQPP is the involvement of the N-atom of the sulphonamido group in the HOMO of MS-2-PQPA but not involved in that of MS-3-PQPA. This observation implies that the sulphonamido group exhibits better electron-donating effect while at position 2 than at 3.

The LUMOs of the four compounds are found to be distributed over the entire quinoxaline ring. The sp^2 N-atom of the pyrazole ring is also involved in the LUMO electron density distributions in the four cases. There is a slight extension of the LUMO electron density to the C-atoms at alpha and beta positions to the sp^2 N-atom of the pyrazole ring in Mt-3-PQPP. The π-electron centre of the C-C group adjoining the pyrazole and the phenyl rings is also involved in the LUMO of Cl-4-PQPP, indicating electron deficiency at this centre. The C-atom of the phenyl ring that is directly attached to the Cl-substituent is also

involved in the LUMO of Cl-4-PQPP, indicating the inductive electron-withdrawing effect of the Cl-group on this carbon.

The quantum chemical parameters for the neutral molecules of the studied compounds are listed in Table 4.32. For Mt-3-PQPP and Cl-4-PQPP, it was observed that Mt-3-PQPP has a higher E_{HOMO}, lower ΔE_{L-H}, and lower η values, which is agreement with its better inhibition performance than Cl-4-PQPP as revealed by experimental measurements. The

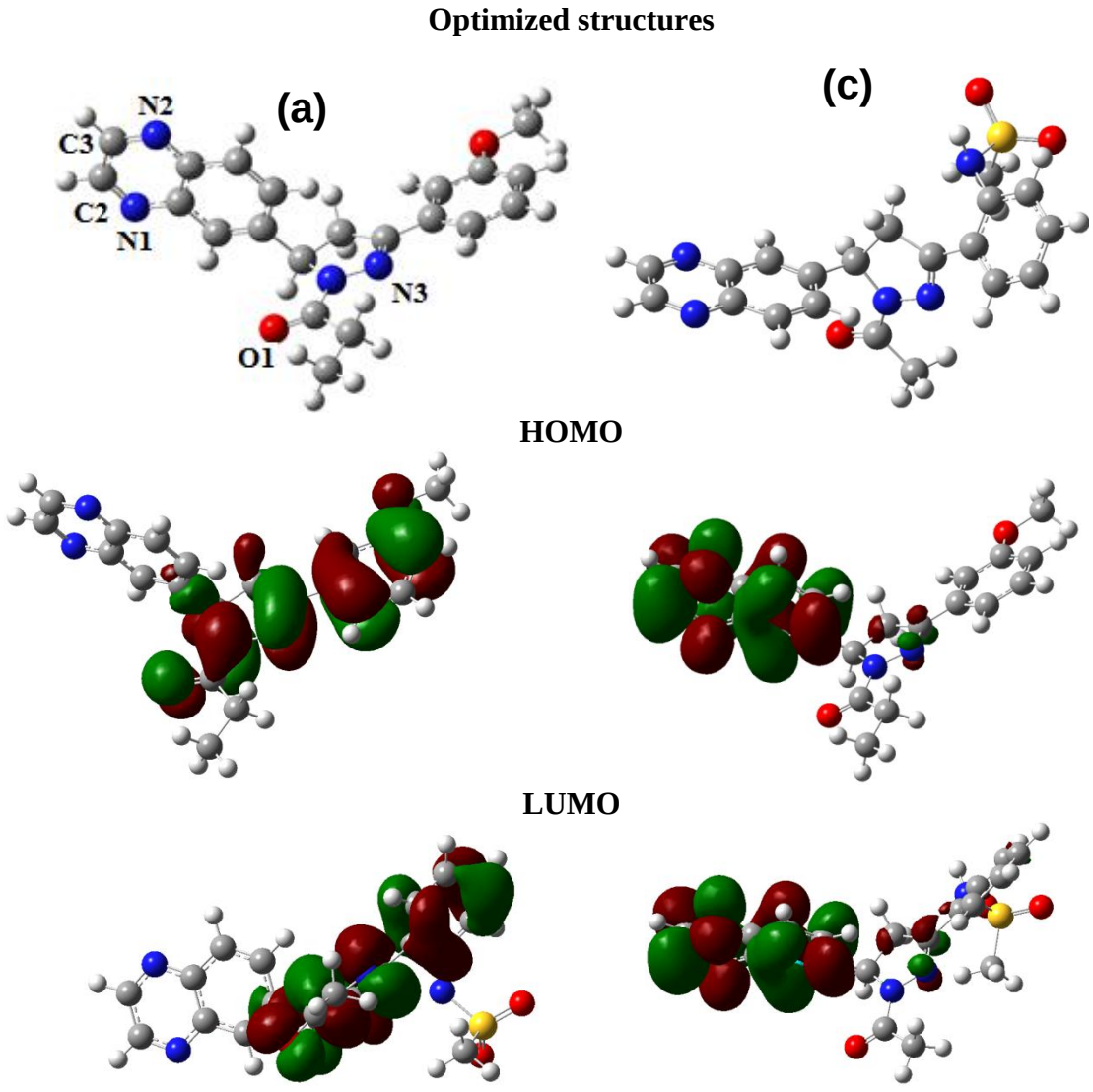

Figure 4.42. Optimized structures, HOMO and LUMO of neutral molecules of (a) Mt-3-PQPP, and (b) MS-2-PQPA at B3LYP/6-31G(d) level of theory. (*Atom labels in (a) were only used to refer to the positions of atoms in the discussion of results*)

FMO parameters and reactivity indices for MS-3-PQPA including the E_{HOMO}, E_{LUMO}, ΔE_{L-H}, and η indicate that it has better corrosion inhibition potential than MS-2-PQPA. This observation agrees with some of the experimental results at certain concentrations but could not be generalized due to the irregular values of the %IE of MS-2-PQPA recorded from the experimental measurements. Mt-3-PQPP also has higher dipole moment than Cl-4-PQPP

Table 4.32. Quantum chemical parameters for the neutral molecules of (a) Mt-3-PQPP, (b) Cl-4-PQPP, (c) MS-2-PQPA, and (d) MS-3-PQPA at B3LYP/6-31G(d) level of theory.

Parameter	Mt-3-PQPP	Cl-4-PQPP	MS-2-PQPA	MS-3-PQPA
E_{LUMO} *(eV)*	-1.879	-1.990	-1.996	-1.998
E_{HOMO} *(eV)*	-5.782	-5.978	-6.197	-5.854
ΔE_{L-H} *(eV)*	3.903	3.988	4.201	3.856
χ *(eV)*	3.830	3.984	4.097	3.926
η *(eV)*	1.952	1.994	2.101	1.928
ΔN	0.812	0.756	0.691	0.797
Dipole moment (Debye)	5.300	2.013	3.212	4.611

which may enhance its corrosion inhibition strength via increased dipole−dipole interactions of its molecules with the metal surface [191].

The graphical images of the Fukui indices for the prospective sites of nucleophilic (f^+) and electrophilic (f^-) attacks Mt-3-PQPP and MS-2-PQPA molecules are shown in Figure 4.45. Fukui functions for Cl-4-PQPP and MS-3-PQPA are shown in Figure AV-7 (Appendix V). The most prospective sites of nucleophilic attack in the molecules are found on the N-atoms of the quinoxaline ring, the π-electron centre of the C2=C3 group in the quinoxaline ring, the sp^2 N-atom of the pyrazole ring and the π-electron centre of the C-C adjoining the pyrazole and the phenyl ring. These observations align with the electron distributions in the LUMO of the molecules. Similarly, the f^- graphical surfaces indicating the most promising

sites/centres for electrophilic attacks in the molecules correspond to what was observed for the HOMO of the molecules, which has been explained earlier in this section.

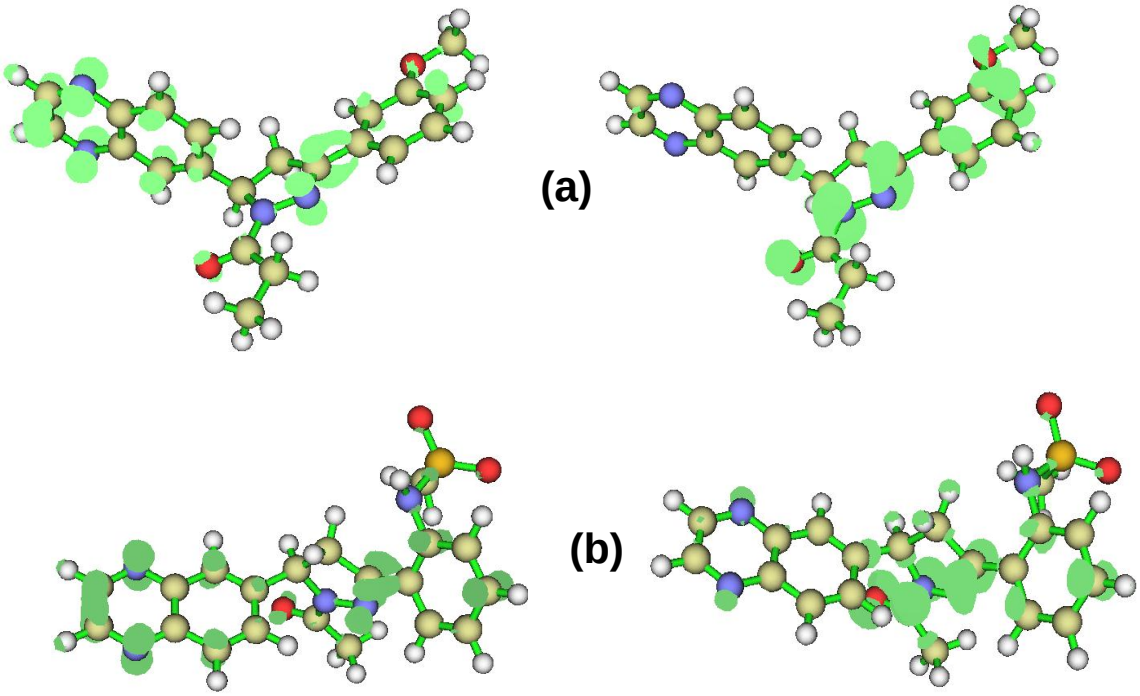

Figure 4.43. Fukui functions, f^{+}(left-hand side) and f^{-} (right-hand side) for (a) Mt-3-PQPP, and (b) MS-2-PQPA (*Isosurface = 0.003*).

4.5.4.2 Protonated species

The possibility of protonation at the basic sites in the molecules were again assessed by carrying out quantum chemical calculations on the singly protonated species of these molecules and the results of PA and GB for the first three most probable sites of protonation in each molecule are listed in Table 4.33. As observed for the other quinoxaline derivatives reported in the previous chapters, the compounds considered in this group also show considerably high values of PA and GB, indicating the possibility of getting protonated in acidic solution. The results in Table 4.33 show that the most probable site of protonation for the all the four compounds is the N1 on the quinoxaline ring.

In addition, there are indications that Mt-3-PQPP can also be protonated at N2 and O1 while Cl-4-PQPP can be protonated at N2 based on the values of ΔPA (and ΔGB). This

observation suggests that Mt-3-PQPP is likely to have more protonated species in solution than Cl-4-PQPP. The increased electron-affinity of protonated species improves adsorption on metallic surface via retro-donation. This supports the higher inhibition performance of Mt-3-PQPP than Cl-4-PQPP. Similar inference could be drawn on the prospect of protonation in MS-2-PQPA and MS-3-PQPA in which case the latter has better chances of having multiple protonated species (at N1, N2 and O1) compared to the former (at N1 and N2) based on the values of ΔPA (and ΔGB). This observation also supports the higher inhibition performance of MS-3-PQPA over MS-2-PQPA.

The quantum chemical parameters and reactivity indices for the protonated species are listed in Table 4.34. The higher values of E_{HOMO} as well as the lower values of ΔE_{L-H} and η for Mt-3-PQPP-$H^{+}_{(N1)}$ compared to Cl-4-PQPP-$H^{+}_{(N1)}$ imply that the former has higher reactivity than the latter and this is partly in relation to its relative ability to still donate electrons (high E_{HOMO}) to an electron-deficient centre, while still capable of accepting electrons from an electron-rich centre (as a protonated specie). This supports the

Table 4.33. Proton affinity (PA) and gas-phase basicity (GB) for the sites of protonation in Mt-3-PQPP, Cl-4-PQPP, MS-2-PQPA, and MS-4-PQPA at B3LYP/6-31G(d) level of theory.

	PA (kJ/mol)/Protonation site			*GB* (kJ/mol)/Protonation site		
Compound	N1	N2	N3/O1*	N1	N2	N3/O1*
Mt-3-PQPP	952.75 (0)	945.95 (-6.80)	947.32* (-5.43)	984.84 (0)	980.27 (-4.57)	978.56 (-6.28)
Cl-4-PQPP	943.30 (0)	936.95 (-6.36)	929.30 (-14.00)	974.30 (0)	971.48 (-2.81)	962.35 (-11.95)
MS-2-PQPA	942.34 (0)	936.41 (-5.93)	923.65 (-18.69)	974.47 (0)	969.49 (-4.98)	953.32 (-21.15)
MS-4-PQPA	949.81 (0)	943.24 (-6.57)	947.80* (-2.01)	982.79 (0)	980.64 (-2.15)	980.13* (-2.65)

In parentheses: Δ*PA* = *PA* (less stable) – *PA* (most stable); Δ*GB* = *GB* (less stable) – *GB* (most stable)

*Means protonation at N3 is more/less stable than at O1 and the more stable protonated forms of Mt-3-PQPP and MS-4-PQPA are the protonated species at O1, while those of Cl-4-PQPP and MS-2-PQPA are the protonated species at N3.

Table 4.34. Quantum chemical parameters for the most stable protonated forms of Mt-3-PQPP, Cl-4-PQPP, MS-2-PQPA, and MS-4-PQPA at B3LYP/6-31G(d) level of theory.

Parameter	Mt-3-PQPP-$H^+_{(N1)}$	Cl-4-PQPP-$H^+_{(N1)}$	MS-2-PQPA-$H^+_{(N1)}$	MS-4-PQPA-$H^+_{(N1)}$
E_{LUMO} *(eV)*	-6.983	-7.093	-6.790	-6.959
E_{HOMO} *(eV)*	-8.003	-8.361	-8.434	-7.963
ΔE_{L-H} *(eV)*	1.019	1.268	1.644	1.004
χ *(eV)*	7.493	7.727	7.612	7.461
η *(eV)*	0.510	0.634	0.822	0.502
ΔN	-0.484	-0.573	-0.372	-0.460
Dipole moment (Debye)	13.504	17.330	10.971	19.034

experimental results that portrayed Mt-3-PQPP as a better inhibitor than Cl-4-PQPP. The higher values of E_{HOMO} together with the lower values of E_{LUMO}, ΔE_{L-H} and η for MS-4-PQPA-$H^+_{(N1)}$ compared to MS-2-PQPA-$H^+_{(N1)}$ imply that the former has higher reactivity than the latter and this is in support of its higher inhibition performances, which were however only observed at some concentrations during the experiments.

4.5.5 Molecular dynamic (MD) simulations

MD simulations were carried out on the inhibitor/Fe(110) systems in order to model the interactions between the studied inhibitor molecules and Fe(110) surface. The lowest energy configurations of the inhibitor/Fe(110) systems obtained from the MD simulations are shown in Figure 4.44 for Mt-3-PQPP and MS-2-PQPA. All the inhibitor molecules interact with the Fe(110) surface in near planar orientations. This tends to ensure maximum interactions between the reactive sites of the inhibitor molecules and the active sites on the Fe surface. The respective binding and interaction energies of the most stable configurations of each inhibitor/Fe(110) systems are listed in Table 4.35. The order of binding energies of the

systems is Mt-3-PQPP/Fe (110) > Cl-4-PQPP/Fe ((110); and MS-3-PQPA/Fe (110) > MS-4-PQPA/Fe (110), which is in agreement with the trend of experimental inhibition efficiency.

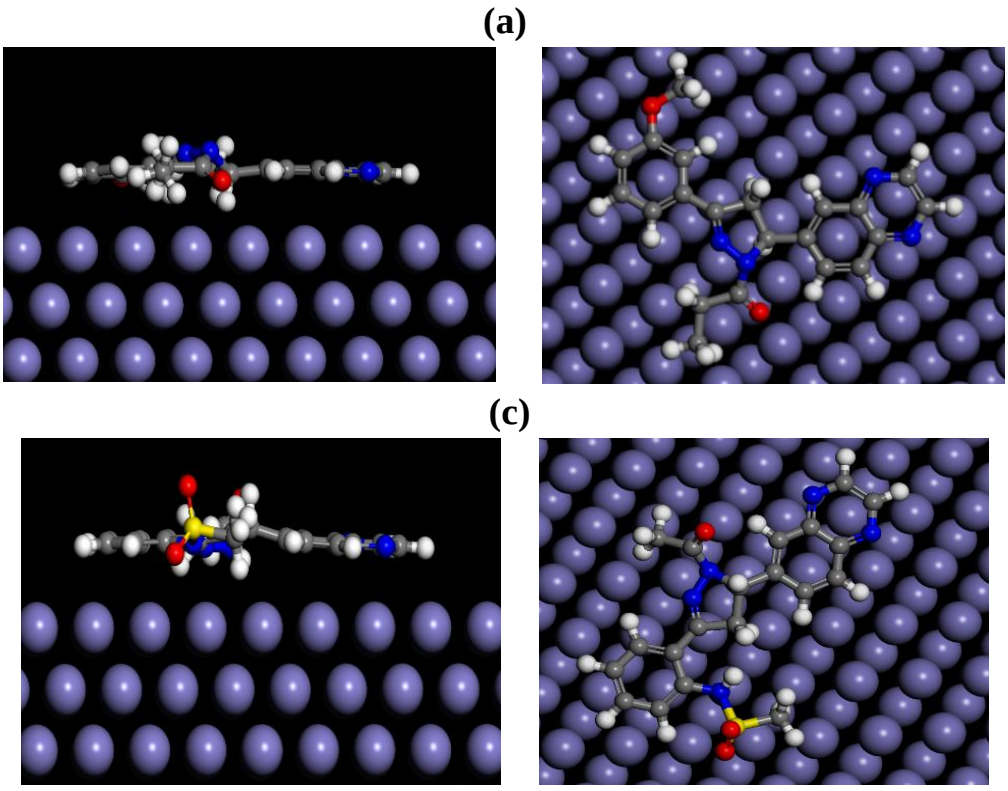

Figure 4.44. Side (left-hand side) and top (right-hand side) views of the most stable configurations of the interactions of (a) Mt-3-PQPP, and (b) MS-2-PQPA with Fe (110) surface using molecular dynamics simulations.

Table 4.35. Selected energy parameters for the adsorption of the studied inhibitors on Fe (110) surface (in kJ/mol)

System	Interaction energy	Binding energy
Fe (110) + Mt-3-PQPP	-812.223	812.223
Fe (110) + Cl-4-PQPP	-767.998	767.998
Fe (110) + MS-2-PQPA	-842.930	842.930
Fe (110) + MS-4-PQPA	-836.202	836.202

CHAPTER 5

CONCLUSIONS AND RECOMMENDATIONS

5.1 Conclusions

The corrosion inhibition properties and adsorption behaviour of seventeen (17) quinoxaline derivatives were investigated for MS in 1 M HCl solution using electrochemical methods, spectroscopic techniques, quantum chemical calculations and MD simulations approaches. The seventeen compounds were divided into five groups (GROUPs I – V), and the following concluding remarks can be derived from the studies.

(1) All the studied compounds showed appreciable protection efficiency for MS in 1 M HCl solution. The trends of corrosion inhibition performances are:

GROUP I: Me-4-PQPB > Mt-PQPB > oxo-1,3-PQPB > Mt-4-PQPB

GROUP II: PQDPP > PQDPB > PPQDPE

GROUP III: MS-3-PQPP > MS-4-PQPP > MS-2-PQPP

GROUP IV: MS-3-PQPMS > MS-2-PQPMS > MS-4-PQPMS

GROUP V: Mt-3-PQPP > Cl-4-PQPP, and also (based on average %IE), MS-2-PQPA > MS-4-PQPA.

(2) All the compounds are mixed-type corrosion inhibitors. The compounds inhibit corrosion by merely adsorbing on the active sites on the steel surface without changing the mechanism of the corrosion process. They adsorb on MS/electrolyte interface and form protective film with pseudocapacitive behaviour. The adsorption of all the compounds obeyed the Langmuir adsorption isotherm model. It can be inferred from the adsorption parameters that the interactions of the inhibitor molecules with MS involve mixed physisorption and chemisorption mechanisms.

(3) Spectroscopic measurements confirmed the occurrence of interactions between the MS and the inhibitor molecules and suggested the formation of inhibitor-Fe complexes.

(4) Quantum chemical calculations established that the studied compounds have great chances of getting protonated in acidic solution and the protonation may occur at

different sites thereby introducing different protonated species in solution. The most promising sites of protonation in various cases include the N-atoms of the quinoxaline ring, the sp^2 N-atom of the pyrazole ring and the O-atom of the carbonyl functional group. The reactivity parameters of the protonated species provide better explanations for the observed inhibition performances of the inhibitors in many cases. The results further suggested that adequate theoretical descriptions of inhibitive effects of compounds with prospective sites of protonation require that calculations be carried out on protonated species.

(5) The HOMO, LUMO and Fukui indices revealed that the quinoxaline ring in all the studied compounds is generally electron-deficient, while the pyrazole ring is relatively rich in π-electrons in agreement with the established general trend of chemical reactivity of heterocyclic compounds. The carbonyl oxygen and the phenyl ring in all the studied compounds were also identified as electron-rich centres and therefore capable of promoting electrophilic attacks by metallic atom/ion during the adsorption process. The results also provided evidence of substantial retro-donation of charges from metal to the inhibitor molecules during the donor-acceptor interactions that lead to the adsorption of the molecules on the steel surface.

(6) The results of the MD simulations on the GROUP I compounds showed that the values of the total energy of the inhibitor/Fe (110) systems are in agreement with the observed trend of inhibition efficiencies of the molecules. The adsorption energies for the inhibitor/Fe (110) systems for the GROUP II compounds were predicted from MC simulations and the results revealed that PQDPP has the highest adsorption energy, and the overall trend of the adsorption energies of the inhibitor/Fe (110) systems are in accord with the trend of experimental inhibition potentials of the molecules. The binding energies of the inhibitor/Fe (110) systems calculated from the MD simulations for the

GROUP III, GROUP IV and GROUP V are also in agreement with the experimental inhibition efficiencies.

(7) In the case of the GROUP II compounds, the chain length/type of carbonyl substituent affects inhibition efficiency of the compounds and the most effective inhibitor (PQDPP) is the one with the shortest carbonyl chain whose reactivity (and inhibition performance) is favoured by the two factors that rule on the trend of carbonyls reactivity, that is, electronic and steric factors. For the GROUPs III and IV, the combined effects of electronic and steric contributions of the methanesulphonamido group substituted on the phenyl ring favour higher inhibition efficiency at position 3 than positions 2 and 4 such that MS-3-PQPP (in GROUP III) and MS-3-PQPMS (in GROUP IV) have the highest inhibition performances in their respective groups.

5.2 Recommendations and future studies

5.2.1 Industrial and academic recommendations

The 6-(3-phenyl-4,5-dihydro-1H-pyrazol-5-yl)quinoxaline derivatives studied in this work are non-toxic and efficient corrosion inhibitors with prospective applications as additives to paints and coating materials to improve their corrosion control properties. These compounds also have potential applications as corrosion inhibitors in various industries that place premium attention to corrosion control. In this regards, they can be used as additives to the industrial waste water, effluents and other routinely used industrial chemicals that cause corrosion of metallic substances.

The present study recommends that researches on corrosion inhibition properties and adsorption characteristics of organic compounds with prospective sites of protonation be supported with possible experimental and theoretical studies on site-protonation in order to provide adequate explanations for the adsorption properties of the molecules. This study also

recommends the use of MD simulations for modelling the interactions between adsorbent and adsorbate especially in corrosion inhibition studies. The MD simulations approach can be used as a relatively inexpensive and quick means of predicting the inhibition potentials of new compounds prior to more comprehensive experimental findings.

5.2.2 Possible future studies

Based on the promising results obtained from the present study, possible future studies on the inhibition performance of the investigated compounds on other metal alloys and corrosive media are suggested. Studies on the inhibition efficiency of the compounds in high temperature corrosion could also be considered in future.

REFERENCES

[1] Badr, G. The role of some thiosemicarbazide derivatives as corrosion inhibitors for C-steel in acidic media. **Corrosion Science. 2009**, 51, 2529-36.

[2] Singh, D., Singh, T., Gaur, B. The role of metal cations in improving the inhibitive performance of hexamine on the corrosion of steel in hydrochloric acid solution. **Corrosion Science. 1995**, 37, 1005-19.

[3] Yadav, D.K., Chauhan, D., Ahamad, I., Quraishi, M. Electrochemical behavior of steel/acid interface: adsorption and inhibition effect of oligomeric aniline. **RSC Advances. 2013**, 3, 632-46.

[4] Zhang, K., Xu, B., Yang, W., Yin, X., Liu, Y., Chen, Y. Halogen-substituted imidazoline derivatives as corrosion inhibitors for MS in hydrochloric acid solution. **Corrosion Science. 2015**, 90, 284-95.

[5] Acidizing: Treatment in oil and gas operators - Briefing paper. **American petroleum institute (API) 2014.** ***Retrieved from:*** http://www.api.org/~/media/files/oil-and-natural-gas/hydraulic-fracturing/acidizing-oil-natural-gas-briefing-paper-v2.pdf (February, 2016).

[6] Li, X., Deng, S., Fu, H., Li, T. Adsorption and inhibition effect of 6-benzylaminopurine on cold rolled steel in 1.0 M HCl. **Electrochimica Acta. 2009**, 54, 4089-98.

[7] Singh, A.K., Quraishi, M. Effect of Cefazolin on the corrosion of MS in HCl solution. **Corrosion Science**. 2010, 52, 152-60.

[8] Zhang, X., Zheng, Y., Wang, X., Yan, Y., Wu, W. Corrosion Inhibition of N80 Steel Using Novel Diquaternary Ammonium Salts in 15% Hydrochloric Acid. **Industrial and Engineering Chemistry Research. 2014**, 53, 14199-207.

[9] da Rocha, J.C., Gomes, J.A.d.C.P., D'Elia, E. Corrosion inhibition of carbon steel in hydrochloric acid solution by fruit peel aqueous extracts. **Corrosion Science. 2010**, 52, 2341-8.

[10] The high cost of corrosion. ***Retrieved from***: http://www.mintek.co.za/2011/11/15/the-high-cost-of-corrosion/ (September 2015).

[11] Popoola, L.T., Grema, A.S., Latinwo, G.K., Gutti, B., Balogun, A.S. Corrosion problems during oil and gas production and its mitigation. **International Journal of Industrial Chemistry. 2013**, 4, 1-15.

[12] Obot, I., Obi-Egbedi, N. 2, 3-Diphenylbenzoquinoxaline: A new corrosion inhibitor for MS in sulphuric acid. **Corrosion Science. 2010**, 52, 282-5.

[13] Obot, I., Obi-Egbedi, N. Indeno-1-one [2, 3-b] quinoxaline as an effective inhibitor for the corrosion of MS in 0.5 MH 2 SO 4 solution. **Materials Chemistry and Physics. 2010**, 122, 325-8.

[14] Erhardt, P.W. In search of the digitalis replacement. **Journal of medicinal chemistry. 1987**, 30, 231-7.

[15] Roth, T., Morningstar, M.L., Boyer, P.L., Hughes, S.H., Buckheit, R.W., Michejda, C.J. Synthesis and biological activity of novel nonnucleoside inhibitors of HIV-1 reverse transcriptase. 2-Aryl-substituted benzimidazoles. **Journal of medicinal chemistry. 1997**, 40, 4199-207.

[16] Seitz, L.E., Suling, W.J., Reynolds, R.C. Synthesis and antimycobacterial activity of pyrazine and quinoxaline derivatives. **Journal of medicinal chemistry. 2002**, 45, 5604-6.

[17] Tomczuk, B.E., Taylor Jr, C., Moses, L.M., Sutherland, D.B., Lo, Y.S., Johnson, D.N., et al. 2-Phenyl-3H-imidazo [4, 5-b] pyridine-3-acetamides as nonbenzodiazepine anticonvulsants and anxiolytics. **Journal of medicinal chemistry. 1991**, 34, 2993-3006.

[18] Chen, A.Y., Yu, C., Gatto, B., LIu, L.F. DNA minor groove-binding ligands: a different class of mammalian DNA topoisomerase I inhibitors. **Proceedings of the National Academy of Sciences. 1993**, 90, 8131-5.

[19] Darabi, H.R., Mohandessi, S., Aghapoor, K., Mohsenzadeh, F. A recyclable and highly effective sulfamic acid/MeOH catalytic system for the synthesis of quinoxalines at room temperature. **Catalysis Communications. 2007**, 8, 389-92.

[20] Heravi, M.M., Bakhtiari, K., Tehrani, M.H., Javadi, N.M., Oskooie, H.A. Facile synthesis of quinoxaline derivatives using o-iodoxybenzoic acid (IBX) at room temperature. **Arkivoc. 2006**, 16, 16-22.

[21] More, S.V., Sastry, M., Wang, C.-C., Yao, C.-F. Molecular iodine: a powerful catalyst for the easy and efficient synthesis of quinoxalines. **Tetrahedron letters. 2005**, 46, 6345-8.

[22] Robinson, R.S., Taylor, R.J. Quinoxaline synthesis from α-hydroxy ketones via a tandem oxidation process using catalysed aerobic oxidation. **Synlett. 2005**, 1003-5.

[23] Venkatesh, C., Singh, B., Mahata, P., Ila, H., Junjappa, H. Heteroannulation of nitroketene N, S-arylaminoacetals with POCl3: A novel highly regioselective synthesis of unsymmetrical 2, 3-substituted quinoxalines. **Organic letters. 2005**, 7, 2169-72.

[24] Abboud, Y., Abourriche, A., Saffaj, T., Berrada, M., Charrouf, M., Bennamara, A., et al. 2, 3-Quinoxalinedione as a novel corrosion inhibitor for MS in 1M HCl. **Materials Chemistry and Physics. 2007**, 105, 1-5.

[25] Benabdellah, M., Tebbji, K., Hammouti, B., Touzani, R., Aouniti, A., Dafali, A., et al. The effect of temperature on the corrosion of steel in 1 M HCl in the presence of quinoxaline compound. **Physical and Chemical News. 2008**, 115-20.

[26] Benabdellah, M., Touzani, R., Aouniti, A., Dafali, A., ELKADIRI, S., Hammouti, B., et al. Investigation of the inhibitive effect of some quinoxaline compounds on the corrosion of steel in HCL solution. **Physical and Chemical News. 2007**, 63-9.

[27] El Adnani, Z., Mcharfi, M., Sfaira, M., Benzakour, M., Benjelloun, A., Touhami, M.E. DFT theoretical study of 7-R-3methylquinoxalin-2 (1H)-thiones (R H; CH 3; Cl) as corrosion inhibitors in hydrochloric acid. **Corrosion Science. 2013**, 68, 223-30.

[28] El Ouali, I., Hammouti, B., Aouniti, A., Ramli, Y., Azougagh, M., Essassi, E., et al. Thermodynamic characterisation of steel corrosion in HCl in the presence of 2-phenylthieno (3, 2-b) quinoxaline. **Journal of Materials and Environmental Science. 2010**, 1, 1-8.

[29] Zarrouk, A., Dafali, A., Hammouti, B., Zarrok, H., Boukhris, S., Zertoubi, M. Synthesis, characterization and comparative study of functionalized quinoxaline derivatives towards corrosion of copper in nitric acid medium. **International Journal of Electrochemical Science. 2010**, 5, 46-55.

[30] Zarrouk, A., Hammouti, B., Touzani, R., Al-Deyab, S., Zertoubi, M., Dafali, A., et al. Comparative study of new quinoxaline derivatives towards corrosion of copper in nitric acid. **International Journal of Electrochemical Science. 2011**, 6, 4939-52.

[31] Zarrouk, A., Zarrok, H., Salghi, R., Hammouti, B., Al-Deyab, S., Touzani, R., et al. A theoretical investigation on the corrosion inhibition of copper by quinoxaline derivatives in nitric acid solution. **International Journal of Electrochemical Science. 2012**, 7, 6353-64.

[32] Terminology Relating to Corrosion and Corrosion Testing. **American Society for Testing and Materials Designation G. 2000**, (Revised), 03.02.

[33] Fontana, M.G. Corrosion Engineering. **New York, McGraw-Hill, 1986**.

[34] Bardal, E. Corrosion and protection. **Springer Science & Business Media, 2007**.

[35] Davis, J.R. Corrosion: Understanding the basics. **ASM International, 2000**.

[36] Stansbury, E.E., Buchanan, R.A. Fundamentals of electrochemical corrosion. **ASM international, 2000**.

[37] Agar, J. Electrochemistry and corrosion. **Transactions of the Faraday Society. 1953**, 49, 533-9.

[38] Cicek, V., Al-Numan, B. Corrosion chemistry. **John Wiley & Sons, 2011**.

[39] Fontana, M.G., Green, N.D. Corrosion Engineering. **McGraw-Hill, New York, 1967**.

[40] Fontana, M.G., Green, N.D. Corrosion Engineering. **McGraw-Hill, New York,** 1978.

[41] Dillon, C.P. Corrosion control in the chemical process industries. C. P. Dillon, **McGraw-Hill New York, 1986**.

[42] Kobrin, G. Materials selection In: Corrosion, ASM handbook, **ASM international, 1987**, 13, 321-7.

[43] Puyear, R.B., Hansen, D.A. Selecting materials for construction. In: corrosion engineering handbook, Schweitzer, P.A. Ed., **Marcel Dekker, Inc., 1996**.

[44] Whitney, F.L., Jr. Factors in the selection of corrosion resistant materials. **Metal Progress. 1957**, 90-5.

[45] Landrum, R.J. Fundamentals of designing for corrosion control: A corrosion aid for the designer. **NACE International, 1989**.

[46] Perrigo, L.D., Jensen, G.A. Fundamentals of corrosion design. N**orth England. 1982**, 13, 16-34.

[47] Benedict, R.I. Anode resistance fundamentals and applications-classic papers and reviews. **NACE International, 1986**.

[48] Heidersbach, R.H. Cathodic protection. In: ASM handbook, **ASM International, 1987**, 13, 466-77.

[49] Morgan, J.H. Cathodic protection. 2nd ed, **NACE International, 1987**.

[50] Locke, C.E. Anodic protection. In: ASM handbook. **ASM International, 1987**, 13, 463-5.

[51] Riggs, O.L., Jr., Locke, C.E. Anodic protection: theory and practice in the prevention of corrosion. **Plenum Press, 1981**.

[52] Locke, C.E. Corrosion: Cathodic and anodic protection. In: Encyclopedia of chemical processing and design, **Marcel Dekker, 1981**, 12, 13-59.

[53] Drisko, R.W., Jenkins, J.F. Corrosion and coatings: An introduction to corrosion for coatings personnel. **The Society for Protective Coatings, 1998**.

[54] Edwards, J. Coating and surface treatment systems for metals: A comprehensive guide to selection. **Finishing Publications Ltd. and ASM International, 1997**.

[55] Davis, J.R. ASM specialty handbook: Carbon and alloy steels. **ASM International, 1996**, 391-572.

[56] Migahed, M.A., Abdul-Raheim, A.M., Atta, A.M., Brostow, W. Synthesis and evaluation of a new water soluble corrosion inhibitor from recycled poly(ethylene terphethalate). **Materials Chemistry and Physics. 2010**, 121, 208-14.

[57] Asegbeloyin, J.N., Ejikeme, P.M., Olasunkanmi, L.O., Adekunle, A.S., Ebenso, E.E. A Novel Schiff Base of 3-acetyl-4-hydroxy-6-methyl-(2H) pyran-2-one and 2, 2'-(ethylenedioxy) diethylamine as Potential Corrosion Inhibitor for MS in Acidic Medium. **Materials. 2015**, 8, 2918-34.

[58] de la Fuente, D., Díaz, I., Simancas, J., Chico, B., Morcillo, M. Long-term atmospheric corrosion of MS. **Corrosion Science. 2011**, 53, 604-17.

[59] Guo, L., Zhang, S.T., Li, W.P., Hu, G., Li, X. Experimental and computational studies of two antibacterial drugs as corrosion inhibitors for MS in acid media. **Materials and Corrosion. 2014**, 65, 935-42.

[60] Sasikumar, Y., Adekunle, A., Olasunkanmi, L., Bahadur, I., Baskar, R., Kabanda, M., et al. Experimental, quantum chemical and Monte Carlo simulation studies on the corrosion inhibition of some alkyl imidazolium ionic liquids containing tetrafluoroborate anion on MS in acidic medium. **Journal of Molecular Liquids. 2015**, 211, 105-18.

[61] Ulaeto, S., Ekpe, U., Chidiebere, M., Oguzie, E. Corrosion inhibition of MS in hydrochloric acid by acid extracts of Eichhornia crassipes. **International Journal of Materials and Chemistry. 2012**, 2, 158-64.

[62] Bradford, S.A. Corrosion control. 2nd ed. Edmonton, Alberta, Canada, **CASTI Publishing, 2001**.

[63] West, J.M. Basic corrosion and oxidation. N**ew York, Halsted Press, 1980**.

[64] Arellanes-Lozada, P., Olivares-Xometl, O., Guzmán-Lucero, D., Likhanova, N.V., Domínguez-Aguilar, M.A., Lijanova, I.V., et al. The inhibition of aluminum corrosion in

sulfuric acid by poly (1-vinyl-3-alkyl-imidazolium hexafluorophosphate). **Materials. 2014**, 7, 5711-34.

[65] Banerjee, S., Mishra, A., Singh, M.M., Maiti, B., Ray, B., Maiti, P. Highly efficient polyurethane ionomer corrosion inhibitor: the effect of chain structure. **RSC Advances. 2011**, 1, 199-210.

[66] Bregman, J.I. Corrosion inhibitors: Principles and application. **John Wiley & Sons, 1998 New York.**

[67] Guo, L., Dong, W., Zhang, S. Theoretical challenges in understanding the inhibition mechanism of copper corrosion in acid media in the presence of three triazole derivatives. **RSC Advances. 2014**, 4, 41956-67.

[68] John, S., Joseph, A. Effective inhibition of MS corrosion in 1 M hydrochloric acid using substituted triazines: an experimental and theoretical study. **RSC Advances. 2012**, 2, 9944-51.

[69] Mourya, P., Banerjee, S., Singh, M. Corrosion inhibition of MS in acidic solution by Tagetes erecta (Marigold flower) extract as a green inhibitor. **Corrosion Science. 2014**, 85, 352-63.

[70] Rao, B.A., Iqbal, M.Y., Sreedhar, B. Electrochemical and surface analytical studies of the self-assembled monolayer of 5-methoxy-2-(octadecylthio) benzimidazole in corrosion protection of copper. **Electrochimica Acta. 2010**, 55, 620-31.

[71] Sastri, V.S. Corrosion inhibitors: Principle and application. **John Wiley & Sons, 1998, New York**.

[72] Awad, M.K., Mustafa, M.R., Elnga, M.M.A. Computational simulation of the molecular structure of some triazoles as inhibitors for the corrosion of metal surface. **Journal of Molecular Structure: THEOCHEM. 2010**, 959, 66-74.

[73] Behpour, M., Ghoreishi, S., Mohammadi, N., Soltani, N., Salavati-Niasari, M. Investigation of some Schiff base compounds containing disulfide bond as HCl corrosion inhibitors for MS. **Corrosion Science. 2010**, 52, 4046-57.

[74] Braun, R.D., Lopez, E.E., Vollmer, D.P. Low molecular weight straight-chain amines as corrosion inhibitors. **Corrosion Science. 1993**, 34, 1251-7.

[75] Deng, S., Li, X. Inhibition by Ginkgo leaves extract of the corrosion of steel in HCl and H 2 SO 4 solutions. **Corrosion Science. 2012**, 55, 407-15.

[76] Hosseini, M., Ehteshamzadeh, M., Shahrabi, T. Protection of MS corrosion with Schiff bases in 0.5 MH 2 SO 4 solution. **Electrochimica Acta. 2007**, 52, 3680-5.

[77] Kosari, A., Moayed, M.H., Davoodi, A., Parvizi, R., Momeni, M., Eshghi, H., et al. Electrochemical and quantum chemical assessment of two organic compounds from pyridine derivatives as corrosion inhibitors for MS in HCl solution under stagnant condition and hydrodynamic flow. **Corrosion Science. 2014**, 78, 138-50.

[78] Roy, P., Pal, A., Sukul, D. Origin of the synergistic effect between polysaccharide and thiourea towards adsorption and corrosion inhibition for MS in sulphuric acid. **RSC Advances. 2014**, 4, 10607-13.

[79] Song, P., Guo, X.-Y., Pan, Y.-C., Shen, S., Sun, Y., Wen, Y., et al. Insight in cysteamine adsorption behaviors on the copper surface by electrochemistry and Raman spectroscopy. **Electrochimica Acta**. 2013, 89, 503-9.

[80] Wahdan, M.H. The synergistic inhibition effect and thermodynamic properties of 2-mercaptobenzimidazol and some selected cations as a mixed inhibitor for pickling of MS in acid solution. **Materials Chemistry and Physics**. 1997, 49, 135-40.

[81] Zheludkevich, M., Yasakau, K., Poznyak, S., Ferreira, M. Triazole and thiazole derivatives as corrosion inhibitors for AA2024 aluminium alloy. **Corrosion Science. 2005**, 47, 3368-83.

[82] Aytac, A., Özmen, Ü., Kabasakaloğlu, M. Investigation of some Schiff bases as acidic corrosion of alloy AA3102. **Materials Chemistry and Physics**. 2005, 89, 176-81.

[83] Ebenso, E., Okafor, P., Ekpe, U. Studies on the inhibition of aluminium corrosion by 2-acetylphenothiazine in chloroacetic acids. **Anti-Corrosion Methods and Materials. 2003**, 50, 414-21.

[84] Ebenso, E.E., Kabanda, M.M., Murulana, L.C., Singh, A.K., Shukla, S.K. Electrochemical and quantum chemical investigation of some azine and thiazine dyes as potential corrosion inhibitors for MS in hydrochloric acid solution. **Industrial and Engineering Chemistry Research. 2012**, 51, 12940-58.

[85] Ghareba, S., Omanovic, S. Interaction of 12-aminododecanoic acid with a carbon steel surface: towards the development of 'green'corrosion inhibitors. **Corrosion Science. 2010**, 52, 2104-13.

[86] Obot, I., Obi-Egbedi, N. Anti-corrosive properties of xanthone on MS corrosion in sulphuric acid: Experimental and theoretical investigations. **Current Applied Physics. 2011**, 11, 382-92.

[87] Qafsaoui, W., Blanc, C., Pebere, N., Srhiri, A., Mankowski, G. Study of different triazole derivative inhibitors to protect copper against pitting corrosion. **Journal of Applied Electrochemistry. 2000**, 30, 959-66.

[88] Thomas, J.G.N. In: the proceedings of the fifth European symposium on corrosion inhibitors, Ferrara, Italy, 1980, p. 453.

[89] Fekry, A., Mohamed, R.R. Acetyl thiourea chitosan as an eco-friendly inhibitor for MS in sulphuric acid medium. **Electrochimica Acta. 2010**, 55, 1933-9.

[90] Soltani, N., Behpour, M., Oguzie, E., Mahluji, M., Ghasemzadeh, M. Pyrimidine-2-thione derivatives as corrosion inhibitors for MS in acidic environments. **RSC Advances. 2015**, 5, 11145-62.

[91] Tang, Y., Yang, X., Yang, W., Chen, Y., Wan, R. Experimental and molecular dynamics studies on corrosion inhibition of MS by 2-amino-5-phenyl-1, 3, 4-thiadiazole. **Corrosion Science. 2010**, 52, 242-9.

[92] Hassan, H.H., Abdelghani, E., Amin, M.A. Inhibition of MS corrosion in hydrochloric acid solution by triazole derivatives: Part I. Polarization and EIS studies. **Electrochimica Acta. 2007**, 52, 6359-66.

[93] Hinds, G. The Electrochemistry of Corrosion. **Corrosion Doctors Publications, 1996**.

[94] Perez, N. Electrochemistry and corrosion science. **Springer Science & Business Media, 2004**.

[95] Steigerwald, R. Electrochemistry of corrosion. **Corrosion. 1968**, 24, 1-10.

[96] Thomas, J. Organic inhibitors of corrosion of metals. **Springer Science & Business Media, 1996**.

[97] Evans, U.R. Metallic Corrosion and protection. **London, Edward Arnold, 1937**.

[98] Wagner, C., Traud, W. Über die Deutung von Korrosionsvorgängen durch Überlagerung von elektrochemischen Teilvorgängen und über die Potentialbildung an Mischelektroden. **Zeitschrift für Elektrochemie und angewandte physikalische Chemie. 1938**, 44, 391-402.

[99] Norio, S. Green Corrosion Chemistry and Engineering: Opportunities and Challenges. Sharma, S.K. Ed., W**iley-VCH Verlag GmbH & Co. , 2012**.

[100] Bard, A.J., Faulkner, L.R. Electrochemical methods: Fundamentals and applications. **John Wiley & Sons, 1980,** New York.

[101] Gamry application note: Getting Started with Electrochemical Corrosion Measurement: Review of the Electrochemical Basis of Corrosion. ***Retrieved from***: https://www.gamry.com/application-notes/corrosion-coatings/basics-of-electrochemical-corrosion-measurements/ (September, 2015).

[102] Kelly, R.G., Scully, J.R., Shoesmith, D., Buchheit, R.G. Electrochemical techniques in corrosion science and engineering, **CRC Press, 2002**.

[103] Flitt, H.J., Schweinsberg, D.P. Evaluation of corrosion rate from polarisation curves not exhibiting a Tafel region. **Corrosion Science. 2005**, 47, 3034-52.

[104] In: Princeton Applied Research Note.Application note AC-1: Basics of electrochemical impedance spectroscopy. ***Retrieved from***: http://www.princetonappliedresearch.com/Literature/index.aspx. (September, 2015).

[105] Hamdy, A.S., El-Shenawy, E., El-Bitar, T. Electrochemical impedance spectroscopy study of the corrosion behavior of some niobium bearing stainless steels in 3.5% NaCl. **International Journal of Electrochemical Science. 2006**, 1, 171-80.

[106] Qiu, J., Tang, C.-b., Zhu, Z.-j., Zhou, G.-x., Wang, J., Yang, Y., et al. XPS and electrochemical impedance spectroscopy studies on effects of the porcelain firing process on surface and corrosion properties of two nickel–chromium dental alloys. **Journal of Materials Science: Materials in Medicine. 2013**, 24, 2519-28.

[107] Gamry Application Note: Basics of Electrochemical Impedance Spectroscopy. ***Retrieved from***: https://www.gamry.com/application-notes/EIS/basics-of-electrochemical-impedance-spectroscopy/. (September, 2015).

[108] Xu, L.-n., Zhu, J.-y., Lu, M.-x., Zhang, L., Chang, W. Electrochemical impedance spectroscopy study on the corrosion of the weld zone of 3Cr steel welded joints in CO2 environments. **International Journal of Minerals, Metallurgy, and Materials. 2015**, 22, 500-8.

[109] Macdonald, J.R., Barsoukov, E. Impedance spectroscopy: theory, experiment, and applications. **History. 2005**, 1.

[110] Hirschorn, B., Orazem, M.E., Tribollet, B., Vivier, V., Frateur, I., Musiani, M. Constant-phase-element behavior caused by resistivity distributions in films I. Theory. **Journal of The Electrochemical Society. 2010**, 157, C452-C7.

[111] Mahdavian, M., Attar, M. Electrochemical behaviour of some transition metal acetylacetonate complexes as corrosion inhibitors for MS. **Corrosion Science. 2009**, 51, 409-14.

[112] Mashuga, M.E., Olasunkanmi, L.O., Adekunle, A.S., Yesudass, S., Kabanda, M.M., Ebenso, E.E. Adsorption, thermodynamic and quantum chemical studies of 1-hexyl-3-methylimidazolium based ionic liquids as corrosion inhibitors for MS in HCl. **Materials. 2015**, 8, 3607-32.

[113] Singh, A., Lin, Y., Liu, W., Kuanhai, D., Pan, J., Huang, B., et al. A study on the inhibition of N80 steel in 3.5% NaCl solution saturated with CO 2 by fruit extract of Gingko biloba. **Journal of the Taiwan Institute of Chemical Engineers. 2014**, 45, 1918-26.

[114] Jorcin, J.-B., Orazem, M.E., Pébère, N., Tribollet, B. CPE analysis by local electrochemical impedance spectroscopy. **Electrochimica Acta. 2006**, 51, 1473-9.

[115] Bojinov, M., Fabricius, G., Laitinen, T., Mäkelä, K., Saario, T., Sundholm, G. Coupling between ionic defect structure and electronic conduction in passive films on iron, chromium and iron–chromium alloys. **Electrochimica Acta. 2000**, 45, 2029-48.

[116] Ogukwe, C., Akalezi, C., Chidiebere, M., Oguzie, K., Iheabunike, Z., Oguziea, E. Corrosion Inhibition and Adsorption of Anthocleista Djalonesis Leaf Extract on the Acid Corrosion of MS. **Portugaliae Electrochimica Acta. 2012**, 30, 189-202.

[117] Quraishi, M.A. 2-Amino-3, 5-dicarbonitrile-6-thio-pyridines: new and effective corrosion inhibitors for MS in 1 M HCl. **Industrial and Engineering Chemistry Research. 2014**, 53, 2851-9.

[118] Gamry application note: The Constant Phase Element (CPE). ***Retrieved from***: https://www.gamry.com/application-notes/EIS/basics-of-electrochemical-impedance-spectroscopy/. (September, 2015).

[119] Jensen, F. Introduction to Computational Chemistry. **John Wiley & Sons Ltd., 2nd, 2007**.

[120] Cramer, C.J. Essentials of Computational Chemistry; Theories and Models. 2nd ed, Wiley, 2004.

[121] Olasunkanmi, L.O. Theoretical study of the molecular geometry, electronic and thermodynamic properties of novel 1,10-phenanthrolino[5,6-f]1,10-phenanthroline and its selected transition metal complexes. Obafemi Awolowo University, Ile-Ife, Nigeria, **MSc. Thesis, 2012**.

[122] Kiyak, H. Synthesis, Characterization and Computational Studies of Oxomolybdenum Compounds with Nitrogen Donor Ligands. Turkey, Izmir Institute of Technology; **MSc. Thesis, 2010**.

[123] Young, D.C. Computational Chemistry: A Practical Guide for Applying Techniques to Real-World Problems, J**ohn Wiley & Sons, Inc., 2001**.

[124] Ramachandran, K.I., Deepa, G., Namboori, K. Computational Chemistry and Molecular Modelling. **Springer, Berlin, 2008**.

[125] Slater, J.C. Atomic shielding constants. P**hysical Review. 1930**, 36, 57.

[126] Slater, J.C., Kirkwood, J.G. The van der Waals forces in gases. **Physical Review. 1931**, 37, 682.

[127] Ema, I., Garcia De La Vega, J., Ramırez, G. López,; Fernádez Rico, RJ; Meissner, H.; Paldus. **Journal of Computational Chemistry. 2003**, 24, 859-68.

[128] Boys, S.F. Electronic wavefunctions. I. A general method of calculation for stationary states of any molecular system. **Proceedings of the Royal Society of London A 1950**, 200, 542-54.

[129] Hunt, P. The Wavefunction. ***Retrieved from:*** http://www.huntresearchgroup.org.uk/teaching/teaching_comp_chem_year4/L2_Wavefunction.pdf. (September, 2015).

[130] Sanusi, S.O. Investigation of Substituent Effects on the Stability Properties of Cyclodextrin. Nigeria, Obafemi Awolowo University, Ile-Ife; **MSc. Thesis, 2011**.

[131] Hehre, W.J., Stewart, R.F., Pople, J.A. Self-consistent molecular-orbital methods. i. use of gaussian expansions of slater-type atomic orbitals. **The Journal of Chemical Physics. 1969**, 51, 2657-64.

[132] Woon, D.E., Dunning Jr, T.H. Gaussian basis sets for use in correlated molecular calculations. III. The atoms aluminum through argon. **The Journal of Chemical Physics. 1993**, 98, 1358-71.

[133] Woon, D.E., Dunning Jr, T.H. Gaussian basis sets for use in correlated molecular calculations. V. Core-valence basis sets for boron through neon. **The Journal of Chemical Physics. 1995**, 103, 4572-85.

[134] Cuevas, J.C. Introduction to Density Functional Theory. **Institut fur¨ Theoretische Festk¨orperphysik Universit¨at Karlsruhe (Germany**), 2015.

[135] Koch, W., Holthausen, M.C. A Chemist's Guide to Density Functional Theory, **Wiley-VCH Verlag GmbH ISBNs, 2001**.

[136] Hohenberg, P., Kohn, W. Inhomogeneous electron gas. **Physical Review. 1964**, 136, B864.

[137] Kohn, W., Sham, L.J. Self-consistent equations including exchange and correlation effects. **Physical Review. 1965**, 140, A1133.

[138] Allen, M.P., Tildesley, D.J. . Computer Simulation of Liquids. **Oxford, 1987**.

[139] Frenkel, D., Smit, B. . Understanding molecular simulation: from algorithms to applications. 2nd ed. **Academic Press, San Diego, 2002**.

[140] Li, J. AtomEye: an efficient atomistic configuration viewer. **Modelling and Simulation in Materials Science and Engineering. 2003**, 11, 173.

[141] Li, J. Basic molecular dynamics. In: Handbook of Materials Modeling, Yip, S. Ed., **Springer, the Netherlands, 2005**, 565–88.

[142] Meller, J. Molecular Dynamics. In: Encyclopedia of life sciences,, **Nature Publishing Group, 2001**.

[143] Nosé, S. A unified formulation of the constant temperature molecular dynamics methods. **The Journal of Chemical Physics. 1984,** 81, 511-9.

[144] Tuckerman, M.E., Martyna, G.J. Understanding modern molecular dynamics: techniques and applications. The Journal of Physical Chemistry B. 2000, 104, 159-78.

[145] Auffinger, P., Westhof, E. Simulations of the molecular dynamics of nucleic acids. **Current Opinion in Structural Biology. 1998**, 8, 227-36.

[146] Frenkel, D., Smit, B. From algorithms to applications. **Academic Press San Diego, CA:, 1996**.

[147] Heile, J.M. Molecular Dynamics Simulations: Elementary Methods. J**ohn Wiley, 1992New York**.

[148] Ansari, K., Quraishi, M., Singh, A. Schiff's base of pyridyl substituted triazoles as new and effective corrosion inhibitors for MS in hydrochloric acid solution. **Corrosion Science. 2014**, 79, 5-15.

[149] Solmaz, R., Şahin, E.A., Döner, A., Kardaş, G. The investigation of synergistic inhibition effect of rhodanine and iodide ion on the corrosion of copper in sulphuric acid solution. **Corrosion Science. 2011**, 53, 3231-40.

[150] Ahamad, I., Quraishi, M.A. Mebendazole: New and efficient corrosion inhibitor for MS in acid medium. **Corrosion Science. 2010**, 52, 651-6.

[151] Abiola, O., Oforka, N. Adsorption of (4-amino-2-methyl-5-pyrimidinyl methylthio) acetic acid on MS from hydrochloric acid solution (HCl)—Part 1. **Materials Chemistry and Physics. 2004**, 83, 315-22.

[152] Quraishi, M. Electrochemical and theoretical investigation of triazole derivatives on corrosion inhibition behavior of copper in hydrochloric acid medium. **Corrosion Science. 2013**, 70, 161-9.

[153] Kokalj, A. Is the analysis of molecular electronic structure of corrosion inhibitors sufficient to predict the trend of their inhibition performance. **Electrochimica Acta. 2010**, 56, 745-55.

[154] Kovačević, N., Kokalj, A. Analysis of molecular electronic structure of imidazole- and benzimidazole-based inhibitors: A simple recipe for qualitative estimation of chemical hardness. **Corrosion Science. 2011**, 53, 909-21.

[155] Obot, I., Gasem, Z. Theoretical evaluation of corrosion inhibition performance of some pyrazine derivatives. Corrosion Science. 2014, 83, 359-66.

[156] Xia, S., Qiu, M., Yu, L., Liu, F., Zhao, H. Molecular dynamics and density functional theory study on relationship between structure of imidazoline derivatives and inhibition performance. **Corrosion Science. 2008**, 50, 2021-9.

[157] Cao, C. On electrochemical techniques for interface inhibitor research. **Corrosion Science. 1996**, 38, 2073-82.

[158] Kovačević, N.a., Kokalj, A. DFT Study of Interaction of Azoles with Cu (111) and Al (111) Surfaces: Role of Azole Nitrogen Atoms and Dipole–Dipole Interactions. **The Journal of Physical Chemistry C. 2011**, 115, 24189-97.

[159] Kokalj, A., Peljhan, S. Density functional theory study of ATA, BTAH, and BTAOH as copper corrosion inhibitors: adsorption onto Cu (111) from gas phase. **Langmuir. 2010**, 26, 14582-93.

[160] Verma, C., Ebenso, E., Bahadur, I., Obot, I., Quraishi, M. 5-(Phenylthio)-3H-pyrrole-4-carbonitriles as effective corrosion inhibitors for MS in 1M HCl: Experimental and theoretical investigation. **Journal of Molecular Liquids. 2015**, 212, 209-18.

[161] Obot, I., Madhankumar, A., Umoren, S., Gasem, Z. Surface protection of MS using benzimidazole derivatives: experimental and theoretical approach. **Journal of Adhesion Science and Technology. 2015**, 29, 2130-52.

[162] Kaya, S., Tüzün, B., Kaya, C., Obot, I.B. Determination of corrosion inhibition effects of amino acids: Quantum chemical and molecular dynamic simulation study. **Journal of the Taiwan Institute of Chemical Engineers. 2015**, 58, 528-535.

[163] Obot, I., Umoren, S., Gasem, Z., Suleiman, R., El Ali, B. Theoretical prediction and electrochemical evaluation of vinylimidazole and allylimidazole as corrosion

inhibitors for MS in 1M HCl. **Journal of Industrial and Engineering Chemistry. 2015**, 21, 1328-39.

[164] Chesseman, G., Cookson, R.F. The Chemistry of Heterocyclic Compounds, Condensed Pyrazines, **John Wiley & Sons, 2009**.

[165] Eicher, T., Hauptmann, S., Speicher, A. The Chemistry of Heterocycles: Structures, Reactions, Synthesis, and Applications 3rd, **John Wiley & Sons, 2013**.

[166] Patidar, A.K., Jeyakandan, M., Mobiya, A.K., Selvam, G. Exploring potential of quinoxaline moiety. **International Journal of PharmTech Research 2011**, 3, 386-392.

[167] Thakuria, H., Das, G. One-pot efficient green synthesis of 1, 4-dihydro-quinoxaline-2, 3-dione derivatives. Journal of Chemical Sciences. 2006, 118, 425-8.

[168] Bansal, R.K. Heterocyclic chemistry. 3rd ed, **New Age International Pvt. Ltd., 2005**.

[169] Raw, S.A., Wilfred, C.D., Taylor, R.J. Tandem oxidation processes for the preparation of nitrogen-containing heteroaromatic and heterocyclic compounds. **Organic and Biomolecular Chemistry. 2004**, 2, 788-96.

[170] More, S.V., Sastry, M., Yao, C.-F. Cerium (IV) ammonium nitrate (CAN) as a catalyst in tap water: A simple, proficient and green approach for the synthesis of quinoxalines. **Green Chemistry. 2006**, 8, 91-5.

[171] Srinivas, C., Kumar, C.N.S.P., Rao, V.J., Palaniappan, S. Green approach for the synthesis of quinoxaline derivatives in water medium using reusable polyaniline-sulfate salt catalyst and sodium laurylsulfate. **Catalysis Letters. 2008**, 121, 291-6.

[172] Heravi, M.M., Taheri, S., Bakhtiari, K., Oskooie, H.A. On water: a practical and efficient synthesis of quinoxaline derivatives catalyzed by CuSO 4· 5H 2 O. **Catalysis Communications. 2007**, 8, 211-4.

[173] Sithambaram, S., Ding, Y., Li, W., Shen, X., Gaenzler, F., Suib, S.L. Manganese octahedral molecular sieves catalyzed tandem process for synthesis of quinoxalines. **Green Chemistry 2008**, 10, 1029-32.

[174] Dong, F., Kai, G., Zhenghao, F., Xinli, Z., Zuliang, L. A practical and efficient synthesis of quinoxaline derivatives catalyzed by task-specific ionic liquid. **Catalysis Communications. 2008**, 9, 317-20.

[175] Heravi, M.M., Bakhtiari, K., Oskooie, H.A., Taheri, S. MnCl2-Promoted synthesis of quinoxaline derivatives at room temperature. **Heteroatom Chemistry. 2008**, 19, 218-20.

[176] Huang, T.K., Shi, L., Wang, R., Guo, X.Z., Lu, X.X. Keggin type heteropolyacids-catalyzed synthesis of quinoxaline derivatives in water. **Chinese Chemical Letters. 2009**, 20, 161-4.

[177] Raju, B.C., Theja, N.D., Kumar, J.A. Efficient and inexpensive synthesis of benzimidazoles and quinoxalines. **Synthetic Communications. 2008**, 39, 175-88.

[178] Cho, C.S., Ren, W.X. A recyclable copper catalysis in quinoxaline synthesis from α-hydroxyketones and o-phenylenediamines. **Journal of Organometallic Chemistry. 2009**, 694, 3215-7.

[179] Shi, D.-Q., Dou, G.-L., Ni, S.-N., Shi, J.-W., Li, X.-Y. An efficient synthesis of quinoxaline derivatives mediated by stannous chloride. **Journal of Heterocyclic Chemistry. 2008**, 45, 1797-801.

[180] Meshram, H., Kumar, G.S., Ramesh, P., Reddy, B.C. A mild and convenient synthesis of quinoxalines via cyclization–oxidation process using DABCO as catalyst. **Tetrahedron Letters. 2010**, 51, 2580-5.

[181] Loriga, M., Nuvole, A., Paglietti, G. Quinoxaline chemistry. III: Selectivity in quinoxaline formation from o-phenylenediamines and phenylglyoxal. J**ournal of Chemical Research. Synopses. 1989**, 202-3.

[182] Obot, I., Obi-Egbedi, N., Odozi, N. Acenaphtho [1, 2-b] quinoxaline as a novel corrosion inhibitor for MS in 0.5 M H_2SO_4. **Corrosion Science. 2010**, 52, 923-6.

[183] Elayyachy, M., Hammouti, B., El Idrissi, A., Aouniti, A. Adsorption and corrosion inhibition behavior of C38 steel by one derivative of quinoxaline in 1 M HCl. **Portugaliae Electrochimica Acta. 2011**, 29, 57-68.

[184] Chitra, S., Parameswari, K., Vidhya, M., Kalishwari, M., Selvaraj, A. Evaluation of Quinoxalines as corrosion inhibitors for MS in acid environment. **International Journal of Electrochemical Science 2011**, 6, 4593-613.

[185] Kabanda, M.M., Ebenso, E.E. Density functional theory and quantitative structureactivity relationship studies of some quinoxaline derivatives as potential corrosion inhibitors for copper in acidic medium. **International Journal of Electrochemical Science 2012**, 7, 8713-33.

[186] Zarrok, H., Zarrouk, A., Salghi, R., Ramli, Y., Hammouti, B., Al-Deyab, S., et al. Adsorption and inhibition effect of 3-methyl-1-propargylquinoxalin-2 (1H)-one on carbon steel corrosion in hydrochloric acid. **International Journal of Electrochemical Science 2012**, 7, 8958-73.

[187] Adardour, K., Kassou, O., Touir, R., Ebn Touhami, M., ElKafsaoui, H., Benzeid, H. Essassi El M., Sfaira M. **Journal of Materials and Environmental Science. 2010**, 1, 129.

[188] Fu, J., Zang, H., Wang, Y., Li, S., Chen, T., Liu, X. Experimental and theoretical study on the inhibition performances of quinoxaline and its derivatives for the corrosion of MS in hydrochloric acid. **Industrial and Engineering Chemistry Research. 2012**, 51, 6377-86.

[189] Davis, J.R. Corrosion: Understanding the basics. **ASM International, Materials Park, USA., 2000**.

[190] Murulana, L.C., Singh, A.K., Shukla, S.K., Kabanda, M.M., Ebenso, E.E. Experimental and quantum chemical studies of some bis (trifluoromethyl-sulfonyl) imide imidazolium-based ionic liquids as corrosion inhibitors for MS in hydrochloric acid solution. **Industrial and Engineering Chemistry Research. 2012**, 51, 13282-99.

[191] Olasunkanmi, L.O., Obot, I.B., Kabanda, M.M., Ebenso, E.E. Some quinoxalin-6-yl derivatives as corrosion inhibitors for MS in hydrochloric acid: Experimental and theoretical studies. **The Journal of Physical Chemistry C. 2015**, 119, 16004-19.

[192] Saha, S.K., Dutta, A., Ghosh, P., Sukul, D., Banerjee, P. Adsorption and corrosion inhibition effect of Schiff base molecules on the MS surface in 1 M HCl medium: a combined experimental and theoretical approach. **Physical Chemistry Chemical Physics. 2015**, 17, 5679-90.

[193] Umoren, S.A., Obot, I.B., Gasem, Z.M. Adsorption and corrosion inhibition characteristics of strawberry fruit extract at steel/acids interfaces: experimental and theoretical approaches. **Ionics. 2015**, 21, 1171-86.

[194] Ahamad, I., Prasad, R., Quraishi, M. Thermodynamic, electrochemical and quantum chemical investigation of some Schiff bases as corrosion inhibitors for MS in hydrochloric acid solutions. **Corrosion Science. 2010**, 52, 933-42.

[195] Elmsellem, H., Harit, T., Aouniti, A., Malek, F., Riahi, A., Chetouani, A., et al. Adsorption properties and inhibition of MS corrosion in 1 M HCl solution by some bipyrazolic derivatives: Experimental and theoretical investigations. **Protection of Metals and Physical Chemistry of Surfaces. 2015**, 51, 873-84.

[196] Ousslim, A., Bekkouch, K., Chetouani, A., Abbaoui, E., Hammouti, B., Aouniti, A., et al. Adsorption and corrosion inhibitive properties of piperidine derivatives on MS in phosphoric acid medium. **Research on Chemical Intermediates. 2014**, 40, 1201-21.

[197] Singh, A., Ahamad, I., Singh, V., Quraishi, M.A. Inhibition effect of environmentally benign Karanj (Pongamia pinnata) seed extract on corrosion of MS in hydrochloric acid solution. **Journal of Solid State Electrochemistry. 2011**, 15, 1087-97.

[198] Singh, A.K., Quraishi, M. Investigation of the effect of disulfiram on corrosion of MS in hydrochloric acid solution. **Corrosion Science. 2011**, 53, 1288-97.

[199] Yadav, D.K., Quraishi, M., Maiti, B. Inhibition effect of some benzylidenes on MS in 1M HCl: an experimental and theoretical correlation. **Corrosion Science. 2012**, 55, 254-66.

[200] Ali, S.A., Saeed, M.T., Rahman, S.U. The isoxazolidines: a new class of corrosion inhibitors of MS in acidic medium. **Corrosion Science. 2003**, 45, 253-66.

[201] Simillion, H. Study of the protective effect of corrosion inhibitors in an organic coating on galvanized steel. Nanocontainers for self-healing coatings. Vrije Universiteit Brussel, **MSc. Thesis 2012**.

[202] Satapathy, A., Gunasekaran, G., Sahoo, S., Amit, K., Rodrigues, P. Corrosion inhibition by Justicia gendarussa plant extract in hydrochloric acid solution. **Corrosion Science. 2009**, 51, 2848-56.

[203] Patil, R., Radhakrishnan, S. Conducting polymer based hybrid nano-composites for enhanced corrosion protective coatings. **Progress in Organic Coatings. 2006**, 57, 332-6.

[204] Loto, R.T., Loto, C.A., Popoola, A.P.I., Fedotova, T. Inhibition effect of butan-1-ol on the corrosion behavior of austenitic stainless steel (Type 304) in dilute sulfuric acid. A**rabian Journal of Chemistry, 2015**. doi:10.1016/j.arabjc.2014.12.024

[205] Kharchouf, S., Majidi, L., Bouklah, M., Hammouti, B., Bouyanzer, A., Aouniti, A. Effect of three 2-allyl-p-mentha-6, 8-dien-2-ols on inhibition of MS corrosion in 1M HCl. **Arabian Journal of Chemistry. 2014**, 7, 680-6.

[206] Umoren, S., Obot, I. Synergistic inhibition between 1-octadecanethiol and iodide ions on X60 pipeline steel for corrosion protection. **Journal of Adhesion Science and Technology. 2014**, 28, 2054-68.

[207] Umoren, S., Obot, I., Madhankumar, A., Gasem, Z. Effect of degree of hydrolysis of polyvinyl alcohol on the corrosion inhibition of steel: theoretical and experimental studies. **Journal of Adhesion Science and Technology. 2015**, 29, 271-95.

[208] Umoren, S.A., Gasem, Z.M., Obot, I.B. Natural products for material protection: inhibition of MS corrosion by date palm seed extracts in acidic media. **Industrial and Engineering Chemistry Research. 2013**, 52, 14855-65.

[209] Tao, Z., Zhang, S., Li, W., Hou, B. Corrosion inhibition of MS in acidic solution by some oxo-triazole derivatives. **Corrosion Science. 2009**, 51, 2588-95.

[210] Li, X., Deng, S., Fu, H., Mu, G., Zhao, N. Synergism between rare earth cerium (IV) ion and vanillin on the corrosion of steel in H 2 SO 4 solution: weight loss, electrochemical, UV–vis, FTIR, XPS, and AFM approaches. **Applied Surface Science. 2008**, 254, 5574-86.

[211] Becke, A.D. Density-functional thermochemistry. III. The role of exact exchange. **The Journal of Chemical Physics. 1993**, 98, 5648-52.

[212] Parr, R.G., Yang, W. Density functional approach to the frontier-electron theory of chemical reactivity. **Journal of the American Chemical Society. 1984**, 106, 4049-50.

[213] Lee, C., Yang, W., Parr, R.G. Development of the Colle-Salvetti correlation-energy formula into a functional of the electron density. **Physical Review B**. 1988, 37, 785.

[214] Brovarets, O.h.O., Zhurakivsky, R.O., Hovorun, D.M. Does the tautomeric status of the adenine bases change upon the dissociation of the A*· A (syn) Topal-Fresco DNA mismatch? A combined QM and QTAIM atomistic insight. **Physical Chemistry Chemical Physics. 2014**, 16, 3715-25.

[215] Lozynski, M., Rusinska-Roszak, D., Mack, H.-G. Hydrogen bonding and density functional calculations: The B3LYP approach as the shortest way to MP2 results. **The Journal of Physical Chemistry A. 1998**, 102, 2899-903.

[216] Samijlenko, S.P., Yurenko, Y.P., Stepanyugin, A.V., Hovorun, D.M. Tautomeric equilibrium of uracil and thymine in model protein− nucleic acid contacts. Spectroscopic and quantum chemical approach. T**he Journal of Physical Chemistry B. 2010**, 114, 1454-61.

[217] Wiberg, K.B. Basis set effects on calculated geometries: 6-311++ G** vs. aug-cc-pVDZ. **Journal of Computational Chemistry. 2004**, 25, 1342-6.

[218] Frisch, M., Trucks, G., Schlegel, H., Scuseria, G., Robb, M., Cheeseman, J., et al. **Gaussian Inc. 2009**.

[219] Koopmans, T. Über die Zuordnung von Wellenfunktionen und Eigenwerten zu den einzelnen Elektronen eines Atoms. **Physica. 1934**, 1, 104-13.

[220] Mendoza-Huizar, L.H., Rios-Reyes, C.H. Chemical reactivity of atrazine employing the Fukui function. **Journal of Mexican Chemical Society. 2011**, 3, 142-7.

[221] Martinez, S. Inhibitory mechanism of mimosa tannin using molecular modeling and substitutional adsorption isotherms. **Materials Chemistry and Physics. 2003**, 77, 97-102.

[222] Pearson, R.G. Absolute electronegativity and hardness: application to inorganic chemistry. **Inorganic Chemistry. 1988**, 27, 734-40.

[223] Gomez, B., Likhanova, N., Dominguez-Aguilar, M., Martinez-Palou, R., Vela, A., Gazquez, J.L. Quantum chemical study of the inhibitive properties of 2-pyridyl-azoles. **The Journal of Physical Chemistry B. 2006**, 110, 8928-34.

[224] Yan, Y., Wang, X., Zhang, Y., Wang, P., Zhang, J. Theoretical evaluation of inhibition performance of purine corrosion inhibitors. **Molecular Simulation. 2013**, 39, 1034-41.

[225] Echegaray, E., Cárdenas, C., Rabi, S., Rabi, N., Lee, S., Zadeh, F.H., et al. In pursuit of negative Fukui functions: examples where the highest occupied molecular orbital fails to dominate the chemical reactivity. **Journal of Molecular Modeling. 2013**, 19, 2779-83.

[226] Li, Y., Evans, J.N. The Fukui function: a key concept linking frontier molecular orbital theory and the hard-soft-acid-base principle. **Journal of the American Chemical Society. 1995**, 117, 7756-9.

[227] Yang, W., Mortier, W.J. The use of global and local molecular parameters for the analysis of the gas-phase basicity of amines. **Journal of the American Chemical Society. 1986**, 108, 5708-11.

[228] Lu, T., Chen, F. Multiwfn: a multifunctional wavefunction analyzer. **Journal of Computational Chemistry. 2012**, 33, 580-92.

[229] Lu, T., Chen, F. Quantitative analysis of molecular surface based on improved Marching Tetrahedra algorithm. **Journal of Molecular Graphics and Modelling. 2012**, 38, 314-23.

[230] Anderson, A.B., Mehandru, S. Acetylene adsorption to Fe (100),(110), and (111) surfaces; structures and reactions. **Surface Science. 1984**, 136, 398-418.

[231] Khaled, K. Monte Carlo simulations of corrosion inhibition of MS in 0.5 M sulphuric acid by some green corrosion inhibitors. **Journal of Solid State Electrochemistry. 2009**, 13, 1743-56.

[232] Arya, A., Carter, E.A. Structure, bonding, and adhesion at the TiC (100)/Fe (110) interface from first principles. **The Journal of Chemical Physics. 2003**, 118, 8982-96.

[233] Arya, A., Carter, E.A. Structure, bonding, and adhesion at the ZrC (100)/Fe (110) interface from first principles. **Surface Science. 2004**, 560, 103-20.

[234] Guo, L., Ren, X., Zhou, Y., Xu, S., Gong, Y., Zhang, S. Theoretical evaluation of the corrosion inhibition performance of 1, 3-thiazole and its amino derivatives. **Arabian Journal of Chemistry. 2015**. doi:10.1016/j.arabjc.2015.01.005.

[235] Luo, X., Zhang, S., Guo, L. Investigation of a Pharmaceutically Active Compound Omeprazole as Inhibitor for Corrosion of MS in H_2SO_4 Solution. **International Journal of Electrochemical Science. 2014**, 9, 7309-24.

[236] Singh, A., Lin, Y., Quraishi, M.A., Olasunkanmi, L.O., Fayemi, O.E., Sasikumar, Y., et al. Porphyrins as Corrosion Inhibitors for N80 Steel in 3.5% NaCl Solution: Electrochemical, Quantum Chemical, QSAR and Monte Carlo Simulations Studies. **Molecules. 2015**, 20, 15122-46.

[237] Tan, J., Guo, L., Lv, T., Zhang, S. Experimental and Computational Evaluation of 3-indolebutyric Acid as a Corrosion Inhibitor for MS in Sulfuric Acid Solution. **International Journal of Electrochemical Science. 2015**, 10, 823-37.

[238] Bunte, S.W., Sun, H. Molecular modeling of energetic materials: the parameterization and validation of nitrate esters in the COMPASS force field. **The Journal of Physical Chemistry B. 2000**, 104, 2477-89.

[239] Liu, G., Chen, S., Hongfang, M., Liu, X. Molecular simulation study of 1, 5-diphenylcarbazide self-assembled monolayers on a copper surface. **Journal of the Serbian Chemical Society. 2007**, 72, 475-84.

[240] McQuaid, M.J., Sun, H., Rigby, D. Development and validation of COMPASS force field parameters for molecules with aliphatic azide chains. **Journal of Computational Chemistry. 2004**, 25, 61-71.

[241] Sun, H., Ren, P., Fried, J. The COMPASS force field: parameterization and validation for phosphazenes. **Computational and Theoretical Polymer Science. 1998**, 8, 229-46.

[242] Yang, J., Ren, Y., Tian, A.-m., Sun, H. COMPASS force field for 14 inorganic molecules, He, Ne, Ar, Kr, Xe, H2, O2, N2, NO, CO, CO2, NO2, CS2, and SO2, in liquid phases. **The Journal of Physical Chemistry B. 2000**, 104, 4951-7.

[243] Olasunkanmi, L.O., Kabanda, M.M., Ebenso, E.E. Quinoxaline derivatives as corrosion inhibitors for MS in hydrochloric acid medium: Electrochemical and quantum chemical studies. **Physica E: Low-dimensional Systems and Nanostructures. 2016**, 76, 109-26.

[244] Al-Amiery, A.A., Kadhum, A.A.H., Mohamad, A.B., Junaedi, S. A novel hydrazinecarbothioamide as a potential corrosion inhibitor for MS in HCl. **Materials. 2013**, 6, 1420-31.

[245] Liu, F., Du, M., Zhang, J., Qiu, M. Electrochemical behavior of Q235 steel in saltwater saturated with carbon dioxide based on new imidazoline derivative inhibitor. **Corrosion Science. 2009**, 51, 102-9.

[246] Zhou, Y., Xu, S., Guo, L., Zhang, S., Lu, H., Gong, Y., et al. Evaluating two new Schiff bases synthesized on the inhibition of corrosion of copper in NaCl solutions. **RSC Advances. 2015**, 5, 14804-13.

[247] de Souza, F.S., Spinelli, A. Caffeic acid as a green corrosion inhibitor for MS. **Corrosion Science. 2009**, 51, 642-9.

[248] Maayta, A., Al-Rawashdeh, N. Inhibition of acidic corrosion of pure aluminum by some organic compounds. **Corrosion Science. 2004**, 46, 1129-40.

[249] Saliyan, V.R., Adhikari, A.V. Quinolin-5-ylmethylene-3-{[8-(trifluoromethyl)quinolin-4-yl]thio}propanohydrazide as an effective inhibitor of MS corrosion in HCl solution. **Corrosion Science. 2008**, 50, 55-61.

[250] Daoud, D., Douadi, T., Issaadi, S., Chafaa, S. Adsorption and corrosion inhibition of new synthesized thiophene Schiff base on MS X52 in HCl and H 2 SO 4 solutions. **Corrosion Science. 2014**, 79, 50-8.

[251] John, S., Kuruvilla, M., Joseph, A. Adsorption and inhibition effect of methyl carbamate on copper metal in 1 N HNO_3: an experimental and theoretical study. **RSC Advances. 2013**, 3, 8929-38.

[252] Chang, D.W., Ko, S.-J., Kim, J.Y., Dai, L., Baek, J.-B. Multifunctional quinoxaline containing small molecules with multiple electron-donating moieties: Solvatochromic and optoelectronic properties. **Synthetic Metals. 2012**, 162, 1169-76.

[253] Marin, L., Lutsen, L., Vanderzande, D., Maes, W. Quinoxaline derivatives with broadened absorption patterns. **Organic and Biomolecular Chemistry. 2013**, 11, 5866-76.

[254] Tamilarasan, R., Sreekanth, A. Spectroscopic and DFT investigations on the corrosion inhibition behavior of tris (5-methyl-2-thioxo-1, 3, 4-thiadiazole) borate on high carbon steel and aluminium in HCl media. **RSC Advances. 2013**, 3, 23681-91.

[255] Choi, Y.-S., Lee, W.-h., Kim, J.-R., Lee, S.-K., Shin, W.-S., Moon, S.-J., et al. Synthesis and Characterization of Quinoxaline-Based Thiophene Copolymers as Photoactive Layers in Organic Photovoltaic Cells. **Bulletin of Korean Chemical Society. 2011**, 32, 417-23.

[256] Yamamoto, T., Zhou, Z.-h., Kanbara, T., Shimura, M., Kizu, K., Maruyama, T., et al. π-Conjugated donor-acceptor copolymers constituted of π-excessive and π-deficient arylene units. Optical and electrochemical properties in relation to CT structure of the polymer. **Journal of the American Chemical Society. 1996**, 118, 10389-99.

[257] Ansari, K., Quraishi, M. Experimental and computational studies of naphthyridine derivatives as corrosion inhibitor for N80 steel in 15% hydrochloric acid. **Physica E: Low-dimensional Systems and Nanostructures. 2015**, 69, 322-31.

[258] Ebenso, E.E., Obot, I.B., Murulana, L. Quinoline and its derivatives as effective corrosion inhibitors for MS in acidic medium. **International Journal of Electrochemical Science. 2010**, 5, 1574-86.

[259] Lebrini, M., Lagrenee, M., Vezin, H., Gengembre, L., Bentiss, F. Electrochemical and quantum chemical studies of new thiadiazole derivatives adsorption on MS in normal hydrochloric acid medium. **Corrosion Science. 2005**, 47, 485-505.

[260] Li, X., Deng, S., Fu, H., Mu, G. Inhibition effect of 6-benzylaminopurine on the corrosion of cold rolled steel in H 2 SO 4 solution. **Corrosion Science. 2009**, 51, 620-34.

[261] Yadav, M., Sharma, D. Inhibition of Corrosion of Copper by 2, 5-dimercapto-1, 3, 4-thiadiazole in 3, 5% NaCl solution. **Indian Journal of Chimical Technology. 2010**, 17, 95-101.

[262] Tao, Z., Zhang, S., Li, W., Hou, B. Adsorption and inhibitory mechanism of 1 H-1, 2, 4-triazol-l-yl-methyl-2-(4-chlorophenoxy) acetate on corrosion of MS in acidic solution. **Industrial and Engineering Chemistry Research. 2011**, 50, 6082-8.

[263] Ehsani, A., Mahjani, M.G., Moshrefi, R., Mostaanzadeh, H., Shayeh, J.S. Electrochemical and DFT study on the inhibition of 316L stainless steel corrosion in acidic medium by 1-(4-nitrophenyl)-5-amino-1 H-tetrazole. **RSC Advances. 2014**, 4, 20031-7.

[264] Farag, A.A., Ali, T.A. The enhancing of 2-pyrazinecarboxamide inhibition effect on the acid corrosion of carbon steel in presence of iodide ions. **Journal of Industrial and Engineering Chemistry. 2015**, 21, 627-34.

[265] Lagrenee, M., Mernari, B., Bouanis, M., Traisnel, M., Bentiss, F. Study of the mechanism and inhibiting efficiency of 3, 5-bis (4-methylthiophenyl)-4H-1, 2, 4-triazole on MS corrosion in acidic media. **Corrosion Science. 2002**, 44, 573-88.

[266] Outirite, M., Lagrenée, M., Lebrini, M., Traisnel, M., Jama, C., Vezin, H., et al. ac impedance, X-ray photoelectron spectroscopy and density functional theory studies of 3, 5-bis (n-pyridyl)-1, 2, 4-oxadiazoles as efficient corrosion inhibitors for carbon steel surface in hydrochloric acid solution. **Electrochimica Acta. 2010**, 55, 1670-81.

[267] Dukhin, S.S., Kretzschmar, G., Miller, R. Dynamics of adsorption at liquid interfaces: theory, experiment, application, **Elsevier Science BV, 1995**, Amsterdam.

[268] Vračar, L.M., Dražić, D. Adsorption and corrosion inhibitive properties of some organic molecules on iron electrode in sulfuric acid. **Corrosion Science. 2002**, 44, 1669-80.

[269] Hmamou, D.B., Salghi, R., Zarrouk, A., Aouad, M.R., Benali, O., Zarrok, H., et al. Weight loss, electrochemical, quantum chemical calculation, and molecular dynamics simulation studies on 2-(Benzylthio)-1, 4, 5-triphenyl-1H-imidazole as an Inhibitor for carbon steel corrosion in hydrochloric acid. **Industrial and Engineering Chemistry Research. 2013**, 52, 14315-27.

[270] Yurt, A., Balaban, A., Kandemir, S.U., Bereket, G., Erk, B. Investigation on some Schiff bases as HCl corrosion inhibitors for carbon steel. M**aterials Chemistry and Physics. 2004**, 85, 420-6.

[271] Lukovits, I., Kalman, E., Zucchi, F. Corrosion inhibitors-correlation between electronic structure and efficiency. **Corrosion. 2001**, 57, 3-8.

[272] Arab, S.T. Inhibition action of thiosemicabazone and some of it is ρ-substituted compounds on the corrosion of iron-base metallic glass alloy in 0.5 M H_2SO_4 at 30 ^oC. **Materials Research Bulletin. 2008**, 43, 510-21.

[273] Casewit, C., Colwell, K., Rappe, A. Application of a universal force field to main group compounds. **Journal of the American Chemical Society. 1992**, 114, 10046-53.

[274] Oguzie, E., Enenebeaku, C., Akalezi, C., Okoro, S., Ayuk, A., Ejike, E. Adsorption and corrosion-inhibiting effect of Dacryodis edulis extract on low-carbon-steel corrosion in acidic media. **Journal of Colloid and Interface Science. 2010**, 349, 283-92.

[275] Popova, A., Christov, M., Deligeorgiev, T. Influence of the molecular structure on the inhibitor properties of benzimidazole derivatives on MS corrosion in 1 M hydrochloric acid. **Corrosion. 2003**, 59, 756-64.

[276] Saha, S.K., Hens, A., RoyChowdhury, A., Lohar, A.K., Murmu, N., Banerjee, P. Molecular dynamics and density functional theory study on corrosion inhibitory action of three substituted pyrazine derivatives on steel surface. **Canadian Chemical Transactions. 2014**, 2, 489-503.

[277] Makowski, M., Raczynska, E.D., Chmurzynski, L. Ab initio study of possible and preferred basic site (s) in polyfunctional N 1, N 1-Dimethyl-N 2-cyanoformamidine. **The Journal of Physical Chemistry A**. **2001**, 105, 869-74.

[278] Raczyńska, E., Makowski, M., Górnicka, E., Darowska, M. Ab Initio Studies on the Preferred Site of Protonation in Cytisine in the Gas Phase and Water. **International Journal of Molecular Sciences. 2005**, 6, 143.

[279] Raczynska, E.D., Darowska, M., Dabkowska, I., Decouzon, M., Gal, J.-F., Maria, P.-C., et al. Experimental and Theoretical Evidence of Basic Site Preference in Polyfunctional Superbasic Amidinazine: N 1, N 1-Dimethyl-N 2-β-(2-pyridylethyl) formamidine. **The Journal of Organic Chemistry. 2004**, 69, 4023-30.

[280] Raczyńska, E.D., Woźniak, K., Dolecka, E., Darowska, M. Superbasic properties of the S=N functional group. **Journal of Physical Organic Chemistry. 2002**, 15, 706-11.

[281] Madhankumar, A., Thangavel, E., Ramakrishna, S., Obot, I.B., Jung, H.C., Shin, K.S., et al. Multi-functional ceramic hybrid coatings on biodegradable AZ31 Mg implants: electrochemical, tribological and quantum chemical aspects for orthopaedic applications. **RSC Advances. 2014**, 4, 24272-85.

[282] Kumar, A.M., Babu, R.S., Obot, I., Gasem, Z.M. Fabrication of nitrogen doped graphene oxide coatings: experimental and theoretical approach for surface protection. **RSC Advances. 2015**, 5, 19264-72.

[283] Wade, J.L.G. Organic Chemistry. 6th ed. **Upper Saddle River, NJ, Pearson Prentice Hall, 2006**.

[284] Amin, M.A., Abd El-Rehim, S.S., El-Sherbini, E.E.F., Bayoumi, R.S. The inhibition of low carbon steel corrosion in hydrochloric acid solutions by succinic acid: Part I. Weight loss, polarization, EIS, PZC, EDX and SEM studies. **Electrochimica Acta. 2007**, 52, 3588-600.

[285] Umoren, S.A., Li, Y., Wang, F.H. Electrochemical study of corrosion inhibition and adsorption behaviour for pure iron by polyacrylamide in H2SO4: Synergistic effect of iodide ions. **Corrosion Science. 2010**, 52, 1777-86.

[286] Al-Amiery, A.A., Kadhum, A.A.H., Mohamad, A.B., Musa, A.Y., Li, C.J. Electrochemical study on newly synthesized chlorocurcumin as an inhibitor for MS corrosion in hydrochloric acid. **Materials. 2013**, 6, 5466-77.

[287] Cang, H., Fei, Z., Shi, W., Xu, Q. Experimental and theoretical study for corrosion inhibition of MS by L-Cysteine. I**nternational Journal of Electrochemical Science. 2012**, 7, 10121-31.

[288] Verma, C., Quraishi, M., Olasunkanmi, L., Ebenso, E.E. l-Proline-promoted synthesis of 2-amino-4-arylquinoline-3-carbonitriles as sustainable corrosion inhibitors for MS in 1 M HCl: experimental and computational studies. **RSC Advances. 2015**, 5, 85417-30.

[289] Ramaganthan, B., Gopiraman, M., Olasunkanmi, L.O., Kabanda, M.M., Yesudass, S., Bahadur, I., et al. Synthesized photo-cross-linking chalcones as novel corrosion inhibitors for MS in acidic medium: experimental, quantum chemical and Monte Carlo simulation studies. **RSC Advances. 2015**, 5, 76675-88.

[290] Cao, P., Gu, R., Tian, Z. Electrochemical and surface-enhanced Raman spectroscopy studies on inhibition of iron corrosion by benzotriazole. **Langmuir. 2002**, 18, 7609-15.

[291] Lozano, I., Mazario, E., Olivares-Xometl, C., Likhanova, N., Herrasti, P. Corrosion behaviour of API 5LX52 steel in HCl and H 2 SO 4 media in the presence of 1, 3-dibencilimidazolio acetate and 1, 3-dibencilimidazolio dodecanoate ionic liquids as inhibitors. **Materials Chemistry and Physics**. 2014, 147, 191-7.

[292] Eldesoky, A., Diab, M., El-Bindary, A., El-Sonbati, A., Seyam, H. Some antipyrine derivatives as corrosion inhibitors for copper in acidic medium: Experimental and quantum chemical molecular dynamics approach. **Journal of Materials and Environmental Science. 2015**, 6, 2148-2165

[293] Quartarone, G., Bellomi, T., Zingales, A. Inhibition of copper corrosion by isatin in aerated 0.5 M H_2SO_4. **Corrosion Science. 2003**, 45, 715-33.

[294] Schultze, J., Wippermann, K. Inhibition of electrode processes on copper by AHT in acid solutions. **Electrochimica Acta. 1987**, 32, 823-31.

[295] Cao, Z., Tang, Y., Cang, H., Xu, J., Lu, G., Jing, W. Novel benzimidazole derivatives as corrosion inhibitors of MS in the acidic media. Part II: Theoretical studies. **Corrosion Science. 2014**, 83, 292-8.

[296] Hassan, H.H. Inhibition of MS corrosion in hydrochloric acid solution by triazole derivatives: Part II: Time and temperature effects and thermodynamic treatments. **Electrochimica Acta. 2007**, 53, 1722-30.

[297] Verma, C.B., Reddy, M.J., Quraishi, M.A. Ultrasound Assisted Green Synthesis of 3-(4-(dimethylamino) phenyl)-1-phenylprop-2-en-1-one and its Heterocyclics Derived from Hydrazine, Urea and Thiourea as Corrosion Inhibitor for MS in 1 M HCl. **Analytical and Bioanalytical Electrochemistry. 2014**, 6, 515-5342014.

APPENDIX I: SUPPLEMENTRARY FIGURES GROUP I

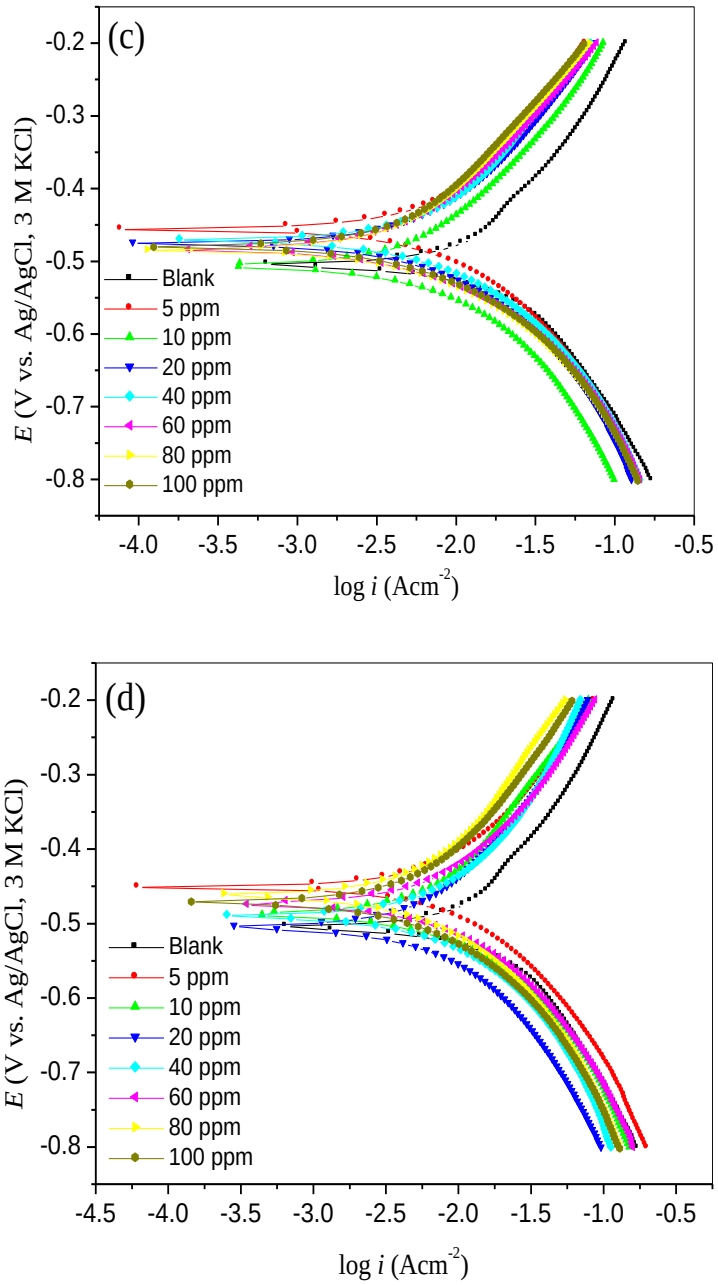

Figure AI-1. Tafel plots for MS in 1 M HCl without and with various concentrations of (c) Mt-3-PQPB and (d) Oxo-1,3-PQPB.

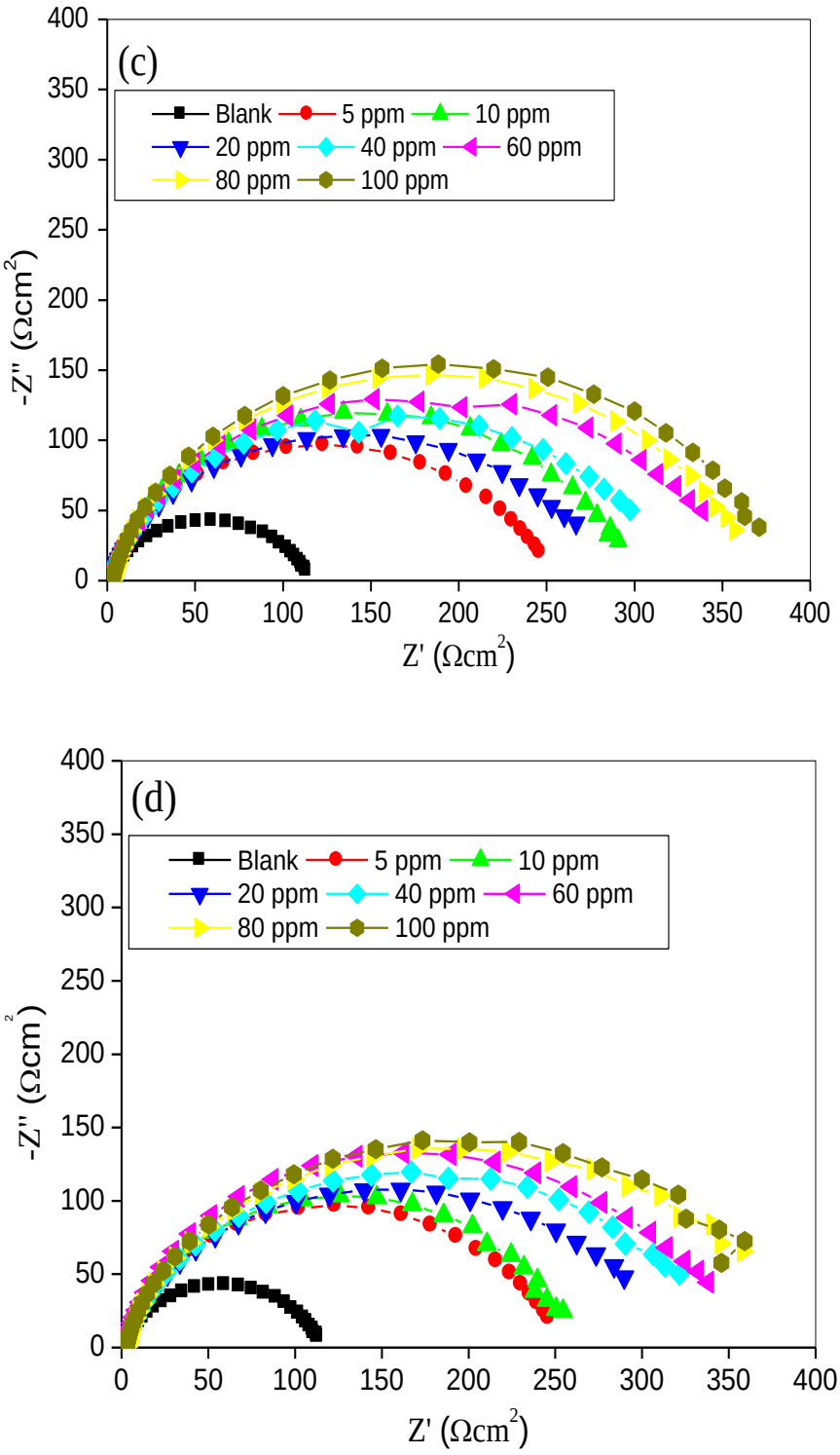

Figure AI-2. Nyquist plots for MS in 1 M HCl without and with various concentrations of (c) Mt-3-PQPB, and (d) Oxo-1,3- PQPB.

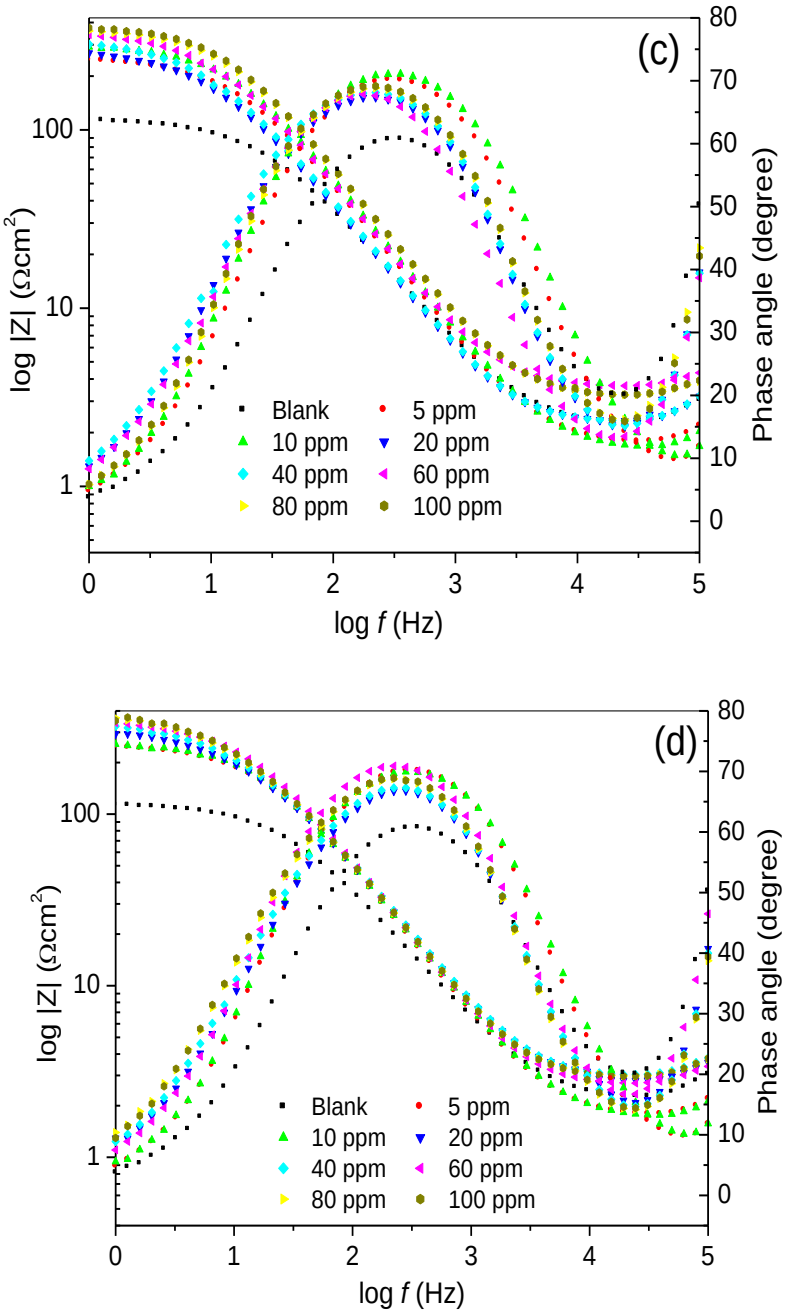

Figure AI-3. Bode plots for MS in 1 M HCl without and with various concentrations of (c) Mt-3-PQPB, and (d) Oxo-1,3-PQPB.

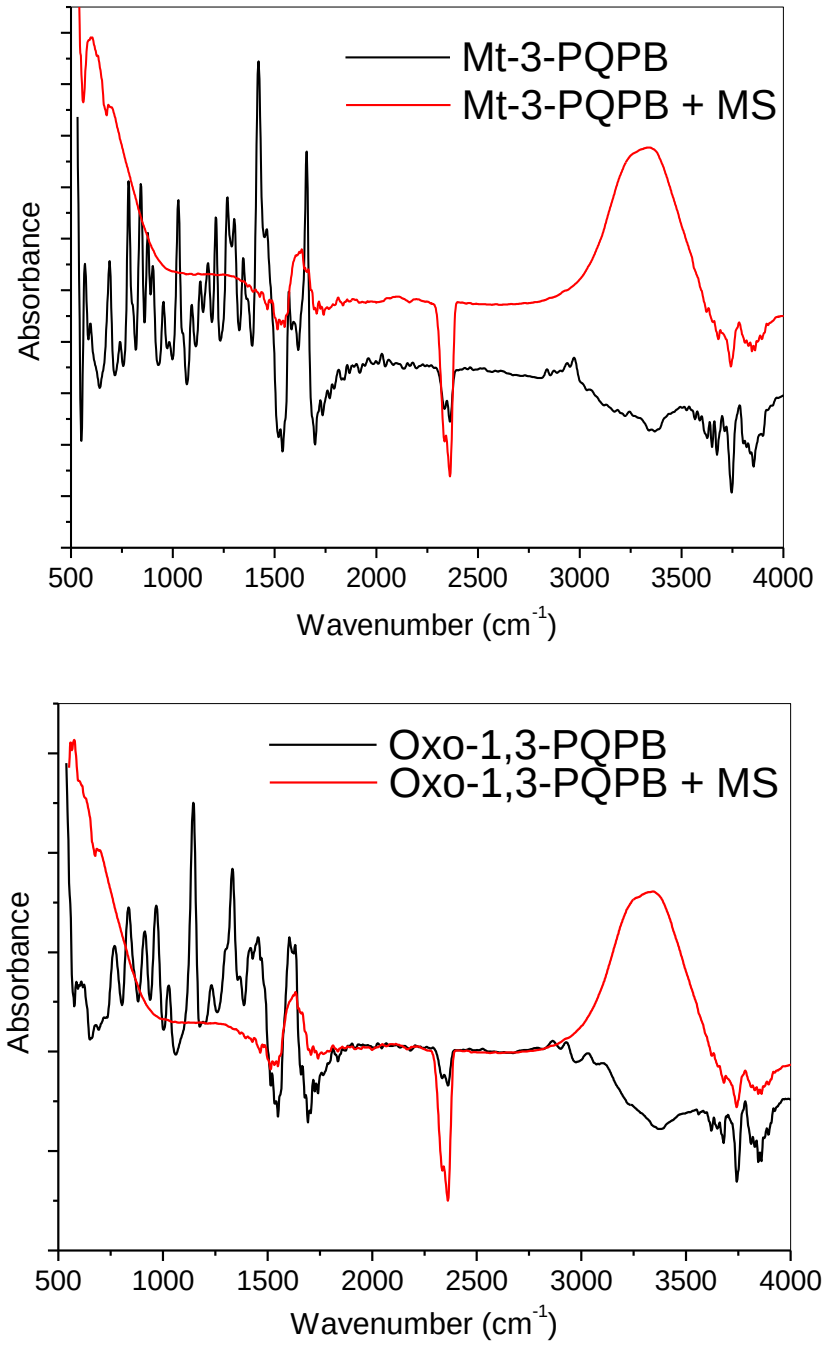

Figure AI-4. FTIR spectra of Mt-3-PQPB and Oxo-1,3-PQPB before and after MS immersion

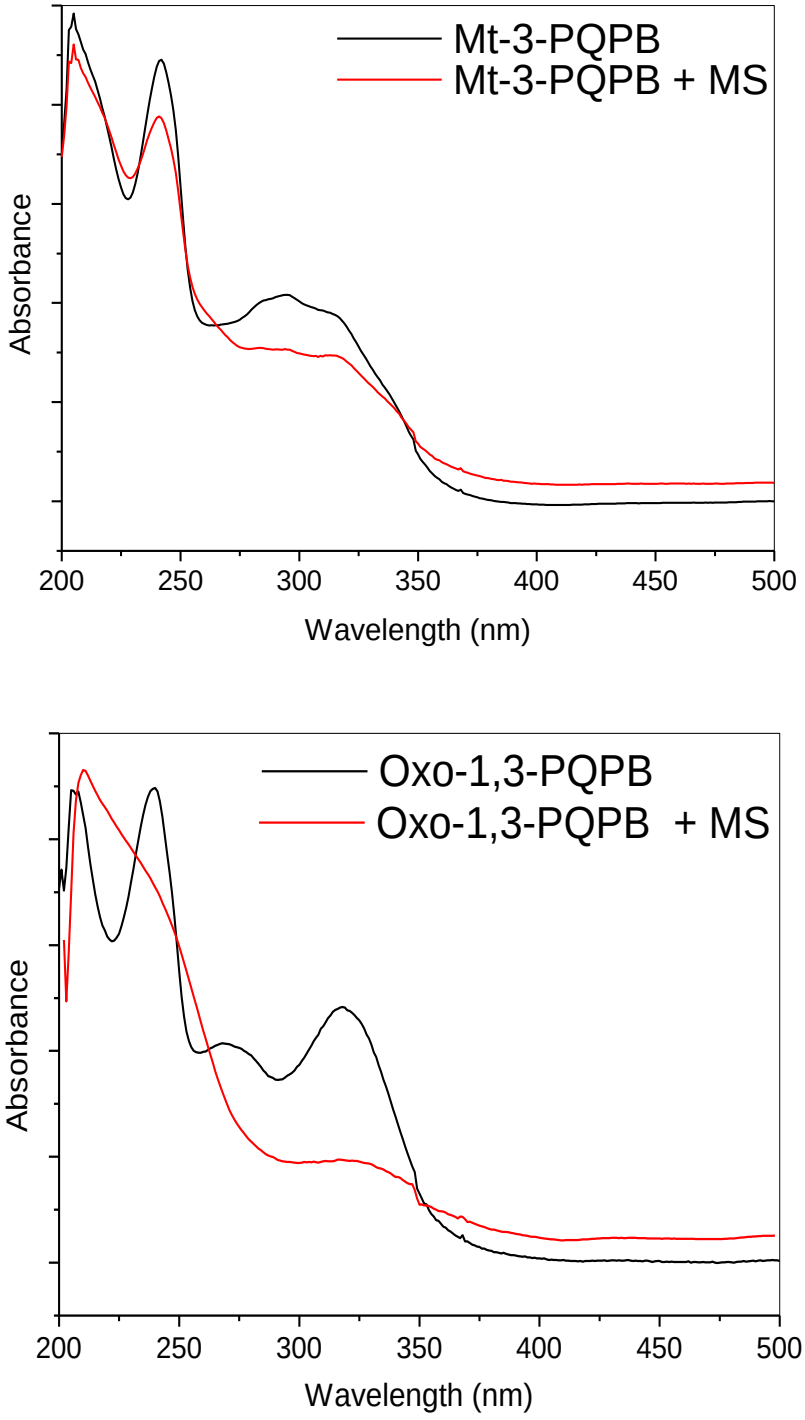

Figure AI-5. UV-vis spectra of Me-4-PQPB and Mt-4-PQPB before and after MS immersion.

Neutral

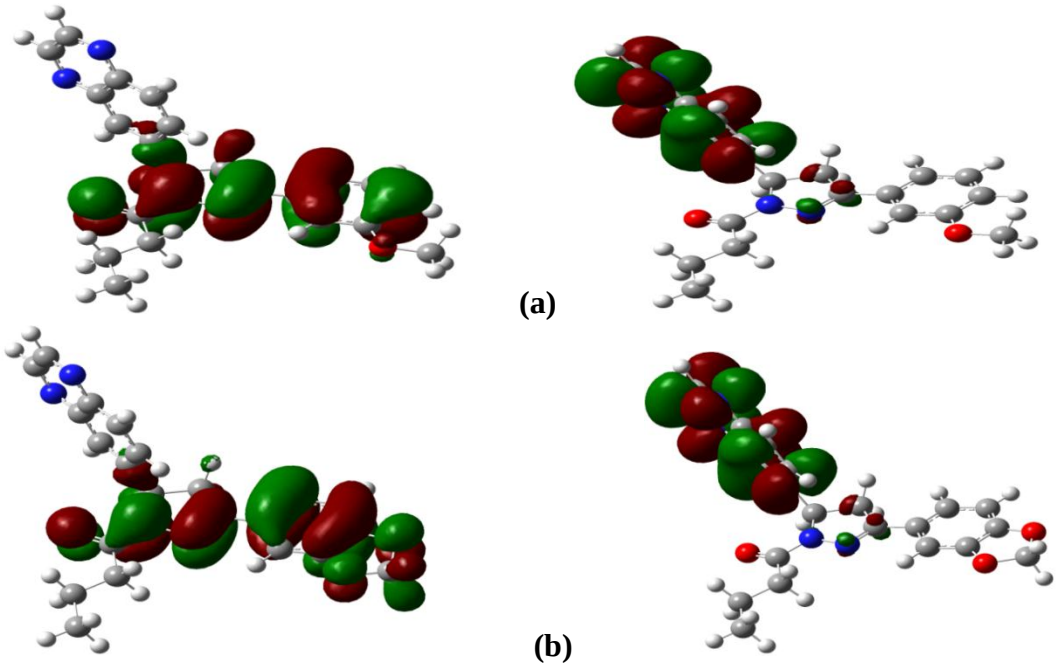

(a)

(b)

Protonated

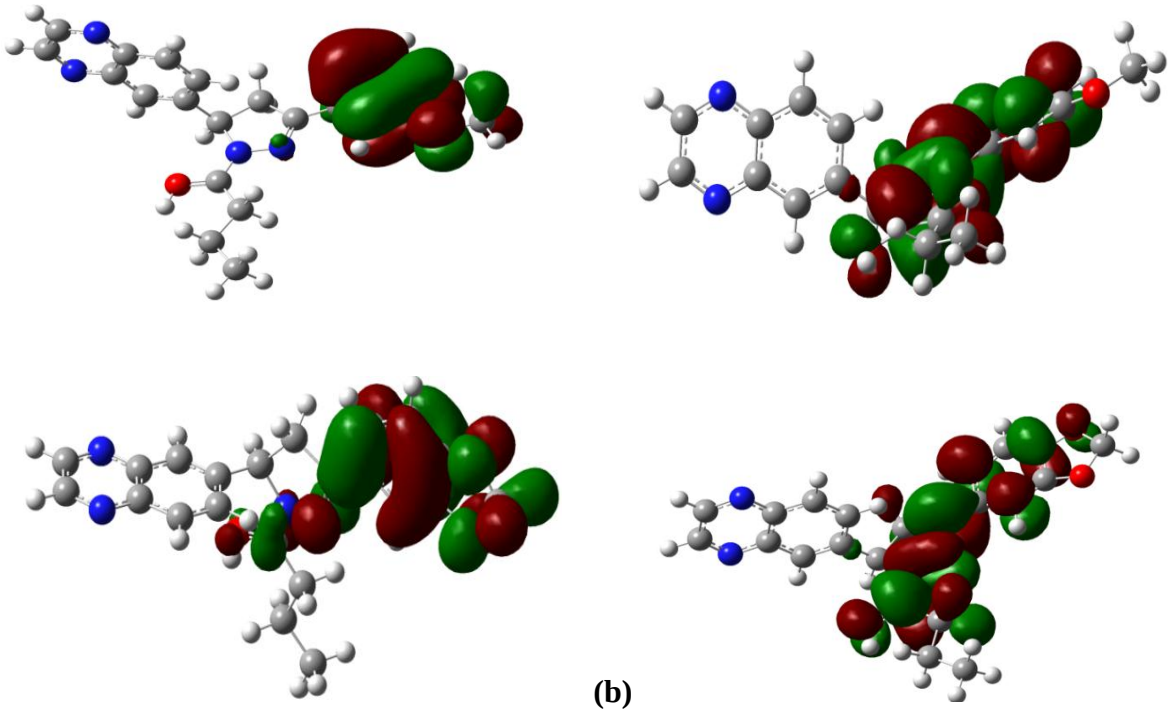

(b)

Figure AI-6. HOMO (left-hand side) and LUMO (right-hand side) electron density isosurfaces of the neutral and most stable protonated forms of (a) Mt-3- PQPB, and (b) Oxo-1,3-PQPB.

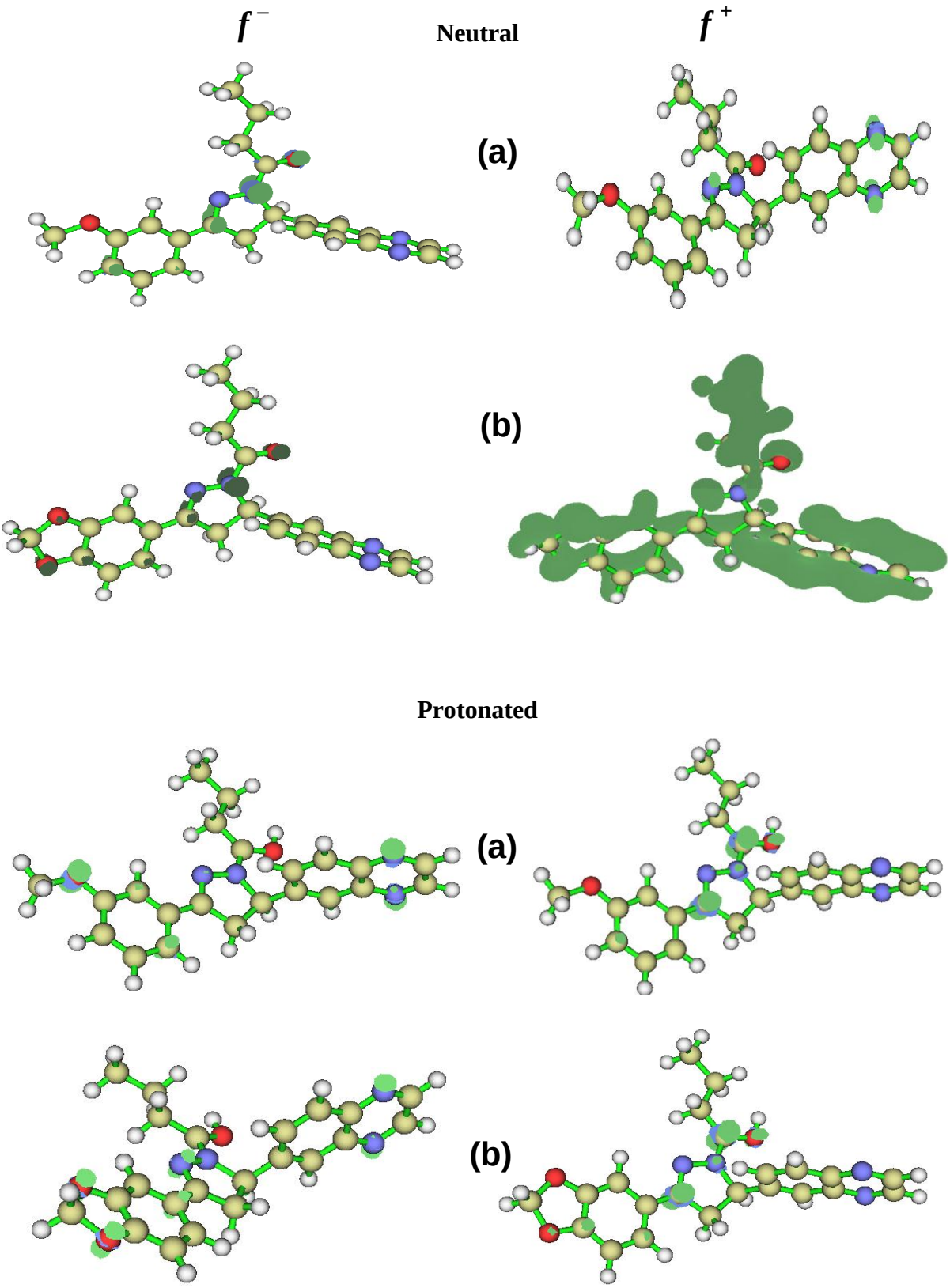

Figure AI-7. Fukui indices, f_k^- and f_k^+ for the neutral and protonated forms of (a) Mt-3-PQPB and (b) Oxo-1,3-PQPB. (*Isosurface = 0.007*)

APPENDIX II: SUPPLEMENTRARY FIGURES GROUP II

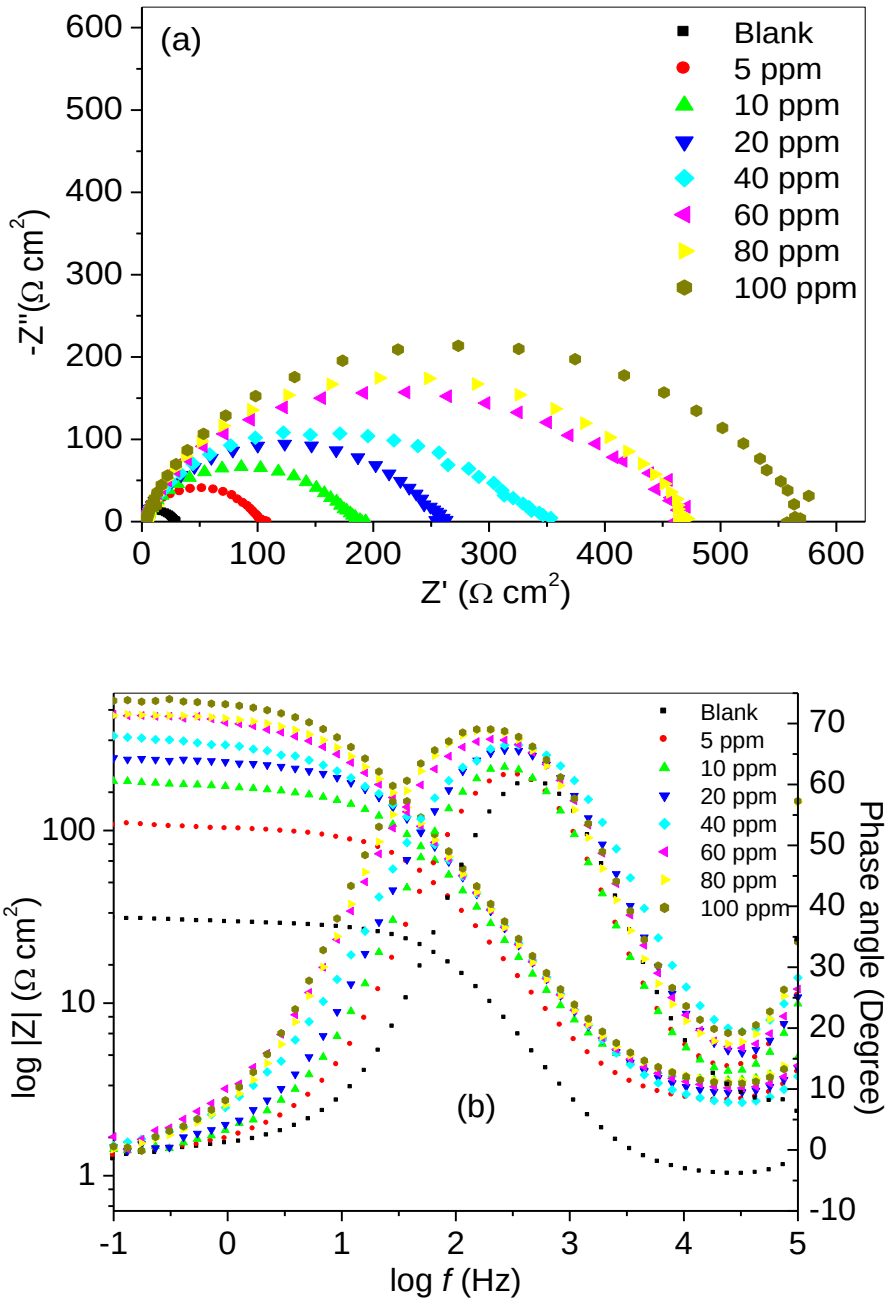

Figure AII-1. Nyquist (a) and Bode (b) plots for MS in 1 M HCl without and with various concentrations of PQDPP.

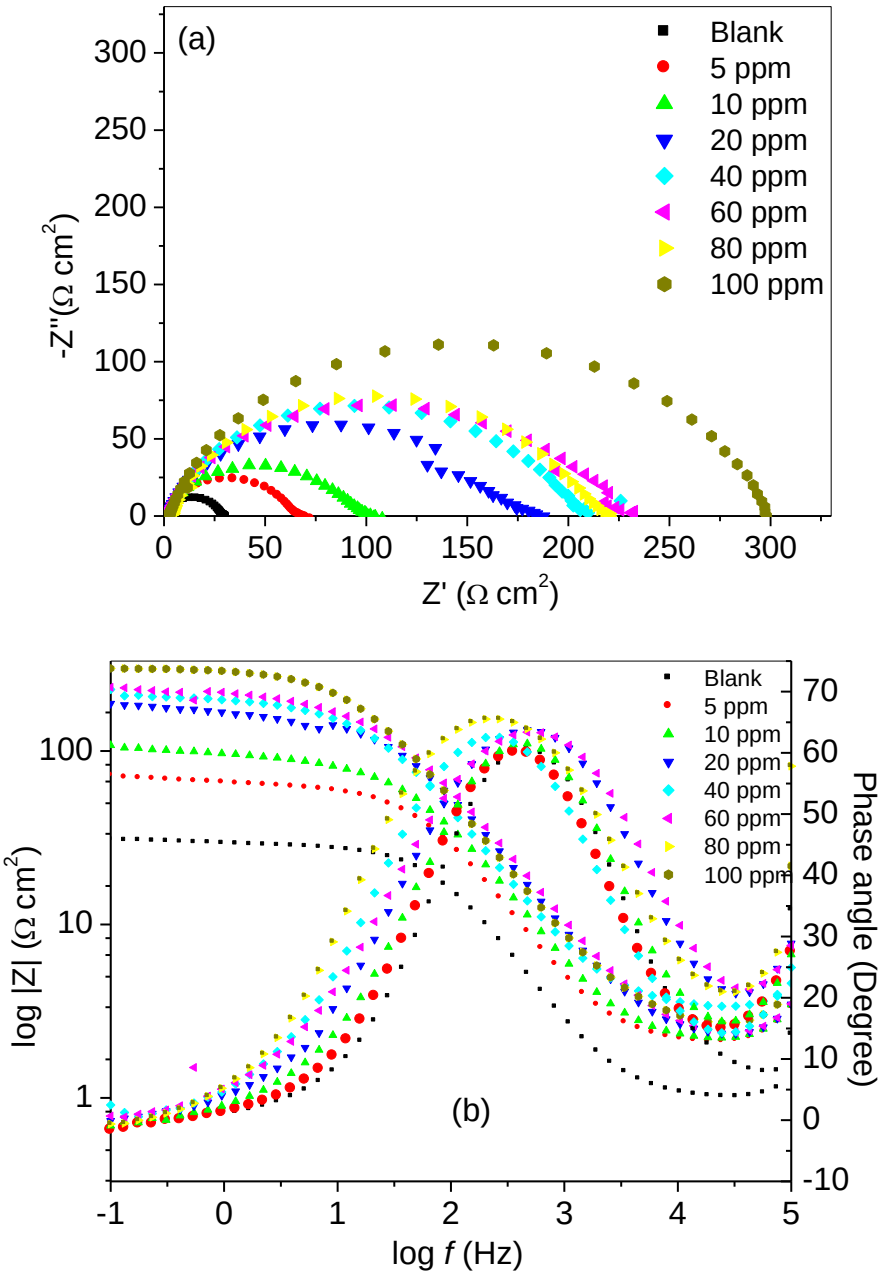

Figure AII-2. Nyquist (a) and Bode (b) plots for MS in 1 M HCl without and with various concentrations of PPQDPE.

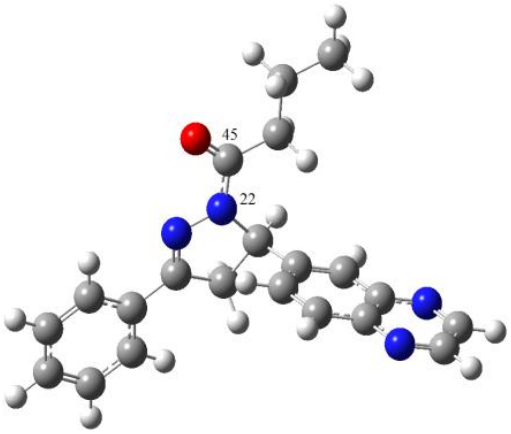

PQDPB

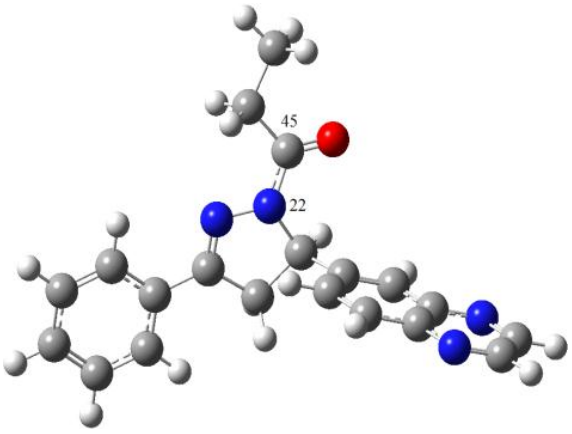

PQDPP

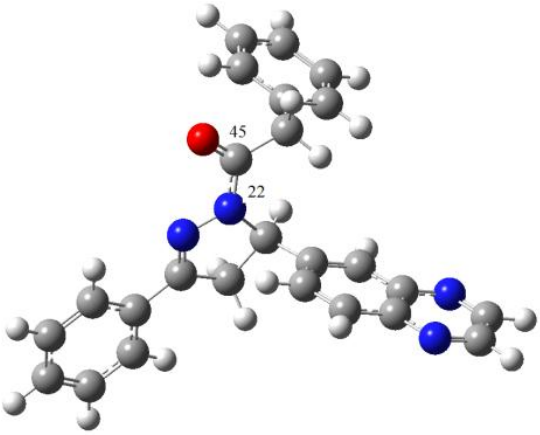

PPDQPE

Figure AII-3. Gas phase optimized structures of the neutral form of the compounds at HF/6-31G(d) level theory.

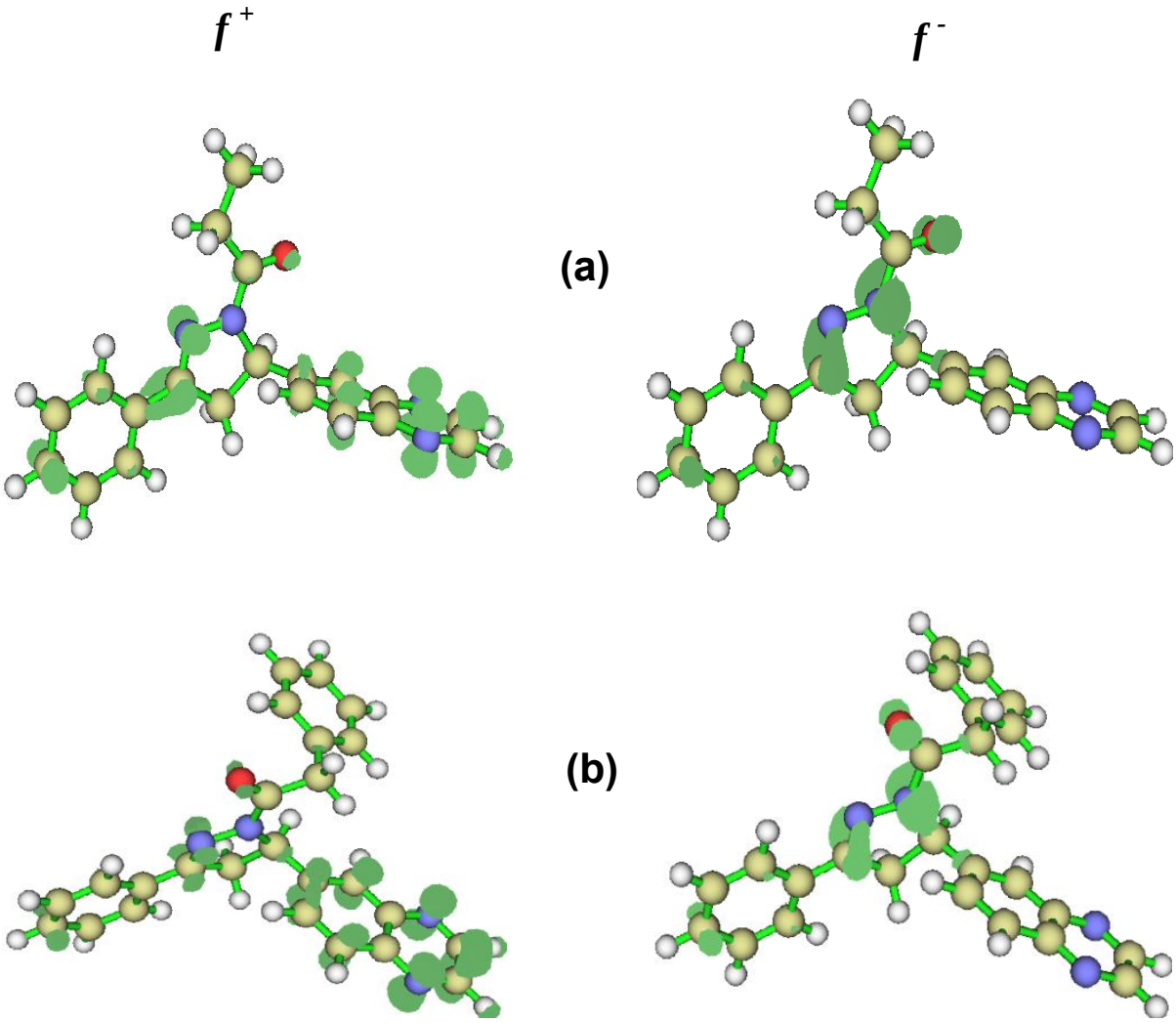

Figure AII-4. Fukui functions for the neutral form of (a) PQDPP and (b) PPQDPE.
(*Isosurface = 0.003 and 0.005 for* f^+ *and* f^- *respectively*)

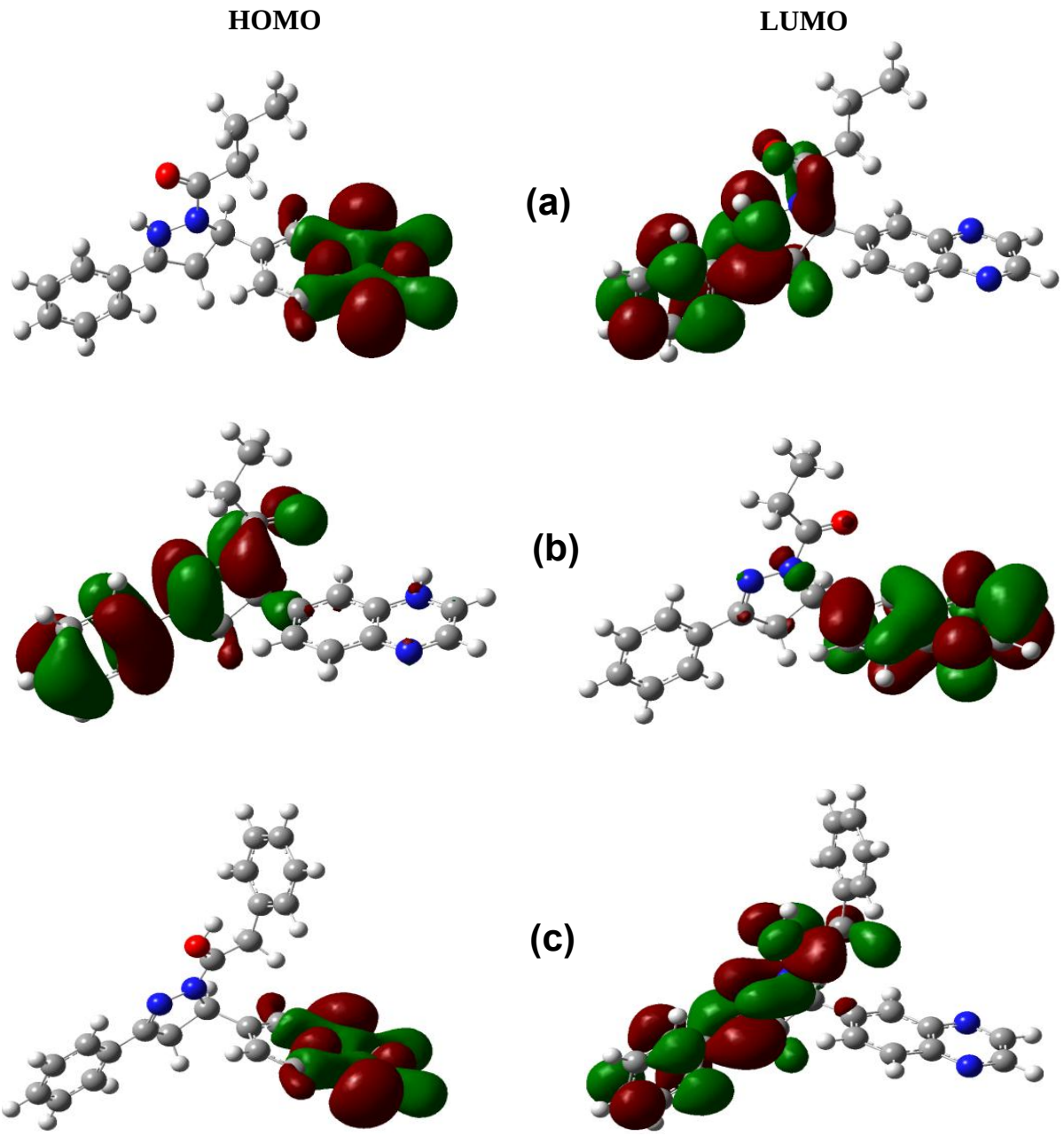

Figure AII-5. HOMO and LUMO electron density isosurfaces of the gas phase optimized structures of the most stable protonated form of (a) PQDPB, (b) PQDPP and (c) PPQDPE at B3LYP/6-31G(d) level.

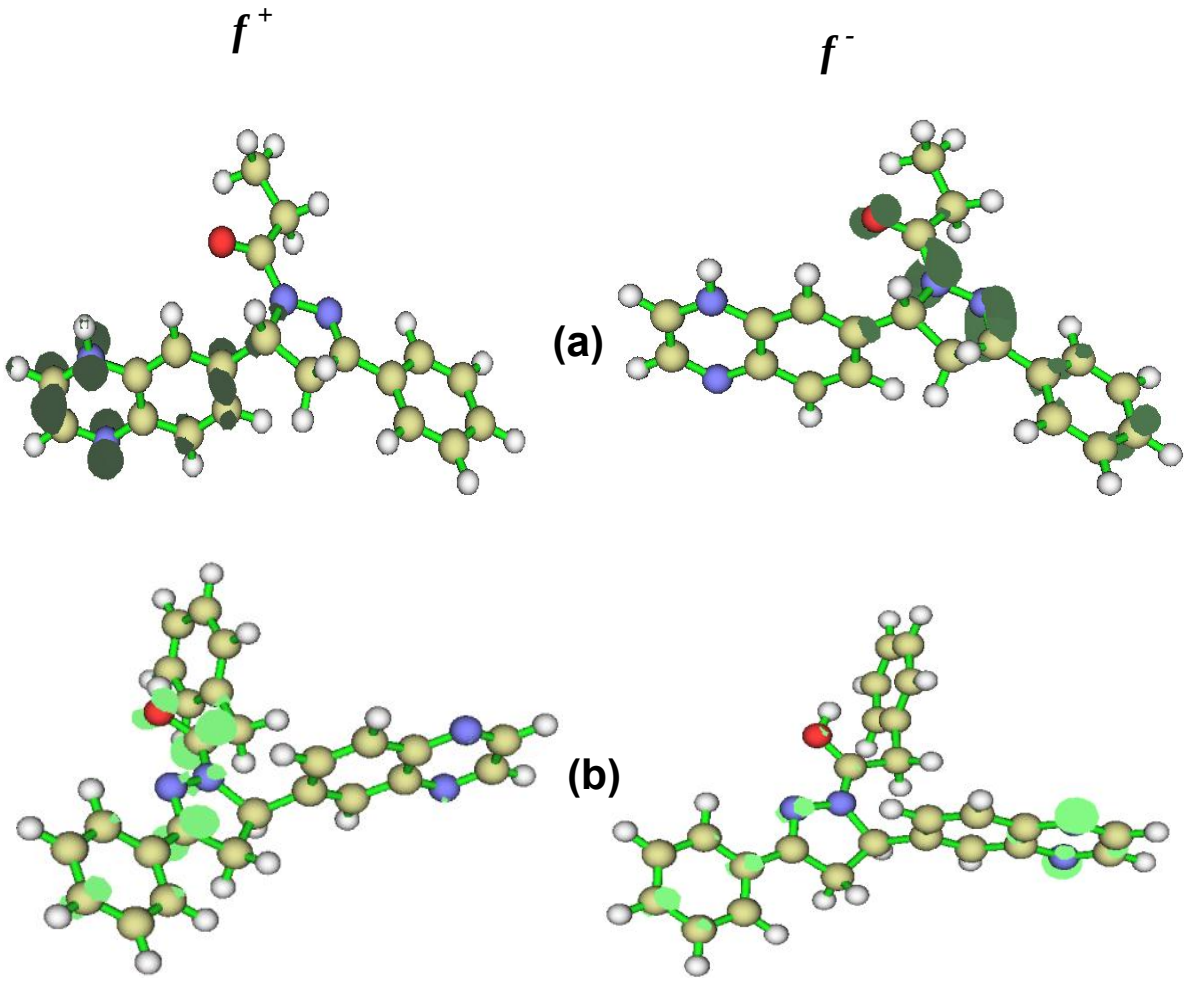

Figure AII-6. Fukui functions for the most stable protonated form of (a) PQDPP and (b) PPQDPE. (*Isosurface = 0.003 and 0.005 for* f^+ *&* f^- *respectively*)

APPENDIX III: SUPPLEMENTRARY FIGURES GROUP III

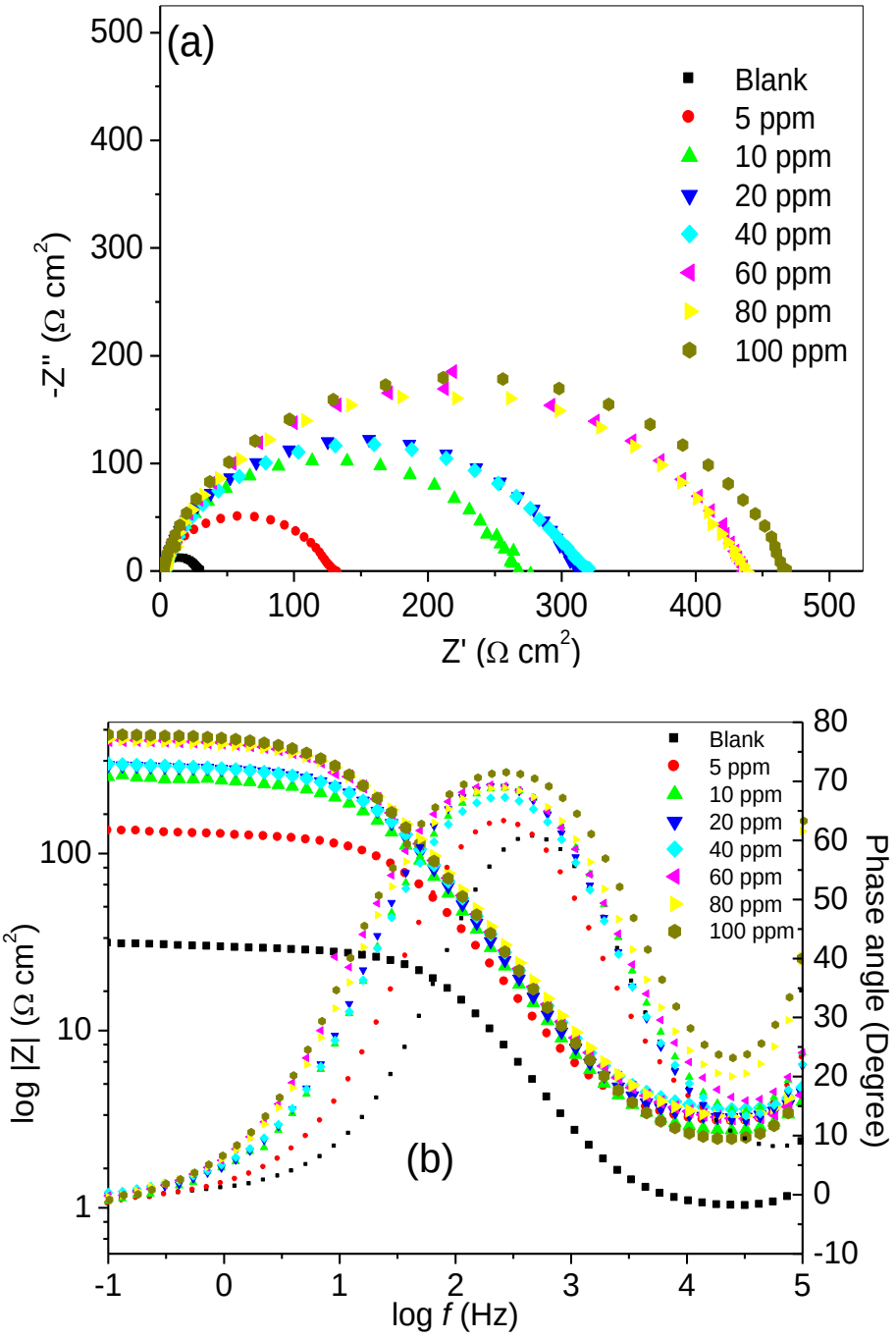

Figure AIII-1. Nyquist (a) and Bode (b) plots for MS in 1 M HCl without and with various concentrations of MS-3-PQPP.

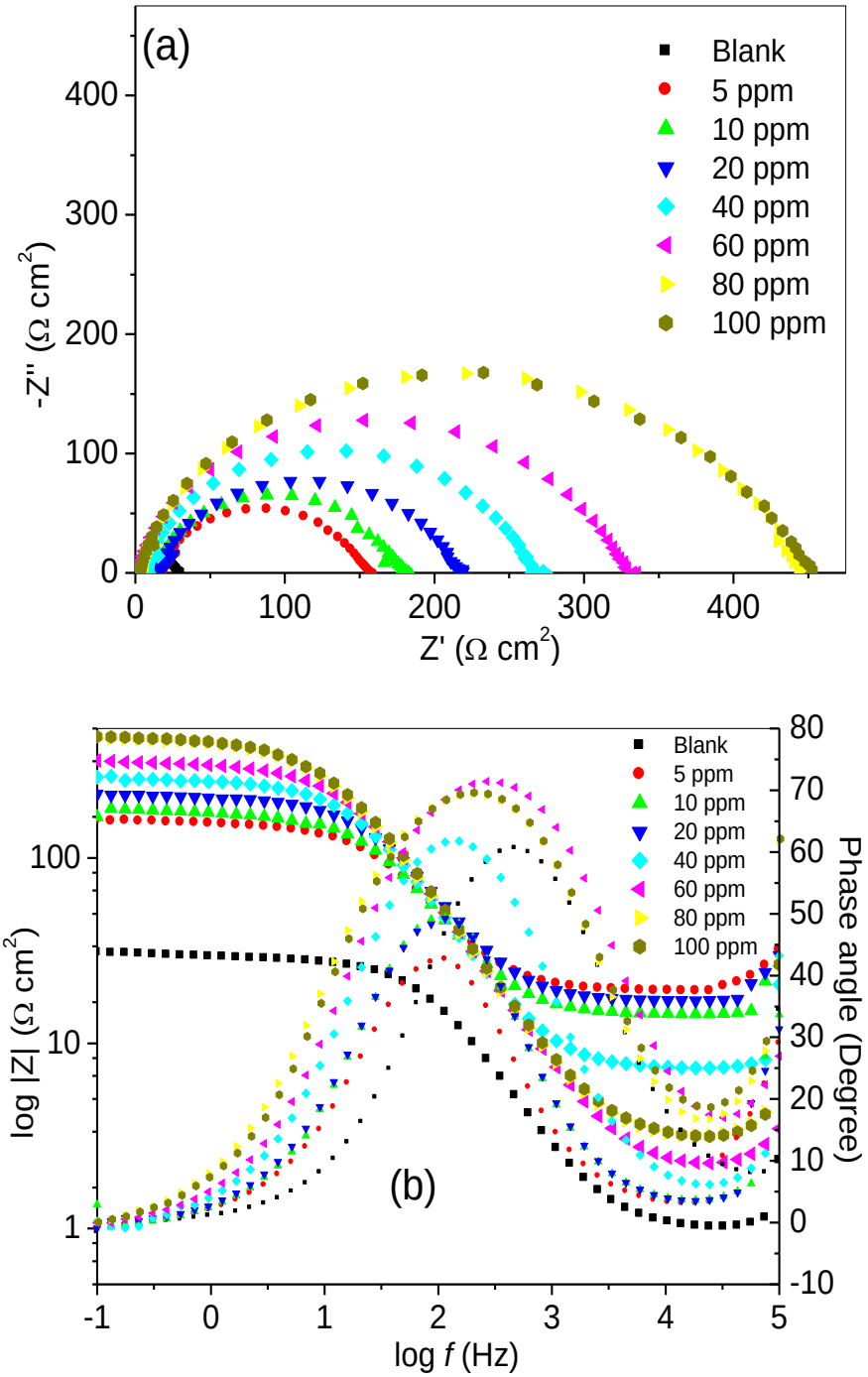

Figure AIII-2. Nyquist (a) and Bode (b) plots for MS in 1 M HCl without and with various concentrations of MS-4-PQPP.

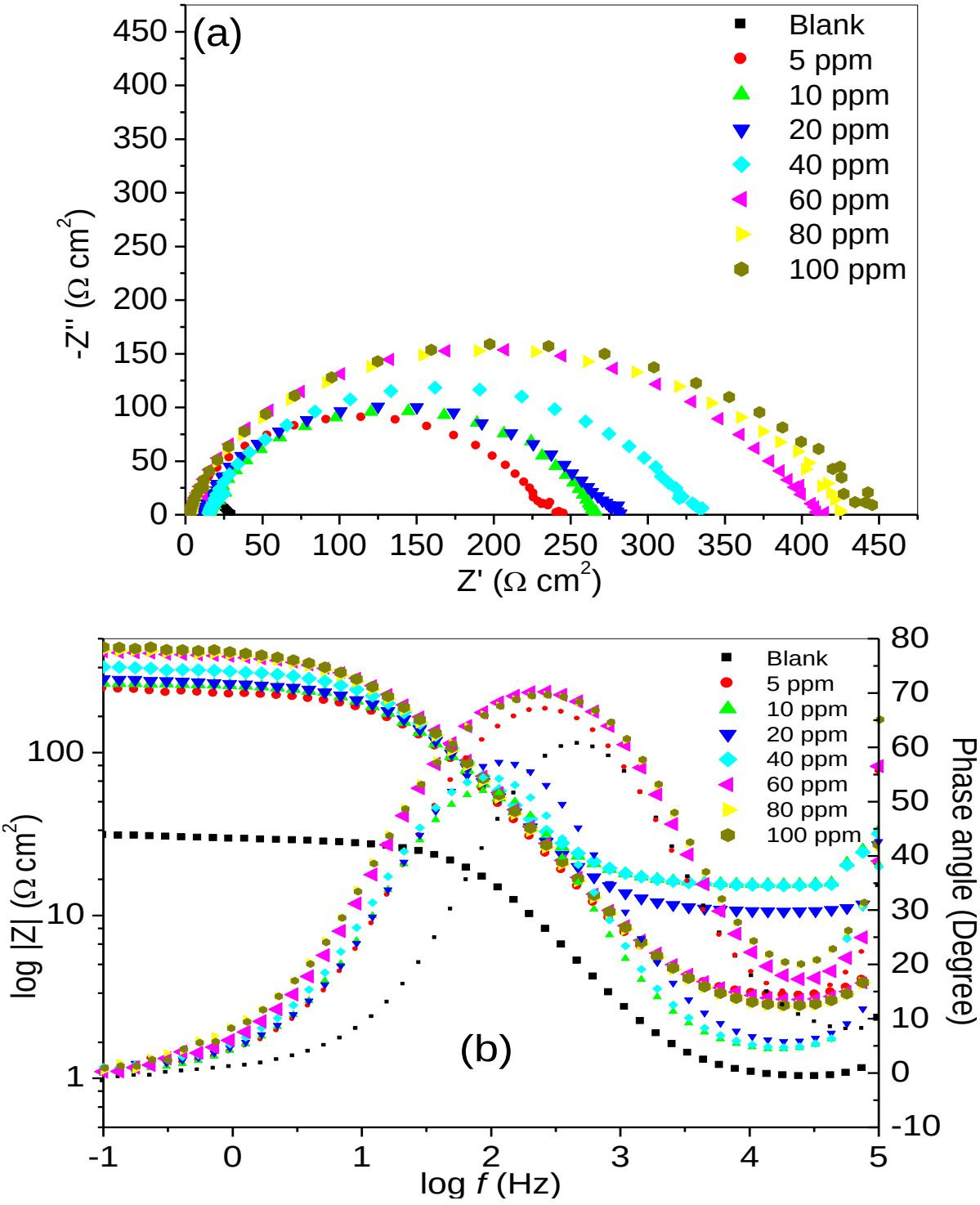

Figure AIV-1. Nyquist (a) and Bode (b) plots for MS in 1 M HCl without and with various concentrations of the inhibitors MS-3-PQPMS.

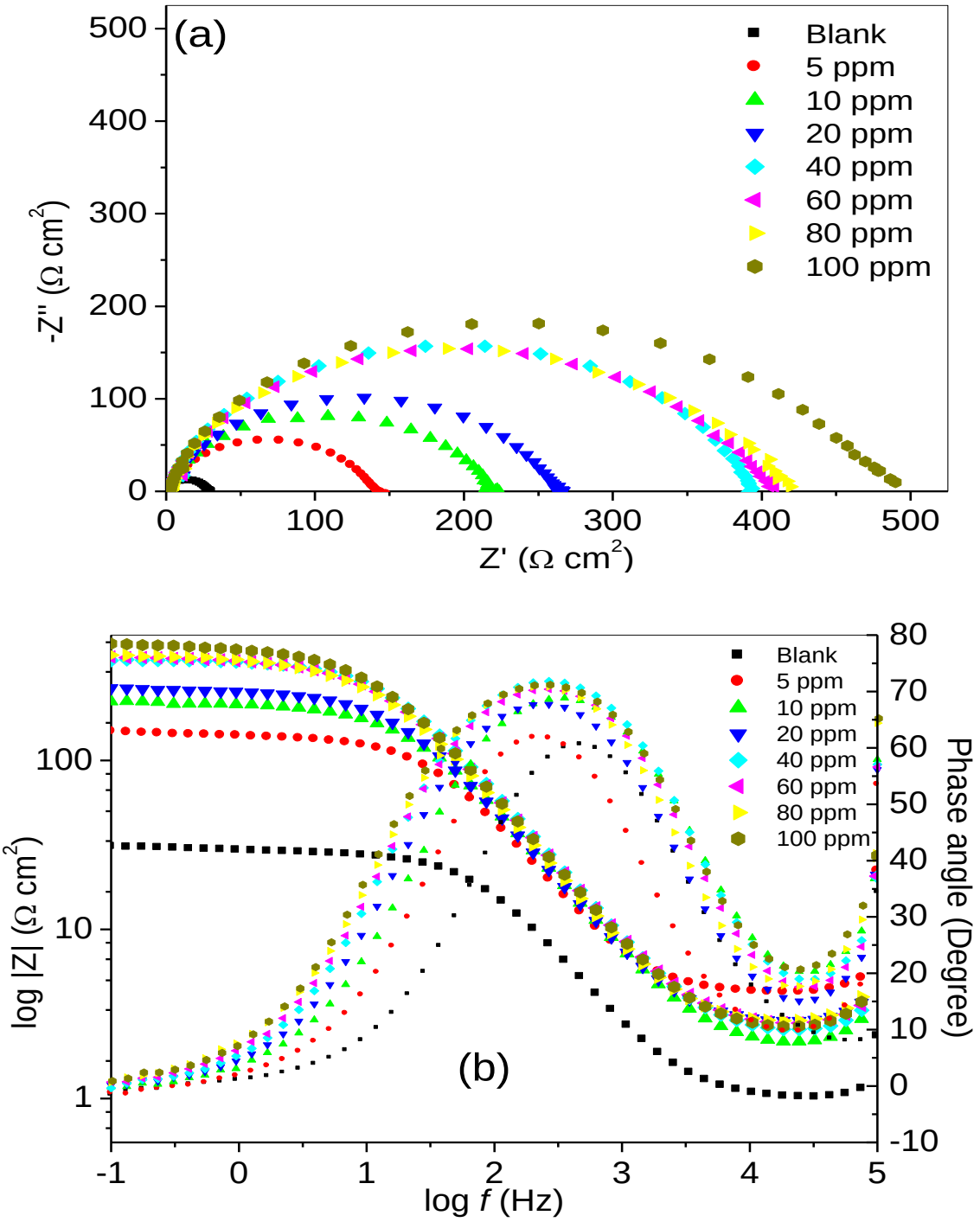

Figure AIV-2. Nyquist (a) and Bode (b) plots for MS in 1 M HCl without and with various concentrations of the inhibitors MS-4-PQPMS.

APPENDIX V: SUPPLEMENTRARY FIGURES AND TABLES FOR GROUP V

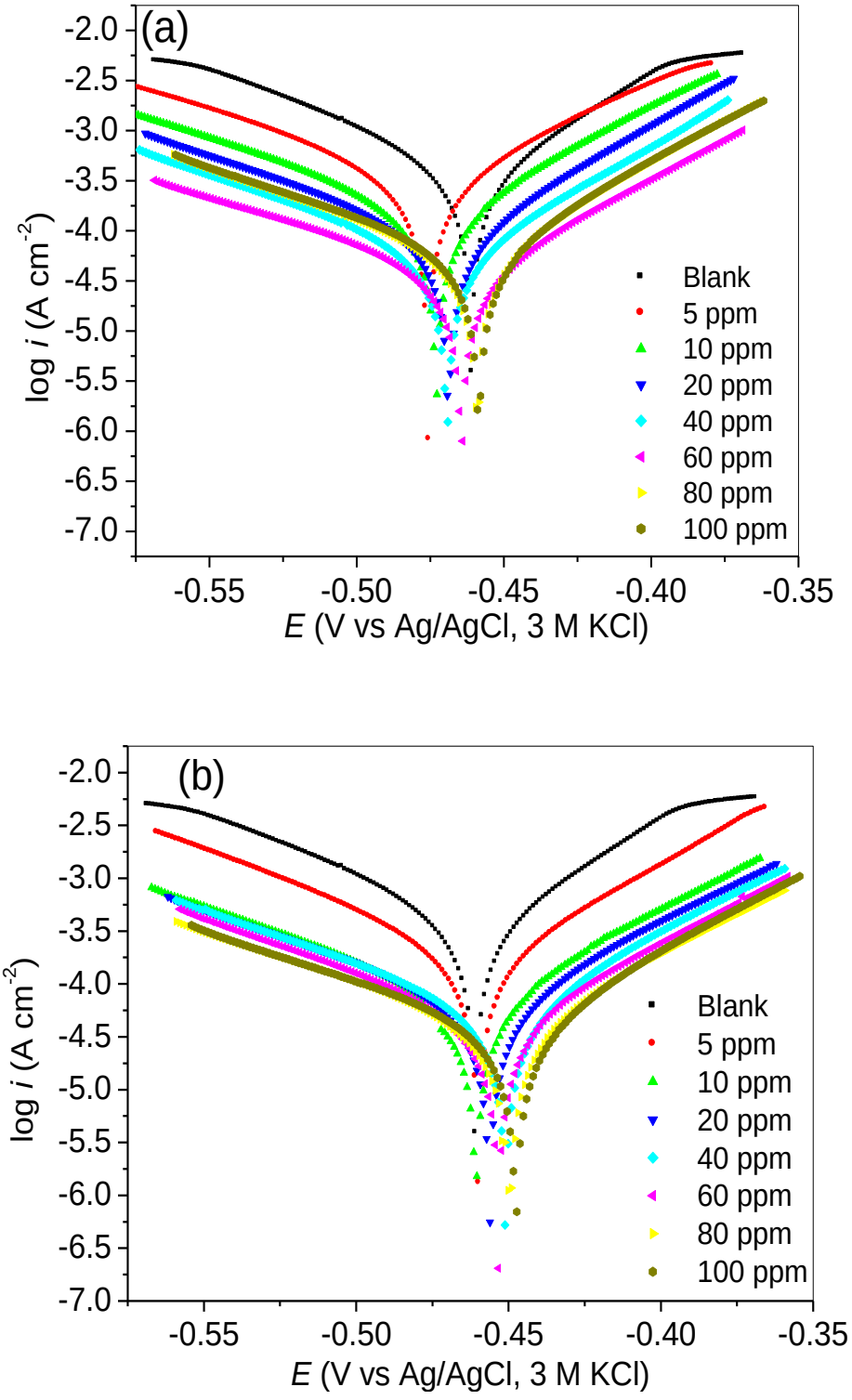

Figure AV-1. Tafel plots for MS in 1 M HCl without and with various concentrations of (a) Cl-4-PQPP, and (b) MS-4-PQPA.

Table AV-1. Tafel parameters and percentage inhibition efficiency for the corrosion of MS in 1 M HCl without and with inhibitors.

Compound	*Conc.* (ppm)	$-E_{corr}$ (mV)	i_{corr} ($\mu A/cm^2$)	β_a (mV/dec)	β_c (mV/dec)	$\%IE_P$
Blank	-	460.60	420.41	89.34	65.27	-
Mt-3-PQPP	5	461.81	95.25	89.20	68.01	77.34
	10	464.85	73.30	100.05	72.61	82.56
	20	462.23	72.53	101.48	70.28	82.75
	40	460.05	55.78	101.31	71.90	86.73
	60	462.49	45.46	104.27	75.70	89.19
	80	449.97	41.78	117.85	69.82	90.06
	100	443.66	40.85	132.42	72.42	90.28
Cl-4-PQPP	5	475.51	361.62	111.68	82.70	13.98
	10	472.99	156.16	104.05	69.06	62.86
	20	468.81	90.49	100.93	62.72	78.48
	40	469.39	56.67	99.40	63.55	86.52
	60	464.38	42.79	122.32	71.77	89.82
	80	459.09	58.98	106.72	63.61	85.97
	100	458.53	64.47	113.05	64.57	84.66
MS-2-PQPA	5	465.04	45.25	93.78	78.28	89.24
	10	463.06	68.29	95.54	76.14	83.76
	20	467.18	89.35	99.18	73.79	78.75
	40	466.87	79.20	99.37	76.04	81.16
	60	456.37	92.02	96.05	72.85	78.11
	80	450.02	47.57	128.98	79.52	88.68
	100	448.86	45.53	119.50	70.83	89.17
MS-4-PQPA	5	459.63	174.74	85.01	66.76	54.44
	10	460.76	75.15	103.82	71.68	82.12
	20	456.23	71.52	111.71	73.51	82.99
	40	451.05	61.76	110.54	69.88	83.38
	60	453.26	45.63	100.90	70.45	89.15
	80	449.62	42.85	118.01	72.12	89.81
	100	448.01	43.03	120.89	65.92	89.76

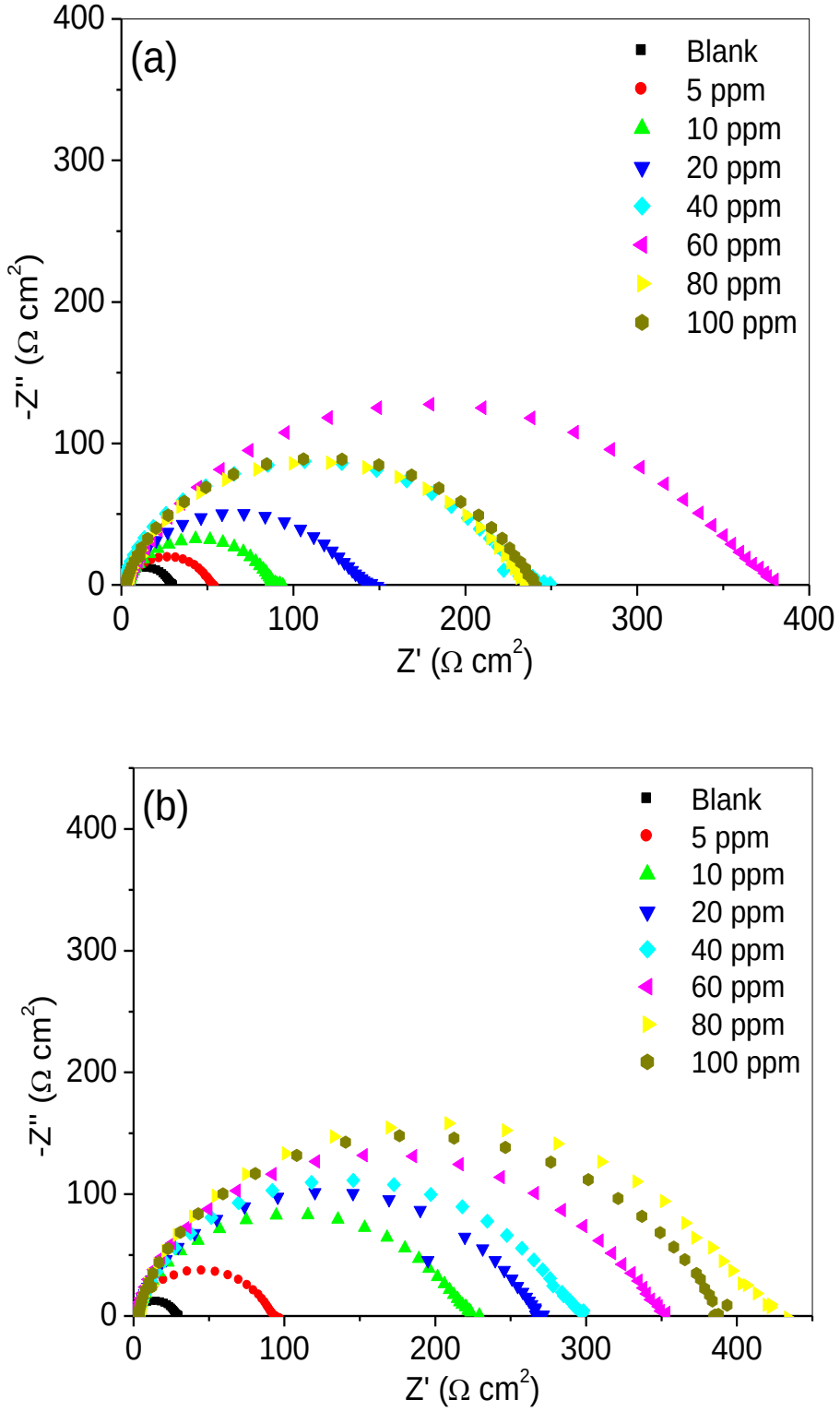

Figure AV-2. Nyquist plots for MS in 1 M HCl without and with various concentrations of the inhibitors (a) Cl-4-PQPP, and (b) MS-4-PQPA.

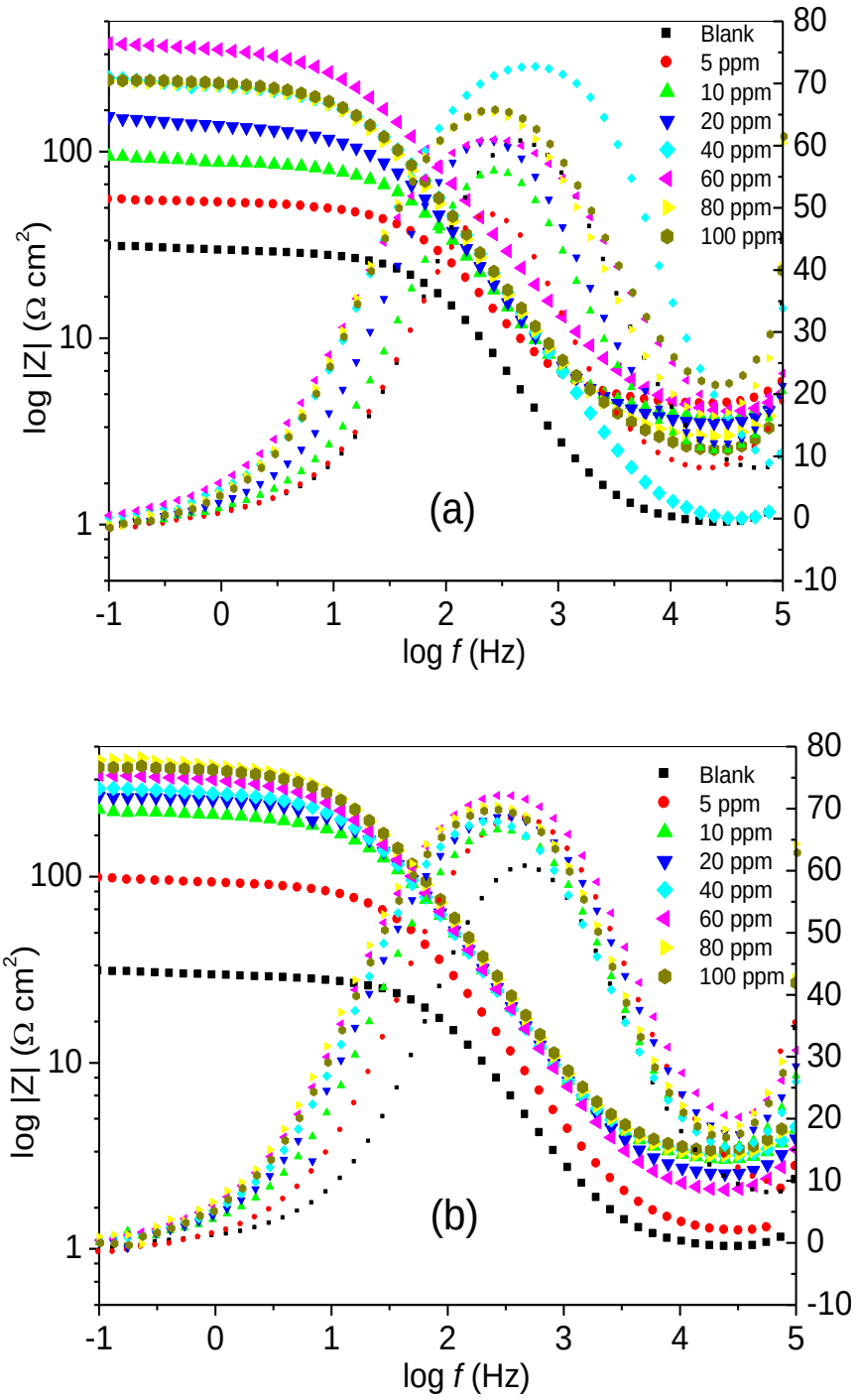

Figure AV-3. Bode plots for MS in 1 M HCl without and with various concentrations of the inhibitors (a) Cl-4-PQPP, and (b) MS-4-PQPA.

Table AV-2. EIS parameters and percentage inhibition efficiency for the corrosion of MS in 1 M HCl without and with various concentrations of the inhibitors.

Compound	*Conc.* (ppm)	R_s (Ωcm^2)	R_{ct} (Ωcm^2)	Y_o ($\mu Ss^n cm^{-2}$)	*n*	$\lvert\Theta\rvert$ (Degree)	$\lvert S\rvert$	$\%IE_I$
Blank	-	1.01	28.20	157	0.893	60.59	0.64	-
Mt-3-PQPP	5	2.36	143	72.9	0.884	65.79	0.76	80.28
	10	2.64	225	65.4	0.875	67.10	0.79	87.47
	20	2.52	236	69.0	0.869	67.33	0.79	88.05
	40	2.98	294	70.5	0.859	66.72	0.80	90.41
	60	2.98	363	71.4	0.842	66.60	0.79	92.23
	80	2.95	399	69.8	0.846	67.66	0.80	92.93
	100	5.68	447	79.1	0.824	62.67	0.76	93.69
Cl-4-PQPP	5	4.43	48.3	123	0.867	48.72	0.59	41.62
	10	3.77	85.0	99.7	0.854	55.96	0.66	66.82
	20	3.45	137	93.7	0.852	60.73	0.73	79.42
	40	1.01	225	59.3	0.895	72.71	0.80	87.47
	60	3.70	365	76.7	0.792	60.96	0.72	92.27
	80	2.80	228	84.7	0.850	65.32	0.78	87.63
	100	2.29	237	85.7	0.837	65.99	0.78	88.10
MS-2-PQPA	5	2.05	330	58.2	0.862	69.91	0.80	91.46
	10	2.25	222	70.3	0.875	68.71	0.80	87.30
	20	2.41	163	74.2	0.867	65.90	0.75	82.70
	40	2.03	196	70.2	0.866	67.82	0.78	85.61
	60	2.27	165	88.4	0.874	66.68	0.79	82.91
	80	21.0	415	55.9	0.864	55.18	0.67	93.20
	100	2.86	391	67.3	0.853	68.69	0.81	92.79
MS-4-PQPA	5	1.23	90.6	85.8	0.899	68.36	0.75	68.87
	10	2.90	214	63.5	0.869	66.61	0.77	86.82
	20	2.39	257	61.0	0.871	68.68	0.79	89.03
	40	3.07	285	65.3	0.868	67.93	0.81	90.10
	60	1.93	336	58.5	0.880	72.09	0.83	91.61
	80	2.93	404	55.2	0.873	70.47	0.83	93.02
	100	3.16	376	51.6	0.877	70.03	0.82	92.50

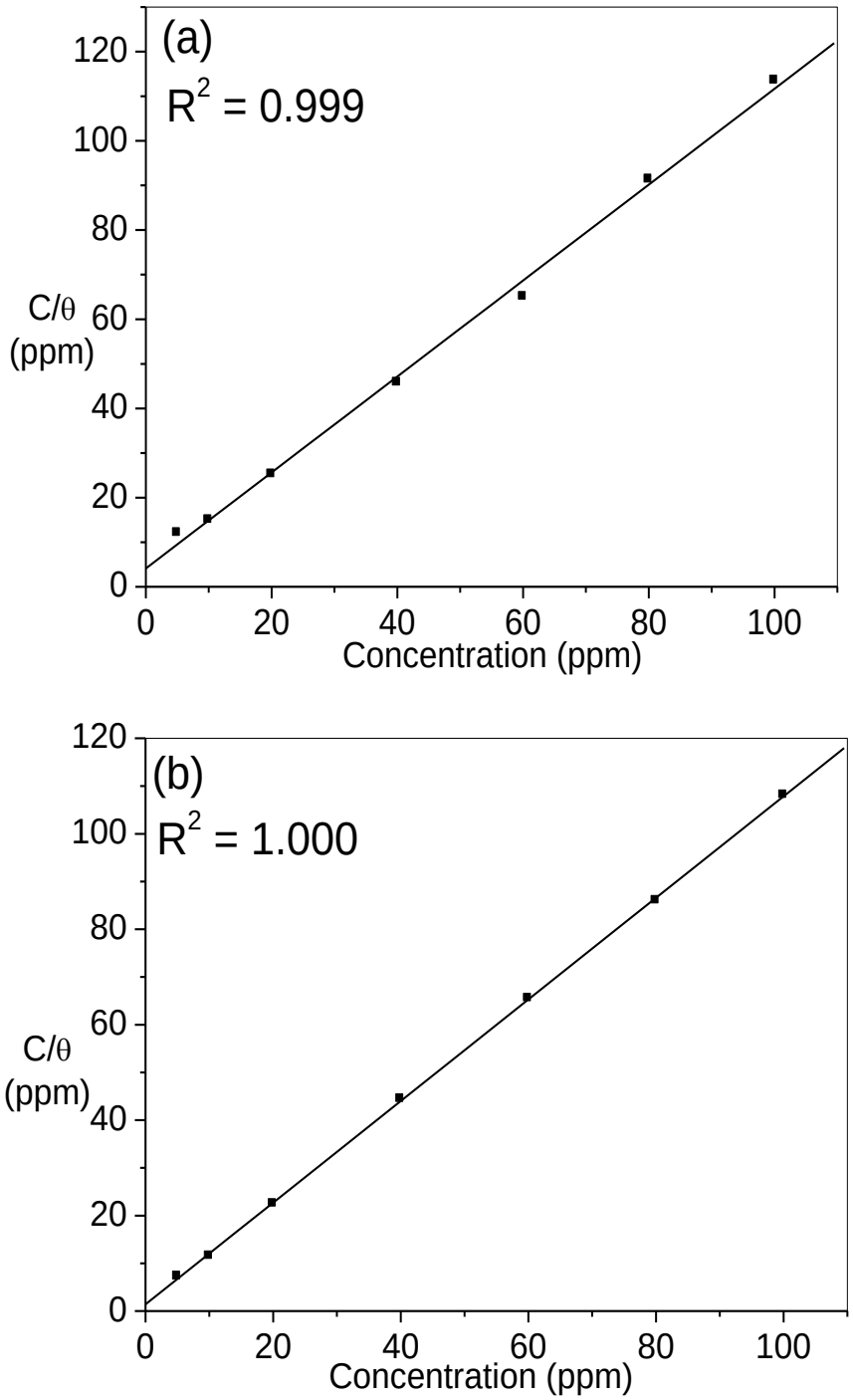

Figure AV-4. Langmuir adsorption isotherms for (a) Cl-4-PQPP, and (b) MS-4-PQPA on MS in 1 M HCl. (*Experimental data were taken from the EIS measurements*).

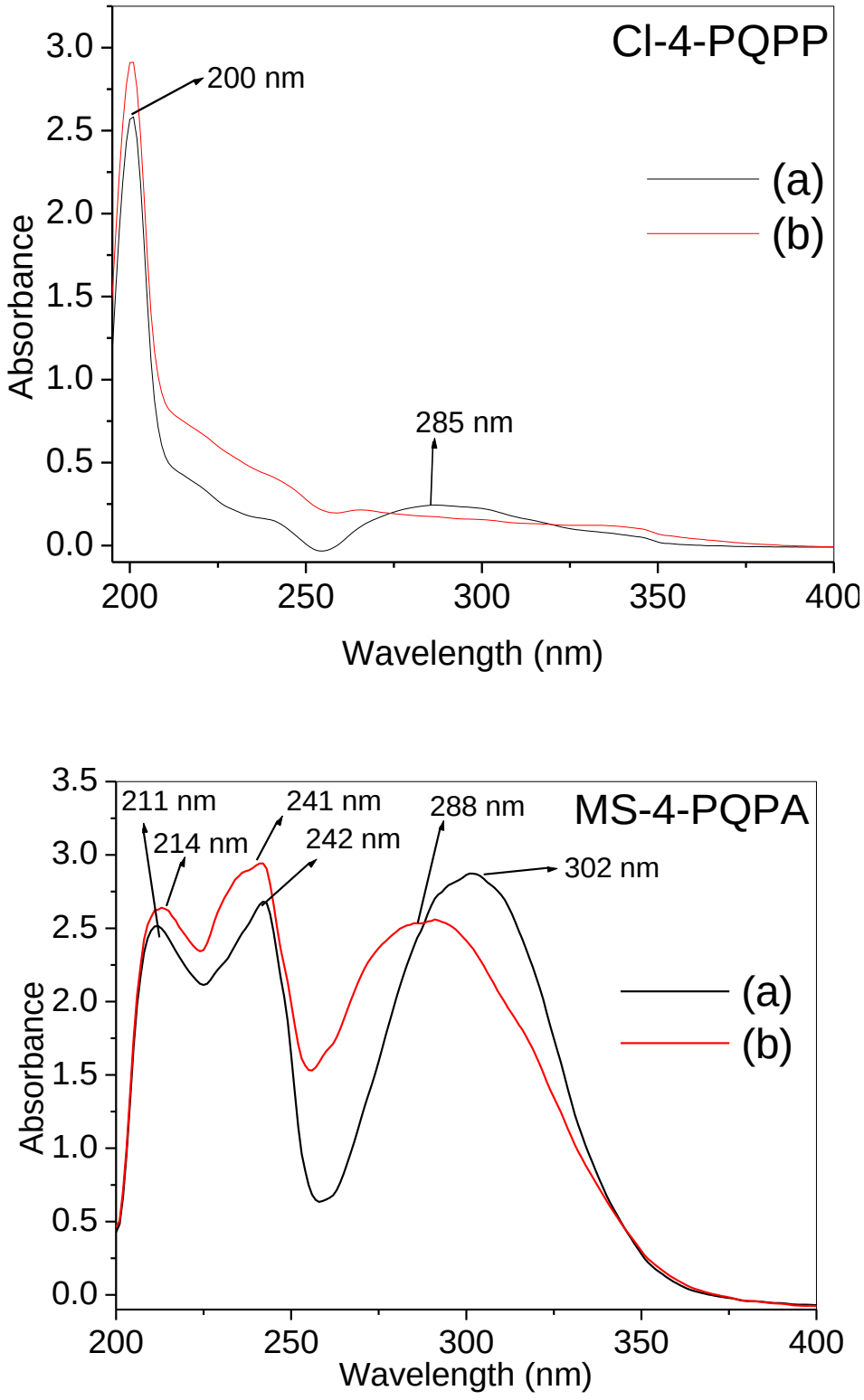

Figure AV-5. UV-vis spectra of the acidic solutions of Cl-4-PQPP and MS-4-PQPA **(a)** before, and **(b)** after MS immersion.

Optimized structures

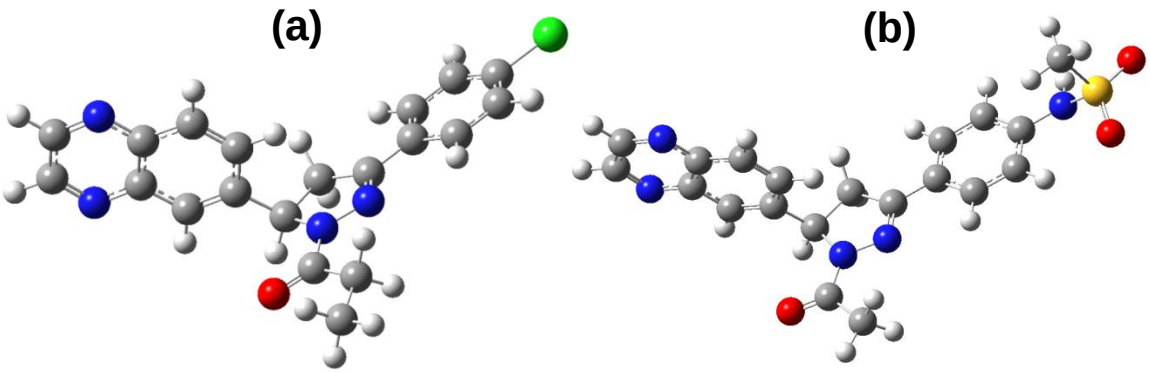

HOMO

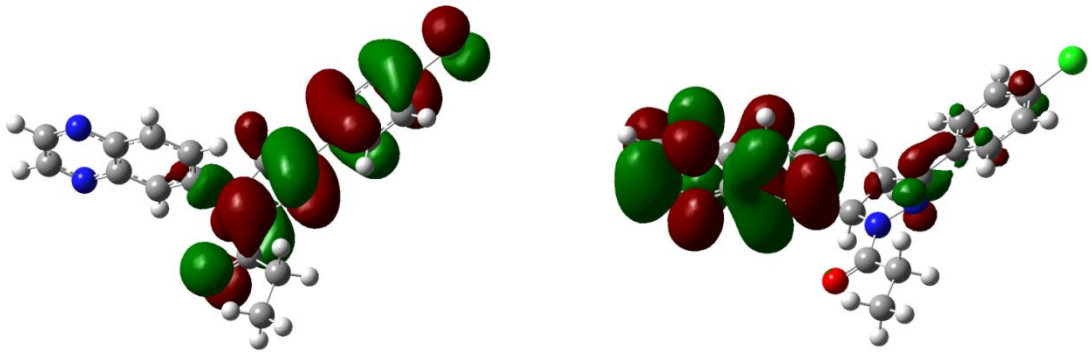

LUMO

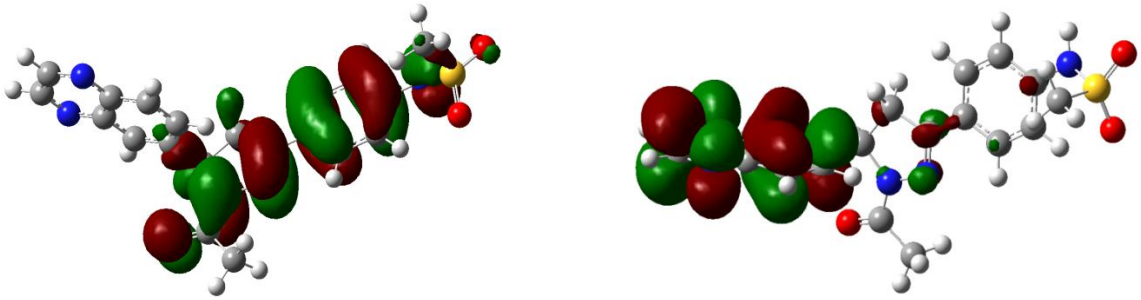

Figure AV-6. Optimized structures, HOMO and LUMO of neutral molecules of (a) Cl-4-PQPP, and (b) MS-3-PQPA at B3LYP/6-31G(d) level of theory.

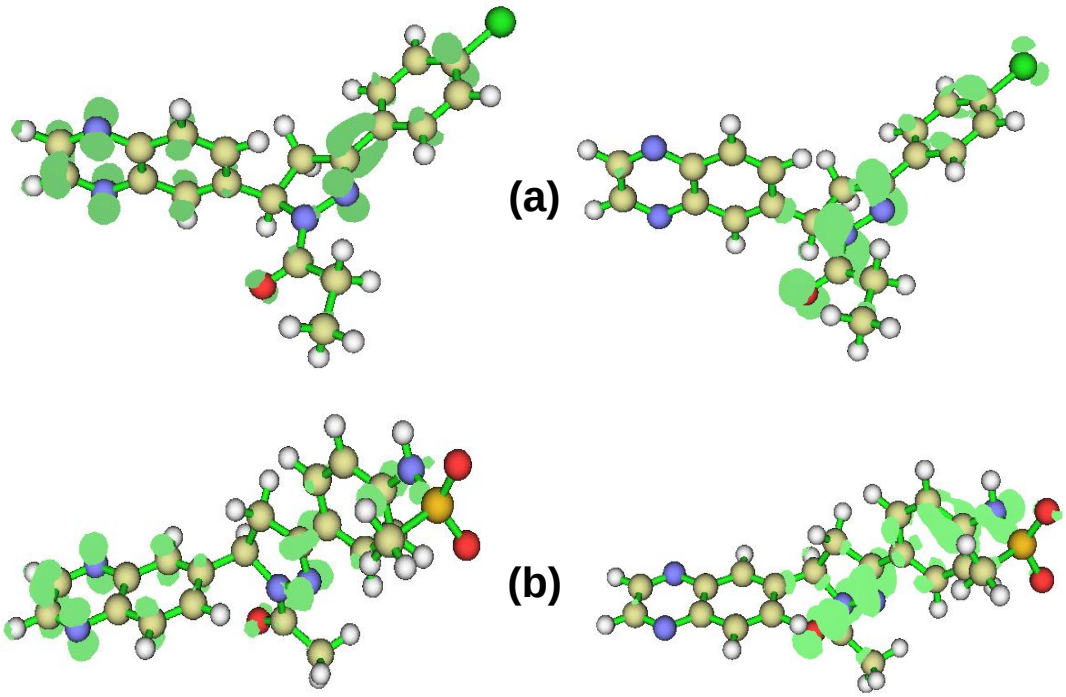

Figure AV-7. Fukui functions, f^{+}(left-hand side) and f^{-} (right-hand side) for (a) Cl-4-PQPP, and (b) MS-3-PQPA. (*Isosurface = 0.003*)

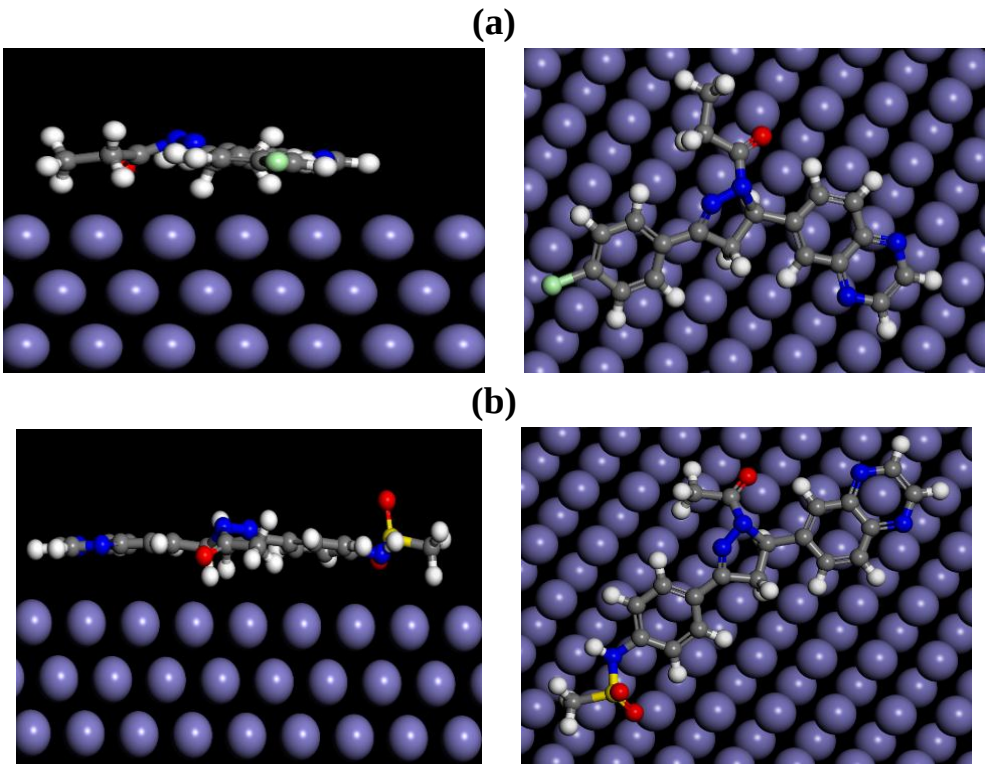

Figure AV-8. Side (left-hand side) and top (right-hand side) views of the most stable configurations of the interactions of (a) Cl-4-PQPP, and (b) MS-3-PQPA with Fe (110) surface using molecular dynamics simulations.

APPENDIX VI: PUBLISHED ARTICLES

1. **Olasunkanmi, L. O.**; Obot, I. B.; Kabanda, M. M.; Ebenso, E. E. Some quinoxalin-6-yl derivatives as corrosion inhibitors for MS in hydrochloric acid: experimental and theoretical studies. **The *Journal of Physical Chemistry C* 2015,** *119,* 16004−16019.
2. **Olasunkanmi, L. O.**; Kabanda, M. M.; Ebenso, E. E. Quinoxaline derivatives as corrosion inhibitors for MS in hydrochloric acid medium: Electrochemical and quantum chemical studies. ***Physica E: Low-dimensional Systems and Nanostructures* 2016,** *76,* 109–126.

APPENDIX VII: SUBMITTED ARTICLES

Olasunkanmi, L. O. and Ebenso, E. E. Adsorption and corrosion inhibition behaviour of some N-{*n*-[1-*R*-5-(quinoxalin-6-yl)-4,5-dihydropyrazol-3-yl]phenyl}methanesulfonamides on MS in 1 M HCl (*n* = 2, 3, 4; *R* = propanoyl, methylsulfonyl): Experimental and theoretical studies.

APPENDIX VIII: CONFERENCES AND WORKSHOPS ATTENDED

1. A workshop on "Introduction to Gaussian (theory and model)" at University of Ulm, Germany – July, 2014.
2. 227TH ECS Meeting, May, 2015 - Hilton Chicago, Illinois, U.S.A.

   Oral presentation: Electrochemical, spectroscopic and quantum chemical calculation studies on some quinoxaline derivatives as corrosion inhibitors for MS in hydrochloric acid medium.
3. SACI Young Chemist Symposium, November, 2015 – University of South Africa (UNISA) Science Campus, Florida, Roodepoort, South Africa.

   Oral presentation: Adsorption and corrosion inhibition characteristics of some quinoxalin-6-yl based sulphonamides on MS in 1 M HCl: Experimental and theoretical studies.
4. 42nd National Convention of the South African Chemical Institute, December, 2015 – Southern Sun Elangeni & Maharani, Durban, South Africa.

   Oral presentation: Experimental and theoretical studies of some quinoxaline-pyrazole-carbonyl compounds as corrosion inhibitors for MS in 1 M HCl.